STEADY CRACK GROWTH THROUGH DUCTILE METALS: COMPUTATIONAL STUDIES

BY

JAMES C. SOBOTKA

DISSERTATION

Submitted in partial fulfillment of the requirements
for the degree of Doctor of Philosophy in Civil Engineering
in the Graduate College of the
University of Illinois at Urbana-Champaign, 2010

Urbana, Illinois

Doctoral Committee:

Professor Robert H. Dodds Jr., Chair
Professor Petros Sofronis
Professor Armand J. Beaudoin
Assistant Professor C. Armando Duarte

Abstract

This thesis examines the crack-front response during sustained ductile tearing in structural metals at quasi-static rates using high resolution finite element computations. At load levels approaching the steady-growth regime, well-established computational methods that model material damage break down numerically as vanishingly small load increments produce increasingly large amounts of crack extension. The computational model adopted here determines the deformation history of a steadily advancing crack directly without the need for a priori (transient) analysis that considers blunting of the pre-existing stationary crack and subsequent growth through the associated initial plastic zone. Crack extension occurs at the remotely applied, fixed loading without the need for a local growth criteria. This numerical scheme utilizes a streamline integration technique to determine the elastic-plastic fields, generalized from a two-dimensional to a fully three-dimensional setting and implemented within mixed Matlab/C++/F-90 based software. Modifications of the conventional finite element formulation lead to an efficient procedure – readily parallelized – and determine the invariant near-front fields, representative of steady-state growth, on a fixed mesh in a boundary-layer framework. In the small-scale yielding regime, the crack front does not sense the existence of remote boundaries, and computational results retain a strong transferability among various geometric configurations where near-front, plastic deformation remains entirely enclosed by the surrounding linear-elastic material. The global stress intensity factor (K_I) and imposed T-stress fully specify displacement constraints along the far-field boundary, and in a three-dimensional setting, the panel thickness reflects the only natural length scale.

The initial studies in this work consider steady crack advance within the small-scale yielding context under plane-strain conditions and mode I loading. These analyses focus on steady crack growth within a hydrogen-charged material to explore primary features of the streamline integration methodology while providing new results relevant to hydrogen embrittlement at engineering scales. Ductile crack propagation occurs through a homogeneous, high solubility material characteristic of niobium and through a steel weld in the presence of hydrogen. The constitutive model includes the influence of hydrogen on elastic-plastic regimes of material response at the continuum level, *e.g.* hydrogen-induced material softening, based on

the hydrogen-enhanced, localized plasticity (HELP) mechanism, and reflects the amount of hydrogen in the material under stress and the intensity of hydrogen-induced softening in the material. Achievements using this two-dimensional framework encouraged further extensions of the research to a fully three-dimensional setting.

Subsequent work, and the focal point of this thesis, develops a finite element formulation to investigate key features of the elastic-plastic fields near a steadily advancing crack under three-dimensional, small-scale yielding conditions. The computational model represents a structurally thin component constructed of a material (*e.g.* Al and Ti alloys) with flow stress and fracture toughness properties that together limit the size of the in-plane plastic zone during steady growth to no more than several multiples of the plate thickness. These studies consider a straight crack front advancing under local and global mode-I loading in a moderately hardening material. The nonsingular T-stress provides a first-order estimate of geometry and loading mode (*e.g.* tension *vs.* bending) effects on elastic-plastic, crack front fields. The T-stress has a marked effect on measured crack-growth resistance curves ($J - \Delta a$) – trends most computational models confirm using a two-dimensional setting. In the first computations of this type to be modeled, the 3D numerical results here demonstrate similarity scaling of the crack front response – stresses, strains, and displacements – in terms of two non-dimensional loading parameters. These fields serve as input to key engineering failure models for brittle and ductile crack growth and provide estimates of the apparent fracture toughness linked to changes of the material flow response, geometry, and applied loading. For the first time in the scientific literature, these studies document 3D analyses of steady-state crack growth and represent a key advance in computational analyses of crack extension.

To My Father and Mother.

Acknowledgments

This project would not have been possible without direction of Prof. Robert H. Dodds Jr. His invaluable guidance, advice, patience, and fastidious proof-reading skills were often required during the composition of this work, and the author greatly appreciates his assistance over these past six years.

I am very grateful to Prof. Petros Sofronis for his thoughtful collaboration during this project. Without his aid, hydrogen effects on ductile metals could not have been included in this work.

Financial support for this research was provided by the Computational Science and Engineering Fellowship Program at the University of Illinois, the NASA Marshall Space Flight Center, the Naval Surface Warfare Center, Carderock Division, the National Science Foundation, and the US Department of Energy.

I would also like to acknowledge and to thank my family, friends, and colleagues at the University of Illinois who have supported me during this time. I am very blessed to have both my mother and brother who have encouraged me with love and compassion over the years. Adam Carlyle, Bogdan Wasiluk, Sureshkumar Kalyanam, and Xudong Quin helped me to adjust to life as a graduate student in the Dodds group. Ghadir Haikal, Arun Prakesh, Daniel Turner, Kristine Cochran, and Kalyanababu Nakshatrala were all instrumental in guiding me through some of the more thorny issues of continuum mechanics. I would also like to recognize Charles Roe, Richard Link, and James Joyce for allowing me to participate in the Naval Research Enterprise Internship Program during the summer of 2007.

Finally, I would like to recognize the late Dr. Jeronymo Pereira who took his life this spring. His death represents a major loss for this department, the discipline of fracture mechanics, and his family and friends. He will be missed.

Table of Contents

List of Tables

List of Figures

Chapter 1

Introduction

1.1 Overview

Advanced engineering applications increasingly rely on the reserve capacity of metallic alloys – aluminums, titainums, and steels – to ensure critical requirements for structural reliability and overall system integrity. Key civilian, defense, power-generation, and transportation applications must resist imposed forces beyond the applied dead loading, operate under extreme conditions that degrade material performance, and remain viable throughout decades long life cycles. Load bearing members (beams, plates, and shells) exhibit lower strength, stability, ductility, and durability than expected from material testing specimens and high-level structural analyses due to structural defects (cracks, grooves, and dents). Crack-like flaws have proven to be a serious type of defect. In thin metallic structures, a sharp, crack-like flaw typically forms by a fatigue mechanism following sustained, but cyclic loading far below the maximum load capacity, *e.g.* repeated expansion and contraction during fill cycles of a pressure vessel. Cracks, even small cracks that cannot be detected by conventional assessment techniques, induce high local stresses under modest loadings characteristic of expected service loadings or a brief dynamic excitation. Sufficiently high and sustained loading then triggers ductile tearing through the blunted crack front.

Structural metals display a rising R-curve ($J - \Delta a$) following crack initiation that provides a reserve toughness capacity. Crack extension continues, if the remote loading maintains an increasing J-value while the crack resharpens through the initially yielded material, and if the remote loading tends to a near constant level once the crack front contacts fresh material without plastic deformation induced by the initial flaw. This additional resistance to crack growth exhibits a strong dependence on the imposed plastic constraint due to the geometry and loading, especially in low constraint configurations that elevate J. In thin panels, triaxiality variation over the thickness leads to pronounced 3D fields that do not correspond with existing analyses based on 2D assumptions (plane strain or plane stress). Material embrittlement reduces ductility, modifies the near-front response, and complicates structural analyses, as is readily apparent for repurposed structures used to transport and store hydrogen. Proper engineering judgments thus require that these

effects be considered at some level of the design and analysis process, either indirectly built into technical standards or directly by computational simulations.

Large computational simulations over moderate time scales persist as an engineering challenge despite the improvement of computational techniques related to solid mechanics problems and the wide-spread use of high performance computers. The relatively simple and effective parallelization schemes that have been developed for dynamic problems do not apply to quasi-static problems that must factor the full structural stiffness matrix multiple times per load step, over hundreds or thousands of load steps. Slowly loaded structures represent an important set of fracture problems: multiple embedded flaws in a pressure vessel, low-rate cyclic fatigue, corrosion and creep analyses under constant load, and 3D crack initiation and growth. For a large, 3D finite element analysis of the crack growth process with sufficient mesh refinement, the model may easily approach half-a-million degrees of freedom. Matrix factorization times then range between 20-30 minutes on common server architectures (8 CPU's and 32 GB's of RAM) using a highly parallelized, commercial direct solver. Consequently, quasi-static studies of crack advance in a 3D framework currently require novel techniques to minimize computational complexity and expose latent parallelism. This thesis focuses on a method to generate the crack-front fields during the steady-state regime of crack advance within a small-scale yielding framework. In particular, the results presented here show the 3D elastic-plastic stresses, strains, and displacements for the first time. Concurrently, this technique applies to a large variety of potential applications investigated within the scientific literature regarding the applied loading, model geometry, and constitutive response.

1.2 Steady-state crack extension

Ductile metals, especially structural aluminum and titanium alloys as well as ferritic steels in the mid-to-upper temperature transition region, exhibit significant ductile tearing (Δa) as the material resistance (K_I) rises, illustrated in Fig. 1.1. At the site of initiation, the crack front blunts [66] from the original crack-like flaw – perhaps sharpened by fatigue – under increasing loads. The combined near-front triaxiality and plastic deformation levels at the applied loading $K_{I-\Delta a}$ induce ductile tearing, often by the micromechanical mechanism of void initiation from second phase particles, growth, and eventual coalescence [42]. The remotely applied loading continues to increase as the crack grows within the material initially yielded by the crack front [3]. Simultaneously, the plastic zone surrounding the crack front expands under higher loading, and the crack front resharpens as it encounters fresh material.

Once the crack advances beyond the initially blunted region, the additional loading required to maintain

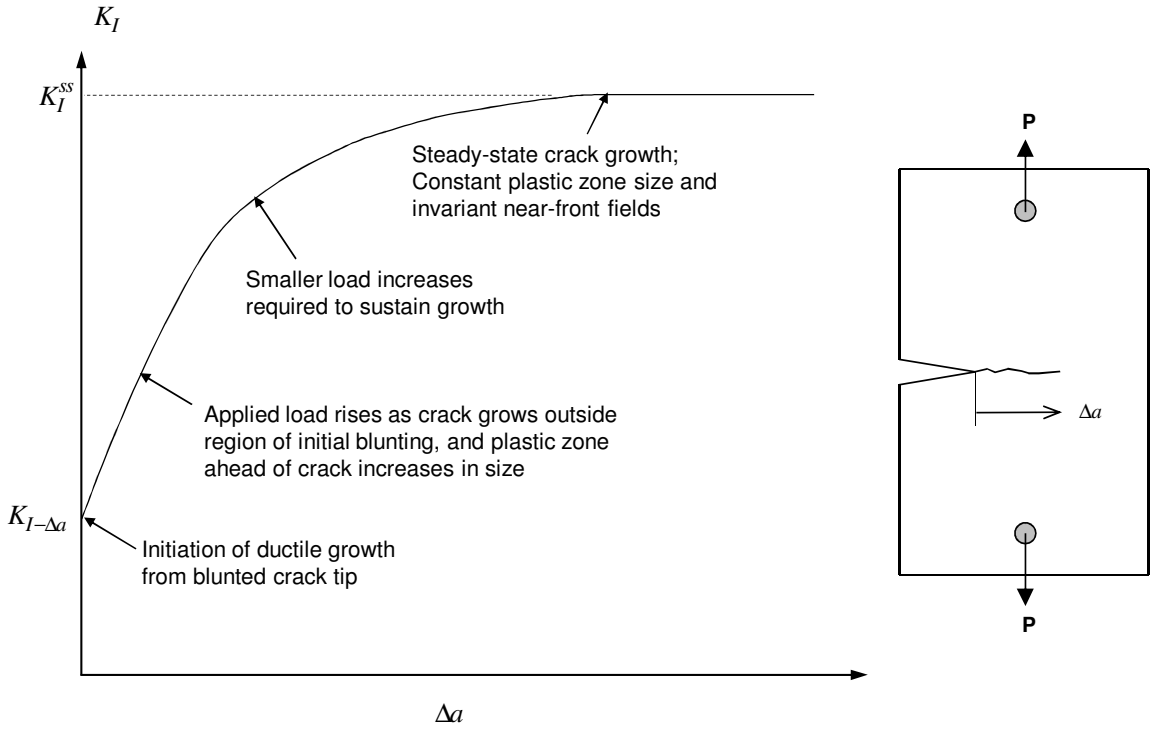

Figure 1.1: Crack growth resistance rises sharply with crack extension after initiation and increases more gradually outside the region of the initially blunted tip. Eventually, cracks may extend steadily as increasingly smaller values of the applied load produce increasingly larger values of crack extension, *i.e.* steady-state crack growth.

crack advance drops and tends to vanishingly small load increments that produce increasingly large amounts of crack extension. At the upper bound of the remotely imposed loading – $K_I \to K_I^{SS}$ – the crack front reaches steady-state conditions where:

$$\frac{\partial K_I}{\partial a}\Big|_{K_I \to K_I^{SS}} \to 0, \tag{1.1}$$

in highly redundant, displacement-controlled structures. Crack extension then continues at a low but near-constant velocity, $\dot{a}$, along the crack plane, *i.e.* quasi-static conditions. The resulting stresses, strains, and displacements, relative to an observer situated on and moving with the crack front, appear invariant during sustained ductile tearing. Mathematically, this relationship can be expressed by a temporal-spatial relationship along material streamlines that represent particle trajectories (τ) as the crack approaches, passes, and recedes from a material point:

$$\frac{\partial\,(\bullet)}{\partial t} = -\dot{a}\frac{\partial\,(\bullet)}{\partial \tau}. \tag{1.2}$$

Equation (1.2) asserts an equivalence for all differential quantities ($\bullet$) integrated through time (t) or along

particle trajectories (τ). During steady crack advance, finite deformation effects only influence an extremely small region very close to the crack front [61], and the results over the majority of the plastic region using small deformation analyses are indistinguishable from results using large deformation analyses [88]. Using the small-strain description, straight streamlines – parallel to the direction of crack advance – then represent particle trajectories during steady-state crack extension [21, 83].

Dean and Hutchinson [21] originally apply the time-distance equivalence along straight streamlines to a finite element, computational model used to describe steady crack advance under mode I and III far-field loading. Critically, this numerical implementation only forms and factors the structural stiffness matrix once, and thus minimizes computational effort. Original applications for this technique focus on the verification of asymptotic analyses, *e.g.* the solution of Drugan et al. [27] for plane-strain crack advance through an elastic, then perfectly-plastic material. Later analytical work by Drugan [24] cautions that key assumptions invoked during asymptotic solutions – *i.e.* variable separation – may not always be valid. These objections do not apply to the full-field solutions produced by the streamline-integration technique, which was rapidly adopted by numerical studies of dynamic fracture [31, 33, 50, 118]. These studies include inertial effects by modifying the otherwise undisturbed principal of virtual work using Eqn. (1.2), and require additional thermodynamic terms to ensure that plastic shocks do not occur in J_2-materials [25]. Quasi-static analyses only apply to cracks that propagate at less than 10% of the shear wave speed of the material [51], and have proven robust in studies of constraint effects [117], nonlinear delamination [125], strain gradient plasticity [126], mixed-mode loading [22], rate-dependent materials [52], crack growth along laser welds [78], adhesive layer properties [29], and micron-scale plasticity [127]. These studies primarily investigate the effects of remote loading and material-flow response on the near-tip stresses and strains, and then link these results to the far-field toughness variation through a local damage parameter, *e.g.* crack-tip opening angle.

1.3 Modified boundary layer model

The main computational framework utilized in these numerical studies is a modified boundary layer model known as small-scale yielding (SSY) [110]. The steady-state crack growth algorithm prohibits material and geometric transitions in the direction of crack advance; otherwise, the validity requirements for Eqn. (1.2) are not satisfied. Consequently, the steady-state, crack-front response for experimental test geometries, *e.g.* C(T), M(T), SEN(B), etc..., cannot directly be determined using the numerical framework suggested by Dean and Hutchinson [21]. However, the SSY framework can incorporate streamlines within a finite element analysis, provided a suitable mesh is designed to facilitate streamline integration. This numerical setting also

enables first-order estimates of constraint effects on the elastic-plastic response due to the remote geometry and loading.

Consider a through-thickness crack front within some large metal panel that responds to increasing deformation according to a linear-elastic, then inelastic constitutive relationship. In the SSY regime, the in-plane material deforming elastically (Hooke's law) contains the entire in-plane region of material deforming inelastically near the crack front. Further, the extent of near-tip, plastic yielding remains significantly smaller than the remaining planar dimensions of the body, *e.g.* crack length, remaining ligament, specimen height, and overall width. Under these conditions, the inelastic crack front response marginally contributes to the far-field response, and can be neglected by an asymptotic analysis of the remote mechanical fields under the imposed structural loading. Williams [128] provides the solution to this problem in a plane-strain or plane-stress framework under primarily tensile loading. Here, the stress intensity factor, K_I, controls the intensity of stresses, strains, and displacements in the linear-elastic material far from the crack front. The imposed T-stress equals a normal traction parallel to the direction of crack advance and provides a first order representation of the loading (tension *vs.* bending) and geometry (M(T) *vs.* C(T)). The requirements for small-scale yielding may easily be met in many structural applications. Standard aluminum alloys with a toughness of 50-60 MPa$\sqrt{\text{m}}$ and low-to-moderate yield stress (350-420 MPa) regularly compose aerospace fuselages with planar dimensions in excess of several meters. A rough estimate for the extent of yielding, $(K_I/\sigma_0)^2$, then suggests no more than 5 mm's of plastic deformation surrounding the crack front, and SSY conditions are clearly satisfied.

Analyses of the SSY region represent the elastic-plastic response found in structural components or experimental test specimens, with boundary conditions (tractions/displacements) equivalent to the K_I and T fields. For 2D analyses, the extent of plastic deformation near the crack front, measured in terms of $(K_I/\sigma_0)^2$ or J/σ_0, provides the only relevant length scale, and the near-front fields exhibit a self-similarity scaling when reported in normalized radial dimensions [110]. For a stationary crack front, Larsson and Carlsson [53] first show that the non-singular T-stress term alters the plastic yielding region in plane strain. Without an imposed T-stress (implicitly $T = 0$), SSY solutions do not approach the results determined for most experimental test specimens. Rice [89] confirms the constraint effect on the plastic yielding region and shows that J-integral values do not change under non-zero levels of the imposed T-stress in plane strain. In contrast, the elastic-plastic fields, *e.g.* the opening-mode stress, do require a two parameter description of the imposed loading [12]. For a stationary crack tip, the plane-strain, opening-mode stress along the uncracked plane decreases in low constraint ($T < 0$) geometries and increases for high constraint ($T > 0$) beyond the zero T-stress stress variation [79].

Quasi-static crack growth studies, from initiation to the steady-state response, often predict the crack growth resistance ($J - \Delta a$) curves based on the mechanical fields during crack advance linked to a damage model. The Gurson flow model [40] couples the mean stress and deviatoric stress states in a void growth model that assumes an initial, average measure for the material void fraction. A key set of plane-strain, crack growth studies [132, 130, 129, 131], indicates element extinction (loss of load carrying capacity) when the void fraction reaches a critical level. The crack front location occurs at the boundary for the extinct and viable elements, within a strip of Gurson cells placed along the crack plane. Xia and Shih [130] apply the Gurson flow model to crack growth studies within a plane-strain, SSY framework under non-zero T-stress levels and determine that crack growth resistance curves exhibit a strong variation with the imposed T-stress. For a material that initially contains a void fraction of 0.5% and that hardens moderately ($N = 0.1$), Fig. 15 in Xia and Shih [130] indicates that the apparent steady-state toughness for $T/\sigma_0 = -0.5$ equals 1.9 times the steady-state toughness for $T/\sigma_0 = 0$, whereas the apparent steady-state toughness for $T/\sigma_0 = +0.5$ equals 0.7 times the steady-state toughness under a zero T-stress. The related studies by Xia et al. [132] and Xia and Shih [129] observe similar trends for the steady-state toughness in numerical simulations of experimental test specimen geometries. A corresponding set of studies [112, 113, 114, 115, 116] investigate crack advance using a traction-separation law [7, 28, 75], implemented within cohesive-zone elements placed along the uncracked plane. For a peak traction of three times the yield stress in Tvergaard and Hutchinson [114], the $T/\sigma_0 = -0.5$ loading produces a steady-state toughness that is 1.5 times greater than the zero T-stress value. Positive T-stress ($T/\sigma_0 = 0.5$) has a negligible on the steady-state toughness in these studies.

In contrast to the load-stepping procedures employed in the preceding studies, Varias and Shih [117] apply the streamline integration technique discussed in Sec. 1.2 to finite element analyses of a plane-strain, SSY model. This formulation does not require a local damage model. A single characteristic length scale based on the intensity of plastic deformation provides a simple indication of T-stress effects on the near-tip fields, and this study suggests that near-tip fields attain maximum values under zero T-stress loadings. Varias and Shih [117] invoke the energy balance arguments of Freund and Hutchinson [32], particularly the following relationship between the energy release rate (G), the stresses (σ_{ij}), the plastic strain rate ($\dot{\varepsilon}^p_{ij}$), and the residual strain energy stored in the trailing plastic wake (U^e):

$$G \approx \frac{1}{\dot{a}} \int_{A_{AYR}} \sigma_{ij} \dot{\varepsilon}^p_{ij} dA + \int_{-h_{pw}}^{h_{pw}} U^e dY. \tag{1.3}$$

In Eqn. (1.3), the first integral is taken over the actively yielding region near the crack front, A_{AYR}, and the second integral is evaluated over the plastic wake height, h_{pw}. For fixed G, a larger values h_{pw} due

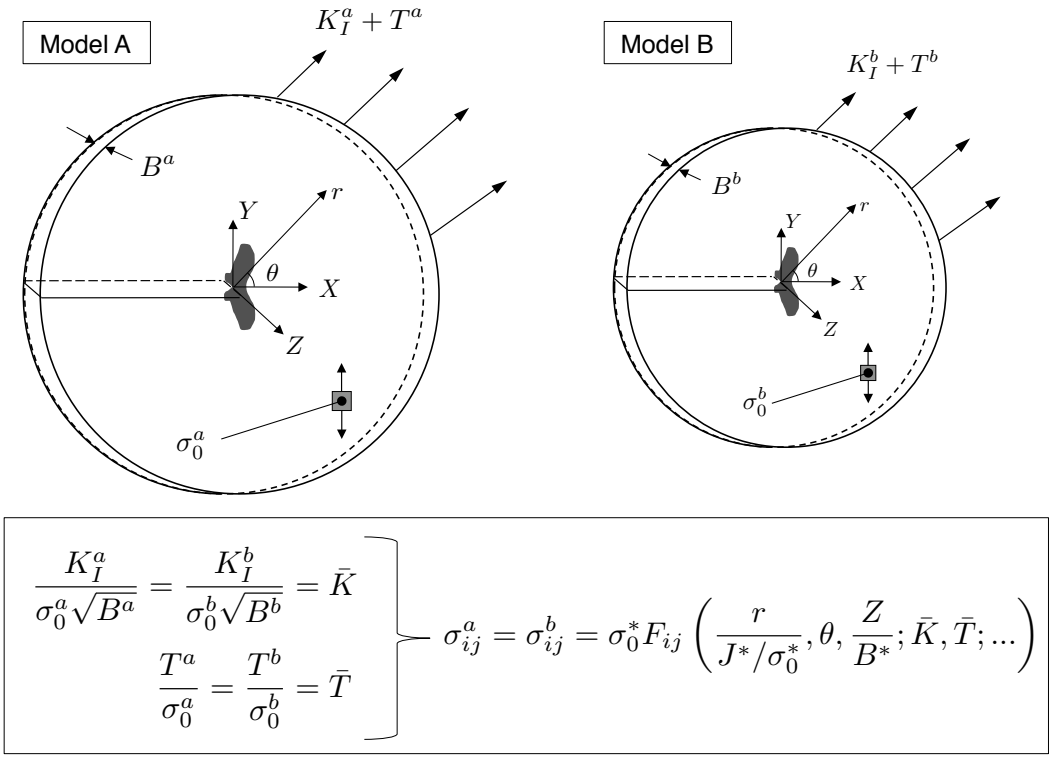

Figure 1.2: Self-similarity scaling relationship for two 3D SSY models, A and B. The remote mode-I stress intensity factor, K_I^*, and imposed T-stress, T^*, quantify the applied displacement field enforced on the far-field boundary. The extent of plastic yielding remains comparable to the plate thickness, B, and the remote, linear-elastic fields follow the plane-stress relationships, *i.e.* $J = K^2/E$, where E equals Young's modulus.

to non-zero T-stress loadings increases the amount of energy trapped in the plastic wake and reduces the resulting elastic-plastic fields. Varias and Shih [117] then adopt a crack-tip opening angle (CTOA) criteria to study constraint effects and determine that the lowest apparent toughness arises for a $T = 0$ loading.

In thin ductile plates, triaxiality loss should strongly affect the near-front fields and alter steady-state toughness values, similar to the preceding studies that show strong constraint effects on the plane-strain, steady-state toughness. Even in the absence of plasticity, 3D effects become significant, *e.g.* higher local J-integral values develop near the interior of elastic plates than the remotely applied J value [71]. The 3D SSY framework extends the streamline integration methodology by relaxing plane-strain/plane-stress constraints on the out-of-plane deformations/tractions. Here, the in-plane extent of plastic yielding remains on the order of the thickness, and the crack-front response changes over the thickness, relative to the amount of in-plane yielded material compared to the thickness. For a straight, stationary crack front, Nakamura and Parks [72] determine that a self-similarity relationship holds characterized by the nondimensional loading

parameter $J/\sigma_0\varepsilon_0 B = (K_I/\sigma_0)^2/B = \bar{K}^2$ (in plane stress where $J = K_I^2/E$) and illustrated by Fig. 1.2. Two 3D SSY models (A and B) with the same material flow properties, but different values of the applied loading, material flow properties, and thickness, exhibit the same elastic-plastic stress variation under the same $\bar{K}$ loading. Similar relationships exist for the strains and displacements. Further 3D SSY studies also demonstrate this 3D self-similar scaling under imposed T-stress [48, 133] and for cracks advancing by a fatigue mechanism under a cyclic loading [95, 96, 97].

Thinner structural plate and shell members with significant three-dimensionally near through-thickness crack fronts are increasingly relevant to engineering applications and justify a re-evaluation of key fracture mechanics behavior. For example, Nakamura and Parks [72] observe that a stationary crack front under ($\bar{K}^2 = 10, \bar{T} = 0$) loading experiences at the mid-thickness a local J-value nearly 30% higher than the applied value at the far-field boundary. Kim et al. [48] later demonstrate that negative T-stress levels in 3D SSY lower local J-values along the crack front. Plane-strain analyses overlook this 3D behavior, resulting in both non-conservative and over-conservative design requirements. Computational analyses of sustained ductile tearing in 3D SSY are especially relevant to thin structural applications composed aluminum and titanium alloys that reach and sustain steady-state conditions following crack initiation. Furthermore, 3D streamline integration within a flexible computational framework would permit novel crack growth simulations in non-SSY geometries that cannot be analyzed in a plane-strain or plane-stress context.

1.4 Material Modeling

Classical J_2-plasticity theory, detailed analytically in [43, 62, 68], provides a phenomenological description of the elastic, then plastic material response of common structural metals, and key numerical texts [9, 17, 102] present accurate and robust computational schemes for Mises plasticity within standard finite element implementations. In particular, the elastic-predictor, then radial-return algorithm efficiently determines the stress-state on the cylindrical yield surface described in principal stress coordinates. The strain increment generates a first estimate of the stress-state assuming an entirely elastic step. The algorithm next computes the true stress-state by calculating the additional plastic strain, in the radial direction from the predicted stress-state to the cylinder center. That is, the algorithm radially returns the stresses to the yield surface. Krieg and Krieg [49] determine that numerical inaccuracies develop in the elastic-predictor, then radial-return computational scheme for large strain increments. Excessive degradation of the numerical results may be prevented using substepping and extrapolation techniques [16].

Material embrittlement (reduction of the tearing resistance) from environmental factors, *e.g.* a hydrogen-

rich atmosphere [94], represents a serious technical problem and material modeling issue. In common metallic alloys, hydrogen atoms become embedded within the matrix microstructure at trapping (dislocation) sites and within the space between the atoms of the crystalline lattice structure, *i.e.* normal interstitial lattice sites (NILS). Birnbaum and Sofronis [14] describe a hydrogen "shielding" mechanism that reduces the repulsive force between dislocations. Hydrogen increases the mobility of dislocations, as shown by the experiments of Tabata and Birnbaum [108], as well as the more recent work of Robertson [93]. Birnbaum and Sofronis [14] argue that this behavior reduces the local flow stress in the presence of hydrogen compared to the local flow stress of the metal without hydrogen. Thus, hydrogen leads to material degradation by enhanced plastic strains localized near the crack tip, known as the hydrogen-enhanced, localized plasticity – HELP – mechanism. Further, hydrogen atoms expand the volume of NILS between host metal atoms, and consequently, the mean stress influences the concentration of hydrogen at NILS, and vice versa, as shown by Sofronis [105]. These observations suggest hydrogen couples the interaction of mean stress and local plastic flow and lead to a constitutive model to predict the inelastic response of a metal in the presence of hydrogen. This model requires hydrogen equilibrium between the trap and lattice sites according to the Oriani [80] relationship, This constraint is easily met during quasi-static crack growth, *e.g.* crack advance at less than 1 mm/s [124].

1.5 Research objectives and scope

This thesis focuses on the determination, characterization, and application of the near-front crack fields within the steady-state growth regime under SSY conditions. These studies document the first analyses of 3D steady crack growth within SSY and represent a major advance in available techniques to study crack extension. This research extends previous plane-strain and plane-stress steady-growth studies to consider 3D triaxiality loss on the crack front. Major aspects of these studies include the following:

- Implementation of the HELP-based constitutive model by Sofronis [105] within a plane-strain, finite element framework that incorporates the streamline integration procedure. Investigations highlight hydrogen-effects on void growth rates during sustained ductile tearing in homogeneous and welded structures under varying levels of T-stress. This work encouraged later studies within a 3D framework by providing a computational setting to test key features of the Dean and Hutchinson [21] methodology.

- Development of a computationally-efficient, 3D finite element framework – FIREFLY – for steady growth analyses that utilizes the OpenMP parallel paradigm (multiple processor, shared memory architecture). The numerical scheme maximizes computational performance while maintaining reasonable code-development time lines by linking multiple programming languages, *i.e.* Matlab, C++, and

F-90, and by incorporating previous subroutines from the plane-strain framework. Critical elements of the solution procedure refer to highly efficient third-party software, *e.g.* the Intel MKL direct sparse solver.

- Demonstration of a key self-similarity scaling for steady crack growth in 3D SSY, based on a functional relationship for the stresses, strains, and displacements at normalized coordinates, and characterized by two non-dimensional loading parameters. Major features of the 3D crack front response depend on the loading levels imposed on the remote boundary, the material flow properties, and model thickness. These studies illustrate high sensitivity to the plate thickness location for the elastic-plastic fields, as is especially apparent for 3D active yielding regions.

- Exploration of constraint effects through the through the remote application of a non-zero T-stress. The imposed T-stress has a marked influence on the active yielding region, as shown by the extent of plastic deformation on the crack plane and the height for the plastic wake. During steady crack advance within a 3D SSY framework, the near-front fields require two loading terms to fully characterize the steady-state response.

- Observations of the crack-front response with respect to the steady-state toughness. The crack-tip opening angle – a local toughness measure for growing cracks that corresponds to the crack-tip opening displacement – shows variations over the thickness and due to the loading level. These steady-state trends reflect earlier experimental and computational studies. Micromechanically-based models for the ductile tearing process and cleavage failure initiation link variations of the far-field, steady-state toughness to the near-front fields under different T-stress levels. In particular, the extension of the earlier void growth model to the 3D context suggest the relative impact of the T-stress levels on the apparent toughness during steady crack advance.

Following the introduction, this thesis contains four chapters on independent, but related research topics, one chapter that reviews the preceding studies, and five appendices of additional material.

Chapter 2 investigates hydrogen and constraint effects on the near-tip fields and void growth rates for a steadily advancing crack through a ductile metal, under plane-strain and quasi-static conditions. The ductile crack propagation simulated in these studies represents that observed in a high-solubility model material, where the diffusion rate can sustain equilibrium of the hydrogen concentration ahead of the steadily advancing crack tip. The mean stress and Mises stress variations exhibit a self-similarity scaling for radial distances normalized by the quantity J/σ_0. The triaxiality measure $(3\sigma_m/2\sigma_e)$ most strongly declines, and the equivalent plastic strain most strongly increases $(\bar{\varepsilon}^p)$, under a large initial reduction of the yield stress,

due to the intensity of plastic softening, ξ, and initial concentration of hydrogen, c_L^0. Imposed T-stress loadings, both positive and negative, reduce triaxiality levels and inelastic deformation. A modified version of the Rice and Tracey [92] void growth model, specialized to compute void growth rates along streamlines, presents a simplified method to relate the near-front fields to the steady-state, crack growth resistance.

Chapter 3 examines the influence of increased dislocation velocity due to hydrogen on the steady-state behavior of a crack propagating under quasi-static conditions in elastic-plastic, matched, over-matched, and under-matched weld materials. Crack growth develops within a ductile metal representative of a pressure vessel steel and along a line equidistant from the weld-base metal boundary. The remotely applied $K_I - T$ fields produce an active yielding region that, in a matched weld metal, extends well into the base metal. Void growth rates suggest strong T-stress effects and a high sensitivity to the weld-base metal mismatch level, particularly in under-matched welds.

Chapter 4 describes key features of the elastic-plastic fields near a steadily advancing crack at quasi-static rates under 3D SSY conditions and subject to zero T-stress loadings. The model represents a structurally thin component constructed of a material (*e.g.* aluminum and titanium alloys) with flow stress and fracture toughness properties that together limit the size of the in-plane plastic zone during steady crack growth to no more than several multiples of the plate thickness, B. The computational approach generalizes the streamline integration procedure used previously for two-dimensional studies (Chapters 2 and 3) into three dimensions to represent steady-state growth on a fixed mesh in a boundary-layer framework. The plate thickness (B) provides the only natural (physical) length scale. Crack extension occurs at the remotely applied, fixed loading (K_I) without the need for a local growth criterion. In the first computations of this type, this chapter considers a straight crack front advancing under local and global mode I loading (K_I) with zero T-stress in a moderately hardening material. In normalized coordinates, fixed at the advancing crack front, the near-front radial and angular variations of the stresses, strains, and displacements exhibit a self-similarity scaling characterized by the loading term $\bar{K} = K_I/\sigma_0\sqrt{B}$. The opening-mode stress along the uncracked plane relates the 3D nonlinear singularity to the linear-elastic, plane-stress singularity over the thickness and indicates the extent of 3D effects on the crack front. An out-of-plane constraint measure ($\sigma_{zz}/0.5\ (\sigma_{xx} + \sigma_{yy})$) signifies that near plane-strain conditions predominate only within some small fraction of the thickness that depends on the loading term $\bar{K}$. Through-thickness variations of the opening displacement trailing the crack front link the results in this chapter to an increasingly popular damage criteria, the crack-tip opening angle (CTOA).

Chapter 5 extends the methodology established in the previous chapter by the application of non-zero T-stress loadings, representative of a wide range of specimen loadings and constraint configurations, to the

3D SSY boundary. This approach does not require any modifications to the computational framework or finite element model. The imposed T-stress alters the nondimensional functional relationship that describes stresses, strains, and displacements, and the resulting self-similarity scaling requires two terms, $\bar{K}$ and $\bar{T} = T/\sigma_0$, to represent loading levels. Constraint effects become more prominent if in-plane dimensions for plastic deformation remain some small fraction of the thickness. Plane-strain conditions then develop over significant radial distances from the crack front. Results from the three-dimensional numerical models are summarized using the principal stresses and the equivalent plastic strain, which often serve as input to more complex micromechanical models. In particular, the first principal stress controls the Weibull stress value – a local damage measure used to probabilistically quantify cleavage failure events that often occur within the ductile-to-brittle temperature transition region of structural ferritic steels. The modified void-growth model relates imposed T-stress levels to the crack growth resistance curve and reveals the clear tendency for crack-front tunneling and shear-lip formation near the outside surface. Furthermore, these results imply minimum toughness values measured within $T \approx 0$ experimental specimens during steady crack advance.

Chapter 6 summarizes key features of this work and suggests future research topics now made possible by the 3D computational framework.

Appendix A outlines key procedures required to solve the steady-state crack growth analyses using the streamline integration procedure. For simplicity, operations are limited to the plane-strain framework, but can easily be extended to a fully 3D context.

Appendix B provides additional information regarding the constitutive model based on the HELP mechanism.

Appendix C details a simple analytical model to quantity the Weibull stress increase during sustained ductile tearing within a ferritic steel. Preliminary computational predictions using a plane-strain SSY model substantially agree with earlier experimental results.

Appendix D presents major features of the special purpose, finite element software – FIREFLY – developed in this thesis to solve the 3D crack-growth analyses at steady-state.

Appendix E suggests an alternate method to represent T-stress effects on steady-state, near-front fields based on a characteristic length scale and similar to the approach adopted by Varias and Shih [117] in plane strain. Initial results suggest a more complex relationship in a 3D setting than observed in the earlier plane-strain study.

Chapter 2

Effects of Hydrogen on Steady, Ductile Crack Growth: Computational Studies

2.1 Introduction

The rising interest in hydrogen as a fuel motivates new concerns for the design and maintenance of facilities employed in the manufacture, transport, and storage of hydrogen. Structural metals exhibit mechanical properties that often differ in hydrogen-charged and hydrogen-free conditions, e.g. the detrimental effect of hydrogen on the resistance to the propagation of crack-like defects [94]. Well-understood methodologies of defect assessment appropriate for hydrogen-free metals will likely require modifications in the presence of hydrogen to reflect metallurgical scale effects. For example, the conventional view of fracture behavior in ductile metals at engineering scales neglects complex interactions that may develop between the mechanical fields and materials in the presence of hydrogen. A key component of defect assessment strategies thus requires an understanding of the engineering behavior and failure mechanisms of hydrogen-charged metals.

Ductile crack propagation occurs in metals most often by the growth of micro-voids ahead of the crack tip that coalesce to form new crack surfaces. High triaxiality levels and large plastic strains accelerate void growth [92] and lead to the onset of void coalescence. Hydrogen facilitates plastic deformation by increasing dislocation velocities which leads to a local flow stress reduction that influences both the local triaxiality and plastic strain in a complex manner. Changes in the local triaxiality and plastic strain in the presence of hydrogen impact void-growth rates at the metallurgical scale and the resistance to macroscopic crack extension at the engineering scale. Studies that describe crack propagation in ductile metals enriched by hydrogen may examine, for example: cyclic fatigue growth, growth emerging from a plastically deforming-blunting crack tip, crack advancement under a sustained load, or slow stable tearing under increased load. The present study focuses on steady crack extension outside the region of material influenced by initial blunting of the pre-existing stationary crack when the tearing resistance approaches a constant value. Such steady-state growth conditions at constant front loading, and where the diffusion rate can sustain equilibrium of the hydrogen concentration ahead of the propagating crack tip, represent the classical Stage II regime of sustained load crack growth [124].

Various numerical studies examine the characteristics of a steadily propagating crack in an elastic-plastic material based on a small-scale yielding (SSY) formulation first suggested by Dean and Hutchinson [21]. Their method integrates the steady-state constitutive relations along planes parallel to an advancing crack tip. Freund and Douglas [31] extend this method to rapidly propagating cracks including inertial forces and, using a critical strain-characteristic distance criterion, generate toughness vs. crack velocity curves in good agreement with experimental results. By imposing positive and negative T-stress conditions in the SSY framework, Varias and Shih [117] determine that key values of stress field ahead of an advancing crack decrease with nonzero values of the remotely imposed T-stress. Landis et al. [52] incorporate a rate dependent, cohesive zone ahead of a propagating crack in an elastic-viscoplastic material; their computations indicate that the steady-state toughness may increase or decrease with increasing crack tip velocity. For cracks propagating within a weld, Niordson [78] employs a cohesive zone model and finds that thinner welds lead to higher values of crack driving force and that crack propagation slightly outside of the weld metal generates lower driving forces. Ferracin et al. [29] extend the steady-state formulation to include finite rotation effects, while retaining small deformation kinematics, to determine the cohesive zone properties of an adhesive bonding two sheets of metal that deform plastically. In a key finding that simplifies models for steady-growth, the asymptotic analyses of Reid and Drugan [88] demonstrate that the size of the blunting region for propagating cracks remains significantly smaller than for a stationary crack, thereby minimizing the need to incorporate finite deformation effects.

The hydrogen-enhanced, localized plasticity mechanism (HELP) represents a viable model for hydrogen-induced material degradation [8, 14]. Over a range of temperatures and strain rates, hydrogen decreases the barriers to dislocation motion [101, 104, 103]. Both experimental observations [103, 104, 93] and theoretical calculations [14, 105, 106] support this interpretation. Thus, the amount of plastic deformation increases within regions of hydrogen accumulation, and, consequently, the fracture event becomes a highly localized process of ductile rupture — not an embrittlement [13].

Sofronis et al. [107] argue that a critical question remains unresolved: how hydrogen-induced material softening at the microscale promotes shear localization at the macroscale with concomitant ductile fracture. Clearly, hydrogen-induced softening promotes inhomogeneous plastic deformation [13], but the mechanistic means by which hydrogen promotes localization of plastic flow remains unclear. Finite element simulations indicate complex interactions of the localized material response and geometric constraint in hydrogen-charged materials. Taha and Sofronis [109] calculate the hydrogen concentrations ahead of a stationary, blunting crack under SSY conditions and in a four-point bend specimen for a non-softening material in the presence of hydrogen. For softening materials, Sofronis et al. [107] predict the conditions for development of shear

bands in the presence of hydrogen. Liang et al. [59] study the influence of material softening, the level of imposed constraint via the T-stress, and the concentration of initial hydrogen on the void-growth rates ahead of a stationary, blunting crack. As predicted in a SSY analysis by Ahn et al. [1] propagating cracks in a hydrogen-charged material exhibit reduced fracture toughness and tearing resistance during the early stages of crack extension within the initial blunting field. The present work extends the efforts of Ahn et al. [1] to represent larger amounts of ductile crack extension when steady-state conditions prevail also in a hydrogen-charged material, with the hydrogen concentration in equilibrium. When the crack-tip velocity, material properties and loading preclude the equilibrium of hydrogen concentration adopted for the present analyses, the interaction effects must be included as in the work of Dadfarnia et al. [18] for austenitic steels in which hydrogen diffusion is extremely slow. From experimental work, Wei et al. [124] conclude that hydrogen diffuses very rapidly through systems such as ferritic steels and that steady crack growth approaching 1 mm/s is sustainable without diffusion limitation. Hence, the assumption of equilibrium conditions for hydrogen ahead of a steadily propagating tip is a valid one for systems in which hydrogen diffuses fast.

This paper begins with a description of the computational model for steady-state crack growth in SSY conditions and the material constitutive model that reflects hydrogen-induced softening. The following section describes key features of the near-tip fields ahead of a steadily propagating crack as influenced by the hydrogen-induced initial reduction of the yield stress, the initial hydrogen concentration in the stress-free material, and the imposed constraint modeled through the T-stress. These crack tip fields drive a simple, damage parameter for void growth as described in the next section to examine the influence of hydrogen on crack-growth resistance. The final section summarizes the major results and conclusions of the present study. Two appendices present additional details for the steady-state formulation and the constitutive implementation of the effect of hydrogen on the plastic deformation in the material.

2.2 Boundary value problem description

2.2.1 Steady-state crack growth

A crack propagates under steady-state conditions if the displacements, stresses, and strains remain invariant with respect to an observer situated at the crack tip. Further, the crack extends in an infinite domain consisting of an elastic-plastic material, and thus reflected stress waves for rapid crack propagation never interact with the crack tip region. The crack has grown a sufficient distance from the initiation site that the effects of early growth through the initial blunting region do not affect the near-tip solution. In the present study, the crack tip advances at a constant, sufficiently small velocity that inertial and rate effects can be

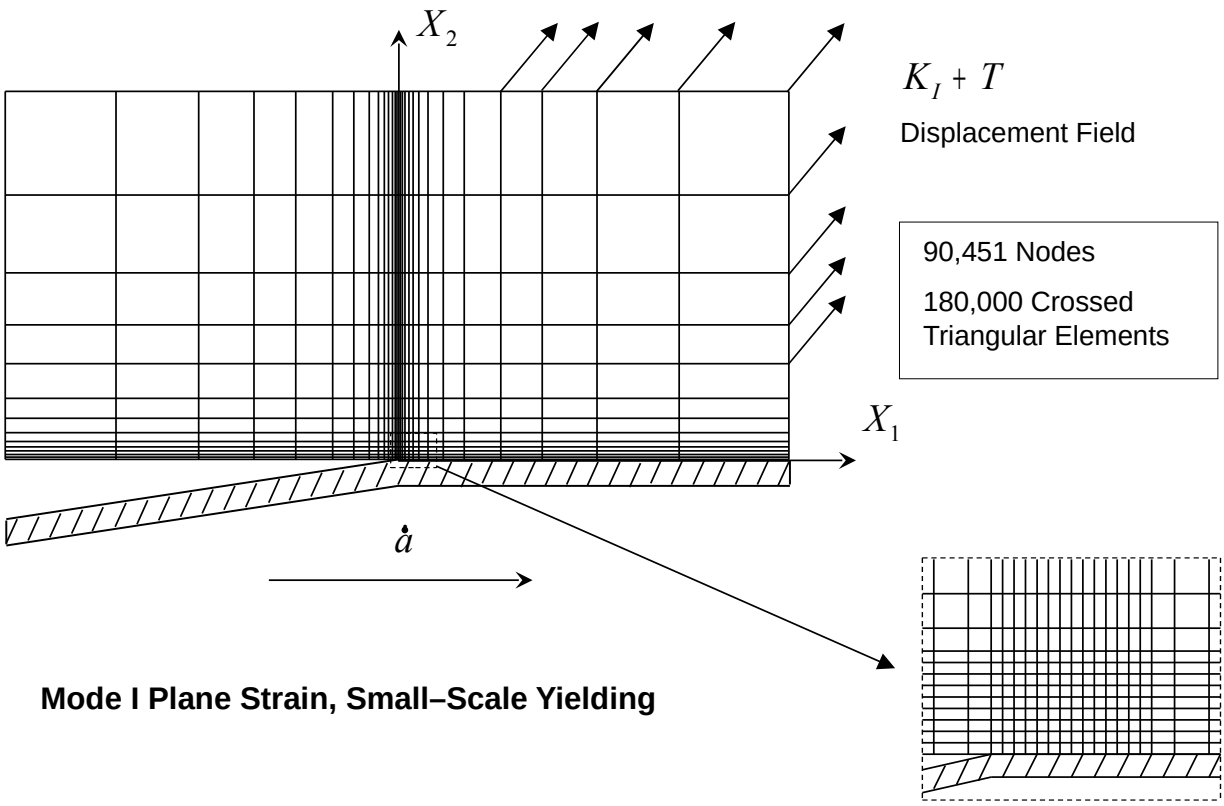

Figure 2.1: Illustration of the steady growth, small-scale yielding mesh with applied displacement boundary conditions (distribution of elements in actual mesh is considerably denser).

ignored, *i.e.* quasi-static conditions prevail. Finally, the adoption of infinitesimal strain theory implies a crack tip that remains sharp under deformation in accordance with the asymptotic results [88].

We compute the solution to this boundary value problem using the algorithm proposed by Dean and Hutchinson [21], as outlined in Appendix A. The element centroids align with streamlines parallel to the direction of crack propagation and for all analyses are arbitrarily set along the X_1 axis. As described in Appendix A, movement of material along streamlines in the direction opposite of the crack propagation equals time incrementation of a fixed point. By adapting this concept to the boundary value problem, the algorithm computes stresses and inelastic strains along the streamlines caused by the propagating crack. Since a refined mesh near the crack tip is required for accurate solutions, the existence of algorithmic streamlines necessarily leads to poor element aspect ratios far from the crack tip; nevertheless, numerical experiments confirm that they have negligible effect on the solutions.

Figure 2.1 illustrates the computational domain defined by a rectangle with the crack tip centered at the origin of the X_1X_2 axes. The boundaries of the finite element model extend a distance greater than 60 times the size of the plastic zone for a steadily propagating crack in a hydrogen-free material under an

Parameter	Value
Young's modulus (E)	115 GPa
Poisson's ratio (ν)	0.34
Yield stress (σ_0)	400 MPa
Hardening constant (N)	0.1
Temperature (Θ)	300 K
Lattice parameter (a)	3.3×10^{-10} m
Initial dislocation density (ρ_0)	10^{10} ll/m^3
Dislocation density parameter (γ)	2×10^{16} ll/m^3
NILS number (β)	1.0
Trap number (α)	1.0
Molar volume (V_M)	1.88×10^{-6} m^3/mol
Partial molar volume of hydrogen (V_H)	1.88×10^{-6} m^3/mol
Trap binding energy (W_B)	29.3 kJ/mol

Table 2.1: Material properties of hydrogen-charged Nb system with high solubility and relatively high diffusivity [6, 119, 107].

imposed, remote T-stress of zero. Crossed, constant strain triangles numbering 180,000 comprise the finite element mesh, and there exists a highly refined mesh of 150×75 quadrilateral elements of crossed triangles of uniform size and shape within a region 0.3×0.15 times the plastic zone size immediately ahead of the crack tip. Less refined regions connect the near-tip regions to the remote boundary. More recent solutions that employ quadratic (8-node) elements reveal no effect of element type at these levels of mesh refinement. The applied loading on the remote, rectangular boundary consists of the K-T displacement terms of the plane-strain, mode I asymptotic expansion (listed in Appendix A).

2.2.2 Overview of the constitutive model including hydrogen effects

The constitutive model couples the mean stress, hydrogen concentrations, and strain hardening to update stresses given the history of deformation and the increment of strain. Hydrogen in a metal enhances plastic flow by intensifying dislocation mobility, which produces highly localized material softening at the microscale. Sofronis and Birnbaum [106] describe the micromechanical details; Appendix B, Sofronis et al. [107], and the WARP3D documentation [38] provide additional details of the constitutive model that reflects hydrogen-induced softening.

For the present studies of crack propagation, the steady-growth computations adopt the properties of a hydrogen-charged, model material with high solubility and relatively high diffusivity as summarized in Table 2.1 (for example, niobium). We do not fix the intensity of hydrogen-induced softening and the initial hydrogen concentration, and vary these quantities over a range of values to examine differing mechanical behavior. Table 2.2 presents the initial reduction of yield stress for the examined sets of material parameters. The post-yield flow stress, σ_y, depends upon the total concentration of hydrogen atoms per solvent atom

c_L^0 (H/M)	ξ	$\sigma_y\left(0, c_L^0\right)/\sigma_0$
0.001	1	1
0.001	-49	0.95
0.001	-99	0.90
0.01	1	1
0.01	-4	0.95
0.01	-9	0.90

Table 2.2: Set of varied material parameters and associated flow stress reduction.

(H/M), c, and the equivalent plastic strain, $\bar{\varepsilon}^p$, according to the hardening relation:

$$\sigma_y\left(\bar{\varepsilon}^p, c\right) = \sigma_0\left(c\right)\left(1 + \frac{\bar{\varepsilon}^p}{\varepsilon_0}\right)^N. \tag{2.1}$$

Material softening follows an assumed relationship:

$$\sigma_0\left(c\right) = \left[\left(\xi - 1\right)c + 1\right]\sigma_0, \tag{2.2}$$

where: ξ denotes a material softening parameter (≤ 1) that describes the intensity of hydrogen-induced softening; and σ_0 defines the initial yield stress of the material in the absence of hydrogen. When $\xi = 1$ and $c = 0$, the material does not soften. Equation (2.2) defines in a continuum sense a local reduction of the yield stress with hydrogen concentration that agrees with experimental observations [108, 69] of the hydrogen effect on the flow properties of materials at the microscale. The model limits allowable values of ξ and c_L^0 to insure a positive, fractional reduction of σ_0. Table 2.2 indicates at most a 10% reduction without loading for the range of specified ξ and c_L^0 values, where c_L^0 denotes initial hydrogen concentration (H/M) in normal interstitial lattice sites (NILS) in the absence of stress. The combined values of specified ξ and computed c_{max} under loading must also lead to acceptable reductions in the yield stress (for the present analyses this corresponds to a maximum 21% reduction). Equation (2.2) and the range of values we use here for the parameter ξ describe, in a macroscopic sense, the observed hydrogen effect at the microscale. This phenomenological model for the flow stress can be improved to reflect a more complex dislocation-based constitutive response. Hydrogen does not affect Young's modulus or Poisson's ratio in this model.

The applied mechanical load influences the amount of hydrogen present in the material. For a constant absolute temperature, Θ, the local mean stress, σ_m, controls the equilibrium constant, K_L, such that

$$K_L = \exp\left(\frac{\sigma_m V_H}{R\Theta}\right), \tag{2.3}$$

where V_H signifies the partial molar volume of hydrogen; and R is the gas constant which equals $8.31 J/\text{mol K}$.

The relationship between the current hydrogen occupancy at NILS, θ_L, and the initial occupancy, θ_L^0, follows the equilibrium relationship [57]:

$$\frac{\theta_L}{1-\theta_L} = \frac{\theta_L^0}{1-\theta_L^0} K_L. \tag{2.4}$$

The hydrogen occupancy at trapping sites, θ_T, is a function of the occupancy at NILS, according to the equilibrium model of Oriani [80]:

$$\frac{\theta_T}{1-\theta_T} = \frac{\theta_L}{1-\theta_L} K_T, \tag{2.5}$$

where the constant K_T depends on the trap binding energy, W_B, and the temperature. The total hydrogen concentration, $c = c(\theta_L, \theta_T)$, used in Eqn. (2.2), can then be determined using the relations found in Appendix B.

Under loads insufficient to cause plastic yielding the total hydrogen concentration, $c = c(\theta_L, \theta_T)$, and thus the initial yield stress, $\sigma_y(\bar{\varepsilon}^p = 0, c) = \sigma_0(c)$, vary over the computational domain with the local mean stress following Eqn. (2.3). Young's modulus and Poisson's ratio are not affected, and material remote from the crack tip approaches an isotropic and linear-elastic constitutive response (with each material point having a potentially different yield stress). Thus the SSY assumptions of a plastic region well contained in a linear-elastic domain ahead of the advancing crack tip remain applicable. Appendix B provides additional details of the constitutive model; Appendix A details the steady-growth formulation for the boundary value problem.

2.3 Hydrogen-plasticity interactions for a growing crack

This section describes stress and strain fields ahead of a steadily advancing crack tip in a material with a high solubility of hydrogen. The first subsection investigates the existence of self-similar behavior of the near-tip fields ahead of stationary and propagating cracks. The following subsections examine the influence of constraint, hydrogen concentration, and material softening on mean stress, triaxiality, and equivalent plastic strain, respectively, along the ligament ahead of a steadily propagating crack. Table 2.2 lists the sets of material parameters used in this study along with the corresponding flow stress, $\sigma_y\left(0, c_L^0\right)$, determined from Eqn. (2.2). The parameters are relevant to the niobium system as data are readily available. The generality of the present approach makes possible the ready application to other high diffusivity systems.

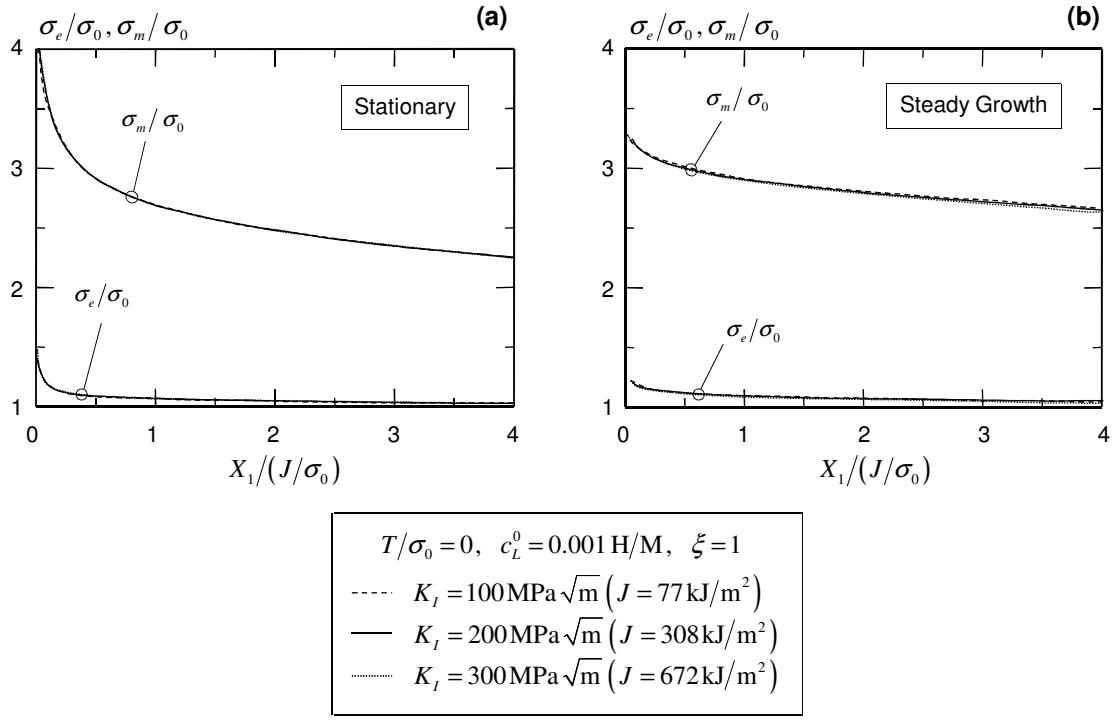

Figure 2.2: Self-similarity of plane-strain, stress fields on the crack plane ahead of (a) a stationary crack and (b) steadily growing sharp crack tip in hydrogen-charged material.

2.3.1 Self-similarity of near-tip fields

Figure 2.2 shows the normalized mean stress and the normalized Von Mises stress, σ_e/σ_0, on the uncracked ligament ahead of a sharp crack when the initial hydrogen concentration in normal interstitial lattice sites $c_L^0 = 0.001\,\mathrm{H/M}$ in the limit of a non-softening material (for simplicity) for the (a) stationary and (b) steady-growth cases. For both cases, the stress fields are shown for three, increasing levels of remote loading, K_I =100, 200, and 300 MPa$\sqrt{\mathrm{m}}$ (corresponding to J-integral values of 77, 308, and 672 kJ/m^2) and T-stress equal to zero. The stationary crack solutions are obtained using the finite element code (WARP3D) and the same constitutive model incorporating hydrogen effects on local plastic flow. The stationary crack solutions reflect plane-strain conditions and a small-strain theory formulations adopted for the steadily growing crack computations.

Similar to the response for a material without hydrogen, the near-tip stress fields for both the stationary and growing cracks exhibit strongly self-similar behavior when distances from the tip are scaled by J/σ_0, or equivalently $(K_I/\sigma_0)^2$. The quantity J/σ_0 defines approximately the value of crack-tip opening displacement and provides a physically meaningful length-scale for normalization. Furthermore, both cases show monotonically increasing stress values as the tip is approached in contrast to a finite strain, blunting crack

tip solution which achieves a peak value near $X_1/(J/\sigma_0)) = 1$ for the stationary crack tip [59]. In both cases, σ_m/σ_0 is significantly higher than σ_e/σ_0, indicating high levels of stress triaxiality. Consistent with the response for materials without hydrogen, the stationary crack exhibits a higher stress gradient than does the growing crack. The present growing crack solutions reflect the asymptotic analyses of Rice and Sorensen [91] who show that opening displacements exhibit a lower order singularity than for a stationary crack. Their results imply reduced strains and stresses for a growing crack, as shown here in Fig. 2.2. Although not shown here, different but self-similar solutions also exist for nonzero values of T-stress as implied from standard dimensional considerations of the SSY conditions. When the T-stress is held constant, for example at $T/\sigma_0 = -0.4$, the fields also exhibit invariance with increasing applied K_I (as exists in the absence of hydrogen). Given the self-similar nature of these steady-growth fields with and without T-stress, all subsequent analyses described here employ a single level of applied remote load $K_I = 200\,\mathrm{MPa}\sqrt{\mathrm{m}}$ ($J = 308\,\mathrm{kJ/m^2}$), with and without T-stress, and normalize the fields appropriately.

2.3.2 Effect of imposed constraint and hydrogen-induced softening on stress fields

Figure 2.3(a) displays the normalized mean stress ahead of the crack tip for the material property set $c_L^0 = 0.001$ H/M, $\xi = 1$ and the constraint levels T/σ_0 =0, 0.4, and -0.4. The stress magnitudes depend slightly upon the level of constraint reflected through the imposed T-stress, but the decay with distance ahead of the crack tip is otherwise unchanged. Results for the nonzero values of T-stress collapse into the same σ_m/σ_0 ratio for this set of material parameters over distances $0 < X_1/(J/\sigma_0) < 3$. The Varias and Shih [117] results presume no hydrogen-material coupling and reveal similar behavior near the tip. At $X_1/(J/\sigma_0) > 3$, solutions for the positive and negative constraint conditions diverge in both hydrogen charged and free ($c_L^0 = 0$) materials. Only a minor difference exists between the mean stress values in the limit of a non-softening material with or without hydrogen when $T/\sigma_0 = 0$.

For $c_L^0 = 0.01$ H/M and $\xi = 1$, which is shown in Fig. 2.3(b), the much larger initial value of hydrogen concentration influences the mean stress by reducing its magnitude relative to the $c_L^0 = 0.001$ H/M, $\xi = 1$ case and by amplifying the effects of differing constraint levels. The stresses for $T/\sigma_0 = -0.4$ are larger than $T/\sigma_0 = 0.4$. The mean stress for $T/\sigma_0 = 0$ remains higher than the mean stress when $T/\sigma_0 \neq 0$, as previously seen in the results for a lower initial concentration of hydrogen. Both positive and negative constraint reduce the mean stress with the reduction depending weakly on the initial hydrogen concentration.

If the material softens, the magnitude of mean stress decreases relative to the value for the limit of a non-softening material ($\xi = 1$), regardless of the imposed constraint level. Figs. 2.3 (c) and (d) show the mean

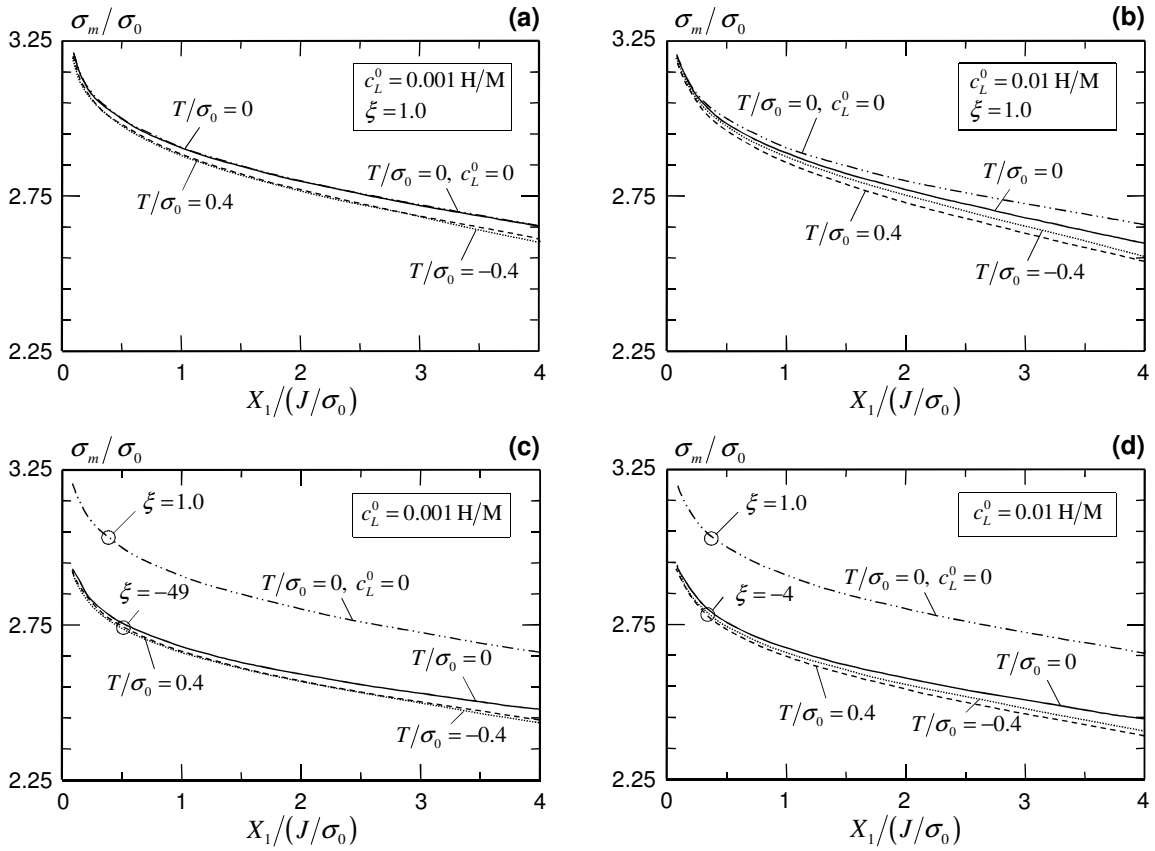

Figure 2.3: Mean stress ahead of a steadily growing crack for various levels of constraint with: (a) moderate initial hydrogen concentration and no softening; (b) high initial hydrogen concentration and no softening; (c) moderate initial hydrogen concentration and softening; (d) high initial hydrogen concentration and softening.

stress along the ligament ahead of an advancing crack tip for $c_L^0 = 0.001$ H/M, $\xi = -49$ and $c_L^0 = 0.01$ H/M, $\xi = -4$, respectively. According to Eqn. (2.2), these parameters produce a five percent reduction of the yield stress at the corresponding initial concentration of hydrogen. The mean stress magnitude does not diminish exactly in proportion to the initial reduction of the yield stress from hydrogen-induced softening, *e.g.* at $X_1/(J/\sigma_0) = 4$, the mean stress for $c_L^0 = 0.001$ H/M, $\xi = -49$ and $c_L^0 = 0.01$ H/M, $\xi = -4$ equals 93% and 92%, respectively, of the mean stress for a hydrogen-free material, if $T/\sigma_0 = 0$. Similar interactions among the mean stress, the imposed constraint levels, and the initial hydrogen concentration occur in both softening and non-softening materials.

Although not shown in a figure, the scaled levels of total hydrogen concentration, c/c_L^0, and normalized Von Mises stress, σ_e/σ_0, demonstrate similar behavior as does $\sigma_{kk}/3\sigma_0$ for the steadily propagating crack. A high concentration of initial hydrogen reduces significantly the magnitude of the c/c_L^0 ratio relative to a lower c_L^0, but the absolute value of the total hydrogen concentration, c, for $c_L^0 = 0.01$ H/M is considerably

larger than the value for $c_L^0 = 0.001$ H/M. The effect of constraint and initial hydrogen concentration on the Von Mises stress declines compared with the corresponding effect on the mean stress. The Von Mises stress depends more strongly on hydrogen-induced material softening than the mean stress, *e.g.* a five percent initial reduction in the yield stress produces a 10% decrease in the Von Mises stress from the non-softening value at $X_1/(J/\sigma_0) = 4$.

2.3.3 Effect of imposed constraint and hydrogen-induced softening on triaxiality

The quantity $3\sigma_m/2\sigma_e$ defines a convenient measure of triaxiality linked to the growth rate of micro-scale voids consistent with the subsequently introduced damage measure. This designation of triaxiality differs slightly from the sometimes used measure, σ_m/σ_e, by a non-dimensional factor of 1.5 that does not lead to any change in the interpretation of the present computational results. Figure 2.4 reveals that hydrogen-induced softening influences strongly the triaxiality well ahead of a steadily growing crack in a hydrogenated material. Hydrogen concentration and imposed constraint levels affect triaxiality to a lesser extent.

Figure 2.4 (a) presents triaxiality values on the ligament ahead of a propagating crack with T/σ_0. Very near the crack tip, *i.e.* over $0 \leq X_1/(J/\sigma_0) \leq 1$, the triaxiality fields group according to the initial value of the local yield stress, $\sigma_y\left(\bar{\varepsilon}^p = 0,\, c_L^0\right)$, with material parameters shown in Table 2.2. Within this region, a high value of initial hydrogen concentration leads to uniformly lower triaxiality values for $\sigma_y\left(0, c_L^0\right) = 0.95\sigma_0$ materials. If $\sigma_y\left(0, c_L^0\right) = 0.90\sigma_0$, then for $X_1/(J/\sigma_0) < 0.5$, a large initial concentration of hydrogen raises the triaxiality values. Farther from the crack tip, *i.e.* $X_1/(J/\sigma_0) > 1$, $3\sigma_m/2\sigma_e$ decays faster receding from the crack tip in a material for $c_L^0 = 0.01$ H/M conditions than for $c_L^0 = 0.001$ H/M conditions. Larger reductions of the initial yield stress enhance the triaxiality values of a propagating crack, and all material combinations in a hydrogen-charged material produce triaxiality values above the triaxiality values found in a hydrogen-free material – in contrast to a stationary crack.

Positive and negative imposed constraint levels reduce slightly the triaxiality far from the tip of a steadily growing crack, but the influence of constraint differences diminishes very near the crack tip. Positive constraint, shown in Fig. 2.4(b), suppresses triaxiality somewhat less than negative constraint configurations, shown in Fig. 2.4(c). Constraint effects manifest more readily in materials with high concentration of initial hydrogen, though these effects also exist for materials without hydrogen. As in the $T/\sigma_0 = 0$ case, large values of initial hydrogen reduce triaxiality far from the crack, and approaching the crack tip, a reduction of the flow stress, $\sigma_y\left(0, c_L^0\right)$, corresponds to an increase of triaxiality.

Generally, the initial reduction of the yield stress dominates the influence of all other variables on tri-

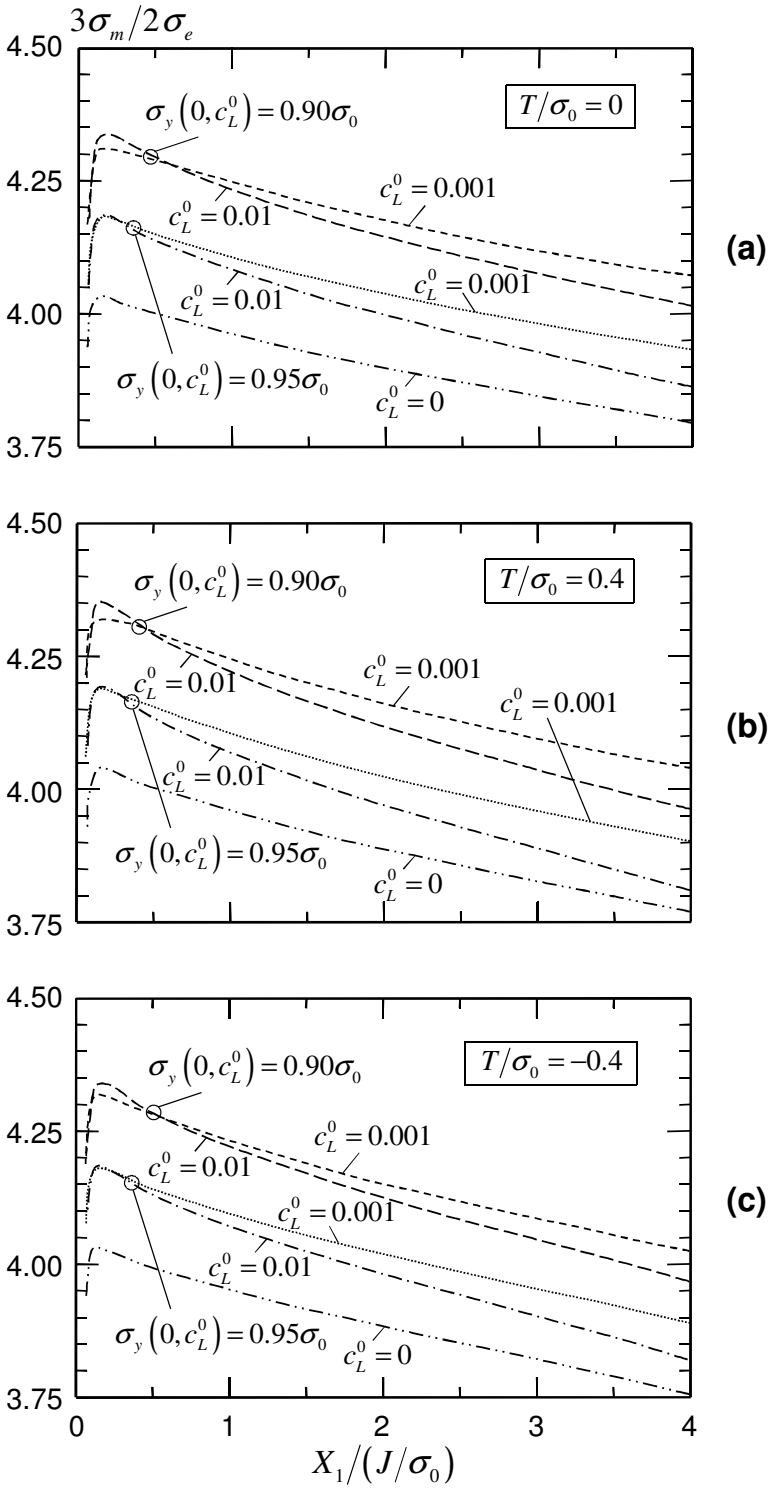

Figure 2.4: Triaxiality values ahead of a steadily growing crack tip for levels of (a) zero T-stress, (b) positive T-stress, and (c) negative T-stress.

axiality. Far from the crack tip, an applied nonzero T-stress decreases modestly the triaxiality; similarly, a high initial concentration of hydrogen suppresses triaxiality development. Near the crack tip, the triaxiality values vary according to the initial reduction of the yield stress. In the present study, no combination of imposed constraint levels or initial hydrogen concentration exists which influences triaxiality levels more strongly than the initial reduction of the yield stress.

2.3.4 Effect of imposed constraint and hydrogen-induced softening on plastic strains

Along the uncracked ligament, the equivalent plastic strain, $\bar{\varepsilon}^p$, rises monotonically and sharply near the crack tip. Let $\bar{\varepsilon}^p_{ref}$ denote a reference field of equivalent plastic strain that develops for a steadily growing crack when $T/\sigma_0 = 0$, $c_L^0 = 0$. Figure 2.5 displays the scaled ratios of $\bar{\varepsilon}^p/\bar{\varepsilon}^p_{ref}$ for a range of imposed levels of constraint, initial concentration of hydrogen, and intensity of hydrogen induced softening. This normalization shows readily the effect of the remote T-stress on the plastic strain without hydrogen and allows for a direct comparison among combinations of material parameters.

For $T/\sigma_0 \geq 0$ (Fig. 2.5(a) and (b)), hydrogen-induced softening promotes development of large plastic strains compared to materials without hydrogen. The largest plastic strain far from the crack tip under an imposed remote loading of $T/\sigma_0 = 0$ occurs for $c_L^0 = 0.01$ H/M, $\xi = -9$, but the case $c_L^0 = 0.001$ H/M, $\xi = -99$ leads to the largest values near the crack tip. The $\bar{\varepsilon}^p/\bar{\varepsilon}^p_{ref}$ ratio exhibits similar behavior between the cases $c_L^0 = 0.01$ H/M, $\xi = -4$ and $c_L^0 = 0.001$ H/M, $\xi = -49$, though a higher initial yield stress leads to lower plastic strains. A high value of initial hydrogen concentration may marginally offset the effects of localized plastic softening on plastic strain, *e.g.* the $\bar{\varepsilon}^p/\bar{\varepsilon}^p_{ref}$ ratio for $c_L^0 = 0.01$ H/M, $\xi = -4$ exceeds that for $c_L^0 = 0.001$ H/M, $\xi = -99$ over $1 \leq X_1/(J/\sigma_0) \leq 2$ under $T/\sigma_0 = 0$ remote loading. Positive constraint, Fig. 2.5(b), lowers all $\bar{\varepsilon}^p/\bar{\varepsilon}^p_{ref}$ ratios below the $T/\sigma_0 = 0$ case and reduces the relative effect of high initial hydrogen concentration on this ratio. The relationships between the plastic strain fields dependent on the sets of material parameters vary minimally in the $T/\sigma_0 = 0.4$ case versus the $T/\sigma_0 = 0$ case.

For the low constraint configuration ($T/\sigma_0 = -0.4$), shown in Fig. 2.5(c), the initial hydrogen concentration affects the differences among the $\bar{\varepsilon}^p/\bar{\varepsilon}^p_{ref}$ fields more strongly than for the $T/\sigma_0 \geq 0$ cases. The negative imposed constraint diminishes the plastic strain relative to the reference value $\bar{\varepsilon}^p$, *i.e.* when $c_L^0 = 0$, $T/\sigma_0 = 0$, but $\bar{\varepsilon}^p$ increases above the value of plastic strain calculated in a hydrogen-free material under the same level of imposed constraint. The material parameters $c_L^0 = 0.01$ H/M, $\xi = -9$ lead to the highest plastic strain far from the crack tip, while the parameters $c_L^0 = 0.01$ H/M, $\xi = -4$ now result in the highest plastic strain over $0.5 \leq X_1/(J/\sigma_0) \leq 1.5$ – in contrast to the trends in Fig. 2.5(a) and (b). Materials

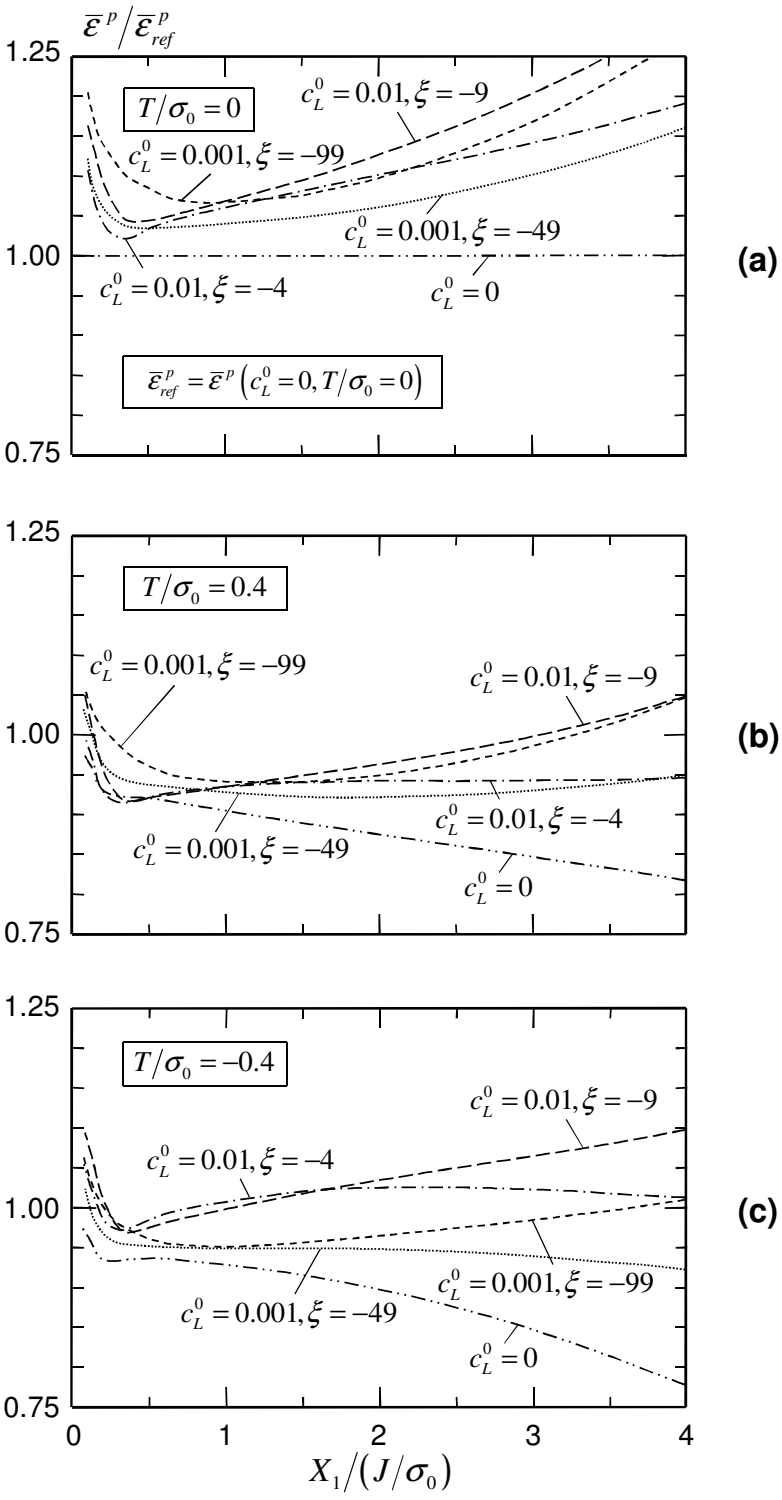

Figure 2.5: Equivalent plastic strain scaled by the reference equivalent plastic strain at the same material point ahead of a steadily growing crack tip for levels of (a) zero T-stress, (b) positive T-stress, and (c) negative T-stress.

with $c_L^0 = 0.001$ H/M and $c_L^0 = 0.01$ H/M exhibit the same general behavior, but the plastic strain rises with increasing initial concentrations of hydrogen irrespective of the initial reduction of the yield stress. Away from the crack tip, the $\bar{\varepsilon}^p/\bar{\varepsilon}^p_{ref}$ ratio exceeds unity for certain material parameter combinations, which correspond to large c_L^0 values.

Overall, hydrogen enhances the plastic flow ahead of a steadily propagating crack, especially at distances $X_1/(J/\sigma_0) > 1$, relative to a material without hydrogen (the $c_L^0 = 0$ case). Both positive and negative constraint conditions ($T/\sigma_0 = \pm 0.4$) reduce the plastic strains relative to the $T/\sigma_0 = 0$ condition, in material with and without hydrogen. These responses influence directly the relative void-growth rates discussed in the following section. In high constraint configurations, *i.e.* $T/\sigma_0 \geq 0$, large initial reductions of the yield stress due to softening lead to larger values of plastic strain with a negligible effect due to the value of initial hydrogen concentration. Highly softening materials with a large initial hydrogen concentration exhibit the largest plastic strain values far from the crack tip, $X_1/(J/\sigma_0) > 1$; near the crack tip, the effect of hydrogen-induced softening on plastic strain becomes more complex.

2.4 Damage parameters for hydrogen assisted steady crack growth

Within a hydrogen-charged material, crack propagation leads to failure through a ductile void growth and coalescence mechanism. The first subsection here adopts a simple and popular measure for the rate of void growth that depends linearly on the equivalent plastic strain rate and exponentially on the triaxiality. The second subsection provides the key results of the numerical simulations and focuses on void growth ahead of a steadily propagating crack as affected by imposed constraint levels, the initial hydrogen concentration, and the initial reduction of the yield stress.

2.4.1 Void-growth damage parameter

Rice and Tracey [92] model the growth of a spherical void in a non-hardening plastic material, which deforms according to the Von Mises flow rule. Mean and uniform deviatoric strain rates applied at the remote boundary lead to an exponential expansion of an isolated void of radius $\bar{R}$ such that the rate of change $\dot{\bar{R}}$ follows the simple relationship:

$$\frac{\dot{\bar{R}}}{\bar{R}} = B\,\dot{\bar{\varepsilon}}^p \exp\left(\frac{3\sigma_m}{2\sigma_e}\right). \tag{2.6}$$

The positive, non-dimensional constant, B, depends on components of the principal strain rates applied at the remote boundary (under uniaxial tension, $B = 0.283$). The simplified model of Eqn. (2.6) neglects a

potential increase in the rate of void growth from internal pressure exerted by the presence of molecular hydrogen that may exist within the void. Hydrogen gas pressures associated with lattice concentrations of 0.01 H/M considered in the present work are negligibly small considering that niobium is an exothermic occluder of hydrogen with heat of solution equal to -8.6 Kcal/mole [54].

The isolated void idealization in Eqn. (2.6) requires consideration of the potential for strong coalescence effects at large void-growth levels. Liang et al. [58] investigate the effect of hydrogen on void coalescence for the same niobium-like material. They demonstrate no influence of hydrogen on void coalescence in a unit cell for triaxiality values ($3\sigma_m/2\sigma_e$) greater than approximately 1.5 when the number of trapping sites per trap (α) equals one, as in the present study. Hydrogen does influence void coalescence in structural metals not considered here. Hydrogen in material with $\alpha = 10$, *i.e.* trapping at stronger defects than dislocations (grain boundaries or precipitates), strongly promotes void coalescence under low triaxiality [58]. Ahn et al. [1] show that hydrogen significantly accelerates void coalescence in an A533B steel where $\alpha = 1$ even for triaxiality values as large as 4.5. Equation (2.6) measures the void-growth rate for a single void without consideration of coalescence with adjacent voids and, for this niobium-like material with $\alpha = 1$, provides a good estimate of void growth ahead of a steadily propagating crack where large triaxiality values occur, as shown in Fig. 2.4.

For a specified initial void radius of $\bar{R}_0$, integration of Eqn. (2.6) over the history of loading – $\bar{\varepsilon}^p(t)$, $\sigma_e(t)$, and $\sigma_m(t)$ – yields the current radius of the void at time t. The variable ζ denotes a convenient, non-dimensional measure of the extent of ductile void growth based on Eqn. (2.6) and defined as

$$\zeta = \ln\left(\frac{\bar{R}}{\bar{R}_0}\right) = \int_0^t B\,\dot{\bar{\varepsilon}}^p \exp\left(\frac{3\sigma_m}{2\sigma_e}\right) dt'. \tag{2.7}$$

Steady-state crack growth conditions reduce the time integral in Eqn. (2.7) to an integration along streamlines parallel to the plane of crack growth.

The reference level of ductile void growth, ζ_{ref}, corresponds to the void growth for $T/\sigma_0 = 0$, $c_L^0 = 0$ under the remote loading level $K_I = 200$ MPa$\sqrt{\text{m}}$, similar to the definition of $\bar{\varepsilon}^p_{ref}$. Figure 2.6 displays the ratio ζ/ζ_{ref} along the ligament ahead of a steadily propagating crack crack, where combinations of imposed constraint, initial hydrogen concentration, and the intensity of hydrogen-induced softening govern the value of ζ. Table 2.2 displays the effect of these parameters on the initial yield stress reduction. A ratio $\zeta/\zeta_{ref} > 1$ indicates acceleration of ductile void growth due to the HELP mechanism with respect to a hydrogen-free material under zero T-stress. This ratio varies with distance ahead of a propagating crack, as well as ahead of a stationary crack tip [59], and depends highly on material and remote loading conditions.

2.4.2 Effect of imposed constraint and hydrogen-induced softening on void growth

Figure 2.6 displays the void-growth damage parameter along the ligament ahead of a steadily propagating crack tip. Relative to the reference case, ζ_{ref}, hydrogen-induced plasticity accelerates void growth for all material parameters in the present study – except for $c_L^0 = 0.01$ H/M, $\xi = -4$ under positive ($T/\sigma_0 > 0$) constraint. Figures 2.5 and 2.6 demonstrate that higher values of the triaxiality parameter lead to the hydrogen-enhanced void growth.

In hydrogen-free materials (the $c_L^0 = 0$ curves), Figures 2.6(b) and (c) show that imposed constraint – both positive and negative – suppresses void growth relative to the $T/\sigma_0 = 0$ constraint level, consistent with the earlier work of Varias and Shih [117]. Taken together, these results suggest that the $J - \Delta a$ crack-growth resistance curves for a hydrogen-charged material will exhibit a reduced resistance to growth compared to materials without hydrogen in both high and low imposed constraint configurations.

The ζ/ζ_{ref} ratios of a zero T-stress configuration, shown in Fig. 2.6(a), depend primarily on the initial reduction of the yield stress due to softening and secondarily on the concentration of initial hydrogen. Hydrogen-induced material softening promotes void growth, while high initial concentrations of hydrogen suppress void growth for a fixed value of initial reduction of the yield stress due to softening. For example, materials having a 10% reduction of the yield stress $\sigma_y\left(0, c_L^0\right)$, exhibit higher levels of void growth than materials with a lower yield stress reduction, irrespective of the value of initial hydrogen, c_L^0. An examination of Figs. 2.4 and 2.5(a). for the same $T/\sigma_0 = 0$ condition, indicates that the differences between the curves in Fig. 2.6(a) arise from triaxiality effects more so than differences in the plastic strain.

Configurations under a positive T-stress, as shown in Fig. 2.6(b), reveal similar relative behavior as do configurations under zero T-stress, but with all ζ/ζ_{ref} ratios declining by approximately 0.25 for all sets of material parameters. Relative to the $c_L^0 = 0$, $T/\sigma_0 = 0.4$ results, hydrogen-induced plasticity again accelerates void growth in all cases under positive constraint, but the void growth in a material with a large initial concentration of hydrogen, *i.e.* $c_L^0 = 0.01$ H/M, and a modest reduction of the initial yield stress, *i.e.* 5% lower than the reference case, ζ_{ref}.

For negative imposed constraint, Fig. 2.6(c) shows that the ζ/ζ_{ref} ratios cluster into two groups differentiated by the initial reduction of the yield stress. The lowest curve on the figure, corresponding to a material without hydrogen, reveals a void-growth damage parameter having similar values to the positive T/σ_0 configuration. This figure also reveals that the negative constraint configuration diminishes the influence of initial values of hydrogen concentration on the void-growth damage parameter compared with the $T \geq 0$ cases. High concentrations of initial hydrogen in a material, under a negative constraint configuration,

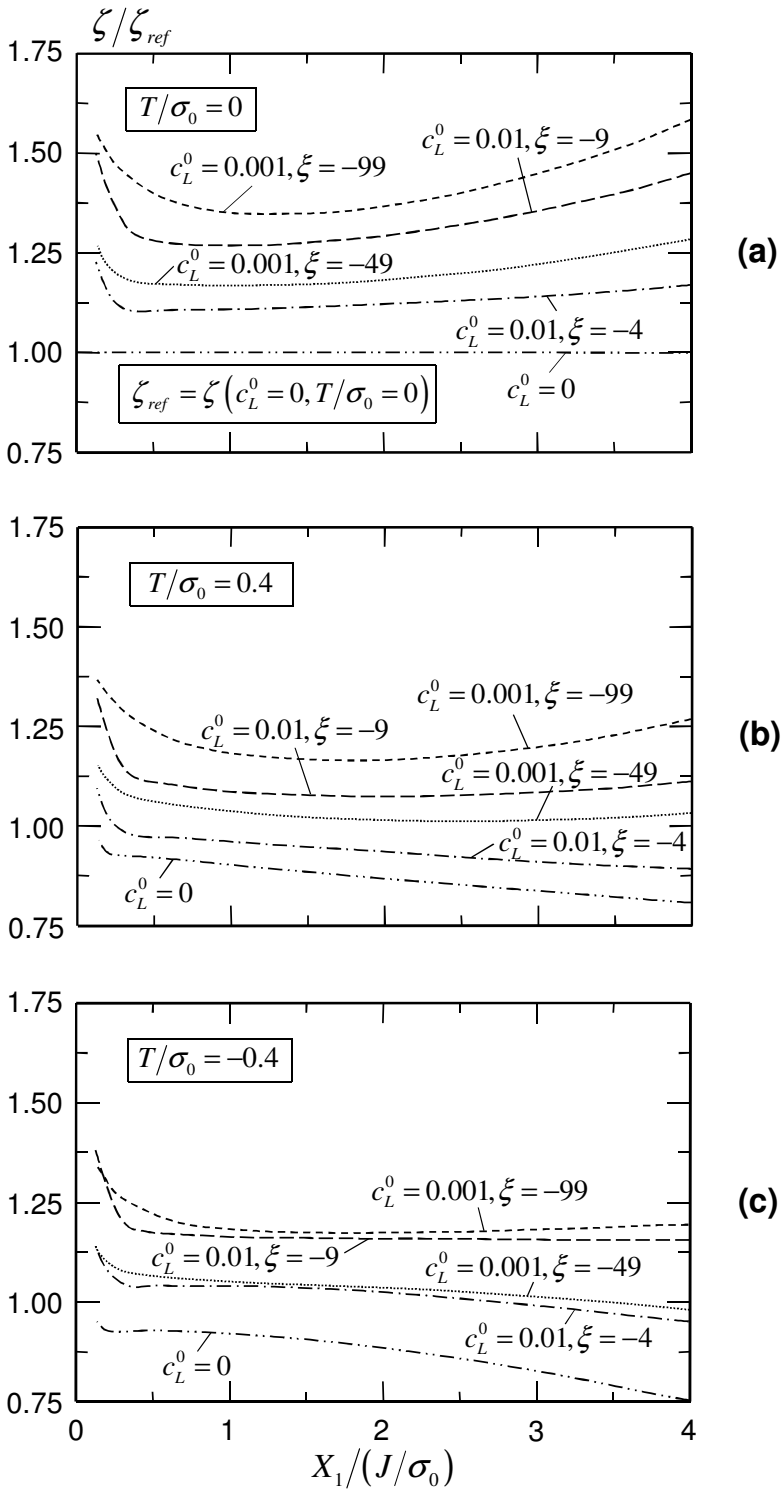

Figure 2.6: void-growth parameter scaled by the reference void-growth parameter at the same point ahead of a steadily growing crack tip for levels of (a) zero T-stress, (b) positive T-stress, and (c) negative T-stress.

generate comparatively higher values of plastic strain and offset the reduced triaxiality in the ζ calculations. Thus, materials with the same initial reduction of the flow stress exhibit very similar void-growth damage parameters in a low constraint configuration.

Numerical results for hydrogenated materials in the limit of a non-softening response are not shown. In such materials, the void-growth damage parameter is always lower than for the hydrogen-free case, $c_L^0 = 0$, at the same level of imposed constraint. The void-growth damage parameter in a moderate initial concentration of hydrogen ($c_L^0 \leq 0.001$ H/M) differs negligibly from the damage parameter in hydrogen-free materials. At larger initial concentrations of hydrogen, the void growth diminishes modestly, *e.g.* for a zero T-stress, the ζ/ζ_{ref} value of a non-softening material with $c_L^0 = 0.01$ H/M at $X_1/(J/\sigma_0) = 1$ equals 0.95, *i.e.* only a five percent reduction. Under negative imposed constraint, the void-growth damage parameter curves for non-softening materials cluster around the hydrogen-free values.

2.5 Discussion and conclusions

This study describes the computational model and key results for steady-state, crack growth analyses in a high solubility material, *e.g.* niobium, under small deformation assumptions in the presence of hydrogen. The constitutive response follows a continuum description predicated on the hydrogen-enhanced, localized plasticity (HELP) mechanism. The hydrogen atoms in lattice and trap sites remain in equilibrium with the mean stress and equivalent plastic strain, $\bar{\varepsilon}^p$. Further, the total hydrogen concentration, c, and the intensity of hydrogen-induced softening, ξ, determine the local flow stress at each material point. In the present study, we examine effects on the near-tip fields by varying: the initial concentration of hydrogen, c_L^0; the initial yield stress, σ_0, which varies with c_L^0; and the imposed constraint, characterized by the remote T-stress. In these small-scale yielding models, near-tip fields of a steadily propagating crack in the presence of hydrogen exhibit self-similar behavior when distances ahead of the crack front are scaled by J/σ_0. This behavior also holds at each level of nonzero T-stress loading, where the normalized crack-tip fields remain self-similar and unique for the T-stress value, invariant of imposed remote K_I levels. All analyses occur here under a stress intensity factor, applied remotely, of $K_I = 200$ MPa$\sqrt{\text{m}}$ selected for convenience to define a well-contained plastic zone within the specified finite element mesh. A void-growth damage parameter, ζ, depends exponentially on a *triaxiality parameter* ($3\sigma_m/2\sigma_e$) and linearly on the equivalent plastic strain. This parameter quantifies the level of damage from void growth along the ligament ahead of an advancing crack tip. From the results of these analyses, the following key conclusions hold:

1. Hydrogen-induced plasticity accelerates void-growth rates relative to the rates of a hydrogen-free ma-

terial subjected to the same crack-tip field. The void-growth rate depends strongly on the complex relationship among the initial concentration of hydrogen (c_L^0), the rate of hydrogen induced softening (ξ), and the applied crack-tip constraint level (T/σ_0). In the damage model adopted here, the void-growth rate increases exponentially with triaxiality ($3\sigma_m/2\sigma_e$); triaxiality rises primarily as the *initial* yield stress decreases and rises secondarily as the hydrogen-induced relaxation of the mean stress decreases due to the reduced dilatation that relaxes the normal stresses. For materials with the same hydrogen-induced reduction of the initial yield stress, $\sigma_y\left(0, c_L^0\right)/\sigma_0$, due to a specific combination of c_L^0 and ξ, the void-growth rate is smaller at the larger initial concentration of hydrogen, due to the reduction of the triaxiality with increasing values for the initial concentration of hydrogen, as shown in Fig. 2.4. In particular, the parameter set $c_L^0 = 0.001$ H/M, $\xi = -99$ generates the largest void-growth levels of all examined material combinations and levels of constraint. The numerical results reveal the increased triaxiality due to the large initial reduction of the yield stress (ten percent of σ_0) coupled with the small initial concentration of hydrogen for this parameter set. Similarly, a high value for the initial concentration of hydrogen leads to the smallest levels of void growth in the limit of a non-softening material. Without softening, a larger initial concentration of hydrogen increases the dilatational effect that lowers the mean stress, that reduces the triaxiality, and that consequently, reduces void growth. However, the effect of material softening in the presence of hydrogen to amplify void growth overwhelms the dilatational effect of hydrogen to lessen void growth. Thus, void growth ahead of a steadily propagating crack increases in the presence of hydrogen compared to the void growth in a hydrogen-free material.

2. As a consequence of the accelerated void growth, lower crack-growth resistance curves (R-curves) are to be expected in a material that exhibits hydrogen-induced softening compared to those for a hydrogen-free material at each constraint level (T/σ_0). Testing programs to assess the impact of hydrogen on fracture toughness through R-curves should be expanded to examine low-constraint configurations, for example SE(T)s, to supplement tests performed on standard high-constraint, deep-notch C(T)s and SE(B)s. Existing practice assumes these high-constraint specimens will always provide the lowest R-curves and will thus be conservative for design and defect assessment purposes. The present results indicate that specimen configurations with lower constraint, SE(T)s, may generate reduced R-curves in the presence of hydrogen. These key observations concur with those in the previous work of Ahn et al. [1, 2], who consider only the earliest states of ductile crack extension in the presence of hydrogen as the crack grows through the initial plastic region formed as the sharp-crack tip blunts before tearing.

3. For stationary cracks without hydrogen, previous work demonstrates that positive (negative) T-stress

increases (decreases) the triaxiality and consequently increases (reduces) void-growth rates. Notably, the same trends do not hold for the steadily propagating crack, as first shown by Varias and Shih [117] in the absence of hydrogen. nonzero imposed constraint levels ($T/\sigma_0 \neq 0$), either positive or negative, suppress void-growth rates in steadily propagating cracks for both hydrogen-charged and hydrogen-free materials, compared to the zero T-stress configuration. During steady-state crack growth, nonzero values of the applied T-stress reduce the mean stress ahead of the propagating crack (see Fig. 2.3). Reduction of the mean stress implies reduction of the triaxiality as can be readily seen in Fig. 2.4 for the hydrogen-free material. The magnitude of the corresponding reduction of void growth depends on the sign of the T-stress. Under high constraint, the relationships of the void-growth damage parameter among the various material sets remain unchanged, but reduced, relative to the zero T-stress configuration. In a low constraint configuration, void-growth rates cluster together depending on the reduction of the initial flow stress due to softening, regardless of the concentration of initial hydrogen. This consistency of response for a propagating crack does not occur in a blunting, stationary crack tip.

4. The triaxiality parameter, $3\sigma_m/2\sigma_e$, connected to the void-growth rate, increases strongly with the initial reduction of the yield stress due to softening and decreases modestly with the initial hydrogen concentration and the imposed, nonzero T-stress. For distances $X_1/\left(J/\sigma_0\right) < 1$, the triaxiality values separate into groups of increasing magnitude, controlled by the initial value of the flow stress reduction.

5. At a fixed level of imposed constraint, hydrogen-induced plasticity raises the plastic strain ahead of a propagating crack, relative to the values of plastic strain for a hydrogen-free material. If $T/\sigma_0 < 0$, then increasing the initial concentration of hydrogen will increase the plastic strain ahead of the crack tip more than increasing the hydrogen-induced reduction of the initial flow stress. Alternatively for $T/\sigma_0 \geq 0$, lowering the initial flow stress facilitates plastic yielding beyond the amount gained by increasing the concentration of initial hydrogen.

The present calculations indicate that acceleration of void growth by hydrogen depends primarily on reduction of the initial yield stress due to softening and secondarily on relaxation of the mean stress by hydrogen-induced dilatation. This result implies that even when the relaxation is small, as in low solubility systems such as steels, the primary driver of increased void growth remains the hydrogen-induced reduction of flow stress. Experimental results do show that hydrogen reduces the flow stress substantially in iron systems [108]. The present results demonstrate that low initial concentrations of hydrogen together with a high reduction rate (ξ) for the flow stress can produce large rates of void growth ahead of extending cracks.

Our results do not suggest the absence of softening for large concentrations of hydrogen under other conditions/material systems. Here we do find that even small hydrogen concentrations and an appropriate rate of hydrogen-induced softening generate high void-growth rates driving ductile fracture processes [36, 11]. Perhaps this lack of strong dependence on the initial concentration of hydrogen supports the assertion that operation of the HELP mechanism does not require large hydrogen accumulations or supersaturations of the host metal lattice. Thus, one might argue the HELP mechanism for fracture through void-growth acceleration operates equally well in low solubility systems, e.g. steels, in which hydrogen dissolves in amounts that are substantially lower than the ones examined in the present study. These studies are presented in the following chapter.

Chapter 3

Effects of Hydrogen on Steady, Ductile Crack Growth in Mismatched Welds of Ferritic Steels: Computational Studies

3.1 Introduction

The degradation of fracture toughness in common steels may limit the economical storage and transport of hydrogen using existing components built with current design standards. Welds join the majority of steel pressure vessel components and remain the most probable location of crack initiation with or without hydrogen present in the material. The structure may tolerate crack initiation in welds and subsequent (limited) crack growth. The results of this study describe the effects of local, crack-tip constraint on steel welds in the presence of hydrogen for slow, stable crack propagation. Under the conditions envisioned here, the diffusion rate sustains equilibrium of the hydrogen concentration ahead of the propagating crack tip and thus represents the classical Stage II regime of sustained load crack growth.

Burstow et al. [15] demonstrate that constraint variations, arising from the combined effects of weld metal-base metal strength mismatch and from the remotely applied loading, influence strongly the near-tip fields ahead of a stationary crack. Lin et al. [60] investigate the influence of weld-base material mismatch on the behavior of a single edge notched bend specimen and determine that the crack-growth resistance curves decrease significantly in under-matched welds. Other researchers examine the influence of constraint on the behavior of steady crack growth with the computational framework proposed by Dean and Hutchinson [21]. nonzero values of the T-stress reduce the near-tip fields ahead of a steadily propagating crack, as established by Varias and Shih [117]. In Niordson [78], highly over-matched welds lead to a significant reduction of the plastic zone size and a corresponding increase of the steady-state fracture toughness.

The presence of hydrogen modifies the continuum solutions for the near-tip fields by changing the local micromechanical behavior of the material. The work of Birnbaum and Sofronis [14] proposes a hydrogen shielding mechanism that reduces the repulsive force between dislocations. The experimental results of Tabata and Birnbaum [108] confirm hydrogen elevates the velocity of dislocations in iron. In the hydrogen-enhanced, localized plasticity (HELP) model [14], the increased dislocation mobility in the presence of hydrogen generates a reduction of the local yield stress, leading to accelerated void growth ahead of the

crack tip. The computational studies, found in Sofronis et al. [107] show that a constitutive response based on the HELP model produces shear localization in metals. The reduction of local flow stress induced by hydrogen in a homogeneous material with properties characteristic of niobium influences significantly ductile void growth ahead of a stationary crack, as determined by Liang et al. [59]. Ahn et al. [1] predict a significant reduction of the crack-growth resistance due to the effect of hydrogen in the earliest stages of growth as the crack tip emerges from the blunted tip. The steady-state fracture toughness of a propagating crack decreases in the presence of hydrogen, as shown in Chapter 2.

In the present study, we extend the steady-state results of Chapter 2 to crack propagation in steel welds. The next section presents a brief overview of the concepts underlying the steady-state algorithm, the hydrogen-enhanced plasticity model, and the computational implementation. Section 3.3 examines the effect on the active yield zone in mismatched welds, and Section 3.4 explores the impact on the hydrogen concentration due to the degree of material mismatch and to the level of the far-field applied constraint (characterized by the T-stress). A simple measure of void growth describes the influence of weld mismatch and far-field constraint in Section 3.5. The final section summarizes the results of the study and the major conclusions.

3.2 Modeling aspects

We consider a crack advancing at a constant velocity, $\dot{a}$, in the positive direction X_1 along the ligament at $X_2 = 0$. The near-tip fields exhibit invariance with respect to the crack tip in a sufficiently large domain beyond the site of crack initiation. The rate of change for a quantity, $\bullet$, with respect to time, t, depends on the distance from a point in the material to the crack tip by:

$$\partial\left(\bullet\right)/\partial t = -\dot{a}\,\partial\left(\bullet\right)/\partial X_1. \tag{3.1}$$

Thus, rate-dependent equations, *e.g.* the constitutive relations, evolve along lines parallel to the X_1 axis, *i.e.* streamlines, and opposite to the direction of crack propagation. The integration of such equations along streamlines determines, without a time-step integrator, the equilibrium value of the stress and inelastic strains. Equation (3.1) also implies that material properties, such as the initial yield stress, may not vary with respect to X_1, but may vary with respect to X_2. Cracks propagating at quasi-static rates generate negligible inertial forces. Varias and Shih [117] present further details of the formulation and the solution procedure.

Hydrogen exists at lattice or trap sites in metals, *e.g.* A533B pressure vessel steel, according to the theory

of Oriani [80], and influences the material response in the elastic and plastic regimes under mechanical load, as in Sofronis et al. [107]. The hydrogen at lattice sites in terms of hydrogen atoms per host metal atoms (H/M), c_L, and the mean stress, σ_m, follow the relationship:

$$c_L = \alpha \left(\beta - c_L\right) \exp\left(\gamma \sigma_m\right). \tag{3.2}$$

The parameters α, β, and γ signify constant material parameters for a steel at a temperature of 300 K with an initial concentration of hydrogen at lattice sites, $c_L^0 = 2.4634 \times 10^{-8}\, H/M$. The amount of hydrogen at trap sites in H/M, c_T, grows with the plastic strains and c_L. The total concentration of hydrogen, $c = c_L + c_T$, decreases the barriers for dislocation movement and leads to a function of the local yield stress, σ_Y, of the form:

$$f\left(\sigma_Y, \sigma_0, c, \bar{\varepsilon}^p\right) = 0. \tag{3.3}$$

In Eqn. (3.3), the local yield stress decreases linearly with increasing values of c and rises according to a power law relationship with $\bar{\varepsilon}^p$; the value of σ_0 denotes the yield stress of the material without hydrogen. For all analyses in the present study, the specified value of c_L^0 produces a one percent reduction of σ_Y. Ahn et al. [1] and Taha and Sofronis [109] present values of the material properties for A533B in the presence of hydrogen. The studies of Sofronis [105], Sofronis et al. [107], and Gullerud et al. [38] provide the theoretical background and computational implementation of the constitutive response.

The crack advances along the center of a weld with 25mm height ($X_2 = \pm 12.5$ mm) in a modified small-scale yield model symmetric about the $X_2 = 0$ plane, illustrated in Fig. 3.1. The boundaries of the rectangular domain of finite elements, composed of 180,000 crossed, constant strain triangular elements, extend to $X_1 \times X_2 = 4000 \times 2000$ (J/σ_0), with the weld-base interface at $X_2/\left(J/\sigma_0^b\right) = \pm 50$, for a remotely applied $K_I = 150\,\mathrm{MPa}\sqrt{\mathrm{m}}$ and the yield stress of the base material without hydrogen, $\sigma_0^b = 400\,\mathrm{MPa}$. The displacements applied to the far-field boundaries follow the first two terms of the Williams' solution, K_I and the T-stress. The steel welds and base plastic follow the same elastic-plastic constitutive model, but the yield stress of the steel weld without hydrogen, σ_0^w, varies to represent mismatch and generate material constraint effects.

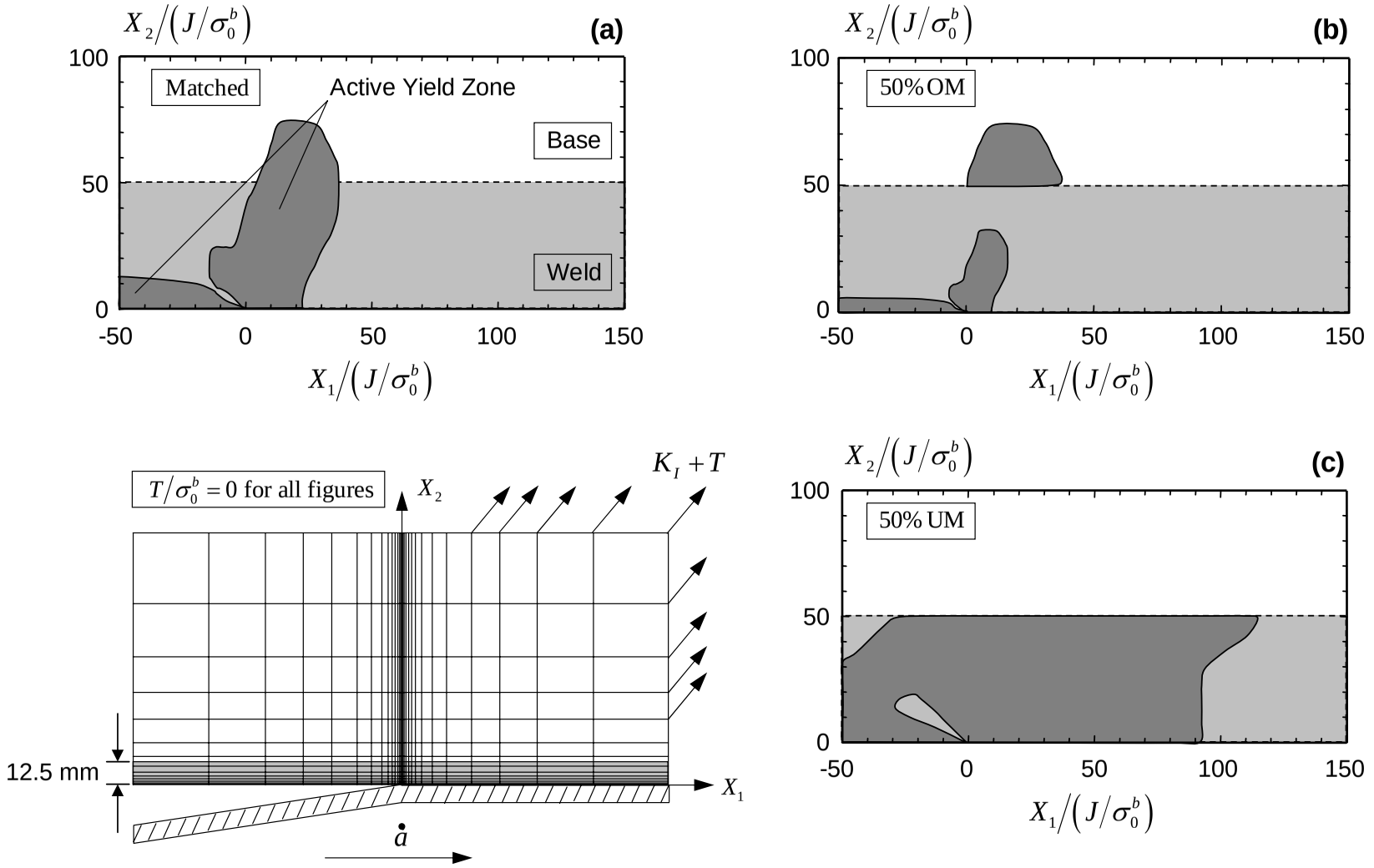

Figure 3.1: Active zone of plastic yielding ahead of a steadily growing crack in a ductile weld with yield strength that is (a) matched, (b) over-matched, and (c) under-matched compared to the yield strength of the base metal.

3.3 Active plastic yielding region of a hydrogen-charged material in a weld

Figure 3.1 displays the zone of active plastic yielding ahead of a crack tip located at $X_1 = 0$ for (a) matched, (b) 50% over-matched, and (c) 50% under-matched welds. The applied constraint, quantified by the T-stress, equals zero for all plots in Fig. 3.1. A positive T-stress restricts slightly the size of the active yield zone and increases yielding behind the crack tip. A negative T-stress promotes the growth of the active yield zone above and ahead of the crack tip.

The degree of weld-base mismatch affects significantly both the size and shape of the active yielding region. For a matched weld, shown in Fig. 3.1 (a), the advancing crack tip develops a continuous, active yield zone that extends to $X_1/\left(J/\sigma_0^b\right) = 20$ along the uncracked ligament. The size and profile of this active yield zone agree with the hydrogen-free results of Varias and Shih [117]; the presence of hydrogen slightly extends the plastic zone boundaries. Within a weld over-matched by 50%, *e.g.* Fig. 3.1 (b), the size of the active yield zone decreases by roughly a factor of two, but within the base metal, the size of the active yield zone remains similar to the matched weld case. Between $35 \leq X_2/\left(J/\sigma_0^b\right) \leq 50$, the weld metal constrains the plastic zone within unyielded material and separates the active yield regions of the weld and base metal. Figure 3.1 (c) presents the active yield zone of a steadily propagating crack through a 50% under-matched weld. The active yield zone expands to $X_1/\left(J/\sigma_0^b\right) = 90$ along the uncracked ligament and terminates at the boundary between the weld and base metal. The higher yield strength of the base metal limits plastic yielding to the weld metal and prevents formation of the steady-state profile of the active yield zone shown in the matched and over-matched welds. A pronounced trailing elastic sector develops behind the crack tip, as in previous studies without hydrogen [21].

3.4 Effect of mismatch and constraint on hydrogen concentration

Figure 3.2 displays the concentration of hydrogen under loading scaled by the initial concentration, c/c_L^0, along the uncracked ligament. The ratio c/c_L^0 varies with distance from the crack tip, the degree of mismatch, and the level of remote constraint, characterized by T/σ_0^b. The hydrogen present ahead of the crack tip influences strongly the deviatoric stresses, plastic strains, and mean stress.

The level of mismatch between the weld and base metal influences strongly the total concentration of hydrogen ahead of a propagating crack. Figure 3.2 demonstrates that the highest ratios of c/c_L^0 develop in (b) over-matched followed by the (a) matched then (c) under-matched welds, *i.e.* the ratio of c/c_L^0 increases

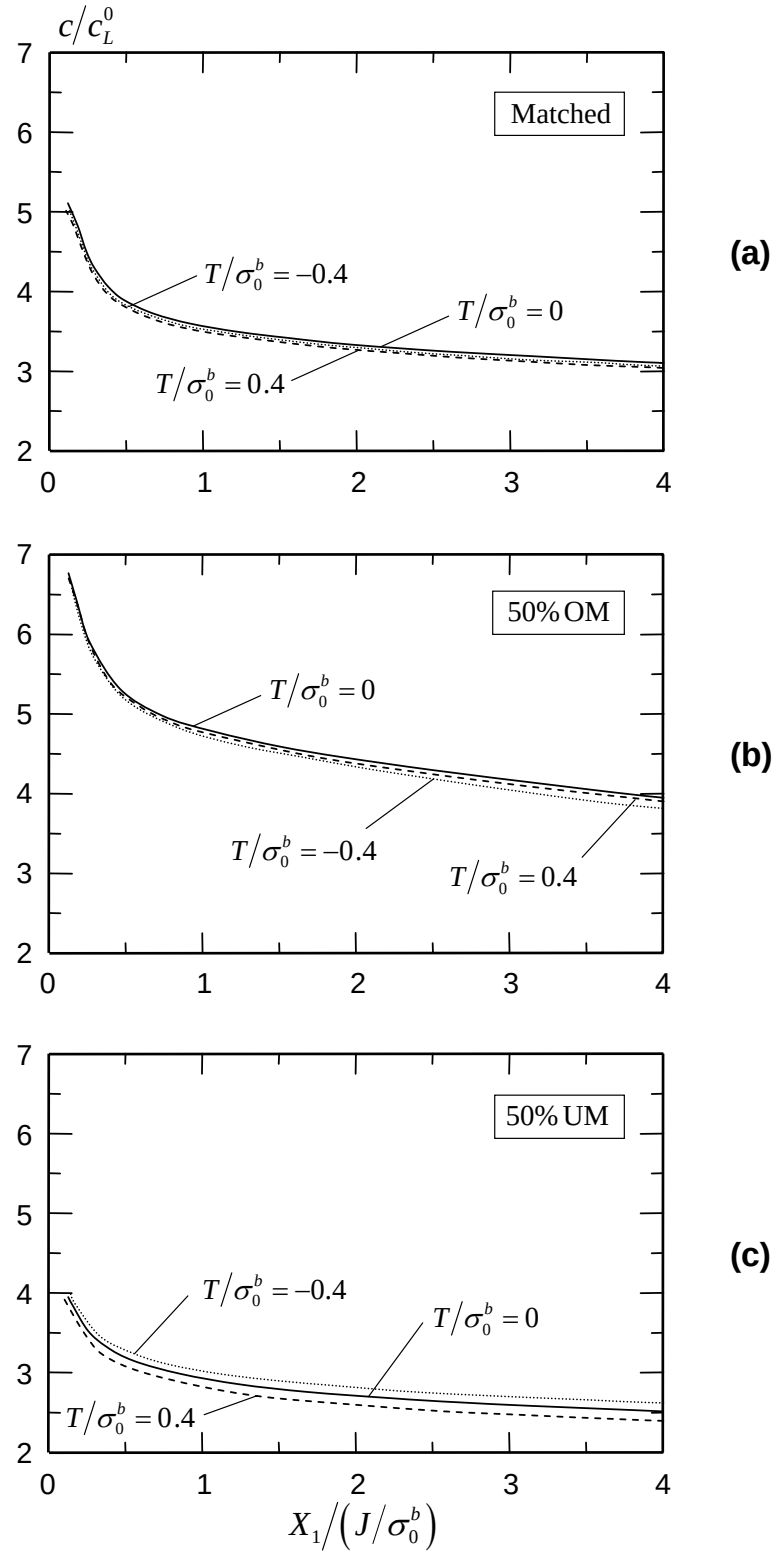

Figure 3.2: Total hydrogen concentration, scaled by the initial concentration of hydrogen, along the uncracked ligament, ahead of a steadily growing crack in a ductile weld with yield strength that is (a) matched, (b) over-matched, and (c) under-matched compared to the yield strength of the base metal.

with the degree of mismatch. The mismatch ratio determines largely the hydrogen concentration ahead of a steadily propagating crack regardless of the T-stress. By implication, over-matched welds develop larger values of hydrostatic stress than under-matched welds, in the presence of hydrogen, but lower plastic strains.

Figure 3.2 shows that the T-stress influences marginally the hydrogen concentration, with the greatest effect in the under-matched weld. In matched and over-matched welds, the hydrogen concentration decreases slightly with the application of a nonzero T-stress. In under-matched welds, a positive T-stress reduces the hydrogen concentration, but a negative T-stress increases slightly the concentration of hydrogen, and implies a higher mean stress, contrary to previous results for a steadily growing crack.

3.5 Effect of mismatch and constraint on void growth

The model of Rice and Tracey [92] provides a simple estimate of the void growth in a material. Let ζ denote $\ln(\rho/\rho_0)$, where ρ represents the current void radius and ρ_0 the original void radius. Then,

$$\zeta(X_1) = \int_{X_{1-R}}^{X_1} B \frac{\partial \bar{\varepsilon}^p}{\partial \lambda} \exp\left(\frac{3\sigma_m}{2\sigma_e}\right) d\lambda. \tag{3.4}$$

In Eqn. (3.4): B is a constant; and σ_e signifies the Von Mises stress. The integration in Eqn. (3.4) occurs along streamlines starting at the rightmost boundary (X_{1-R}) to the point X_1. The value of ζ increases monotonically on approach to the crack tip along the uncracked ligament. The reference void growth, ζ_{ref}, describes the void growth produced in a matched weld under a remote constraint of $T/\sigma_0 = 0$ in the presence of hydrogen. Figure 3.3 presents the normalized value of void growth along the uncracked ligament. The extent of weld to base strength mismatch, and to a lesser degree the level of applied T-stress, influences the magnitude of the void-growth parameter. Hydrogen elevates the void-growth parameter ahead of the uncracked ligament, irrespective of the degree of mismatch.

Hydrogen influences the mean stress, Von Mises stress, and plastic strain and, thus, generates competing effects in values of the void-growth parameter, ζ. Detailed evaluation of these quantities along the uncracked ligament reveals that differences in the plastic strain, $\bar{\varepsilon}^p$, due to strength mismatch generate the majority of variations in values of ζ. The triaxiality parameter, $3\sigma_m/2\sigma e$, varies marginally for these combinations of strength mismatch and T-stress, and does not exceed $\pm 5\%$ of the value in a matched weld with $T/\sigma_0 = 0$ over distances $0 \leq X_1/(J/\sigma_0) \leq 4$.

Figure 3.3 (a) displays the void growth in a matched weld for the applied constraint levels of $T/\sigma_0^b = 0, \pm 0.4$. The ratio ζ/ζ_{ref} remains largely constant with respect to distance ahead of the crack tip. nonzero values of the T-stress reduce the magnitude of void growth by suppressing plastic strain, and configurations

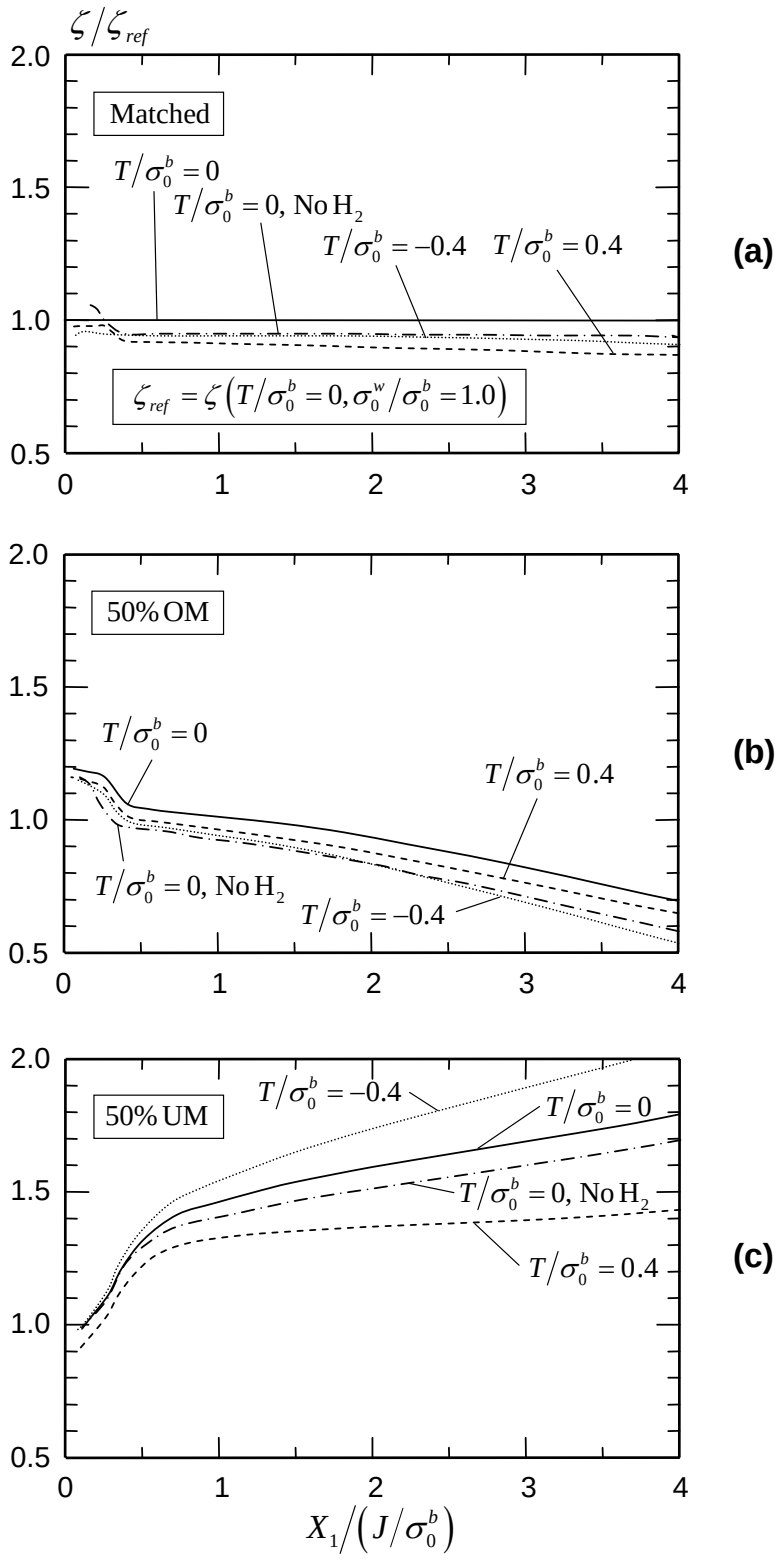

Figure 3.3: Void-growth parameter scaled by the reference void-growth parameter at the same point along the uncracked ligament, ahead of a steadily growing crack in a ductile weld with yield strength that is (a) matched, (b) over-matched, and (c) under-matched compared to the yield strength of the base metal.

under high constraint produce less plastic strain than configurations under low constraint. In Fig. 3.3 (b), values of the void-growth parameter decline in an over-matched weld compared to a matched weld, again largely due to the reduction in plastic strain. nonzero values of the T-stress further reduce void growth, but in over-matched welds, negative T-stress prevents void growth more effectively than positive T-stress.

Under-matched welds promote the development of significant void growth, as shown in Fig. 3.3 (c), through a substantial increase of plastic strain. These high values of ζ/ζ_{ref} imply substantial damage to the material prior to approach of the advancing crack and suggest a lower $J-\Delta a$ curve. The magnitude of void growth in an under-match weld exceeds the magnitudes of void growth in the matched and over-matched welds. Furthermore, the application of a negative T-stress leads to void growth above values found in the zero T-stress configuration and generates the largest void-growth values found in the present study.

3.6 Summary and Conclusions

The present study examines the near-tip fields of a steadily growing crack in mismatched steel welds in the presence of hydrogen for the Stage II regime of sustained load crack growth. A constitutive relation, based on the hydrogen-enhanced localized plasticity (HELP) mechanism, describes the effect of hydrogen through changes in the local flow stress. Constraint effects due to the degree of weld mismatch and to the remotely applied loading (T-stress) generate substantial changes in the shape and size of the active yielding region, the hydrogen concentration, and the void growth.

Weld metal-base metal mismatch of the yield stress leads to extensive changes in the near-tip fields. The region of active yielding shrinks in over-matched welds and expands in under-matched welds. The mean stress, and consequently the hydrogen concentration, in a weld increase with increasing levels of over-match, but the reduction in plastic strain due to the over-match diminishes the effects of increased triaxiality, thereby leading to a net decrease in comparable void growth. Void growth increases significantly for under-matched conditions due to increased plasticity and suggests that the steady-state fracture toughness of an under-matched weld may be significantly lower than a matched or over-matched weld.

The relative impact of remotely applied, far-field constraint, characterized by the T-stress, depends on the mismatch of the weld. The T-stress – positive or negative – generates a minimal reduction of the pointwise values of hydrogen concentration, c/c_L^0, in matched and over-matched welds; in under-matched welds, this ratio increases with a negative T-stress and decreases with a positive value of the T-stress. The T-stress influences marginally the void growth in matched and over-matched welds in this material, A533B. In under-matched welds, the void growth depends strongly on the level of T-stress. Positive T-stress values

suppress void growth, but negative T-stress values accelerate void growth, producing the highest void growth for steadily propagating cracks found in this study.

Chapter 4

Steady Crack Growth in a Thin, Ductile Plate under Small-Scale Yielding Conditions

4.1 Introduction

In structurally thin metallic components, ductile fracture commonly initiates at a crack-like defect sharpened by prior fatigue cycles at relatively low loads, followed by plastic blunting of the stationary crack front then ductile tearing at increased load. The present work focuses on the conditions during extended, approximately steady-state ductile tearing of a sharp, macroscopic crack observed in common structural alloys having a yield strength comparatively large relative to the tearing resistance, *e.g.*, aluminum, titanium and some high-strength steels). Newman et al. [76] and Seshadri et al. [100], for example, describe the laboratory fracture testing of large aluminum panels, exceeding 1 m in size, representative of aerospace structures.

For structurally thin plates of such materials, the strength and toughness combine to support significant amounts of ductile crack extension while the in-plane plastic zone remains comparable in size to at most a few multiples of the plate thickness, B, and well confined by surrounding linear-elastic material. Remote from the advancing crack front, a thin flat plate experiences linear-elastic, plane-stress response which transitions to increasing levels of elastic-plastic, generally plane-stress deformation nearer to the front, and finally to a region where the mechanical fields exhibit stronger, through-thickness changes. Deep within the plastic zone, along the crack front at distances of a small fraction of the thickness, the stresses approach those of plane strain over the middle-thickness region of the plate. We refer to these conditions as three-dimensional, small-scale yielding (3D SSY). The plate thickness, B, defines the only relevant structural dimension given the large planar dimensions and comparatively small plastic zones.

To provide a specific context, consider a large thin sheet (B = 1-5 mm) fabricated from an aluminum alloy with a yield strength of 350 MPa and a toughness of 40 MPa$\sqrt{\text{m}}$. The crack plane lies parallel to the rolling direction (a T-L orientation), which tends to favor a local "flat" mode I fracture process rather than a local "slanted" (across the thickness), mixed-mode process. The plastic zone size ahead of the crack front at the onset of tearing for a zero T-stress configuration is then approximately 2-4 mm, and (in-plane) SSY conditions clearly exist for a component of size larger than 75-100 mm. The plastic zone size

increases slightly during the early stages of growth as the crack extends through the initial blunting region. Essentially steady conditions evolve as the crack front advances further over distances of several thicknesses, characterized by a flat-to-nearly flat tearing resistance curve. Values of K_I and the non-singular T-stress describe approximately the effects of remote loading on the linear-elastic region enclosing the crack-front plastic zone. This thin plate behavior lies in sharp contrast to the continuing large increases of macroscopic tearing resistance measured in conventional $J-\Delta a$ tests using thick bend specimens of high-toughness alloys where crack extension reaches only a fraction of the thickness and the remaining ligament fully yields.

These crack front and structural conditions described for thin plates have been explored extensively through a computational, boundary-layer framework in plane-strain and plane-stress studies. Larsson and Carlsson [53] and many others examine stationary cracks. Tvergaard and Hutchinson [112] and Petti and Dodds [86] among others study the early stages of (transient) crack extension. Studies of steady-state, elastic-plastic crack extension in SSY conditions have also been limited to plane-stress and plane-strain conditions. Dean and Hutchinson [21] first outline the computational strategy for steady-state crack growth analyses in two-dimensional models based on integration of the elastic-plastic constitutive relations along streamlines to determine the stress history. Subsequent studies using this strategy examine steady crack growth in plane-stress [20], [73, 74] and in plane strain with T-stress effects (see [117] and Chapter 2). These studies neglect finite deformation effects – although Ferracin et al. [29] include finite rotations. In critical work that supports use of the small-strain formulation in computational studies, Reid and Drugan [88] establish the smaller influence of finite deformation effects on near-front fields for steady growth compared to a blunting stationary crack. They find minimal differences between asymptotic analyses including finite deformations and analyses that employ a small-strain formulation over microstructurally relevant distances at the advancing crack front.

Levy et al. [56] seem to have first suggested the 3D boundary-layer model for small-scale yielding with a stationary crack by introducing a finite thickness, B. Hom and McMeeking [44] use the 3D SSY model to examine void growth ahead of a stationary crack. Nakamura and Parks [72] provide a thorough study of 3D effects on the elastic-plastic fields for a sharp stationary crack. For elastic-plastic conditions with zero T-stress, they find the near-front fields exhibit a self-similarity scaling with the non-dimensional loading parameter, $\bar{J} = J^{far}/\varepsilon_0\sigma_0 B$. In contrast, the plane-stress and plane-strain solutions have no length scale other than inelastic deformations self-generated by the loading, *i.e.*, J/σ_0 or $(K_I/\sigma_0)^2$. The Nakamura and Parks [72] analyses show the 3D response differs from uniform fields over the thickness at distances from the crack front smaller than $r/B \approx 1.5$ for $\bar{J} \lesssim 5$. Yuan and Brocks [133] examine T-stress effects for stationary cracks, and Kim et al. [48] explore multi-term asymptotic expansions to describe the stationary crack fields,

with both works adopting the 3D SSY model. Roychowdhury and Dodds [96, 97] exploit the 3D SSY model and similarity scaling to investigate plasticity-induced, crack-closure effects during fatigue crack advance.

The present study extends for the first time the computational strategy of Dean and Hutchinson [21] for streamline integration to the 3D SSY framework. We describe the near-front, 3D displacements, strains, and stresses for elastic-plastic, steady crack advance derived from a refined finite element model. This initial 3D work limits consideration to a straight, flat crack front extending at quasi-static rates under remote mode I loading with zero T-stress. The outside surface of the plate is smooth (no side-grooves). These first computational results focus on key features of the crack-front fields and demonstration of the self-similar scaling described by the non-dimensional loading parameter $\bar{K} = K_I/\sigma_0\sqrt{B}$. The crack opening profiles on the outside surface reveal a "wedge-like" shape that supports the concept of fracture testing methods based on measured values of the crack-tip opening angle, *e.g.*, ASTM E 2472-06 [5].

The remainder of the paper follows this organization. Section 4.2 provides background material: SSY conditions for a growing crack; self-similarity scaling for near-front fields characterized by a non-dimensional loading parameter; and the basis for streamline integration. Section 4.3 summarizes the numerical procedures, including the 3D SSY finite element model, the algorithm to determine the material constitutive response, and comparisons of results from the current work with earlier results for plane-strain conditions. Section 4.4 describes the development of 3D plastic zones for the steadily advancing crack and compares them to the plane-strain and plane-stress solutions. Results in Section 4.5 demonstrate the self-similarity scaling for stresses, strains, and displacements surrounding the crack front based on the loading parameter, $\bar{K} = K_I/\sigma_0\sqrt{B}$. Section 4.6 examines more closely the 3D effects (constraint) near the crack front. Section 4.7 investigates the crack opening profiles over the thickness at increasing (relative) load levels. Section 4.8 provides the key observations and conclusions from this study and discusses future extensions of this computational framework.

4.2 Steady-state crack extension

This section summarizes key features of the 3D SSY framework for elastic-plastic crack extension under steady-state conditions. Section 4.2.1 describes the global structure and local loading/material conditions that support development of a boundary-layer model with only one geometric length scale, the plate thickness (B). Section 4.2.2 proposes that the near-front fields exhibit a self-similarity scaling in terms of the non-dimensional loading parameter $\bar{K} = K_I^{SS}/\sigma_0\sqrt{B}$, which characterizes the relative size of the steady-state, in-plane plastic zone size to the plate thickness. Section 4.2.3 describes generalization of the streamline

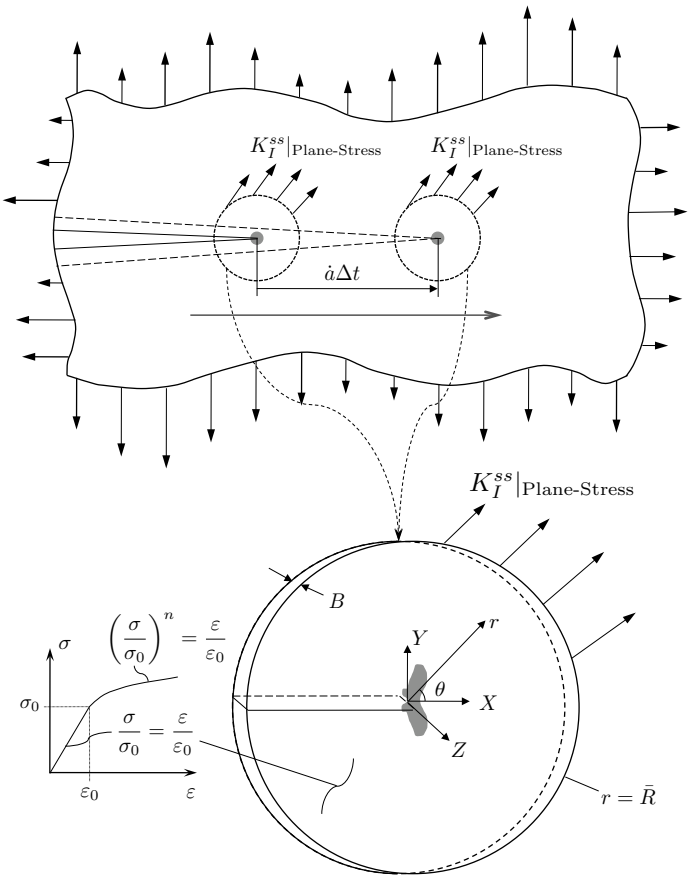

Figure 4.1: Section of a thin plate with a through-thickness, straight crack front advancing steadily at a constant velocity, $\dot{a}$, under mode I small-scale yielding (SSY) conditions. For the present study, $\dot{a}$ remains at quasi-static rates and inertial effects are neglected. The symmetric, remotely applied loading and displacement boundary conditions impose a constant, steady-state ("SS") value of $K_I^{SS}|_{\text{Plane-Stress}}$. The mechanical fields appear invariant to an observer situated on the straight crack front at the centerplane ($Z = 0$) and moving with the crack front, *i.e.* the origin for the coordinate axes.

integration approach to 3D which enables relatively straightforward solutions for steady-growth.

4.2.1 Three-dimensional, small-scale yielding conditions for a steadily growing crack

Figure 4.1 illustrates the framework for a sharp crack propagating at quasi-static rates under mode I, small-scale yielding (SSY) conditions in a thin ductile plate of uniform thickness, B. At all considered load levels, planar dimensions of the component (crack length, remaining ligament, height and width) remain much greater than the in-plane, plastic zone size at the advancing crack front. Material deforming inelastically near the crack front remains well contained within a surrounding region of plane-stress, linear-elastic material

with mechanical fields characterized by K_I and the T-stress. The crack advances by ductile tearing before the plastic zone size violates the in-plane SSY conditions. Laboratory tests using C(T) and M(T) specimens of common aluminum alloys, for example, that have in-plane dimensions (75-100 mm, or larger) compared to thickness (1-5 mm) readily exhibit large amounts of ductile tearing with plastic zones extending to a few multiples of the thickness.

The boundary-layer computational model for 3D SSY, also shown in Fig. 4.1, comprises a disk-shaped volume centered about the crack front with radius $r = \bar{R}$ and uniform thickness B. The specified $\bar{R}$ must satisfy: $\bar{R} \gg B$ and $\bar{R} \gg r_p$ to insure SSY conditions, where r_p denotes the maximum in-plane extent of the plastic zone. The disk-shaped region facilitates finite element mesh generation but otherwise the boundary shape plays no role. The extent and strength of 3D fields at the crack front in this model vary with the size of r_p relative to B generated by the remote loading (K_I, T) and material flow properties. The strongest 3D effects develop along the crack front for $r_p < B$ and diminish at increased loading when r_p exceeds B. With further loading, $r_p \gg B$ and much of the plastic zone has a simple plane-stress state.

In plane-stress and plane-strain versions of the SSY model, the near-front fields exhibit self-similar scaling with distances from the crack tip normalized by a convenient measure of plastic deformation: size of the plastic zone (r_p) – J/σ_0, $(K_I/\sigma_0)^2$ – or crack-tip opening displacement (δ). In the 3D SSY model, the fields differ with the size of the in-plane plastic zone relative to B, and the simple scaling observed in plane-strain/stress breaks down [72].

Under 3D SSY conditions, applied loading on the plate produces plane-stress mechanical fields in the linear-elastic material surrounding the crack front that derive from the asymptotic Williams solution [128]. The symmetric remote loading depicted in Fig. 4.1 produces mode I crack front fields characterized by the stress intensity factor, K_I, and potentially nonzero values for the T-stress that reflect a first-order estimate of in-plane constraint variations from geometry and loading effects (*e.g.*, tension *vs.* bending). For quasi-static loading, the remote boundary of the model at $(r = \bar{R}, \theta)$ has imposed displacements u_x and u_y,

$$u_x(\bar{R}, \theta, Z) = \frac{K_I}{2\mu}\sqrt{\frac{\bar{R}}{2\pi}}\cos\left(\frac{\theta}{2}\right)\left[\kappa - 1 + 2\sin^2\left(\frac{\theta}{2}\right)\right] + \bar{R}\cos(\theta)\,\frac{T}{E}, \tag{4.1}$$

$$u_y\left(\bar{R}, \theta, Z\right) = \frac{K_I}{2\mu}\sqrt{\frac{\bar{R}}{2\pi}}\sin\left(\frac{\theta}{2}\right)\left[\kappa + 1 - 2\cos^2\left(\frac{\theta}{2}\right)\right] - \nu\bar{R}\sin(\theta)\,\frac{T}{E}. \tag{4.2}$$

In Eqns. 4.1 and 4.2: μ and E are the shear and Young's modulus, respectively; the constant $\kappa = (3 - \nu)/(1 + \nu)$ in plane stress, where ν is Poisson's ratio. The u_z displacement on $(r = \bar{R}, \theta, Z > 0)$ may be set to the plane-stress values or left unspecified without affecting the crack-front fields [48].

During steady crack growth, the near-front fields appear invariant to an observer situated on and moving

with the crack front. The fields at one time and crack front location remain identical to the near-front fields at another time and the same crack front location during steady-state crack growth, shown in Fig. 4.1. The crack advances through the material with a prescribed, constant shape along the front, either straight along the Z-axis in Fig.4.1 or curved (tunneled). All analyses here impose a straight crack front shape. For quasi-static crack growth examined in this study: the crack velocity $\dot{a} \to 0$; no stress waves reflect from the boundary at $r = \bar{R}$; and inertial effects become negligible and are ignored. The crack propagates under a constant value of the applied loading in the SSY region surrounding the crack front such that $K_I(\Delta a) \to K_I^{SS}$ (at steady-state). Inelastic behavior occurs ahead of the crack front, and leaves a trailing plastic wake of material behind the crack front.

For the steadily advancing crack front in a rate-independent, elastic-plastic material, the singularity of strains and stresses weakens, *e.g.* $\sigma_{ij} \propto r^{\alpha}$ with $\alpha > -\frac{1}{2}$, in a plane-strain setting. The value for the J-integral computed over a local path enclosing the crack tip, J^{local}, becomes undefined [70] for the advancing crack. The far-field value from the imposed loading in the boundary-layer model, J^{far}, and its correspondence with the surrounding linear-elastic field remains clear, $J^{far} = \left(K_I^{SS}\right)^2/E$. Consequently, we have not attempted to compute and report J^{local} values at locations along the 3D crack front, for example, as shown in Fig. 5 of Nakamura and Parks [72] for the stationary crack.

4.2.2 Three-dimensional, self-similar fields

Material points in the thin plate remote from the steadily advancing crack front experience linear-elastic, plane-stress values for the displacements, strains, and stresses. As the crack front approaches material points near the crack plane, the fields transition to a complex, 3D state with features controlled by the magnitude of far-field loading, the material flow properties, and the plate thickness. nonzero stresses $\sigma_{i,3}$ develop over the interior, extend ahead of the crack front to some fraction of the plastic zone size, $r_p \propto (K_I^{SS}/\sigma_0)^2$, and vary with position over the thickness near the crack front.

Plane-strain [21] and plane-stress analyses [20] of steady crack growth under SSY conditions subject to mode I loading demonstrate self-similarity for the near-tip fields when the radial distance from a material point to the crack tip, r, is normalized by a measure of the plastic deformation, *e.g.*, J^{far}/σ_0. Plane-strain analyses with a nonzero applied T-stress [117] also reveal self-similar scaling with a measure of the active yielding region. Stresses maybe written in the general form:

$$\sigma_{ij} = \sigma_0 f_{ij}\left(\frac{r}{J^{far}/\sigma_0}, \theta; \frac{T^{far}}{\sigma_0}; \frac{E}{\sigma_0}, n, \nu\right), \tag{4.3}$$

where J^{far} and T^{far} correspond to the linear-elastic fields imposed on the boundary $\bar{R}$. This self-similar scaling holds for an observer situated on the steadily advancing crack tip.

Analogous behavior occurs for a steadily propagating crack in the 3D model of a thin plate when the size and shape of the in-plane (X–Y) plastic region remains unchanged relative to the thickness, r_p/B, under SSY conditions. Dimensional considerations suggest, and computational results from the present study support, a similarity scaling of the near-front fields (displacements, strains, and stresses) surrounding a steadily growing crack. Stresses, for example, follow a relationship of the form:

$$\sigma_{ij} = \sigma_0 F_{ij}\left(\frac{r}{J^{far}/\sigma_0}, \theta, \frac{Z}{B}; \frac{K_I^{far}}{\sigma_0\sqrt{B}}; \frac{E}{\sigma_0}, n, \nu\right), \tag{4.4}$$

where $K_I^{far} = K_I^{SS}$ sets the amplitude of boundary displacements in Eqns. (4.1, 4.2), and $J^{far} = (K_I^{far})^2/E$. The remotely applied T-stress may be included in the 3D SSY framework similar to Eqn. (4.3), but the present work limits consideration to the $T = 0$ case.

In Eqn. 4.4: the first three terms, $(r/\left(J^{far}/\sigma_0\right), \theta, Z/B)$, describe the location of a material point relative to an observer situated on the crack front at the centerplane, $X = Y = Z = 0$ as shown in Fig. 4.1; the final three terms, $(E/\sigma_0, n, \nu)$, denote the material elastic and flow properties; and the term $K_I^{far}/\sigma_0\sqrt{B}$ sets the far-field loading. The quantity $\bar{K} = K_I^{far}/\sigma_0\sqrt{B}$ defines a non-dimensional loading measure which relates the size of the active yielding region to the plate thickness. For fixed elastic and hardening material properties, the 3D crack-front fields in scaled coordinates $(r/\left(J^{far}/\sigma_0\right), \theta, Z/B)$ remain unchanged when K_I^{far}, the yield stress (σ_0) and B vary to maintain a constant value of $\bar{K}$. Non-dimensional relationships having the same form as Eqn. 4.4 describe the strain and displacement fields. Subsequent discussions drop the "far" notation on K_I and J for simplicity.

Earlier studies examine features of near-front fields for a stationary, straight crack in thin plates undergoing plastic deformation and modeled in the 3D SSY framework. Nakamura and Parks [72] find that the region over which the HRR-fields exist is linked to the non-dimensional loading level $J/\sigma_0\varepsilon_0 B = (K_I/\sigma_0)^2/B$. Building on their work, Roychowdhury and Dodds [96] observe the scaling of crack-face opening loads with $K_{max}/\sigma_0\sqrt{B}$ in 3D SSY simulations of fatigue crack extension. Specifically, when K_{max}, σ_0, and B vary to maintain a constant value of this ratio, the load (K_{op}) at which the crack becomes fully open on reloading in each cycle, K_{op}/K_{max}, remains unchanged. Section 4.5 demonstrates this 3D self-similarity relationship for steadily propagating cracks using refined finite element models, and explores effects of the loading parameter, $K_I/\sigma_0\sqrt{B}$, on features of the 3D near-front fields.

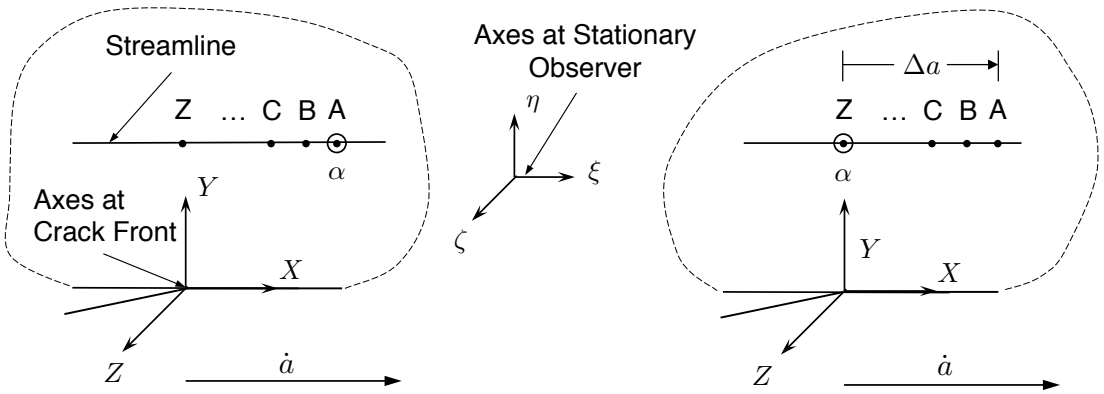

Initial Time: t_0

$$\sigma_{ij}^{A} = \sigma_{ij}(\varepsilon_{ij}(A))$$
$$\sigma_{ij}^{\alpha} = \sigma_{ij}(\varepsilon_{ij}(\alpha))$$
$$\sigma_{ij}^{\alpha} = \sigma_{ij}^{A}$$

Current Time: $t = t_0 + \Delta t = t_0 + \Delta a/\dot{a}$

$$\sigma_{ij}^{Z} = \sigma_{ij}(\varepsilon_{ij}(A) + d\varepsilon_{ij}(\Delta a = X^A \rightarrow X^Z))$$
$$\sigma_{ij}^{\alpha} = \sigma_{ij}(\varepsilon_{ij}(A) + d\varepsilon_{ij}(\Delta t))$$
$$\sigma_{ij}^{\alpha} = \sigma_{ij}^{Z}$$

Figure 4.2: Eulerian (axes fixed on the advancing crack front, X-Y-Z) and Lagrangian (axes fixed outside of material, ξ-η-ζ) descriptions of motion for a crack advancing at steady-state imply an equivalence between motion along streamlines and temporal variance. This equivalence enables the time dependence of quantities – displacements, strains, and stresses – to be interpreted as the evolution of these quantities along streamlines.

4.2.3 Streamline integration

Dean and Hutchinson [21] first outline the streamline integration technique that enables computation of near-front fields for a steadily propagating crack using a fixed finite-element mesh. Here we extend their work from 2D plane-stress/strain models to 3D models. Figure 4.2 depicts a mode I crack steadily advancing along the X-axis from left to right (arbitrarily) at constant velocity, $\dot{a}$. Streamlines may be envisioned to exist parallel to the direction of crack propagation. A set of material points labeled from right to left as A, B, C, ..., Z lies along each such streamline. These points remain fixed in location with respect to a coordinate system, X-Y-Z, attached to and moving with the crack front. Another coordinate system, ξ-η-ζ, indicates the location for a stationary observer and defines the point α located at A for some relative time t_0. The crack advances by the distance $\Delta a = X^A - X^Z$ under steady conditions over time Δt. The material located at α passes through the points A, B, C, ..., Z (as viewed by the stationary observer) and experiences the mechanical fields at each location on the streamline in this process: $(\varepsilon_{ij}^{A}, \sigma_{ij}^{A}) \rightarrow (\varepsilon_{ij}^{Z}, \sigma_{ij}^{Z})$. Consequently, the evolution of near-front fields through time and crack advance equals the evolution of near-front fields

along the streamlines. The evolution of field quantities, $\bullet$, with respect to time, t, under steady conditions follows the relationship:

$$\frac{\partial(\bullet)}{\partial t} = -\dot{a}\frac{\partial(\bullet)}{\partial X} \ . \tag{4.5}$$

This simple form requires adoption of the linear strain-displacement relations to retain the treatment of streamlines as undeformed during crack propagation. Otherwise, a large deformation framework leads to curved streamlines around the crack front, and Eqn. 4.5 must include additional terms to ensure that integration for a material point continues along unique but curved streamlines.

Equation 4.5 reduces the integration of otherwise time-dependent differential equations for plastic flow to the integration of these equations along streamlines. Streamlines must pass through all material points in the model that undergo plastic deformation. This includes the region of active plastic flow ahead of the crack front and the plastic wake behind the crack front that extends to the far-field ($-X$) boundary. In the current 3D framework, streamlines composed of material points exist over the thickness of the model and lay parallel to the X-axis on planes at constant locations Y and Z, whereas for a 2D framework, only one such thickness plane exists.

The strain-stress history for material surrounding the crack front develops along streamlines, and integration of the material response reflects this concept. Along the streamline illustrated in Fig. 4.2, suppose the mechanical fields for material point A: σ_{ij}^A, ε_{ij}^A, *etc...*, are known. Further, a trial estimate for the strains at material point B, ε_{ij}^B, exists. Integration along the streamline from A to B provides the updated stresses for material point B. The updated mechanical fields at A provide the starting conditions at B. The incremental change of strain $\Delta\varepsilon_{ij} = \varepsilon_{ij}^B - \varepsilon_{ij}^A$ drives the elastic-plastic stress updating process at B.

This integration procedure continues sequentially from right to left along each streamline, starting from the rightmost boundary of the yielding region to the leftmost model boundary. The first (rightmost) material point on each streamline must remain linear-elastic, and thus an estimate of the strain at that material point provides an estimate of the updated stress without the need for any history information. Integration of different streamlines may occur concurrently which creates opportunities for computational efficiencies through parallel processing. Section 4.3.2 details the integration techniques adopted in the present study to determine the material response along the 3D streamlines.

4.3 Computational procedures

This section describes the procedures developed to compute near-front fields for a steadily propagating crack in the 3D SSY framework. Section 4.3.1 outlines the finite element representation of the 3D SSY

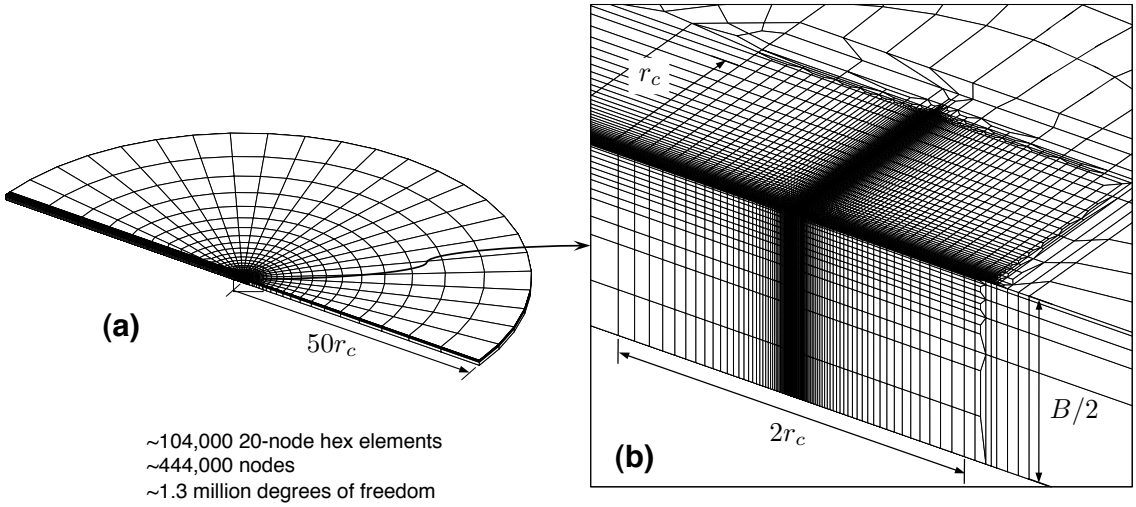

Figure 4.3: Finite element model for steady crack growth analyses composed of 20-node hex elements. Elements over the thickness and near the crack front are rectangular prisms arranged to support the definition of streamlines along Gauss points. Mesh refinement near the remote boundary (a) is significantly lower than refinement for the mesh near the crack front (b) (5 thickness layers compared to 15 thickness layers). Plastic deformation does not extend beyond the region shown in the inset of rectangular prism elements.

model, with a focus on the levels of mesh refinement necessary to capture gradients in the near-front fields, while supporting the streamline formulation. Section 4.3.2 briefly summarizes element-level features of the implementation: Gauss integration rules and refinements in the stress updating computations using an elastic predictor-radial return approach to accommodate large strain increments. Section 4.3.3 compares near-tip stress fields obtained in the current work using plane-strain conditions imposed on the 3D SSY model with asymptotic plane-strain solutions and with earlier solutions from plane-strain, finite element models. The excellent agreement across these solutions provides a measure of verification for the numerical models.

4.3.1 Finite element model

Figure 4.3 displays the SSY model developed for finite element analyses of steady crack growth in the 3D framework. The crack front lies parallel to the Z-axis at $X = 0$, $Y = 0$. At the highest loads considered, plastic deformation remains contained over $X \leq r_c \cup |Y| \leq r_c$, and within this region the element arrangement provides streamlines parallel to the X-axis that pass through the Gauss points. The streamlines begin ahead of the crack front at $X \sim r_c$ and end at the remote boundary ($X \rightarrow -50\, r_c$). Outside of this highly refined region, the material remains linear-elastic. The remote boundary lies at a distance from the crack front ~ 50 times greater than r_c. Applied displacements on the remote boundary equal the plane-stress values from the Williams solutions given in Eqns 4.1 and 4.2 with $T = 0$. The steadily advancing crack front under a mode

I (tensile) loading has symmetry planes $Y = 0$ and $Z = 0$, which reduce the meshing and computational requirements.

The element refinement shown in Fig. 4.3 varies over the thickness (Z) and in-plane ($X - Y$) with increasing distance from the crack front. For $|X| \leq r_c \cup |Y| \leq r_c$, the mesh provides the highest resolution to capture the near-front fields. More than three-quarters of the model elements reside in this highly refined region. Behind the crack front ($X \leq -r_c \cup |Y| \leq r_c$), the reduced level of mesh refinement in the direction of crack advance reflects the greater uniformity of the mechanical fields. The mesh refinement increases non-uniformly over the thickness of the model to capture the higher stress gradients present near the outside surface (illustrated in Fig. 4.3). Overall, the yielding region ($X \leq r_c \cup |Y| \leq r_c$) contains 6480 streamlines over 15 (Z = constant) element planes for the half-thickness. Outside of the yielding region, the mesh transitions to 5 thickness layers and significantly reduced in-plane refinement. The yielding region has a mesh design that transitions with topologic compatibility to the coarser, far-field region. The entire, quarter-symmetric model consists of 104,145 20-node hex elements and 443,654 nodes with approximately 1.3 million displacement degrees of freedom.

4.3.2 Material response

The elastic-plastic material response follows isotropic, J_2-theory with incremental changes for the plastic strains proportional to the current deviatoric stress at each material point. In uniaxial tension, the material strain hardens in the elastic-plastic range following the power-law stress-strain ($\sigma - \varepsilon$) relationship shown in Fig. 4.1:

$$\left(\frac{\sigma}{\sigma_0}\right)^n = \left(\frac{\varepsilon}{\varepsilon_0}\right), \qquad \varepsilon \geq \varepsilon_0 \ , \tag{4.6}$$

where σ_0 and ε_0 reflect the yield stress and yield strain for the material respectively, and n denotes the hardening exponent. Within the yield surface, the response follows linear-elastic behavior with $E = \sigma_0/\varepsilon_0$ and Poisson's ratio, ν.

Initial analyses revealed that reduced Gauss numerical integration ($2 \times 2 \times 2$) of the stiffness matrices and internal forces ($\int \boldsymbol{B}^T \boldsymbol{\sigma} dV$) for the 20-node elements leads to severe, hour-glass deformation modes in elements near the crack front and in the plastic wake. Full integration ($3 \times 3 \times 3$) eliminates the hour-glass modes, but may produce volumetric locking in the incompressible limit of incremental J_2 plasticity [23]. Checks of the present analyses with full integration reveal that all Gauss points exhibit volumetric plastic strains, $\left|\varepsilon^p_{xx} + \varepsilon^p_{yy} + \varepsilon^p_{zz}\right|$, on the order of $10^{-6} \times \varepsilon_0$. This extremely low magnitude for the volumetric plastic strains indicates the absence of locking.

Strain increments between adjacent Gauss points, $\Delta\varepsilon_{ij}$, rise sharply on streamlines near the crack front

and may lead to inaccurate stresses from truncation errors during integration of the plasticity rate equations [49]. Strain substepping and stress extrapolation techniques improve the accuracy of stress computations [16] in the elastic predictor–radial return algorithm. For currently unyielded points, the stress update process first determines the fraction of the strain increment that places the linear-elastic stresses on the yield surface. The final stress state determined for the remaining fraction of the strain increment is computed over one and then two, equal substeps of strain. This enables an estimate for the required number of substeps (N_{sub}) to reduce the truncation error in the updated stresses below a specified tolerance (limit of $N_{sub} = 10$). Stresses are updated over N_{sub} substeps using the elastic-plastic, radial return algorithm. Finally, the procedure minimizes the remaining error by extrapolating from stress states determined for two and N_{sub} substeps to a final stress state. Overall, this approach reduces the truncation error inherent in the elastic-predictor, radial-return algorithm for large strain increments. Further, the number of global iterations (high cost per iteration) decreases slightly for a minimal computational cost at the Gauss point level, which operates with full parallel efficiency.

If the new estimate for stresses at the Gauss points from the streamline integration procedure satisfies the equilibrium conditions ($\boldsymbol{R} = \boldsymbol{P} - \int \boldsymbol{B}^T \boldsymbol{\sigma} dV = \boldsymbol{0}$), then the residual forces ($\boldsymbol{R}$) at the nodes become negligible, and the solution has converged. Here, $\boldsymbol{P}$ indicates the external nodal forces/reactions induced by the applied displacements. The convergence check uses the norm of the nodal residual forces, $\| \boldsymbol{R}_i \|$ for iteration i compared to $\| \boldsymbol{R}_1 \|$, with the norm computed for nodes in the region $|X| \leq r_c \cup |Y| \leq r_c$. A tolerance value of 5×10^{-6} suffices; results for much larger and smaller tolerances show no differences in the converged solution. Displacements obtained from a new solution to the global equilibrium equations provide the next estimate for the total strains. The 3D SSY analysis reported here requires typically 500 global iterations to reach convergence. Appendix A discusses this iterative strategy in detail for the plane-strain framework.

4.3.3 Comparison of plane-strain solutions

Quasi-static, steady-growth under mode I, plane-strain conditions has been studied extensively for a non-hardening material. Figure 4.4 compares the results from several such solutions for the angular variation of the σ_{xx}, σ_{yy}, and σ_{xy} stress components. These solutions exhibit self-similarity when physical coordinates are normalized by a measure of the plastic deformation: $(K_I/\sigma_0)^2$ or J/σ_0. Drugan et al. [27] determine the analytic form of the asymptotic, near-tip stresses for J_2 plasticity. Their solution for $\nu = 0.3$ is given by the solid line in Figure 4.4. Dean and Hutchinson [21] present the near-tip stresses around a rectangular path (non-constant r) enclosing the crack tip computed with a finite element analysis that incorporates

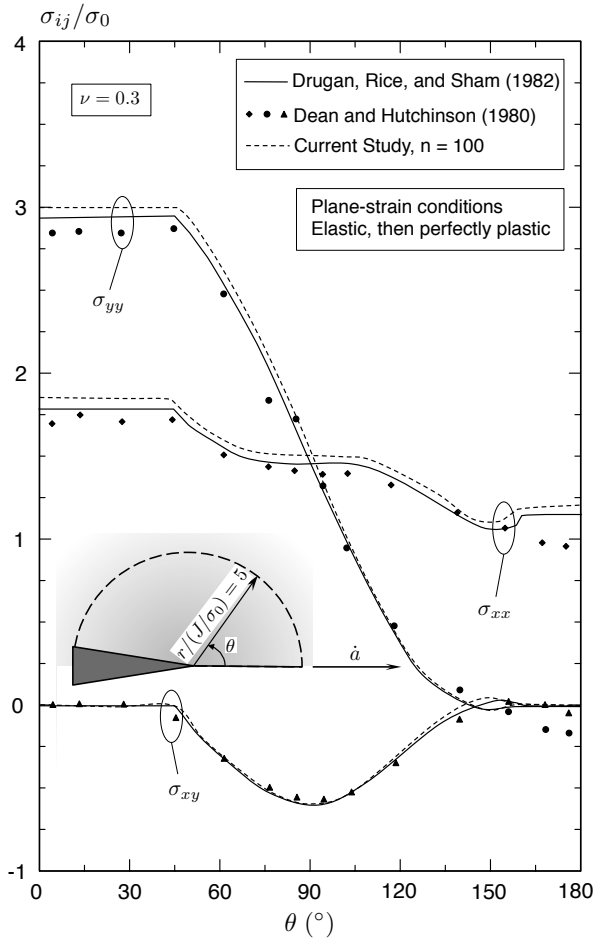

Figure 4.4: Angular variation of the normalized near-tip stresses surrounding a steadily growing crack under plane strain and SSY conditions for an elastic-perfectly plastic material. Drugan et al. [27] provides an analytical solution from asymptotic methods. Values from Dean and Hutchinson [21] and the current study derive from finite element analyses and the streamline integration method.

streamline integration. Figure 4.4 shows the discrete values from their analysis (digitized from the original paper). The values of σ_{xx} and σ_{yy} from Dean and Hutchinson [21] deviate slightly from the analytical solution – computational capabilities at that time limited the level of mesh refinement. In later finite element studies, Varias and Shih [117] employed the same computational procedure, but with much increased mesh refinement, and found stresses in agreement with the analytical solution (see Fig. 9 in that study).

The dotted line solution in Fig. 4.4 at a normalized, radial distance from the crack tip, $r/(J/\sigma_0) = 5$, is obtained from a 3D finite element analysis using the new research code FIREFLY developed for this work. Appendix A provides additional details about the FIREFLY code. To model plane-strain conditions with this 3D code, the out-of-plane displacements (u_z) for all nodes remain fixed at zero, and the applied

displacements on the remote boundary match the plane-strain values from the Williams solution at the specified K_I. These boundary conditions impose plane-strain conditions throughout the 3D finite element model enforcing $\varepsilon_{zz} = 0$ at all Gauss points. To approximate non-hardening material flow properties, n is set to 100 in the power-law hardening model of Eqn. 4.6.

The near-tip stresses computed with FIREFLY agree very well with the asymptotic solution. The small amount of strain hardening in the material ($n = 100$) leads to near-tip stresses slightly above those from the analytical and plane-strain finite element solutions that have an elastic-perfectly plastic material. The σ_{xx} and σ_{yy} stress components differ more from the analytical solution by Drugan et al. [27] than does the σ_{xy} stress component. The finite element solution by Dean and Hutchinson [21] also shows this trend. Values of the stress components for $0^\circ \leq \theta \leq 180^\circ$ for the present solution quite closely match values from the asymptotic solution.

4.4 Plastic zones

The plane-strain and plane-stress solutions for steady crack growth illustrate key features expected in the evolution of plastic zones over the thickness, with increasing distance from the crack front and under increased loading for the 3D model. Figure 4.5 shows a half-symmetric view of active yielding regions during steady crack advance for plane strain [21, 90, 117] and plane stress [20, 73, 74] with a moderately hardening material. Both solutions reflect a zero T-stress loading. These active yielding regions display a similarity scaling with $(K_I/\sigma_0)^2$ or J/σ_0. Key dimensions indicated on the figure include the extent of the plastic zone on the crack plane, r_{p0}, and the height of the active plastic zone above the crack plane, h_{pw}, which also sets the height of the plastic "wake" behind the advancing front. Material located in the plastic wake has unloaded elastically from the active yielding state that existed prior to passage of the advancing crack, and thus has locked-in, residual plastic strains.

In plane strain, the active yielding region ahead of the crack tip appears similar in shape/orientation to the plastic zone for a stationary crack also in plane strain (with $T = 0$), but differs considerably behind the crack front in material near the crack plane. Consider the streamline marked with the designation A in Fig. 4.5a and located at $Y/(K_I/\sigma_0)^2 < 0.02$. Material points on this streamline experience active yielding while located ahead of the crack tip, pass through a linear-elastic unloading region just behind the crack tip, and then undergo further active yielding at larger distances behind the crack tip caused mainly by tensile σ_{xx} stresses. The plane-stress plastic zone in Fig. 4.5b has a distinctly different shape, extends much farther ahead of the advancing crack tip (r_{p0}), and does not develop a re-yielding region of material behind the

crack front.

In their SSY plane-strain analyses, Varias and Shih [117] describe the work balance requirement of energy dissipation as the crack advances steadily at fixed $J = K_I^2(1-\nu^2)/E$. An increase in the size of plastic wake, h_{pw}, from nonzero T-stress effects in plane strain necessarily lowers plastic strain and stress in the active yielding region. Their analyses confirm that the $T = 0$ configuration produces the highest constraint levels in plane-strain, steady growth. The work-balance situation in 3D steady growth becomes far more complex as both h_{pw} and r_{p0} vary over the thickness and material in the active yielding region does not experience entirely plane-strain conditions.

Figure 4.6 and Table 4.1 provide a description of active yielding regions computed with the 3D model for steady growth at loading levels $\bar{K} = K_I/\sigma_0\sqrt{B}$ =1, 2, 3, and 5. The material properties are: $E/\sigma_0 = 250$,

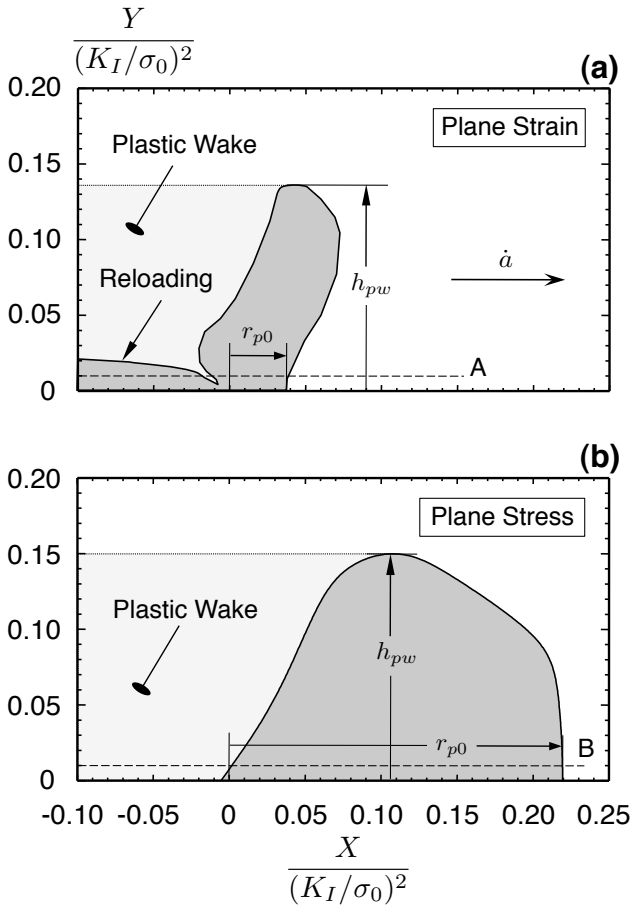

Figure 4.5: Active yielding regions for steadily advancing cracks under plane-strain [117] and plane-stress [74] conditions in a low-hardening material. This figure defines the extent of active yielding above the crack plane, h_{pw}, and the extent of yielding ahead of the advancing tip on the crack plane, r_{p0}.

$n = 10$, and $\nu = 0.33$, and the applied $T = 0$. In Fig. 4.6, the straight crack front advances in the positive X direction along the crack plane ($Y = 0$). The in-plane physical dimensions (X, Y) are scaled by J/σ_0; the through thickness dimension (Z) is scaled by B. The axes on each graph maintain the same scales to facilitate comparisons. A dark shade of gray indicates the active plastic zone on the crack plane and on the centerplane. Black shading signifies active yielding on the outside surface, and the boundary over the interior of the plate is shown using a light shade of grey.

Table 4.1 reveals that the ratio of r_{p0}/B on the centerplane ($Z/B = 0$) increases proportionally with the square of $\bar{K}$, *i.e.* $r_{p0}/B \propto \bar{K}^2$, and thus, $r_{p0} \propto (K_I/\sigma_0)^2$, as in earlier studies of stationary and steadily advancing cracks in a 2D SSY framework. This result supports definition of the non-dimensional loading parameter $\bar{K} = K_I/\sigma_0\sqrt{B}$, which measures the size of the active yielding region relative to the thickness.

In Fig. 4.6, consider first graph (d) and the dimensions listed in Table 4.1 for this relatively high loading level of $\bar{K} = 5$. The plastic zone has a uniform size over the full thickness and a uniform (boundary) shape over the thickness characteristic of the plane-stress solution in Fig. 4.5b. The plastic zone extends $6.4B$ ahead of the crack front and to a height of $4B$ above the crack plane.

At the smallest load level examined, $\bar{K} = 1$, the plastic zone extends to $0.25B$ ($\approx 62J/\sigma_0$) on the crack plane at mid-thickness in Fig. 4.6a. The boundary of the plastic zone on $Z/B = 0$ has a mostly plane-strain shape, especially on the trailing (vertical) portion behind the crack front. Both r_{p0} and h_{pw} decrease smoothly over the thickness until near the outside surface. There the active yielding region expands rapidly in height above the crack plane, reaching almost the centerplane level, but r_{p0} nearly vanishes along the uncracked ligament at the outside surface. Re-yielding of material near the crack plane develops behind the crack front over the entire thickness – a distinguishing feature of the plane-strain solution. Even though material at the outside surface experiences plane-stress traction boundary conditions ($\sigma_{i,3} = 0$), the boundary shape of the active yielding region in the 3D solution has a markedly different character than the plane-stress yielding region in Fig. 4.5b. The resolution of severe gradients near traction free corners on a crack front always poses a challenge for finite-element methods. A model with even greater refinement compared to that here – 15, 20-node hex elements over the half-thickness with stronger gradation of smaller elements near the outside surface – may be required to confirm the unusual features in the present solution near the outside surface at this (relatively) small load level.

At increased loading level from $\bar{K} = 1 \rightarrow 2$ (Fig. 4.6b), the boundary shape of the active plastic zone transforms to a distinctly intermediate configuration between the plane-strain and plane-stress conditions in Fig. 4.5. The extent of the plastic zone on the crack plane, r_{p0}, has a nearly uniform value of $\approx B$, with a height above the crack plane that increases by about 25% over the thickness nearing the outside

$\bar{K} = K_I/\sigma_0\sqrt{B} = 1$				
$\frac{Z}{B}$	$\frac{r_{p0}}{J/\sigma_0}$	$\frac{r_{p0}}{B}$	$\frac{h_{pw}}{J/\sigma_0}$	$\frac{h_{pw}}{B}$
0	61.8	0.247	73.2	0.293
0.4	53.3	0.213	48.2	0.193
0.5	0.3	0.001	66.4	0.266

$\bar{K} = K_I/\sigma_0\sqrt{B} = 2$				
$\frac{Z}{B}$	$\frac{r_{p0}}{J/\sigma_0}$	$\frac{r_{p0}}{B}$	$\frac{h_{pw}}{J/\sigma_0}$	$\frac{h_{pw}}{B}$
0	66.6	1.06	44.6	0.714
0.4	61.8	0.99	51.3	0.820
0.5	64.7	1.03	56.6	0.906

$\bar{K} = K_I/\sigma_0\sqrt{B} = 3$				
$\frac{Z}{B}$	$\frac{r_{p0}}{J/\sigma_0}$	$\frac{r_{p0}}{B}$	$\frac{h_{pw}}{J/\sigma_0}$	$\frac{h_{pw}}{B}$
0	63.6	2.29	38.0	1.37
0.4	63.6	2.29	42.0	1.51
0.5	64.7	2.33	44.6	1.61

$\bar{K} = K_I/\sigma_0\sqrt{B} = 5$				
$\frac{Z}{B}$	$\frac{r_{p0}}{J/\sigma_0}$	$\frac{r_{p0}}{B}$	$\frac{h_{pw}}{J/\sigma_0}$	$\frac{h_{pw}}{B}$
0	63.6	6.36	40.4	4.04
0.4	63.6	6.36	40.4	4.04
0.5	63.6	6.36	40.4	4.04

Table 4.1: Key dimensions for the active yielding region during steady crack advance in 3D SSY. The extent of the plastic zone ahead of the front on the crack plane, r_{p0}, and the height for the plastic wake, h_{pw}, are shown at three through-thickness locations, $Z/B = 0$, 0.4, and 0.5. Figure 4.5 defines r_{p0} and h_{pw}. K_I and $J = K^2/E$ denote the remotely applied loading in the boundary-layer model.

surface. The leading boundary of the plastic zone over the thickness approaches the shape of the plane-stress solution. On $Z/B = 0$, the trailing (vertical) edge of the plastic zone has diminishing features of the plane-strain shape with a less pronounced unloading region just behind the crack tip. Re-yielding of material behind the crack front (near the crack plane) is now more extensive near the outside surface than elsewhere across the thickness. Moreover, ahead of the crack front at the outside surface, a small volume of material within the otherwise large active yielding region ceases to accumulate plastic strains (unloads elastically). This forward elastic sector extends from the outside surface towards the centerplane over a distance $(0.495 \sim 0.498) \leq Z/B \leq 0.5$. We explored several details of the numerical modeling as a possible cause for the development of this region, including the use of: a uniform mesh size over the thickness, reduced integration for the element stiffness and strain-stress updating, and a material that has constant, linear hardening. The small, forward elastic sector persists in each of these different analyses, and perhaps is not an artifact of the numerical procedures.

At still higher loading levels of $\bar{K} = 3$ in Fig. 4.6c and $\bar{K} = 5$ in Fig. 4.6d, active yielding regions over the thickness develop essentially uniform shape and normalized size relative to J/σ_0, with a leading boundary shape of the plane-stress solution. In the plastic wake, the re-yielding region just above the crack plane disappears near mid-thickness. At the outside surface, the shape of this re-yielding region changes significantly as $\bar{K}$ increases and varies strongly with $X/\left(J/\sigma_0\right)$ and Z/B. The normalized (by J/σ_0) size of the small, forward elastic sector near the outside surface shrinks as $\bar{K}$ increases from $2 \rightarrow 3$ and disappears at $\bar{K} = 5$.

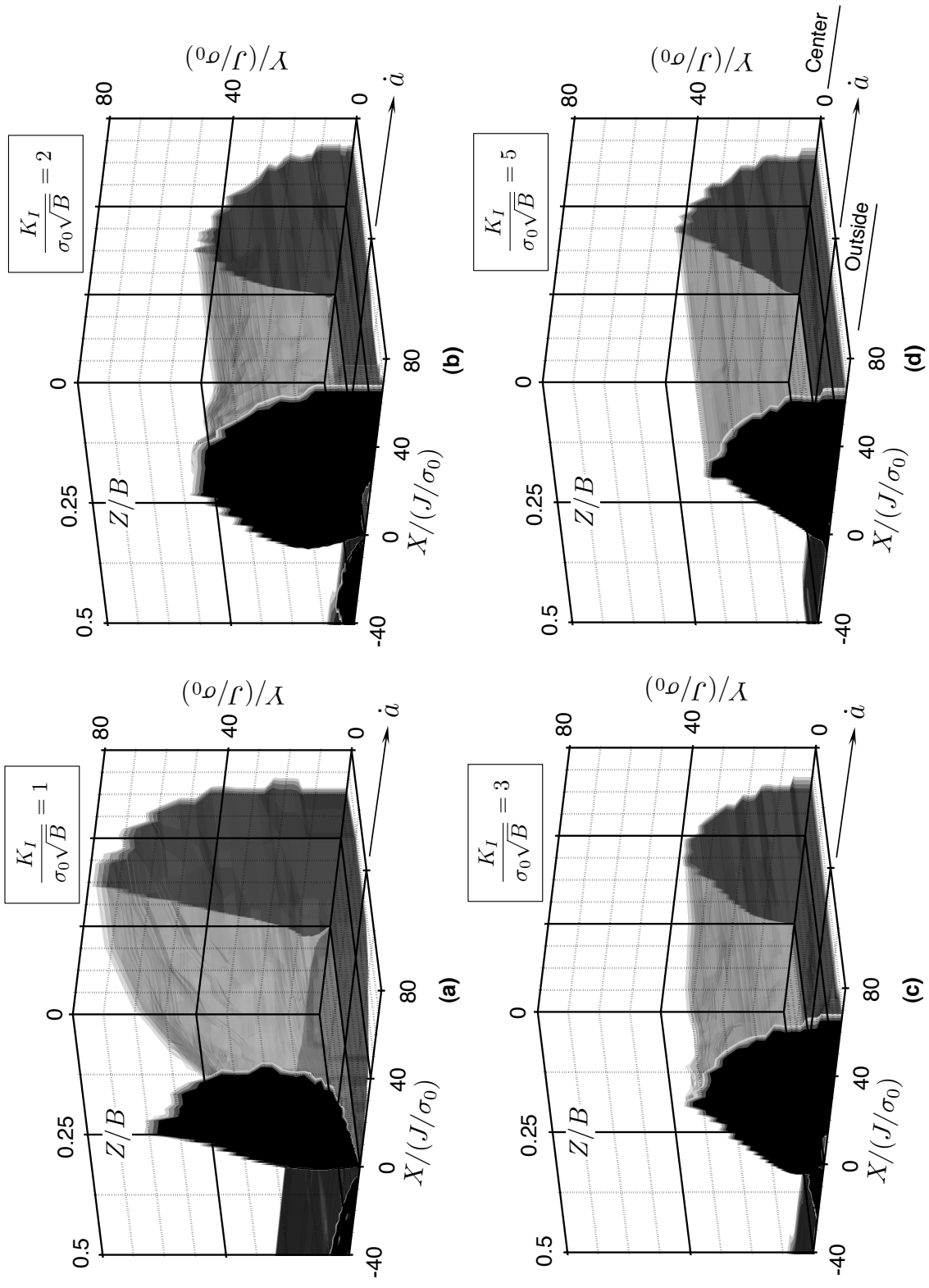

Figure 4.6: Active yielding regions for straight cracks advancing steadily in the 3D SSY model of a thin ductile plate. Non-dimensional loading levels shown are: $\bar{K}$ =1, 2, 3, and 5.

4.5 Similarity scaling in 3D SSY of steady crack growth

This section demonstrates that the near-front fields exhibit a similarity scaling with the non-dimensional loading parameter $\bar{K} = K_I/\sigma_0\sqrt{B}$ and provides key values of stresses, strains, and displacements from the numerical solutions. Results here focus on locations at mid-thickness and near the outside surface.

4.5.1 Opening-mode stresses on the crack plane

Figure 4.7 presents the normalized opening-mode stresses (σ_{yy}/σ_0) ahead of the crack front at mid-thickness ($Z/B = 0$) and near the outside surface ($Z/B = 0.495$) for loading levels $\bar{K} = 1$ in Fig. 4.7a and $\bar{K} = 3$ in Fig. 4.7b. Each figure shows the results from two solutions at the same value of $\bar{K}$. The thickness, B, varies in the two solutions with K_I adjusted to maintain constant values of $\bar{K}$ in each case. The material properties – σ_0/E, ν, and n – do not change in these analyses. For the $\bar{K} = 1$ loading, the thicknesses are $B = 1.0\bar{B}$ and $B = 1.6\bar{B}$; for the $\bar{K} = 3$ loading, $B = 1.0\hat{B}$ and $B = 0.6\hat{B}$. The selected values for $\bar{B}$ and $\hat{B}$ ensure that the size of the active yielding region, $r_p \propto (K_I/\sigma_0)^2$, remains large compared to the near-front element size to maintain mesh refinement for high resolution of the near-front fields. For reference, Fig. 4.7 also shows stress values for a steadily growing crack under plane-strain conditions. In these scaled coordinates, the plane-strain solution remains unchanged with the magnitude of the remotely applied loading.

The identical stress values in each of Figs. 4.7 (a,b) demonstrate self-similar scaling of the opening-mode stress (σ_{yy}/σ_0) with the 3D loading parameter $\bar{K} = K_I/\sigma_0\sqrt{B}$ under SSY conditions. Other stress components also exhibit this same scaling with $\bar{K}$. At $\bar{K} = 1$ in Fig. 4.7a, the opening-mode stress varies strongly over the thickness from the centerplane to the outside surface. At mid-thickness, opening-mode stresses match plane-strain values for $X/(J/\sigma_0) \lesssim 4$, while σ_{yy} values near the outside surface have yield stress levels except very near the crack front. Higher values of loading ($\bar{K} = 3$ in Fig. 4.7b) reduce the opening-mode stress at a constant scaled location $X/(J/\sigma_0)$ ahead of the crack on the centerplane and lead to more uniform values across the thickness of the plate. Only within $X/(J/\sigma_0) \lesssim 1$ does the opening-mode stress at mid-thickness tend to plane-strain levels at $\bar{K} = 3$. Near the outside surface, the values for σ_{yy}/σ_0 vary little for $X/(J/\sigma_0) \gtrsim 1$ as $\bar{K}$ increases from 1 to 3.

4.5.2 Angular variation of opening-mode stress

Figure 4.8 displays the angular variation of σ_{yy}/σ_0 around the crack front at the scaled radial distance $r/(J/\sigma_0) = 5$. Figure 4.8a shows values near the centerplane ($Z/B = 0.0625$), and Fig. 4.8b shows values near the outside surface ($Z/B = 0.4965$). Each figure again shows the results from two solutions at the

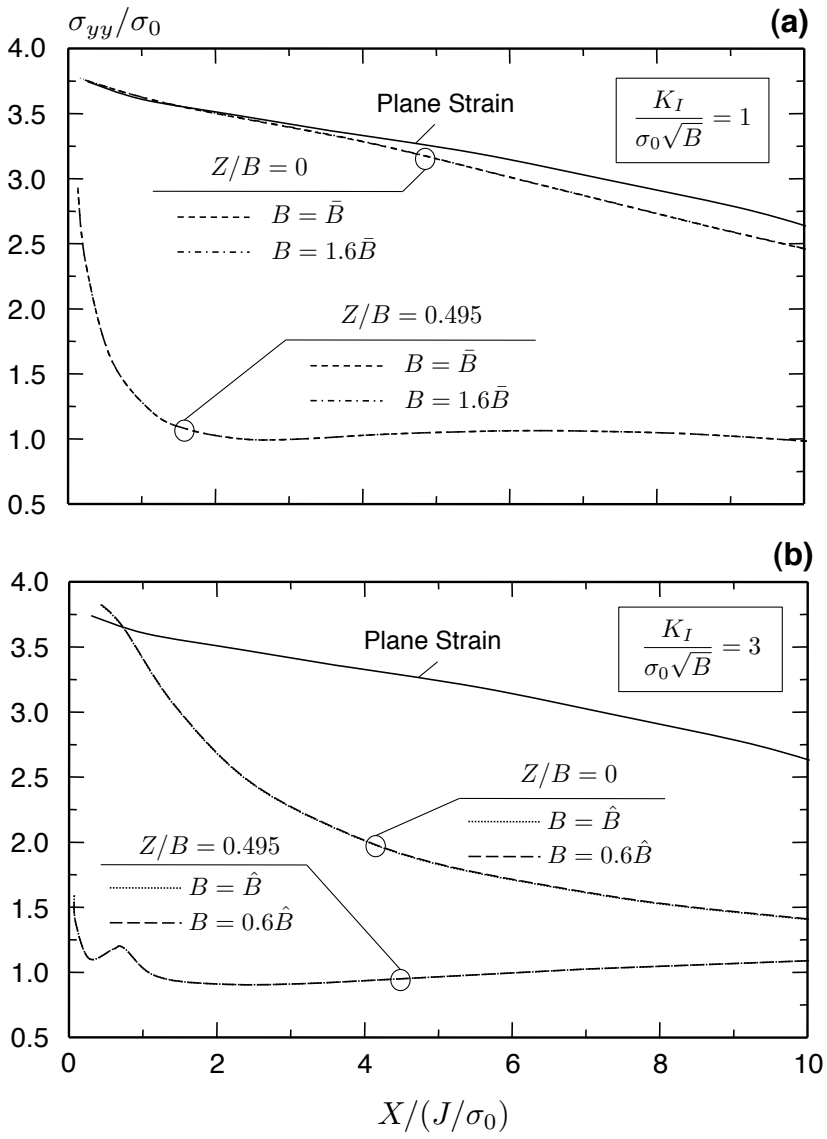

Figure 4.7: Normalized opening-mode stress, σ_{yy}/σ_0, with scaled physical distance from the crack front, $X/(J/\sigma_0)$, along the crack plane ($Y = 0$) ahead of the steadily growing crack at mid-thickness ($Z/B = 0$) and near the outside surface ($Z/B = 0.495$). Load levels are: (a) $K_I/\sigma_0\sqrt{B} = 1$ and (b) $K_I/\sigma_0\sqrt{B} = 3$. Essentially identical results obtained with different values for the thickness, B, and for the mode I applied remote loading, K_I, but the same value of the non-dimensional parameter $K_I/\sigma_0\sqrt{B}$ indicate self-similarity of this stress component. The steady-growth, plane-strain solution is also shown for reference.

same value of $\bar{K}$. The thickness, B, varies in the two solutions with K_I adjusted to maintain constant values for $\bar{K} = 1, 3$ in each case. Figure 4.8 also includes the angular variation of σ_{yy}/σ_0 for the steady-growth, plane-strain solution at $r/(J/\sigma_0) = 5$.

The essentially identical solutions shown in Fig. 4.8 at each $\bar{K}$ for the two thickness values show that the angular variation of σ_{yy}/σ_0 around the crack front scales with $\bar{K}$. The other stress components also display

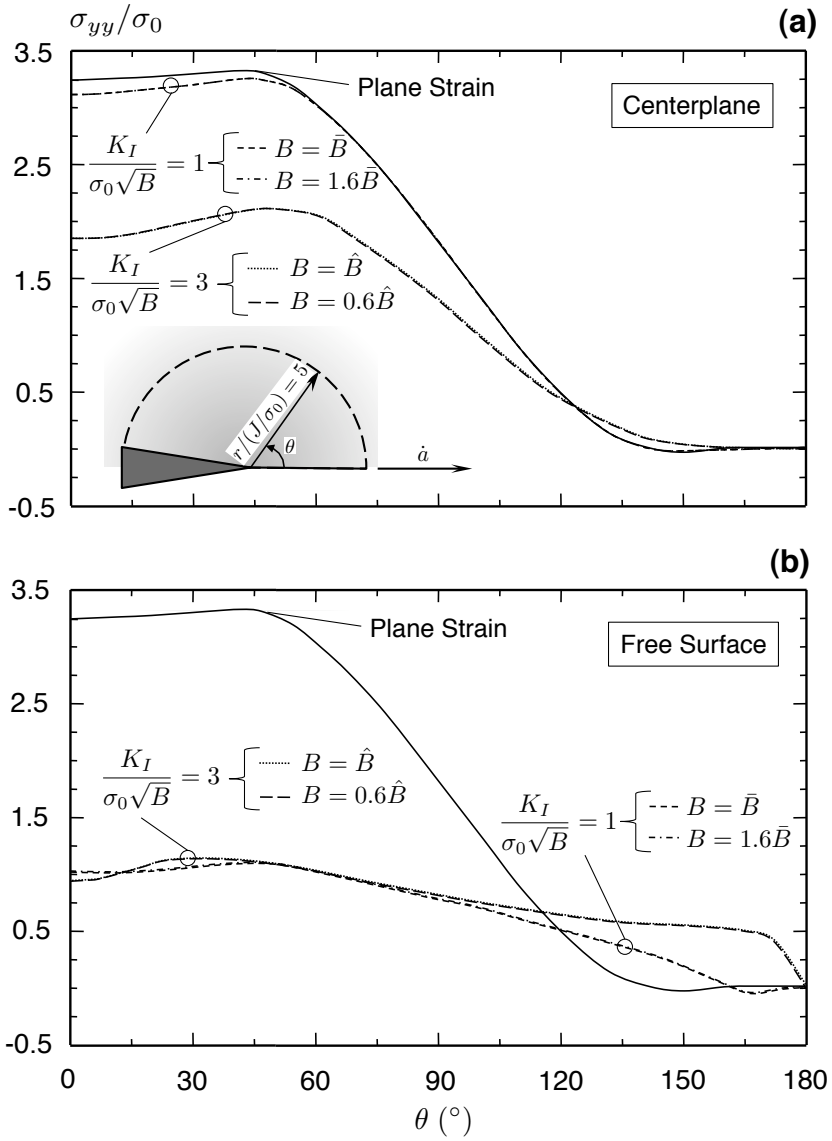

Figure 4.8: Normalized angular variation of σ_{yy}/σ_0 around the crack front at a constant scaled distance $r/(J/\sigma_0) = 5$ for two loading levels, $K_I/\sigma_0\sqrt{B} = 1$ and $K_I/\sigma_0\sqrt{B} = 3$ on (a) the centerplane ($Z/B = 0.0625$) and (b) the outside surface ($Z/B = 0.4965$). Essentially identical results obtained with different values for the thickness, B, and for the mode-I applied remote loading, K_I, but the same value of the non-dimensional parameter $K_I/\sigma_0\sqrt{B}$ indicate self-similarity of this stress component. The steady-growth, plane-strain solution is also shown for reference.

self-similarity, *i.e.*, the results in Fig. 4.7 and Fig. 4.8 demonstrate that Eqn. 4.4 holds for the triad of all scaled points $(r/(J/\sigma_0), \theta, Z/B)$.

The solutions in Figure 4.8a show the angular variation of σ_{yy}/σ_0 on the centerplane for two quite different loading levels. For $\bar{K} = 1$, values at mid-thickness essentially match the plane-strain solution, except over

the sector $|\theta| \leq \pm 60°$, where the plane-strain values are (just) slightly larger. For loading $\bar{K} = 3$, values from the 3D solution lie well below the plane-strain values, indicating the transition towards plane-stress conditions at this distance from the front.

Near the outside surface (Fig. 4.8b), the angular variation of σ_{yy}/σ_0 around the crack front no longer has any features of the plane-strain solution. The values of σ_{yy}/σ_0 at $\bar{K} = 1$ and 3 differ by less than $0.1\sigma_0$ except near the crack flank.

4.5.3 Opening-mode strain on the crack plane

Figure 4.9 shows the opening-mode strain normalized by the yield strain, $\varepsilon_{yy}/\varepsilon_0$, ahead of the crack front at mid-thickness and outside surface for the loading levels (a) $\bar{K} = 1$ and (b) $\bar{K} = 3$. The figures again show solutions for two different thicknesses, B, with K_I adjusted to maintain constant values of $\bar{K}$. The identical strain values shown in Fig. 4.9 for the two thicknesses at fixed $\bar{K}$ demonstrate the same similarity scaling relationship for strains as described for stresses in Eqn. 4.4.

Figure 4.9a shows the normalized opening-mode strain ahead of the crack front for $\bar{K} = 1$ at mid-thickness ($Z/B = 0$) and near the outside surface ($Z/B = 0.495$). For this loading level, values on the centerplane exceed slightly the plane-strain values. Near the outside surface, the opening-mode strain remains far below the centerplane values and also well below plane-strain values.

As shown in Fig. 4.9b, the normalized opening-mode strain now varies more strongly over the thickness at the higher loading level $\bar{K} = 3$. Here, values at mid-thickness reveal a gradient quite similar to the plane-strain solution, but larger in magnitude by several multiples of ε_0. High values for $\bar{K}$ reduce the near-front constraint and enable development of these large plastic strains at mid-thickness. Larger plastic strains increase the total strains (shown in Fig. 4.9) and reduce the stresses (shown in Figs. 4.7 and 4.8). Near the outside surface ($Z/B = 0.495$), $\varepsilon_{yy}/\varepsilon_0$ reaches a near-constant value of $\sim 1.8\varepsilon_0$ from strain hardening and reflects the essentially plane-stress conditions that exist for $X/(J/\sigma_0) \geq 1$.

4.5.4 Opening profiles

Figure 4.10 shows the opening profile behind the steadily advancing crack front. Opening displacements and physical distances are scaled by J/σ_0 for the loading levels $\bar{K} = 1$ and 3. The opening profiles maintain the same similarity scaling at fixed $\bar{K}$ as do the stresses and strains shown in the previous figures of this section.

At $\bar{K} = 1$ shown in Fig. 4.10a, the crack opening profile at mid-thickness matches closely the plane-strain solution for $X/(J/\sigma_0) \gtrsim -4$. Figure 4.10b indicates that at higher loading levels, the crack opening

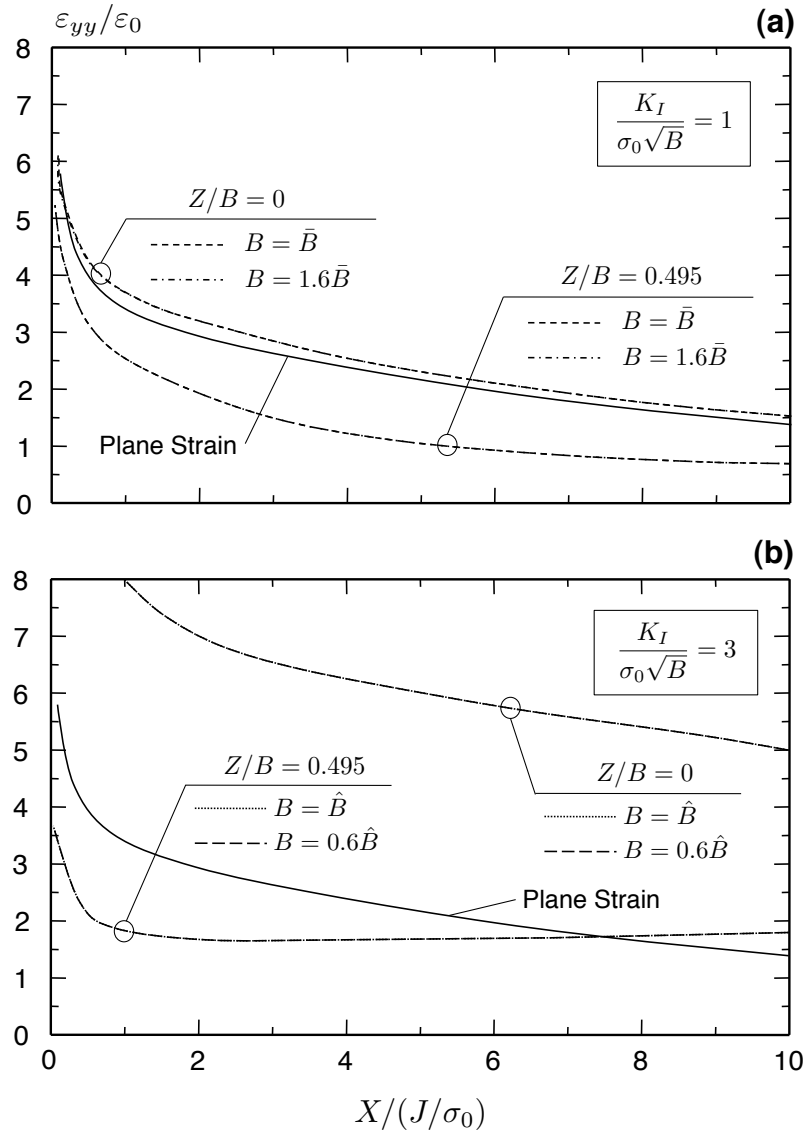

Figure 4.9: Normalized opening-mode strain, $\varepsilon_{yy}/\varepsilon_0$, with scaled distance from the crack front, $X/(J/\sigma_0)$, along the crack plane ($Y = 0$) at mid-thickness ($Z/B = 0$) and near the outside surface ($Z/B = 0.495$). Load levels are: (a) $K_I/\sigma_0\sqrt{B} = 1$ and (b) $K_I/\sigma_0\sqrt{B} = 3$. Essentially identical results obtained with different values for the thickness, B, and for the mode I applied remote loading, K_I, but the same value of the non-dimensional parameter $K_I/\sigma_0\sqrt{B}$ indicate self-similarity of this strain component. The steady-growth, plane-strain solution is also shown for reference.

profile becomes substantially more uniform over the thickness. The crack opening displacements at mid-thickness exceed outside surface values for $\bar{K} = 1$ and 3. The opening profile for $\bar{K} = 1$ and $\bar{K} = 3$ takes on a "wedge-like" shape for $X/(J/\sigma_0) \leq -2$ at the outside surface. The wedge-like opening profile on the outside surface leads to a nearly constant crack opening angle computed from any two points between $-10 \leq X/(J/\sigma_0) \leq -2$. Section 4.7 explores the practical implications of this result in fracture testing.

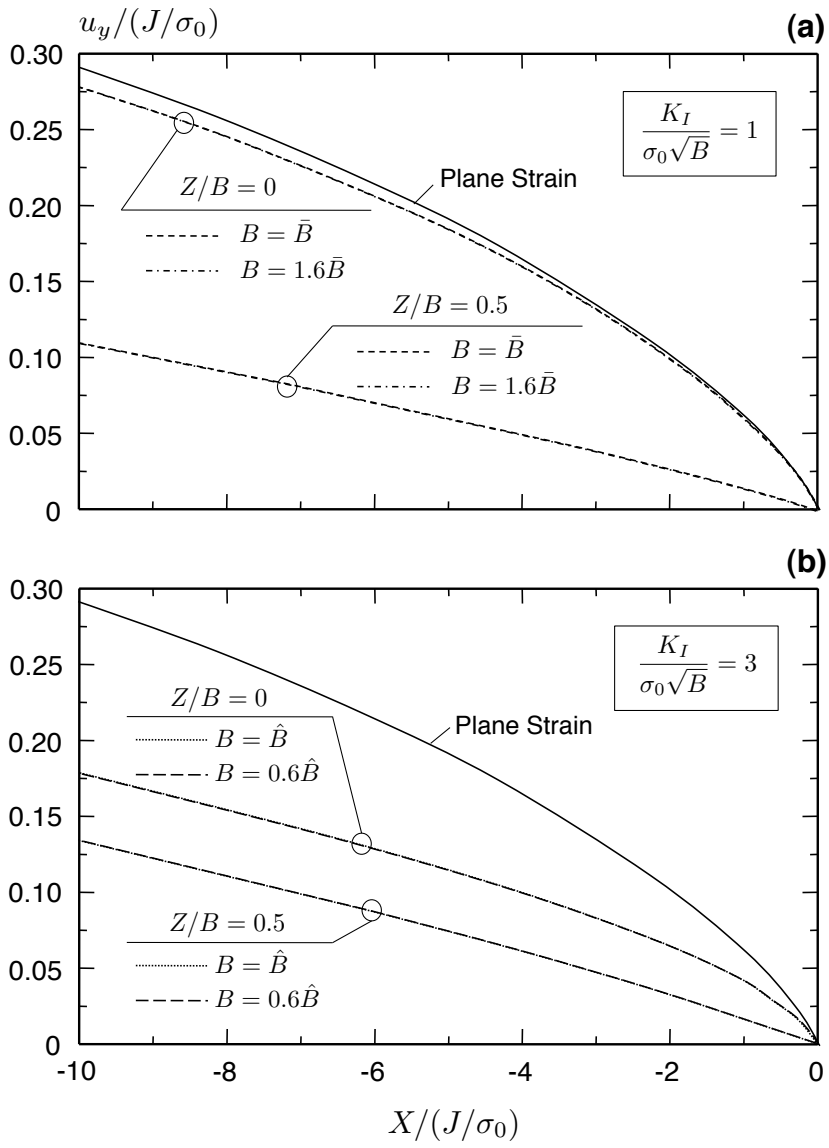

Figure 4.10: Scaled crack opening profiles with the distance behind the steadily growing crack front along the crack plane ($Y = 0$) at mid-thickness ($Z/B = 0$) and near the outside surface ($Z/B = 0.495$). Load levels are: (a) $K_I/\sigma_0\sqrt{B} = 1$ and (b) $K_I/\sigma_0\sqrt{B} = 3$. Essentially identical results obtained with different values for the thickness, B, and for the mode I applied remote loading, K_I, but the same value of the non-dimensional parameter $K_I/\sigma_0\sqrt{B}$ indicate self-similarity of this displacement component. The steady-growth, plane-strain solution is also shown for reference.

The wedge-like shape ($u_y \propto r$) for $X/\left(J/\sigma_0\right) \leq -2$ near the outside surface implies a reduced singularity in the strain field for the steadily propagating crack. Under plane-strain conditions, u_y is proportional to $\ln(1/r)$ during steady crack growth in a perfectly plastic material [27]. As expected, this result suggests a much smaller region near the outside surface where high stresses/strains develop during crack growth than predicted in the plane-strain solution.

4.6 Extent of three-dimensional response

Figures 4.11 and 4.12 examine further the extent of 3D effects ahead of the advancing front and over the thickness. At sufficient distance from the crack front and over the full thickness, the 3D SSY solution must match the Williams [128] solution for a stationary sharp crack under linear-elastic, plane-stress conditions (the 3D boundary layer solution imposes quasi-static crack advance). Figure 4.11 shows 3D elastic-plastic, opening-mode stresses normalized by the opening-mode stress field from the Williams solution, $\sigma_{yy}/\sigma_{yy}^{pl-\sigma}$, ahead of the crack front at two extreme thickness planes – on the centerplane ($Z/B = 0$) and near the outside surface ($Z/B = 0.495$). The thickness of the plate, B, normalizes distances from the crack front, X. Results are shown at three increasing loading levels, $\bar{K} = 1$, 2, and 3, and for reference, marker lines at distances taken from Table 4.1 indicate r_{p0} at mid-thickness on the crack plane. The stress values as normalized in Fig. 4.11 for the steadily advancing crack front bear a striking similarity to those for the stationary crack front fields examined by Nakamura and Parks [72].

Consider first locations at $X/B \geq 1.5$ in Fig. 4.11. For $\bar{K} = 1$, the opening-mode stresses at mid-thickness and near the outside surface become identical and match the Williams linear-elastic solution at about $X/B = 1.5$. This distance is 6 times the plastic zone on the crack plane at mid-thickness (r_{p0}). For $\bar{K} = 2$, the mid-thickness and near outside surface stresses become identical for $X/B \geq 2.5$, but remain slightly above the (plane-stress) linear-elastic solution at 5 times the plastic zone size ($X = 5r_{p0}$). The stresses for $\bar{K} = 3$ at mid-thickness and near the outside surface also become identical for $X/B \geq 2.5$, but do not decrease to the level of the Williams solution at five times the thickness. The elevated, linear-elastic stresses in the 3D solution shown for $\bar{K} = 2,\ 3$ reflect plane-stress conditions (no thickness variation) but with values exceeding the Williams solution to compensate for the comparatively smaller stresses nearer to the crack front caused by plasticity.

Now examine $\sigma_{yy}/\sigma_{yy}^{pl-\sigma}$ at $\bar{K} = 1$ in Fig. 4.11 for $X/B \leq 1.5$ as $X/B \to 0$. Approaching the crack front, normalized values of $\sigma_{yy}/\sigma_{yy}^{pl-\sigma}$ at mid-thickness and near the outside surface tend to zero, though at quite different rates, leading to significant through-thickness variations. The normalized values here decrease towards zero because the strength of the asymptotic singularity from the linear-elastic solution ($1/\sqrt{r}$) exceeds the singularity produced by the 3D nonlinear solution. Nakamura and Parks [72] observe this result in their 3D SSY solutions for nonlinear response of a (sharp) stationary crack front. Further, steadily propagating cracks under elastic-plastic, plane-strain conditions exhibit lower-order singularities than those produced by stationary cracks under the same conditions [90]. At mid-thickness for $\bar{K} = 1$, $\sigma_{yy}/\sigma_{yy}^{pl-\sigma}$ reaches a maximum value at $X < 0.01B$ due to the near plane-strain conditions very deep within the active yielding region. Plane-stress like conditions develop on the free surface, and yielding does not

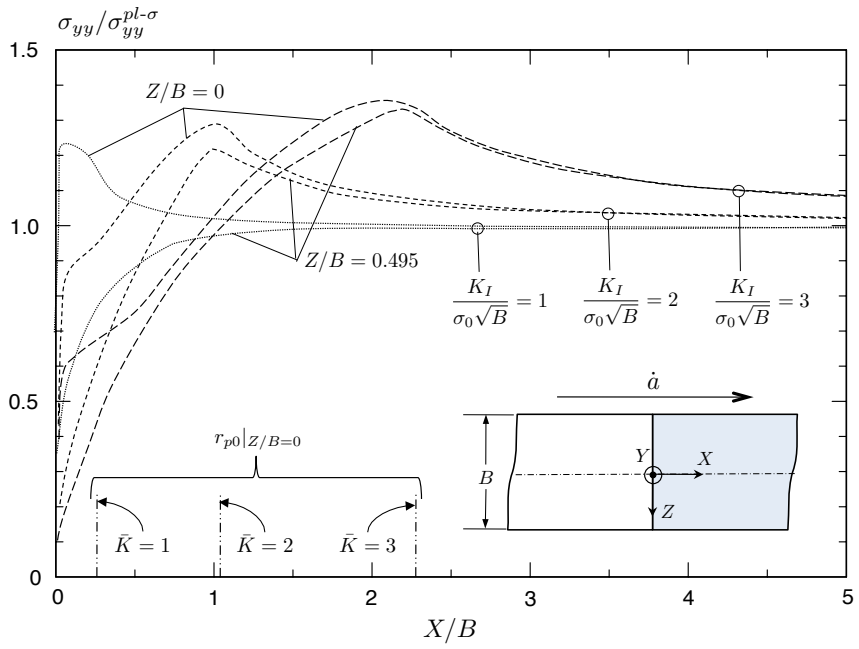

Figure 4.11: Three-dimensional values of opening-mode stress normalized by the opening-mode stress for a stationary crack under linear-elastic, plane-stress conditions, $\sigma_{yy}^{pl-\sigma}$. The normalized stress values are shown for increasing values of the loading parameter $K_I/\sigma_0\sqrt{B}$ and at the centerplane ($Z/B = 0$) and near the outside surface ($Z/B = 0.495$).

occur except at vanishingly small distances from the crack front (see Table 4.1). The near constant value of $\sigma_{yy} \approx \sigma_0$ over this region (see Fig. 4.7a) leads to the smoothly decreasing, normalized stresses here for $X/B \leq 1$.

Figure 4.12 illustrates the transition in 3D features of the solution over the thickness and with increasing distance from the crack front on the crack plane for $\bar{K} = 1$ and 3. Opening-mode stresses (σ_{yy}/σ_0) and a normalized through-thickness constraint measure $\sigma_{zz}/0.5\,(\sigma_{xx} + \sigma_{yy})$ vary over the thickness of the plate from the center plane ($Z/B = 0$) to the free surface ($Z/B = 0.5$) and along the uncracked ligament from $0.01 \leq r/B \leq 0.25$. The parameter $\sigma_{zz}/0.5\,(\sigma_{xx} + \sigma_{yy})$ quantifies the relative amount of out-of-plane constraint at a point and reaches one for plane strain. The traction boundary condition on the free surface requires that $\sigma_{zz} \to 0$ and thus $\sigma_{zz}/0.5\,(\sigma_{xx} + \sigma_{yy}) \to 0$ at $Z/B = 0.5$. Stress values reflect interpolation from Gauss points values to lines of nodes parallel to the Z-axis. The near-front fields retain their plane-strain character along the crack front over a very small fraction of the plate thickness, even at values of $\bar{K} > 1$. Opening-mode stresses exceed $3\sigma_0$ at distances out to $r/B \approx 0.03 - 0.05$ at both loading levels over the middle 60-70% of the thickness. The constraint parameter, $\sigma_{zz}/0.5\,(\sigma_{xx} + \sigma_{yy})$, exhibits a similar near uniform value over the same fraction of B and to the same distances from the crack front. At the closest

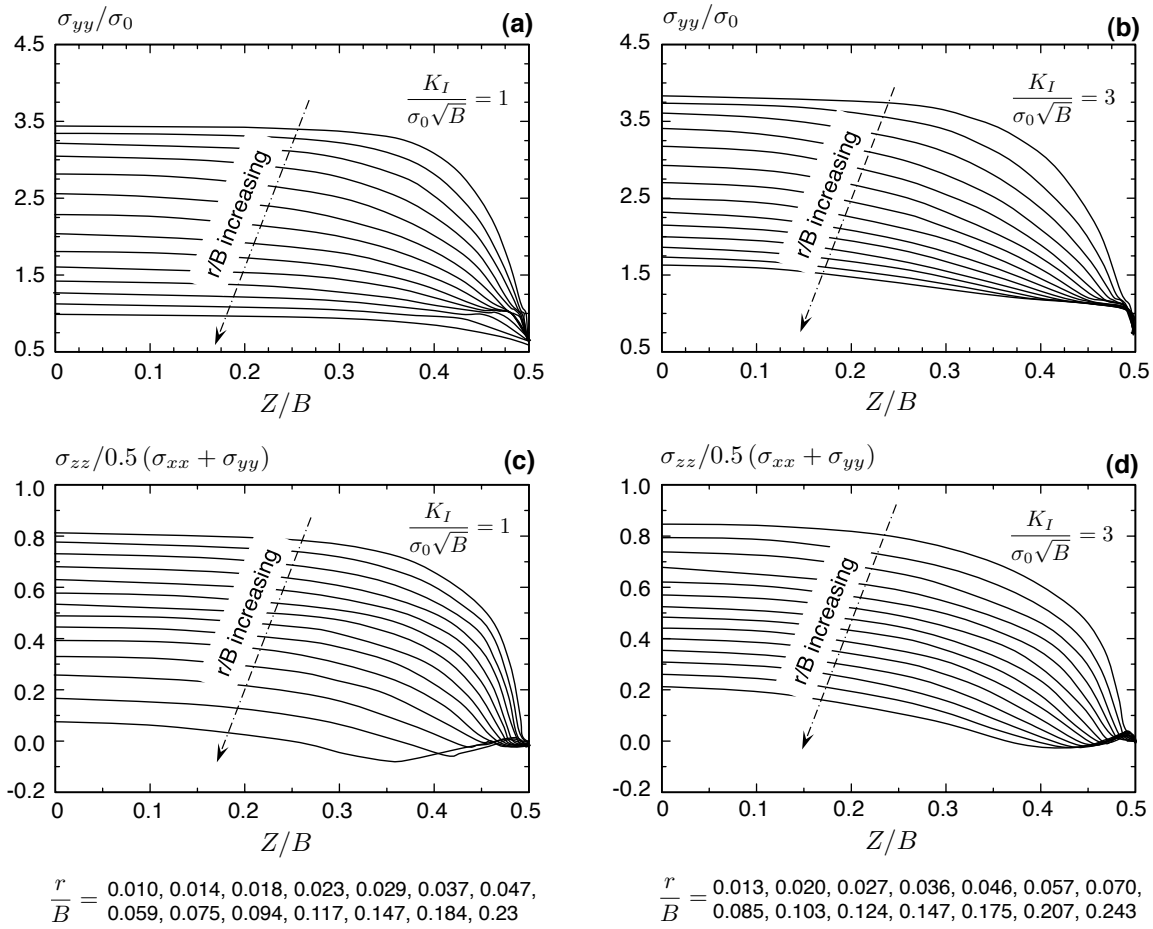

Figure 4.12: Through-thickness variations of opening mode stresses and a constraint measure at constant values r/B on the crack plane ahead of the steadily propagating crack.

distance shown, $r/B \approx 0.01$, the through-thickness constraint reaches 80-85% of plane-strain level. The through-thickness constraint is high, but is *not* at the plane-strain value.

At larger distances from the crack front for $\bar{K} = 1$, the opening-mode stress decreases steadily, reaching uniaxial yield levels (σ_0) at the edge of the plastic zone, $r_{p0} = 0.25B$, over 80% of the thickness and decreasing further near the outside surface, where r_{p0} essentially vanishes. For $\bar{K} = 3$, the opening-mode stress at mid-thickness shows an elevation ($1.6\sigma_0$) at $r/B = 0.24$ from remaining constraint (≈ 0.2) and strain hardening.

Taken together, the results in this section indicate the onset of 3D response at distances from the crack front exceeding the thickness, where the center plane and outside surface stresses begin to differ. The distances depend on the relative load level and vary from $X/B = 1.5 \rightarrow 2.5$ for $\bar{K} = 1 \rightarrow 3$. Deep within the

plastic zone, near plane-strain conditions elevate the opening mode stress to distances of $r/B \approx 0.03 - 0.05$ over 60-70% of B, with a weak dependence on the loading level.

4.7 Crack opening angles

Conventional fracture test practices, *e.g.* ASTM E 1820-09 [4], to measure toughness for ductile tearing in metals ($J-\Delta a$ curves) restrict specimen geometries and permitted amounts of crack extension that precludes testing of thin components of the type considered here. A relatively new test standard, ASTM E 2472-06 [5], supports laboratory testing to measure the crack tip opening angle (CTOA) for toughness characterization in thin metallic panels. Both C(T) and M(T) specimens may be tested with crack extensions (Δa) exceeding multiples of (to many times) the thickness – test specimen thickness should match thickness in the intended application. Schwalbe et al. [99] discuss various concepts and details of this standard which employs optical and other methods to record the opening displacements on the specimen surface at distances of 0.5-1.5 mm behind the current location of the advancing crack front. The "wedge-like" opening profile at the outside surface (Fig. 4.10) for different $\bar{K}$ values, computed in the present work and representing conditions at extended amounts of crack growth, provides additional modeling support for this approach to test thin components.

Experimental studies [77] find initially high CTOA values as the tearing crack forms and emerges from the plastically blunted, previously sharp fatigue pre-crack. As the crack advances through the plastic zone generated by loading/blunting of the fatigue crack, the measured CTOA values decrease, eventually reaching a near-constant, steady value. The steady CTOA values vary for different materials and with specimen thickness for a specific material. The experiments of Mahmoud and Lease [63] using a 2024-T351 aluminum alloy show a decrease of measured CTOA on the outside surface as the thickness of the specimen (B) increases.

Conventional 2D and 3D finite element models with nonlinear material response and crack growth by node release at prescribed CTOA values obtained from experiments capture blunting of the fatigue pre-crack, the early stages of ductile tearing and overall specimen load-crack growth response [19, 39, 64]. At larger amounts of crack extension, approaching steady conditions as the crack growth resistance curve becomes flat, the finite increments of crack growth dictated by the element size in these type of analyses cause numerical instabilities. The steady-growth formulation overcomes these numerical issues but with the inability to model the early, transient stages of tearing. The present analyses enforce 3D steady growth at a specified, fixed-value of remote loading, which may be interpreted as the SSY toughness for a material having the

elastic and flow properties employed in the computations ($E/\sigma_0 = 250$, $\nu = 0.33$, $n = 10$). The 3D solutions then provide the corresponding, steady-state crack-opening profiles, CTOA values, and their variation over the thickness. The $\bar{K}$ scaling makes the normalized computational results applicable for a wide range of thicknesses and SSY material "toughness" values.

Figure 4.13 provides the 3D crack opening profiles at six locations over the thickness for increasing load levels $\bar{K} = 1, 2, 3$. The plane-strain opening profile given in Fig. 4.13d conveniently normalizes the 3D profiles for comparisons. Table 4.2 lists CTOA (ψ°) values on the outside surface for $\bar{K} = 1$, 2, 3, and 5. For each $\bar{K}$, the CTOA is computed at normalized distances $X/\left(J/\sigma_0\right) = -2$, -5, and -10 using the expression $\psi = 180/\pi \times \tan\left(2u_y/X\right)$. The best-fit, rate-of-change for the CTOA with respect to $\bar{K}$ is also shown.

The opening profiles, and thus CTOA values, vary strongly over the thickness at relatively low-load levels, $\bar{K} = 1$ in Fig. 4.13a, where the plastic zone at mid-thickness extends $r_{p0} \approx 0.25B \approx 62J/\sigma_0$. The mid-thickness opening very closely matches the plane-strain profile out to distances of $10J/\sigma_0 \approx 0.04B$, which for a moderate strength and toughness aluminum alloy [$K_{Ic} = 40$ MPa$\sqrt{\text{m}}$, $\sigma_0 = 350$ MPa] is roughly 0.5 mm ($\bar{K} = 1$). The 3D opening profiles follow the plane-strain shape, indicated by the near horizontal lines in Fig. 4.13 away from the crack front. The higher $\bar{K} = 2,\ 3$ loadings show similar trends but with the through-thickness changes in the opening displacements now smaller and all merging towards approximately 50-60% of plane-strain values.

The trends in Figure 4.13 and the CTOA values in Table 4.2 follow the experimental observation of decreasing CTOA values at the outside surface with increasing thickness – for a fixed value of remote, steady loading K_I. As B increases with a fixed K_I, $\bar{K}$ decreases and the CTOA values decrease, as more directly seen in Table 4.2. Mahmoud and Lease [63] report CTOA values at steady-growth of $\approx 5^\circ$ for an Al 2024-T351 material at thicknesses of $2.3 - 6.4$ mm. The smaller CTOA values here of $\approx 1.5^\circ - 2.0^\circ$ for a reasonably similar analysis material ($E/\sigma_0 = 250, n = 10$) do not reflect the additional opening displacements over the fracture process zone from metallurgical-scale damage ahead of the advancing front. Moreover, their tests conducted with a T-L orientation (crack plane perpendicular to the rolling direction) exhibit a flat-to-slant fracture transition at these thicknesses which complicates interpretation of their CTOA values relative to results of computations here (*e.g.*, the $B = 6.4$ mm specimen transitioned to slant fracture over the first 18 mm of crack extension).

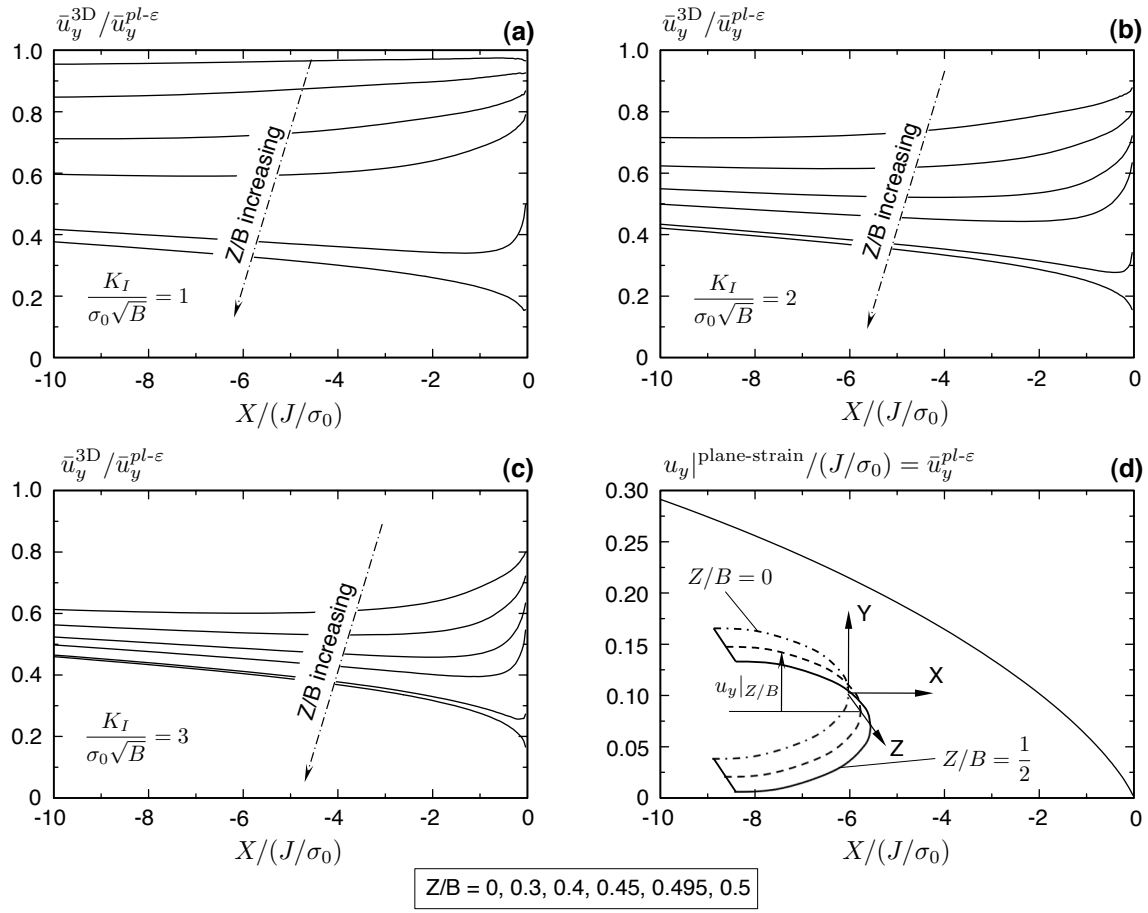

Figure 4.13: Crack opening profiles over the thickness, $\bar{u}_y^{3D}$, normalized by the plane-strain, steady-growth opening profile, $\bar{u}_y^{pl-\varepsilon}$, at three loading levels: $\bar{K} = K_I/\sigma_0\sqrt{B} = 1, 2, 3$. The plane-strain profile is shown for reference in (d) with distances and opening displacements normalized by J/σ_0.

4.8 Summary and conclusions

The present study describes the first three-dimensional (3D) numerical analyses of steady-state, elastic-plastic crack growth. The computational model reflects the experimental conditions realized in the fracture testing of comparatively thin ductile specimens where the material flow stress and toughness combine to limit the maximum plastic zone size during extended crack advance to at most a few multiples of the thickness. Such 3D small-scale yielding (3D SSY) conditions are readily achieved, for example, in laboratory testing of aluminum alloys for aerospace applications. In test specimens and structural components, the in-plane dimensions often exceed 100-500 (or more) times the thickness (B). Crack advance beyond the blunting region formed at an initial fatigue pre-crack occurs with an essentially fixed plastic zone size. Laboratory testing and structural configurations that impose globally mode I loading may generate locally mode I ("flat") fracture or mixed-mode ("slant") fracture. The present work focuses on the conditions of global and

	ψ (°)				
$X/(J/\sigma_0)$	$\bar{K}=1$	$\bar{K}=2$	$\bar{K}=3$	$\bar{K}=5$	$d\psi/d\bar{K}$
-2	1.52	1.67	1.85	2.10	0.146
-5	1.38	1.54	1.69	1.87	0.121
-10	1.26	1.41	1.53	1.63	0.09

Table 4.2: 3D values of the crack-tip opening angles (CTOA) at the outside surface computed from opening displacements at increasing distances behind the advancing crack front. (ψ).

local mode I fracture.

The 3D boundary-layer model constructed here using a finite element framework has a straight, through-thickness crack front advancing at a steady, quasi-static velocity under constant, far-field loading. Plane-stress mode I displacements, with magnitude set by a fixed value of the remote stress intensity factor, $K_I^{far} = K_I$ (for simplicity), and applied on the far-field boundary, provide the loading. The computational model has one natural geometric length scale – the plate thickness, B – and requires no criteria for continued crack advance. The model generates spatially invariant, elastic-plastic fields relative to an observer located on the advancing crack front. The current work investigates the effect of applied load levels, material yield stress, and thickness, on the crack front strain, stress and displacement fields.

The work reported here supports the following key observations and conclusions:

1. Within a small deformation framework, 3D implementation of the streamline integration framework developed by Dean and Hutchinson [21] for two-dimensional models becomes relatively straightforward. In the 3D setting, straight streamlines parallel to the crack plane are also defined in parallel planes over the thickness direction (Z) of the SSY model to pass through element Gauss points. Following the original 2D framework, integration of the nonlinear constitutive relations at Gauss points along each streamline on the fixed mesh equals integration over crack advance and determines the elastic-plastic material response. Extensive computational demands of the 3D implementation are easily accommodated through code design and execution to leverage parallel computing features of current systems – streamline integration of the constitutive relations, for example, executes fully in parallel as do most other phases of the solution.

2. Dimensional analysis suggests, and present computations demonstrate, the similarity scaling of displacements, strains, and stresses during steady crack advance for 3D SSY conditions described by the non-dimensional loading parameter, $\bar{K} = K_I/\sigma_0\sqrt{B}$. For fixed elastic and material flow properties, the 3D crack-front fields in scaled coordinates relative to the extending crack front $(r/(J/\sigma_0), \theta, Z/B)$ remain unchanged when K_I, the yield stress (σ_0) and B vary to maintain a constant value of $\bar{K}$ [where $J = K_I^2/E$]. The solutions in this study refer to the zero T-stress configuration.

3. Three-dimensional effects on the stress fields begin to appear on the crack plane at distances of about (1.5-2.5)B ahead of the advancing front over the (relatively) large range of loadings considered, $\bar{K} = 1 \rightarrow 3$. At these distances, for example, the otherwise equal values of opening-mode stress at mid-thickness and the outside surface characteristic of a plane-stress state, begin to differ with the mid-thickness region maintaining larger stress values on approach to the crack front. These distances for the onset of 3D effects during steady growth agree remarkably well with those for a stationary crack in the 3D SSY model [72].

4. The loading parameter $\bar{K}$ provides a strong indicator of the 3D character of the steady growth fields, with smaller values representing reduced plastic zones relative to the thickness and more highly constrained conditions in the crack front region. For the power-law hardening material considered here ($n = 10$, $E/\sigma_0 = 250$, $\nu = 0.33$), $\bar{K}$ over the range $1 \rightarrow 5$ corresponds to plastic zone sizes at mid-thickness from $0.25B$ to $6.4B$ on the crack plane. A $\bar{K} = 1$ loading leads to a plastic zone size of $0.25B$ on the crack plane at mid-thickness and to near plane-strain fields (strains, stresses, displacements) extending to distances of (4-6)J/σ_0 ($\approx 0.015B$) from the crack front over the middle 70% of the thickness. At larger distances from the crack front and near the outside surface, the fields transition to those of plane stress. At mid-thickness, for example, the opening-mode stress on the crack plane reduces to the linear-elastic, plane-stress value of the K_I field at a distance of $X \approx 1.5B$ for $\bar{K} = 1$.

5. The plastic zone size on the crack plane at mid-thickness increases with $(K_I/\sigma_0)^2$, reaching $2.3B$ for $\bar{K} = 3$. At $\bar{K} = 5$, the plastic zone on the crack plane develops a uniform size of $6.4B$ over the thickness on the crack plane and a constant height above the crack plane of $4B$ over the thickness. At these larger loading levels, much of the plastic zone experiences plane-stress or near plane-stress conditions, yet there remains a small region of high constraint along the crack front. At $\bar{K} = 3$, this high constraint region on the center plane exists over distances smaller than J/σ_0 ($\approx 0.035B$) and only over the center 40% of the thickness.

6. The opening profiles behind the steadily advancing crack provide additional insight for the increasing number of experimental programs that adopt the crack-tip opening angle (CTOA) as a macroscopic measure of the toughness in thin metallic components for sustained amounts of crack extension [5]. At loading $\bar{K} = 1$, the curvature and magnitude of the opening profile vary strongly over the thickness. At mid-thickness, the 3D profile matches the curved, plane-strain profile over distances behind the crack front of (6-7) $J/\sigma_0 = 0.026B$. At the outside surface, the profile becomes more "wedge-like" with 1/3 the centerplane opening at the distance of (6-7) $J/\sigma_0 = 0.026B$. At increased loading, $\bar{K} = 3$, the

center-plane opening profile has less curvature and decreases to 60% of the plane-strain opening value at (6-7) $J/\sigma_0 = 0.22B$, and is only 1.5 $\times$ the opening at the outside surface. The computed CTOA values at the outside surface increase from 1.3-1.5 degrees for $\bar{K} = 1$ (plastic zone size of $0.25B$ at mid-thickness) to 1.6-2.1 degrees at $\bar{K} = 5$ (plastic zone size of $6.4B$ at mid-thickness). These CTOA values are roughly 30-40% of those often reported in laboratory testing for materials with these toughness levels. The smaller values here may be anticipated as the numerical model does not incorporate: (a) damage (*e.g.*, void growth) ahead of the crack front, and (b) crack front tunneling.

Our future studies will examine other aspects of steady crack growth in this 3D SSY framework. We expect nonzero values for the remotely applied T-stress to have a marked effect on crack front fields over the mid-thickness region at the smaller $\bar{K}$-values, where near plane-strain conditions for T=0 prevail in the current work. Experiments often reveal crack front tunneling caused by the higher-constraint levels at mid-thickness relative to the outside surface. By simple re-meshing, the present computational model may be readily extended to accommodate steady growth with a fixed, curved crack front. Side-grooves are often used to minimize tunneling effects and to enforce locally flat fracture, and may be included easily in the present framework, again by re-meshing, to examine their effectiveness in maintaining more uniform conditions over the crack front.

Chapter 5

T-Stress Effects on Steady Crack Growth in a Thin, Ductile Plate under Small-Scale Yielding Conditions

5.1 Introduction

The elastic-plastic, ductile tearing process in thin structural components often leads to plastic zone sizes comparable to at most a few multiples of the thickness, B, especially for alloys with high yield strength relative to toughness. During structural overloads or laboratory tests, a sharp crack formed by fatigue (for example) blunts under plastic deformation and begins to extend by a ductile tearing mechanism. As the crack advances (Δa) through the plastic zone formed during the initial blunting and early growth stages, the tearing resistance (*e.g.* J) increases, but at a decreasing rate with continued Δa, as the crack extends through material that has already experienced high (triaxial) stress, plastic strain and damage (*e.g.*, void nucleation-growth) [3]. The present study focuses on this fracture process where the material's (local) tearing toughness, combined with (comparatively) high yield strength, cannot sustain a plastic zone size of more than a few thicknesses.

Continued crack advance occurs under globally plane-stress and essentially steady-state conditions when the in-plane dimensions of the structural component or laboratory specimen exceed many times the thickness and amount of crack extension. The immediate crack-front material over the mid-thickness region experiences elastic-plastic, near plane-strain conditions which quickly become elastic-plastic, plane stress and then simply linear-elastic, plane-stress conditions with increasing radial distance from the crack front. Aerospace applications with thin components (a few mm's) constructed from modern aluminum alloys (*e.g.*, yield stress of 350 MPa, toughness of 40 MPa$\sqrt{\text{m}}$) readily create these conditions of three-dimensional, small-scale yielding (3D SSY) — see for example the laboratory fracture tests conducted in Newman et al. [76] and Seshadri et al. [100] on aluminum panels that exceeded 1 m in size.

In Chapter 4, we describe the implementation and application of a computational framework for steady-state crack growth obtained by extending the Dean and Hutchinson [21], streamline-integration methodology from plane-stress/strain conditions to three dimensions. For a straight crack front, the plate thickness, B, then provides a geometric length-scale in addition to deformation scales of plastic-zone size and crack-tip

opening. This computational setting directly yields the steady-state solution (3D displacement, strain, and stress fields) for elastic-plastic crack growth on a fixed finite element mesh. The model requires no crack growth criterion to drive crack extension — steady crack advance occurs at the loading defined by the plane-stress, K_I displacements imposed on the remote boundary. Previous studies adopt the plane-stress/strain formulations of the elastic-plastic, steady-growth methodology to examine various features of the fracture process, including inertial effects [31], near-tip energy-balance requirements [33, 81], constraint effects [117, 118], and mixed-mode crack advance [22]. Other investigators employ the 3D SSY model successfully with a stationary crack to explore dimensional scaling effects of thickness [72], to compare computational with analytical void growth rates [44], and to investigate the crack-front blunting process in a finite deformation framework [45].

This study extends our 3D SSY framework in Chapter 4 for steady crack growth to include the potential effects of T-stress on the elastic-plastic, fracture process — examined for a stationary crack front by Yuan and Brocks [133] and Kim et al. [48], and for a crack advancing under cyclic loading by Roychowdhury and Dodds [97]. The linear-elastic T-stress provides a first-order estimate of geometry and loading mode (*e.g.*, tension *vs.* bending) effects on near-front, elastic-plastic fields. The far-field loading in the 3D SSY model becomes the combined plane-stress displacements generated by the imposed K_I and T-stress values. Experiments by Joyce and Link [46, 47] reveal the strong impact of negative T-stress on $J - \Delta a$ curves obtained by testing bend specimens with varying a/W ratios. Negative T-stress configurations exhibit a marked increase in tearing resistance during crack extension but minimal effect at the onset of tearing (J_{Ic}).

Tvergaard and Hutchinson [114] model T-stress effects on mode I crack growth from a blunting, stationary crack using the plane-strain, SSY framework with a cohesive fracture criterion. At crack growth amounts exceeding twice the plastic zone size at initiation and approaching steady conditions, negative T-stress elevates the toughness while positive T-stress has negligible effect. Xia and Shih [130] consider the same plane-strain, SSY framework as Tvergaard and Hutchinson but employ a computational cell model, with void-growth response defined by a Gurson-Tvergaard constitutive relationship [40, 111], to drive crack extension. They find toughness levels near steady-state conditions increase for negative T-stress, but decrease below $T = 0$ levels for an imposed, positive T-stress.

Within a plane-strain, SSY framework to model steady crack extension using the streamline methodology, Varias and Shih [117] show that the near-tip fields – stresses, strains, and displacements – display a self-similarity scaling with a characteristic length dependent on the T-stress. Moreover, non-zero imposed values of the T-stress – positive and negative – impact the mechanical fields similarly, *e.g.* opening-mode stresses ahead of the advancing crack tip reach a peak value under $T = 0$ loading. From these analyses, Varias and

Shih [117] predict minimum, steady-state toughness values in zero T-stress configurations based on a simple, crack-tip opening angle criterion during continued growth.

Based on their results for the 3D SSY model with a stationary crack, Nakamura and Parks [72] suggest a similarity scaling for crack-front fields in terms of the non-dimensional loading parameter, $\bar{J} = J^{far}/\sigma_0\varepsilon_0 B$ (alternatively $\bar{K} = K_I^{far}/\sigma_0\sqrt{B}$). In Chapter 4, we demonstrate this same $\bar{K}$-scaling develops for steady growth in the 3D SSY model under zero T-stress loading. The $\bar{K}$-scaling provides solutions to a wide range of actual loadings and material flow properties for a minimal set of finite element analyses. When the far-field loading (K_I^{far}), yield stress (σ_0), and thickness (B) vary but maintain a constant value of $\bar{K}$, the same stresses, strains, and displacements exist at locations around the crack front described in non-dimensional, cylindrical coordinates ($r/(J^{far}/\sigma_0)$, θ, and Z/B), where Z denotes the through-thickness, crack-front position. The 3D SSY analyses for both stationary and steadily-growing cracks indicate significantly diminished, three-dimensional effects at distances of $1-3\times B$ ahead of the front (for $\bar{K}$ in the range of $1-3$).

In this chapter, we demonstrate the continued similarity scaling of crack-front fields in 3D SSY steady growth, with combined $\bar{K}$ and $\bar{T} = T/\sigma_0$ loadings, for a moderately hardening material characteristic of a structural aluminum. Two levels of $\bar{K} = 1,\ 3$ are considered for $\bar{T}$ levels ranging from $+0.25$ to -0.50. For reference, the plastic-zone size at mid-thickness extends $0.25B$ at $\bar{K} = 1$ and $2.3B$ at $\bar{K} = 3$ ahead of the front ($\bar{T} = 0$). The analyses reveal a strong effect of T-stress on the crack-front fields for $\bar{K} = 1$, where near plane-strain conditions with high triaxiality levels develop ahead of the crack front over the mid-thickness region. For $\bar{K} = 3$ loading, the T-stress has much less impact on the fields, *i.e.* much of the plastic zone approaches plane-stress conditions. The presentation of elastic-plastic, principal stress values in the crack-front region for the ($\bar{K}$, $\bar{T}$) loadings leads to a discussion of potential T-stress effects on a stress-controlled, cleavage fracture process that may terminate ductile growth (*e.g.*, the common fracture behavior of ferritic steels at upper transition temperatures). To understand the combined effects of T-stress on triaxiality and plastic-strain levels for a local ductile fracture mechanism, normalized values from the Rice and Tracey [92] void-growth model are compared over the crack plane for $\bar{K} = 1$ loading. The comparisons reveal the tendency for crack-front tunneling, shear-lip formation near the outside surfaces, and minimum steady-state toughness under a zero T-stress configuration.

The paper follows this organization. Section 5.2 describes the 3D SSY framework for steady growth with non-zero T-stress and the expected similarity scaling. Section 5.3 summarizes the numerical methods employed here: essential features of the streamline-integration methodology for steady-state analyses, the finite element model, and material properties. Section 5.4 reports the effect of T-stress on key measures for the active yielding region (extent of plastic deformation directly ahead of the crack front and the height

for the plastic wake). Section 5.5 demonstrates the continued similarity scaling during steady growth for non-zero T-stress in 3D SSY. Section 5.6 presents the variations of principal stress and plastic strain values for combinations of ($\bar{K}$, $\bar{T}$). Section 5.7 incorporates a simple void-growth measure to quantify the potential impact of ($\bar{K}$, $\bar{T}$) loadings on steady-state toughness levels for sustained ductile tearing. Section 5.8 summarizes key results.

5.2 Steady-State Crack Extension

This section outlines the 3D small-scale yielding (SSY) computational framework and key features of the crack-front fields for steady crack advance in a thin ductile plate. Section 5.2.1 describes the 3D modified boundary-layer model as the representation for a broad class of large, thin structural configurations with a crack extending by ductile tearing over distances of at least multiple plate thicknesses. Section 5.2.2 expands the similarity relationship for the crack-front fields from Chapter 4 that incorporates applied loading, material properties, and geometry to include additional effects from a remotely imposed T-stress.

5.2.1 Three-dimensional, small-scale yielding conditions for a steadily growing crack

Consider the large, thin structural panel loaded in-plane as shown in Fig. 5.1 that contains a steadily-advancing, through-thickness crack front under local and global mode I conditions. The crack front extends at the constant quasi-static velocity, $\dot{a}$, arbitrarily from left to right. An active yielding region of fixed size and shape continually develops ahead of the advancing crack front which becomes part of the trailing plastic wake once the crack-front passes. The active yielding region has radial dimensions significantly less than the surrounding, planar structural dimensions: crack length, remaining ligament, height, and width. Thus plate thickness, B, defines the only (natural) physical length scale relevant to the near-front, inelastically deforming material. For example, the in-plane dimensions of thin laboratory specimens (a few millimeters thick) made from common aluminum and titanium alloys readily exceed 100 times the maximum plastic zone dimensions during sustained ductile tearing. Consequently, a region (here taken as a disk) centered at the advancing crack front and consisting largely of elastically deforming material enclosing the plastic zone defines the computational model. Under these conditions, disk material a few thicknesses from the crack front and beyond exhibits a plane-stress response. Loading of material in the disk region is described by the linear-elastic, plane-stress mode I field with amplitude K_I and by the non-singular T-stress.

The computational model reflects conditions after an initially sharp crack forms (perhaps from fatigue

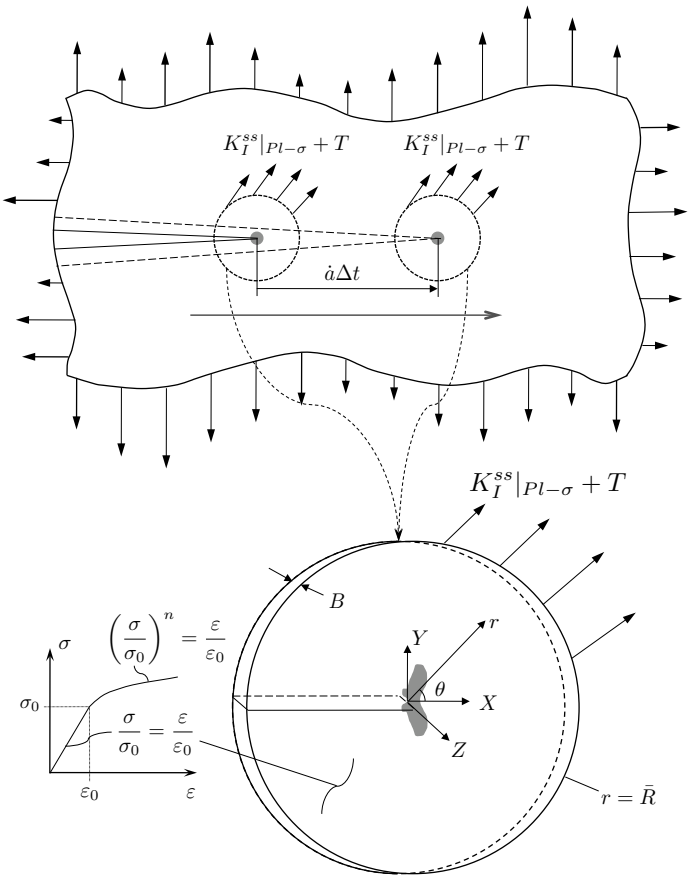

Figure 5.1: Section of a thin plate with a through-thickness, straight crack front advancing steadily at constant velocity, $\dot{a}$, under mode I small-scale yielding (SSY) conditions. The symmetric, remotely applied loading and displacement boundary conditions impose a constant, steady-state ("SS") value of the plane-stress, mode-I stress intensity factor, $K_I^{SS}|_{Pl-\sigma}$, and T-stress.

loading), blunts under local plastic deformation, and then extends by tearing well-beyond the initial blunting plastic zone. During steady-state growth, the crack advances at constant applied loading, K_I^{SS} (and T-stress), and the near-front fields appear invariant for an observer situated at the advancing crack front. A single SSY analysis thus provides the near-front fields for all subsequent extension of the crack, illustrated in Fig. 5.1. The numerical procedures impose a specified value of K_I^{SS} and T-stress on the disk boundary and effectively force steady-crack advance at that remote loading. No requirement exists for a local, crack-front fracture criterion. The numerical procedures compute fully 3D, crack-front fields for a material having the specified elastic and flow properties, under the imposed K_I^{SS} for the corresponding T-stress level.

The disk model for 3D SSY depicted in Fig. 5.1 has a specified radius $r = \bar{R}$ that significantly exceeds the relevant length scales: the maximum in-plane size for the crack-front plastic zone, r_p, and the uniform plate thickness, B. These analyses neglect tunneling during crack advance and prescribe a straight crack at

$X/B = 0$ over the thickness (Z/B). The modeling framework described here readily accommodates crack advance, for example, with a constant, curved crack-front profile and/or side-grooves — to be explored in future work. The asymptotic Williams solution [128] characterizes the plane-stress response of the linear-elastic material far from the crack-front. The shear modulus, μ, and constant $\kappa = (3-\nu)/(1+\nu)$, where ν equals Poisson's ratio, define the elastic material properties. Modifications to the Williams' solution become necessary when inertial effects increase for crack speeds, $\dot{a}$, greater than approximately 10% percent of the shear wave speed [51]. The present work considers slow, steady growth where inertial effects may be neglected. At the remote boundary $r = \bar{R}$, the imposed displacements for mode I crack-front loading have the form:

$$u_x(\bar{R},\theta,Z) = \frac{K_I}{2\mu}\sqrt{\frac{\bar{R}}{2\pi}}\cos\left(\frac{\theta}{2}\right)\left[\kappa - 1 + 2\sin^2\left(\frac{\theta}{2}\right)\right] + \bar{R}\cos(\theta)\frac{T}{E}, \tag{5.1}$$

$$u_y\left(\bar{R},\theta,Z\right) = \frac{K_I}{2\mu}\sqrt{\frac{\bar{R}}{2\pi}}\sin\left(\frac{\theta}{2}\right)\left[\kappa + 1 - 2\cos^2\left(\frac{\theta}{2}\right)\right] - \nu\bar{R}\sin(\theta)\frac{T}{E}. \tag{5.2}$$

The T-stress term imposes a constant, axial stress parallel to the plane of crack extension. In finite components undergoing linear-elastic deformations, the T-stress and K_I values are coupled through the loading mode (tension *vs.* bending), and geometry by the relation (Leevers and Radon [55])

$$T = \frac{\beta K_I}{\sqrt{\pi a}}, \tag{5.3}$$

where β denotes the non-dimensional geometry factor invariant of loading level. Within the framework of the 3D SSY model, the K_I and T-stress values are decoupled and may be imposed with any combinations of interest. The next section discusses the significant role of non-zero T-stress values on crack-front fields during plastic deformation.

5.2.2 Three-dimensional, self-similar fields

Chapter 4 demonstrates the existence of a self-similarity scaling for the near-front displacements, strains and stresses during steady crack advance within the 3D SSY framework with zero T-stress. The near-front stresses, for example, follow the relationship:

$$\sigma_{ij} = \sigma_0 F_{ij}\left(\frac{r}{J^{far}/\sigma_0}, \theta, \frac{Z}{B}; \frac{K_I^{far}}{\sigma_0\sqrt{B}}; \frac{E}{\sigma_0}, n, \nu\right). \tag{5.4}$$

Self-similar relationships having this form exist for the strains, ε_{ij}, and displacements, u_i. In Eqn. (5.4), $J^{far} = K_I^{far}/E$ quantifies the far-field applied loading, and E/σ_0, n, and ν denote material properties

described further in Section 5.3.3. On the centerplane, the non-dimensional loading parameter, $\bar{K} = K_I^{far}/\sigma_0\sqrt{B}$, quantifies the size of the in-plane, crack-front plastic zone, $r_p \propto \left(K_I^{far}/\sigma_0\right)^2$, relative to the plate thickness, B.

When the far-field loading, $K_I^{far} = K_I^{SS}$, yield stress (σ_0), and thickness (B) vary but maintain a constant value of $\bar{K}$, the same stresses, strains, and displacements exist at locations around the crack front described in non-dimensional forms by $\left(r/\left(J^{far}/\sigma_0\right), \theta, Z/B\right)$, with material strain hardening, elastic modulus and Poisson's ratio must remaining unchanged as indicated in Eqn. (5.4). At small values of $\bar{K}$ ($\lesssim 1$), r_p remains a small fraction of B, leading to conditions that approach plane strain along and very near the crack front except in a small region at the outside (free) surface, $|z/B| \to 0.5$. Elsewhere the fields transition from a fully 3D character to simple plane stress with $\sigma_{zz} \to 0$ over the thickness, and no through-thickness gradients of in-plane stresses exist at radial distances beyond approximately $1.5B$. At higher (relative) loading ($\bar{K} \gtrsim 3$), r_p compares in size to B, much of the plastic zone exhibits a plane-stress condition, yet near plane-strain conditions prevail along the crack front. Nakamura and Parks [72] observe this same similarity scaling for sharp, stationary crack fronts that exhibit quite comparable features to those of the steady growth fields (shown in Chapter 4). Roychowdhury and Dodds [95] show the same form of similarity scaling for crack-opening loads, K_{open}/K_{max}, during each load cycle in 3D SSY computations of plasticity-induced crack closure.

For a stationary crack, Larsson and Carlsson [53] first demonstrate the strong impact of T-stress on elastic-plastic, crack-tip fields under plane-strain conditions. Negative T-stress values lower crack-tip triaxiality, reduce opening-mode stress levels, and increase plastic zone sizes. Positive T-stress values have less effect but do increase stress levels ahead of the crack tip. Many subsequent investigations explore the role of T-stress on crack-tip fields for stationary and (early stage) growing cracks under plane-strain conditions, and the consequences on apparent fracture toughness measured in laboratory testing, see Joyce and Link [46, 47] for representative examples. Under plane-stress conditions, the T-stress does not show a pronounced effect on the elastic-plastic, crack-tip fields. The zero through-thickness stress from the plane-stress condition severely restricts the achievable range of stress triaxiality from the T-stress loading.

Varias and Shih [117] employ the steady-growth, SSY framework in plane strain to investigate T-stress effects on crack-tip fields. They find non-zero T-stress values – both positive and negative – reduce stress levels within an angular region centered about and ahead of the advancing crack tip. This contrasts sharply to T-stress effects on stationary cracks where triaxiality decreases monotonically from high levels for $T > 0$ to low levels for $T < 0$. Using the crack-tip opening angle as simple model for ductile fracture, Varias and Shih [117] demonstrate the shielding effect of non-zero T-stress on crack-tip conditions, with the zero

T-stress imposing the most severe loading.

Introduction of T-stress loading into the 3D SSY framework with steady crack advance suggests extension of Eqn. (5.4) for the near-front stresses,

$$\sigma_{ij} = \sigma_0 F_{ij}\left(\frac{r}{J^{far}/\sigma_0}, \theta, \frac{Z}{B}; \frac{K_I^{far}}{\sigma_0\sqrt{B}}, \frac{T}{\sigma_0}; \frac{E}{\sigma_0}, n, \nu\right), \tag{5.5}$$

where 3D near-front fields during steady crack growth now follow a two-parameter characterization based on $\bar{K}$ and the level of imposed T-stress, $\bar{T} = T/\sigma_0$. The imposed T-stress restricts or promotes plastic deformation in material surrounding the advancing crack front for a given level of $\bar{K}$. Thus, T-stress alters the 3D, elastic-plastic fields. Remote from the immediate crack front, the material experiences plane-stress conditions with a diminishing impact expected for the T-stress. The previous study by Kim et al. [48] employs the 3D SSY framework for a stationary crack with T-stress loading and suggests the correctness of the functional relationship in Eqn. (5.5). They find non-zero T-stress values expand the plastic zone size along the entire crack front at both low ($\bar{K} = 1$) and relatively higher ($\bar{K} \approx 3.2$) loading levels. The T-stress has a strong influence on the opening-mode stress ahead of the crack front for the lower loading but has less effect for the higher loading.

Using new numerical results obtained in this study, Section 5.5 demonstrates the 3D self-similarity relationships characterized by $\bar{K}$ and $\bar{T}$ in Eqn. (5.5) during steady crack growth. The computations consider T-stress values imposed during steady crack advance of $\bar{T}$ =+0.25, 0, −0.25, and −0.50, that represent a wide-range of conditions present in test-specimens and structural components. The new numerical results focus on $\bar{K} = 1$ and $\bar{K} = 3$ loading levels that generate plastic zone sizes on the crack plane at mid-thickness of about $0.25B$ and $2.3B$, respectively, for the $T = 0$ condition.

5.3 Numerical Procedures

This section summarizes numerical procedures employed in the steady crack growth analyses to generate results shown in the following sections. Chapter 4 provides a more complete description. Section 5.3.1 highlights the aspects of crack extension analyses at steady state that differ from traditional finite element analyses of the 3D SSY model, particularly the integration along straight streamlines located parallel to crack plane that invokes time-distance equivalence. Section 5.3.2 presents the finite element discretization of the 3D SSY framework constructed to define straight streamlines passing through Gauss integration points of the isoparametric brick elements. Section 5.3.3 briefly considers the elastic-plastic material properties and computational operations executed at Gauss points.

5.3.1 Computational framework for steady-state crack growth

The special purpose finite element code, FIREFLY, implements the computational framework adopted to model steady-state crack growth. This software incorporates the temporal-spacial relationship between quantities ($\bullet$) on streamlines – lines parallel to the crack growth direction – first employed in steady crack growth studies in plane stress/strain studies by Dean and Hutchinson [21]:

$$\frac{\partial\,(\bullet)}{\partial t} = -\dot{a}\frac{\partial\,(\bullet)}{\partial X}\ . \tag{5.6}$$

The crack advances steadily in positive X-direction at constant velocity, $\dot{a}$. Equation (5.6) indicates that translation opposite to crack advance ($dX < 0$) along straight streamlines at fixed time is equivalent to time progression for a fixed material point. Consequently, the solution procedures that employ the material integration scheme of Dean and Hutchinson [21] adopt finite element models with element meshes designed to have streamline pass through Gauss points. Equation (5.6) implies use of the small strain-displacement relations to maintain straight streamlines; otherwise, material point trajectories become curved on approaching the crack front.

Equation (5.6) describes the essential difference between conventional analyses of a stationary crack and analyses for the steadily advancing crack – streamline integration of the elastic-plastic, constitutive rate equations. Several studies detail implementation of the streamline updating procedure within a finite element framework [117, 21, 78, 83, 81]. The 3D steady-growth model significantly increases the computational requirements for integration along streamlines: many "planes" of streamlines exist over the thickness in the 3D model (2D models have one such plane), and the constitutive equations are 3D not plane strain. The stress-updating procedure at Gauss points along a single streamline must occur sequentially, *e.g.* from right to left in Fig. 5.1, but the processing of different streamlines may occur concurrently. The FIREFLY program exploits this feature by the simultaneous evaluation of multiple streamlines through parallel code/data design and execution using the OpenMP (thread-parallel, shared-memory) paradigm. Benchmarking of FIREFLY analyses indicate that the overall streamline integration procedure requires insignificant overhead (stop/start of threads) and maintains a high level of parallel efficiency. As partial verification of FIREFLY, Chapter 4 shows that the near-front stresses within a plane-strain framework (3D model with plane-strain displacement boundary conditions over the thickness) substantially match asymptotic analyses and earlier plane-strain finite element solutions.

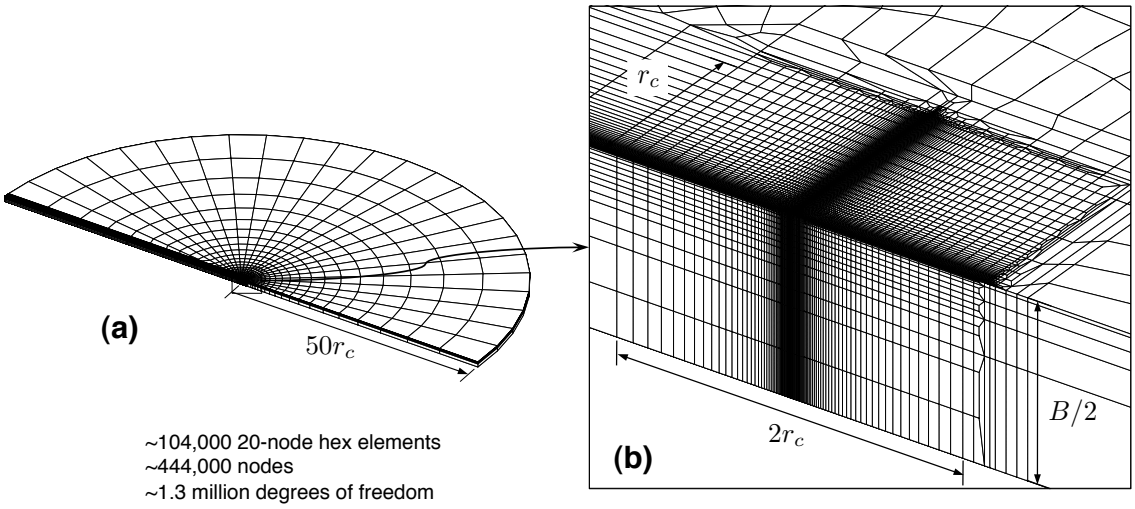

Figure 5.2: Finite element model for steady crack growth analyses composed of 20-node hex elements. Elements over the thickness and near the crack front are rectangular prisms to support the definition of streamlines along Gauss points. Plastic deformation does not extend outside of this region.

5.3.2 Finite element model

The steady-state formulation for sustained ductile tearing requires a finite element mesh designed for integration of the material response along straight streamlines, as shown in Fig. 5.2. Critically, the element arrangement must enable streamlines in the crack growth direction to be defined through the Gauss points. The streamlines extend parallel to the X-axis from r_c ahead of the crack front to the far-field boundary at $-50r_c$ and exist within the region bounded by $|Y| \leq r_c$ and $|Z| \leq B/2$. Elements outside the streamline region must not yield during the steady crack growth solution.

In the present model, the crack front lies along the Z-axis and extends through the thickness from $-B/2 \leq Z \leq B/2$. Equations (5.1) and (5.2) provide the radial and angular variation for the remotely applied displacements on the 3D SSY boundary for a given combination of K_I and T. The remote mode I loading leads to two symmetry planes ($Y = 0$ and $Z = 0$) that reduce meshing as indicated in Fig. 5.2.

In the $X - Y$ plane, mesh refinement reaches the maximum level near the crack front over the region $|X| \leq r_c \cup |Y| \leq r_c$ that contains streamlines. Larger elements connect these fine-scaled elements to the remote boundary, and a well-defined transition region smoothly links the finer and coarser mesh regions. Regions that contain streamlines have 15 layers of 20-node hex elements with significantly greater refinement near the free surface ($Z/B = 0.5$) than near the centerplane. Five sets of three thickness layers each merge into five total thickness layers farther from the crack front and outside of the region that deforms plasticity. Here, a nearly 2D plane stress response develops, and the additional through-thickness element layers are

unnecessary. The 20-node hex elements adopted here require full integration ($3 \times 3 \times 3$) of the element stiffness matrices to prevent severe, hour-glass deformation modes otherwise present in analyses with reduced integration ($2 \times 2 \times 2$).

5.3.3 Material response

Incremental J_2-theory, applicable for structural metals (aluminums, titaniums, and steels), describes the 3D elastic-plastic response in these analyses. The yield surface expands isotropically to model hardening with the uniaxial flow response ($\sigma - \varepsilon$) defined by

$$\left(\frac{\sigma}{\sigma_0}\right)^n = \left(\frac{\varepsilon}{\varepsilon_0}\right), \qquad \varepsilon \geq \varepsilon_0 \ . \tag{5.7}$$

The quantities σ_0 and ε_0 set the uniaxial yield stress and yield strain, respectively. The constant exponent, n, characterizes the hardening rate. Linear-elastic response prior to yielding and while unloading once the crack passes is described by Young's modulus, $E = \sigma_0/\varepsilon_0$, and Poissons' ratio, ν. All analysis results shown in the present work have $E/\sigma_0 = 250$, $n = 10$, and $\nu = 0.33$.

Chapter 4 describes details of the numerical procedures for streamline integration and for integration of the constitutive plasticity rate equations at each Gauss point. The accuracy for the elastic-predictor, radial-return algorithm decreases with certain strain increments as inputs [49]. The FIREFLY code implements a mix of sub-stepping and stress extrapolation techniques to limit the effect of truncation errors (as shown in [16]) during numerical integration of the constitutive relations.

5.4 *T*-Stress Constraint Effects on Active Yielding

The shape and size of the active plastic zone reflect the varying levels of triaxiality generated by the T-stress. The active yielding regions for the simpler, plane-strain SSY condition illustrate the expected effects in the 3D SSY solutions. Figure 5.3 displays (in a half-symmetric image) the active yielding regions during steady crack growth for three levels of imposed $T/\sigma_0 = 0, +0.25$, and -0.25. Similarity scaling of the elastic-plastic fields holds in plane strain for the normalized coordinates ($X/(J/\sigma_0)$, $Y/(J/\sigma_0)$). Each figure depicts two key dimensions, r_{p0} and h_{pw}, that describe the active plastic zone. The extent of active yielding above the crack plane, h_{pw}, represents the height for the trailing plastic wake. The distance r_{p0} denotes the extent of active yielding on the crack plane ahead of the advancing front. For the plane-strain conditions illustrated in Fig. 5.3, the comparatively small $T/\sigma_0 = +0.25$ causes a reduction in h_{pw} and a counterclockwise rotation of the plastic zone. Negative T-stress of the same magnitude has a much greater effect of expanding the

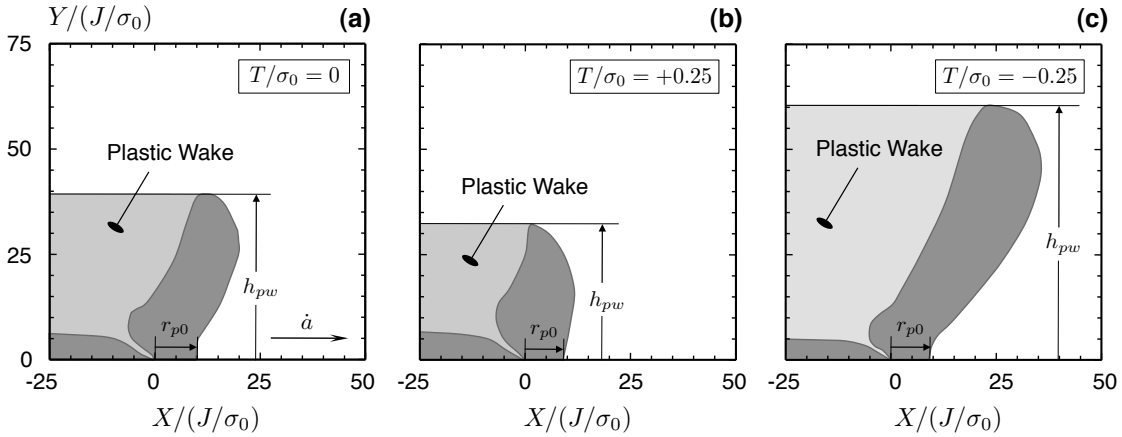

Figure 5.3: Active yielding regions for steadily advancing crack under plane-strain conditions for imposed T/σ_0 levels: $0.0, +0.25$, and -0.25. This figure defines the extent of active yielding above the crack plane (also the plastic wake height), h_{pw}, and the extent of yielding ahead of the advancing crack front on the crack plane, r_{p0}.

plastic zone size and height above the crack plane, Fig. 5.3(c).

Varias and Shih [117] link differences in h_{pw} and r_{p0} to constraint effects that develop from imposed T-stress during steady crack growth and to their role in crack-tip energy balance (see Eqn. (4.10) in Freund and Hutchinson [32] and related discussion). Elastic strain energy becomes trapped within the plastic wake during steady crack advance and cannot alter crack-front inelastic deformation. For a constant applied loading in plane strain, $J = K_I^2\left(1-\nu^2\right)/E$, larger plastic wakes (increasing h_{pw}) under varying T-stress levels remove energy that otherwise would be available for near-front loading. Thus, the T-stress effect limits the amount of plastic deformation ahead of the advancing crack front (reduces r_{p0}). The magnitudes of near-front field quantities – displacements, strains, and stresses – therefore decrease under the imposed T-stress, both positive and negative, as Varias and Shih [117] demonstrate. Based on these results, Varias and Shih [117] employ a ductile fracture criterion for continued growth – the crack tip opening angle – and determine that the steady-state, apparent toughness reaches a minimum value under a zero T-stress loading.

For a steadily advancing crack in 3D SSY, the two dimensions r_{p0} and h_{pw} may vary over the thickness and with different trends for the loading levels $\bar{K}$ and $\bar{T}$. Tables 5.1 and 5.2 list values of r_{p0} and h_{pw} normalized with two different length-scales for comparison: B and J/σ_0, where J follows from the plane-stress K_I displacements imposed on the remote boundary ($J = K_I^2/E$). The tables provide values for $\bar{K} = 1$ and 3, and four T-stress levels ($T/\sigma_0 = +0.25, 0, -0.25, -0.5$) at each $\bar{K}$ value. The tables list the normalized plastic zone sizes in three planes at locations (Z/B) over the crack front: mid-thickness ($= 0.0$), the outside surface ($= 0.5$), and a plane near the outside surface ($= 0.4$).

	$T/\sigma_0 = +0.25$		$T/\sigma_0 = 0$		$T/\sigma_0 = -0.25$		$T/\sigma_0 = -0.50$	
$\bar{K} = 1$	$r_{p0}/\left(J/\sigma_0\right)$	r_{p0}/B	$r_{p0}/\left(J/\sigma_0\right)$	r_{p0}/B	$r_{p0}/\left(J/\sigma_0\right)$	r_{p0}/B	$r_{p0}/\left(J/\sigma_0\right)$	r_{p0}/B
$Z/B = 0$	87.9	0.352	61.8	0.247	49.5	0.198	41.3	0.165
$Z/B = 0.4$	58.6	0.234	53.3	0.213	51.9	0.201	48.1	0.192
$Z/B = 0.5$	54.3	0.217	0.3	0.001	0.2	0.001	0.2	0.001
$\bar{K} = 3$	$r_{p0}/\left(J/\sigma_0\right)$	r_{p0}/B	$r_{p0}/\left(J/\sigma_0\right)$	r_{p0}/B	$r_{p0}/\left(J/\sigma_0\right)$	r_{p0}/B	$r_{p0}/\left(J/\sigma_0\right)$	r_{p0}/B
$Z/B = 0$	68.2	2.45	63.6	2.29	62.1	2.24	60.4	2.17
$Z/B = 0.4$	68.2	2.45	63.6	2.29	60.4	2.17	58.6	2.11
$Z/B = 0.5$	70.2	2.53	64.7	2.33	62.1	2.24	58.6	2.11

Table 5.1: Extent of the active yielding region (r_{p0}) on the crack plane ($Y = 0$) during steady crack advance in 3D SSY at three through-thickness locations, Z/B =0, 0.4, and 0.5. Distances are normalized by the far-field value of J/σ_0 and by the thickness, B. Results are shown for $\bar{K} = 1$ and for $\bar{K} = 3$ at four values of imposed T/σ_0: $+0.25, 0, -0.25$, and -0.50.

Several general observations are readily apparent from the tables:

- The maximum extent of the plastic zone on the centerplane for $\bar{K} = 1$ loading at all T-stress levels remains a fraction of the plate thickness: $r_{p0}/B = 0.35$ and $h_{pw}/B = 0.44$.
- The minimum extent of the plastic zone on the centerplane for $\bar{K} = 3$ loading at all T-stress levels exceeds the plate thickness: $r_{p0}/B = 2.2$ and $h_{pw}/B = 1.4$.
- The through-thickness variations of r_{p0} and h_{pw} nearly vanish for $\bar{K} = 3$ at all T-stress levels.
- For $\bar{K} = 1$ loading, r_{p0} effectively vanishes at the outside surface for zero and negative T-stress values. r_{p0} is notably larger at mid-thickness for $T/\sigma_0 = +0.25$, and retains a comparable value over the thickness including at the outside surface. r_{p0} at mid-thickness decreases monotonically with increasingly negative T-stress.
- For $\bar{K} = 1$ loading, h_{pw} has the largest values at mid-thickness and the outside surface, with the smallest mid-thickness value developing for the zero T-stress loading.

For these $\bar{K}$ and $\bar{T}$ loadings, negative (positive) T-stress reduces (increases) the extent of active yielding on the crack plane (r_{p0}) over the thickness compared to the corresponding yielded region for a zero T-stress. At low-load levels with pronounced 3D effects ($\bar{K} = 1$), $r_{p0}/\left(J/\sigma_0\right)$ varies strongly through the thickness with higher values at the centerplane ($Z/B = 0$) than near the free surface ($Z/B = 0.5$). Positive T-stress increases $r_{p0}/\left(J/\sigma_0\right)$, especially near the free surface under $\bar{K} = 1$ loading where the slightly higher (biaxial) stress enables the plastic zone to expand significantly farther ahead of the crack front.

Plastic wake heights behind the steadily advancing crack in the 3D SSY framework – shown in Table 5.2 – largely follow the earlier plane-strain trends in [117]. Negative T-stress expands the plastic zone size above

	$T/\sigma_0 = +0.25$		$T/\sigma_0 = 0$		$T/\sigma_0 = -0.25$		$T/\sigma_0 = -0.50$	
$\bar{K} = 1$	$h_{pw}/(J/\sigma_0)$	h_{pw}/B	$h_{pw}/(J/\sigma_0)$	h_{pw}/B	$h_{pw}/(J/\sigma_0)$	h_{pw}/B	$h_{pw}/(J/\sigma_0)$	h_{pw}/B
$Z/B = 0$	75.2	0.301	73.2	0.293	83.1	0.332	109.7	0.439
$Z/B = 0.4$	47.1	0.189	48.2	0.193	61.4	0.246	109.7	0.439
$Z/B = 0.5$	61.4	0.246	66.4	0.266	86.5	0.346	137.0	0.548
$\bar{K} = 3$	$h_{pw}/(J/\sigma_0)$	h_{pw}/B	$h_{pw}/(J/\sigma_0)$	h_{pw}/B	$h_{pw}/(J/\sigma_0)$	h_{pw}/B	$h_{pw}/(J/\sigma_0)$	h_{pw}/B
$Z/B = 0$	42.5	1.53	38.0	1.37	50.1	1.81	89.8	3.23
$Z/B = 0.4$	45.3	1.63	42.0	1.51	54.3	1.95	91.9	3.31
$Z/B = 0.5$	47.1	1.70	44.6	1.61	55.5	2.00	91.9	3.31

Table 5.2: Heights of the plastic wake (h_{pw}) during steady crack advance in 3D SSY at three through-thickness locations, Z/B =0, 0.4, and 0.5. Distances are normalized by the far-field value of J/σ_0 and by the thickness, B. Results are shown for $\bar{K} = 1$ and for $\bar{K} = 3$ at four values of imposed T/σ_0: $+0.25, 0, -0.25$, and -0.50.

the uncracked plane beyond the zero T-stress level, whereas positive T-stress shows the same but smaller effect. In general, triaxiality loss near the free surface generates a response more characteristic of plane stress that exhibits higher h_{pw} values; conversely, the higher triaxiality that develops at the plate interior leads to lower h_{pw} values. In contrast with the plane-strain solution shown in Fig. 5.3(b) and the general 3D SSY trends, the $\bar{T} = +0.25$ loading for $\bar{K} = 1$ slightly increases h_{pw} at $Z/B = 0$ and reduces h_{pw} approaching the outside surface.

Relative to J/σ_0, the plastic wake height shrinks at higher loading levels. Here, the active yielding region approaches the plane-stress shape through a more uniform h_{pw} over the thickness and by reduction of h_{pw} relative to r_{p0}. In contrast, the more plane-strain conditions for $\bar{K} = 1$ loading produce a plastic zone shape closer to those shown in Fig. 5.3 with $h_{pw} > r_{p0}$.

In summary, the effects of T-stress at the smaller loading, $\bar{K} = 1$, reflect the general trends found for plane-strain conditions. At higher loading, $\bar{K} = 3$, the plastic zone becomes large relative to the thickness with much of the plastic zone volume in a plane-stress or approaching a plane-stress condition (more on this in the next section), and the T-stress then has less impact.

5.5 Similarity Scaling in 3D SSY of Steady Crack Growth

This section expands the prior work of Chapter 4 on similarity scaling of the near-front fields to include varying in-plane constraint effects through application of non-zero T-stress loads. The earlier study considers only $\bar{T} = T/\sigma_0 = 0$ and demonstrates that the non-dimensional loading parameter $\bar{K} = K_I/\sigma_0\sqrt{B}$ describes a similarity scaling for the near-front fields. This section examines opening-mode stress values (σ_{yy}) at the centerplane ($Z/B = 0$) and near the free surface ($Z/B = 0.495$) on the crack plane and the angular variation at a constant, scaled radial distance from the front. These results demonstrate the proposed similarity

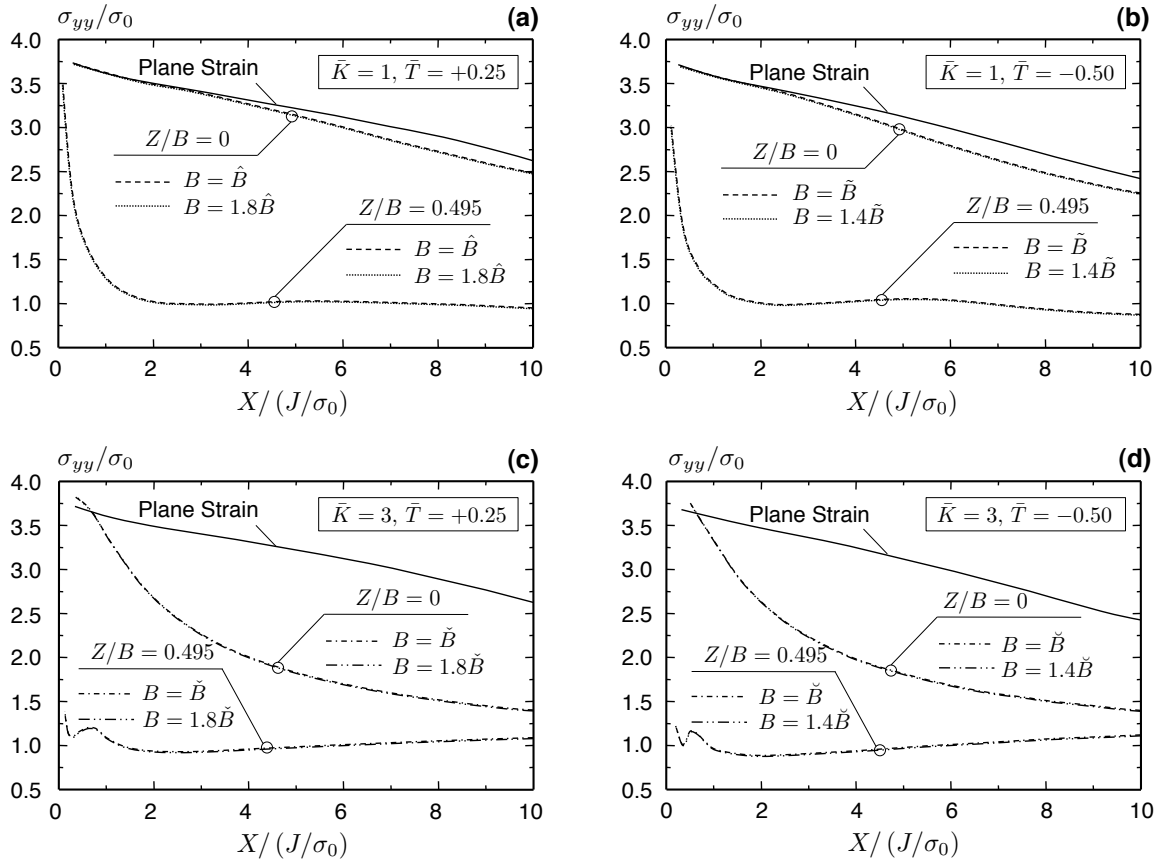

Figure 5.4: Normalized values of opening-mode stress, σ_{yy}/σ_0, with scaled physical distance from the crack front, $X/\,(J/\sigma_0)$, along the crack plane ($\theta = 0°$) ahead of the steadily growing crack front. Results are shown at mid-thickness ($Z/B = 0$) and near the outside surface ($Z/B = 0.495$). The steady-growth, plane-strain solution at each $\bar{T}$ value is shown for reference. Essentially identical stresses obtained with different values for the thickness, B, but the same value of the non-dimensional parameters $\bar{K} = K_I/\sigma_0\sqrt{B}$ and $\bar{T} = T/\sigma_0$ indicate self-similarity of this stress component.

scaling in Eqn. (5.5) applies for both positive and negative T-stress values at constant $\bar{K}$. That is, when the far-field loading (K_I and T), plate thickness (B) and yield stress (σ_0) vary but maintain the same ($\bar{K}$, $\bar{T}$) loading values, the crack-front fields remain unchanged in terms of the normalized coordinates, as reflected in Eqn. (5.5) (E/σ_0, Poisson's ratio and the hardening response must remain unchanged).

Figure 5.4 displays the normalized opening-mode stresses (σ_{yy}/σ_0) over the scaled distance $0 \le X/\,(J/\sigma_0) \le 10$ ahead of the advancing crack front for non-dimensional load levels ($\bar{K} = K_I/\sigma_0\sqrt{B} = 1, 3$ and $\bar{T} = T/\sigma_0 = +0.25, -0.50$). Each subfigure shows the near-front stresses at the two crack-front locations obtained from two finite element analyses, where each analysis refers to a different plate thickness. The applied loading level K_I varies with the plate thickness to maintain a constant value of $\bar{K} = 1$ or 3. In Fig. 5.4(a), for example, the first analysis has an applied loading of $K_I = \hat{K}_I$ on the 3D SSY model with a thickness $B = \hat{B}$;

for the second analysis, the applied loading increases to $K_I \simeq 1.34\hat{K}_I$ with $B = 1.8\hat{B}$, which leads to $\bar{K} = 1$ in both analyses. The range of values selected for K_I, T, and B in Fig. 5.4 insure the plastic zones remain confined to the small mesh region described in Section 5.3.2. For reference, the figures also include the opening-mode stresses at the two values of $\bar{T} = +0.25, -0.50$ under plane-strain conditions. Within the steady-growth context, Varias and Shih [117] show the invariance of near-front fields in scaled coordinates (*e.g.*, $r/(J/\sigma_0)$) for a specified non-zero value of the imposed T-stress.

Under these 3D SSY conditions, near-indistinguishable differences appear between the opening-mode stresses in the different analyses for each $(\bar{K} - \bar{T})$ pair in Figs. 5.4(a-d). This result demonstrates the similarity scaling in terms of the two non-dimensional loading parameters $\bar{K}$ and $\bar{T}$. Although not shown, other components of stress and the strain components also exhibit the same scaling with $\bar{K}$ and $\bar{T}$.

In comparing Figs. 5.4(a-b), only small differences occur between opening-mode stresses for $T/\sigma_0 = +0.25$ and -0.50 at the centerplane and the outside surface, including the plane-strain, steady-growth solutions for the two T-stress levels. Figure 4.7(a) of Chapter 4 shows that the 3D and plane-strain stresses during steady growth for $T/\sigma_0 = 0$ are slightly larger than those here for $T/\sigma_0 = -0.50$ but closely match the $T/\sigma_0 = +0.25$ stresses. Figure 3 in [48] examines the same stress distributions on the centerplane for a stationary, sharp crack front in 3D SSY with varying T-stress. In sharp contrast to the present steady-growth results, opening-mode stresses for the stationary crack decrease rapidly with increasingly negative T-stress levels and reveal small increases for positive T-stress.

At the higher loading, $\bar{K} = 3$, Figs. 5.4(c-d) effectively show no influence on the crack-plane opening stresses for $T/\sigma_0 = +0.25$ and -0.50. The centerplane stress levels decrease significantly at this higher loading level. The more plane-stress regions of the plastic zone lie outside normalized distances of $X/(J/\sigma_0) \gtrsim 2$. Centerplane stresses very near the crack front, $X/(J/\sigma_0) \lesssim 0.5$, attain near plane-strain levels. Figure 4.7(b) of Chapter 4 for the 3D SSY steady-growth solution with $\bar{K} = 3$ and $T/\sigma_0 = 0$ shows crack-plane opening stresses essentially identical to those here. Figure 8 in [48] reveals a modest reduction of the crack-plane, opening-mode stresses (due to the negative T-stress) for the 3D SSY stationary crack at mid-thickness under a higher, $\bar{K} \approx 3.2$, loading. At the outside surface, Fig. 10 in [48] shows T-stress, positive and negative, has no effect on the opening stresses.

Figure 5.5 presents values of stress component (σ_{yy}/σ_0) surrounding the steadily advancing crack front $(0 \leq \theta \leq 180^\circ)$ at a constant scaled radial distance, $r/(J/\sigma_0) = 5$, for load levels $\bar{K} = 1$, 3 and $\bar{T} = +0.25$, -0.50. These results again focus on stress levels at the mid-thickness $(Z/B = 0)$ and near the free surface $(Z/B = 0.495)$. Stress distributions are shown for two analyses in each subfigure with different thicknesses, but identical $\bar{K}$ values, to demonstrate the continued similarity scaling in Eqn. (5.5). The stresses for plane-

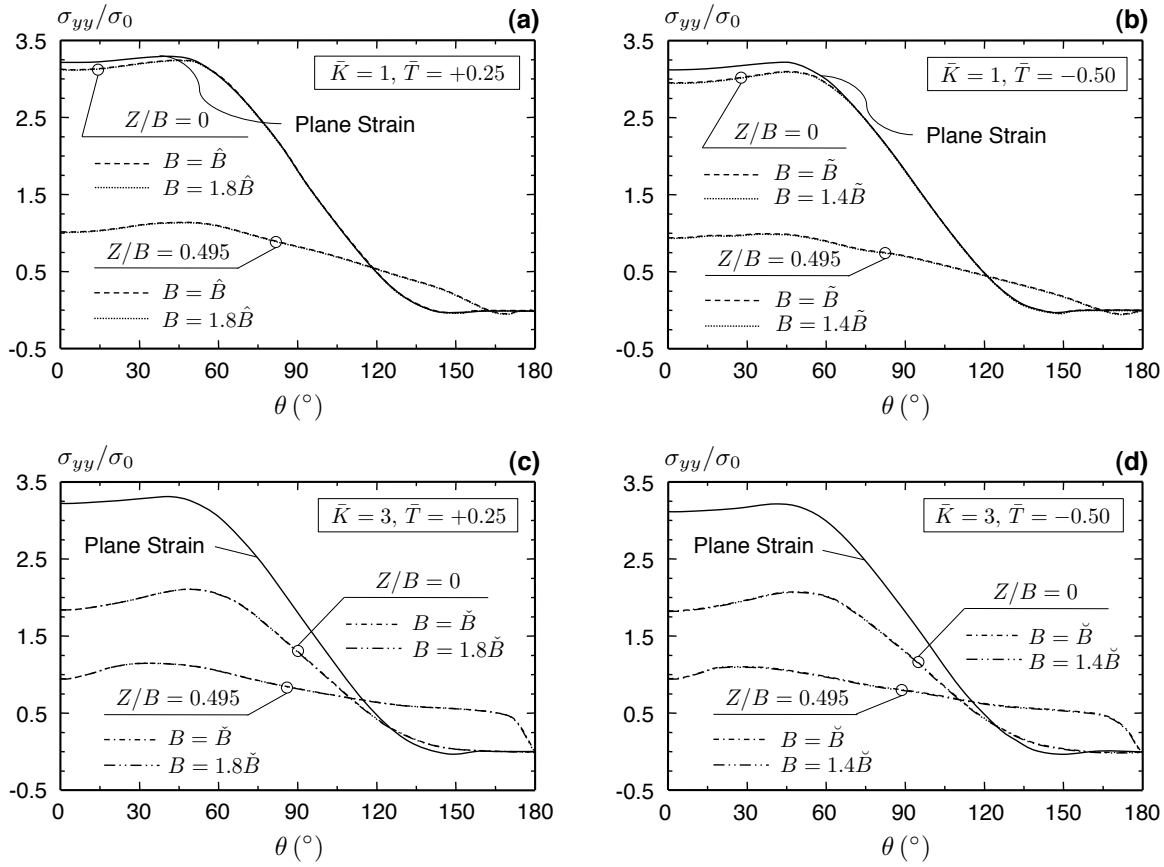

Figure 5.5: Normalized values of stress component, σ_{yy}/σ_0 around the steadily growing crack front at constant radial location ($r/\left(J/\sigma_0\right) = 5$). Results are shown at mid-thickness ($Z/B = 0$) and near the outside surface ($Z/B = 0.495$). The steady-growth, plane-strain solution at each $\bar{T}$ value is also shown for reference. Essentially identical stress distributions obtained with different values for the thickness, B, but the same value of the non-dimensional parameters $\bar{K} = K_I/\sigma_0\sqrt{B}$ and $\bar{T} = T/\sigma_0$ indicate self-similarity of this stress component.

strain conditions are also shown for reference at two values of $\bar{T}$. Near-indistinguishable differences develop between the opening-mode stresses for analyses with thickness changes at the same loading levels in Figs. 5.5(a-d), thus demonstrating the similarity scaling in terms of $\bar{K}$ and $\bar{T}$. The remaining stress components and the strain components also exhibit the same scaling with $\bar{K}$ and $\bar{T}$.

5.6 *T*-Stress Effects on Three-Dimensional fields

This section describes T-stress effects on key stress and strain fields often employed to compute values for micromechanical failure models. The results in Section 5.5 and the functional relationship of Eqn. (5.5) indicate that each field component varies radially ($r/\left(J/\sigma_0\right)$), angularly ($\theta$), and through the thickness (Z/B)

for each combination of the applied loading level $\bar{K}$ and $\bar{T}$. To provide specific examples of potentially useful fields in a compact form, this section limits consideration to the $\bar{K} = 1$ loading (which has strong 3D and T-stress effects), and to the principal stresses and the equivalent plastic strain.

5.6.1 *T*-stress effect on the maximum principal stress and equivalent plastic strain

Figure 5.6 presents the normalized (maximum) principal stress (σ_1/σ_0) with normalized radial distance ($r/(J/\sigma_0)$) surrounding the steadily advancing crack front. The imposed T-stress values range over $\bar{T}$ =+0.25, 0, -0.25, and -0.5 for loading $\bar{K} = 1$. The figure shows values at two locations across the crack front – along the crack plane and along two radial lines ($\theta = 27°$ and $54°$). For reference, the figure includes the principal stresses for the $\bar{T} = 0$ configuration in plane strain. The radial dimensions in Fig. 5.6 lie deep within the 3D active yielding region; $r/(J/\sigma_0) = 20$ corresponds to one-third of the distance from the crack front to the plastic zone boundary on the crack plane (r_{p0}), as Table 5.1 indicates. Figure 5.7 shows the equivalent plastic strain values, $\bar{\varepsilon}^p = \int \sqrt{\frac{2}{3}\dot{\varepsilon}^p_{ij}\dot{\varepsilon}^p_{ij}}dt$, along the same radial lines, at the same loading levels, and through-thickness locations examined in Fig. 5.6.

The largest principal stress plays a key role in stress-controlled failure models of the micromechanical fracture process. Specifically, the Weibull stress model [10] for probabilistic cleavage prediction of ferritic steels directly incorporates σ_1/σ_0 into the "local" driving force description along the crack front. In the context of a crack front tearing by a ductile fracture mechanism, cleavage frequently intervenes in the mid-to-upper region of the ductile-to-brittle, temperature transition (see review article by Pineau [87]). At least two effects contribute to this phenomena: (1) additional material sampled at high stress levels as the crack front pushes forward increases the probability of encountering a critical, triggering particle, and (2) an increase in the intensity of the stress fields caused by the ductile tearing process, where the stationary crack fields and those during early stages of tearing often exhibit relatively low constraint [41, 46, 35, 98, 34]. The 3D steady-growth fields here enable the stress-intensification role to be examined during ductile crack advance characteristic of test specimens and components that impose a range of T-stress values.

The results shown in Fig. 5.6 are for an "aluminum-like" alloy ($E/\sigma_0 = 250$, $\nu = 0.33$, and $n = 10$), but the broader trends should remain applicable to other flow properties. For the $\bar{K} = 1$ loading, σ_1/σ_0 tends to the $\bar{T} = 0$, plane-strain values quite near the advancing crack front for the considered levels of imposed T-stress. Thus, once the crack front propagates outside of the initially blunted region of the stationary crack, resharpens, and reaches steady or near steady-state ductile growth, the specimen or component's T-stress appears to have minimal impact on the cleavage fracture process zone, typically $r/(J/\sigma_0) \leq 5$

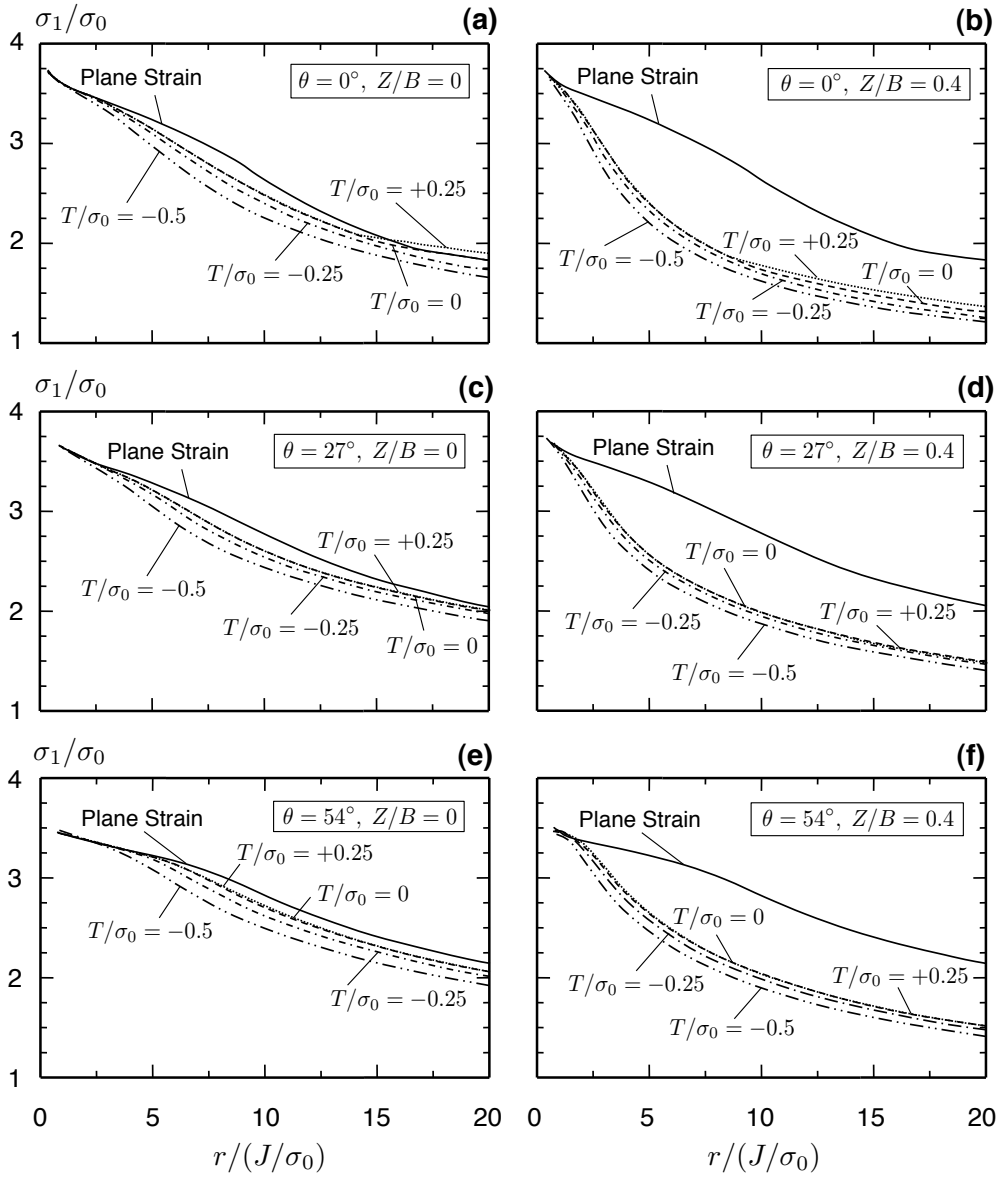

Figure 5.6: Normalized values of the first (maximum) principal stress component, σ_1/σ_0, with scaled radial distance under $\bar{K} = 1$ loading and four levels of $\bar{T}$ =+0.25, 0, -0.25, and -0.5. Results are given along three radial lines from the crack front at two through-thickness locations. The steady-growth, plane strain solution at $\bar{T} = 0$ is also presented for reference.

where $\sigma_1/\sigma_0 \gtrsim 3.0$. Further studies using the 3D framework of steady-state crack growth remain to quantify T-stress effects on the Weibull stress model for typical ferritic steels.

Figure 5.6 indicates the strong effect of through-thickness location on the principal stress values. At the centerplane ($Z/B = 0$), high triaxiality enables the principal stress to reach plane-strain levels very near the crack front, but σ_1/σ_0 decreases strongly near the free surface ($Z/B = 0.4$). Lower principal stress values at $Z/B = 0.4$ reflect significantly lower triaxiality away from the mid-thickness region.

On the centerplane, the principal stresses along constant angular rays ($|\theta| = 0$, 27°, and 54°) all lie below the plane-strain, T=0 solution, exhibit small differences on the three rays, and decrease with more negative T-stress. At mid-thickness, an angular wedge of comparatively high stresses (even for large, negative T-stress) thus pushes forward ahead of the crack front.

Plastic strains generally impact the local driving force measures for micromechanical models of ductile fracture, *e.g.* void nucleation-growth-coalescence [37]. In Fig. 5.7(a-c-e), plastic strains at the centerplane remain quite similar along the $\theta = 0$ and $\theta = 27°$ rays. Values are larger than plane-strain ($\bar{T} = 0$) levels and increase with more positive values of imposed T-stress. The $\theta = 54°$ radial line approaches the usual orientation of maximum shear strain around the crack front, and here shows the following: larger plastic strains extending to greater distances from the front, increasing values near the crack front with more positive T-stress, and essentially matching plane-strain, $\bar{T} = 0$ levels for $r/(J/\sigma_0) < 3 - 5$. The plastic strain levels exceeding those of plane-strain conditions indicate a relative loss of triaxiality at the centerplane in the 3D SSY model. This trend agrees with those for the centerplane in Fig. 5.6 which show a smaller value of the maximum principal stress along the radial lines compared to plane-strain values. Figure 12 of Varias and Shih [117] indicates a reduction of $\bar{\varepsilon}^p$ for $\bar{T} = +0.5$ and $+1.0$ during plane-strain, steady growth, which contrasts with the current results for $\bar{K} = 1$ loading in 3D SSY. The plane-strain solutions maintain the highest possible out-of-plane constraint and thus experience less impact from a positive T-stress.

Levels of plastic strain intensify at the $Z/B = 0.4$ crack-front location, well-above centerplane and plane-strain values as shown in Fig. 5.6(b-d-f). The maximum principal stress, and thus triaxiality along these radial lines on $Z/B = 0.4$, shows a sharp reduction, which supports the increased levels of plastic strain. The trend of increasing plastic strain with increasingly positive T-stress continues in these results at $Z/B = 0.4$.

In summary, Figs. 5.6 and 5.7 describe a clear picture of high stress triaxiality (but below plane-strain levels), with relatively small plastic strains in an angular wedge advancing ahead of the crack front at mid-thickness. At the $Z/B = 0.4$ crack front location near the outside surface, the response becomes one of comparatively low stress triaxiality. The maximum principal stress decreases sharply, well below plane-strain levels, with a corresponding increase in plastic strain levels well above plane-strain values. The examined

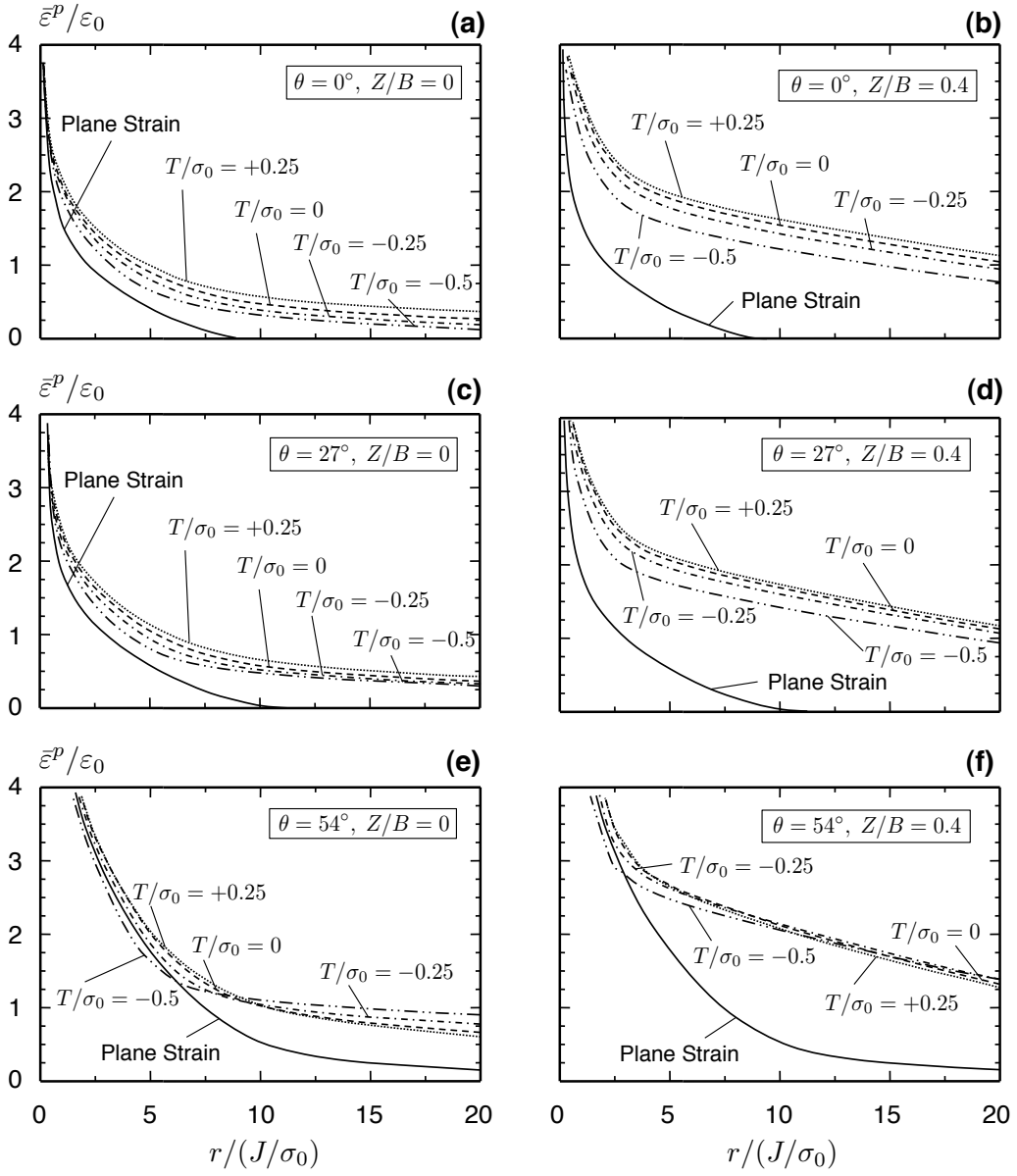

Figure 5.7: Normalized values of equivalent plastic-strain, $\bar{\varepsilon}^p/\varepsilon_0$, along radial lines from the crack front at two locations over the thickness. Distances are scaled by J/σ_0 (far field value). Applied loading is $\bar{K} = 1$ loading with four levels of: $\bar{T}$ =+0.25, 0, -0.25, and -0.5. The steady-growth, plane-strain solution at $\bar{T} = 0$ is also presented for reference.

T-stress values have similar effects at both crack-front locations: the maximum principal stress and plastic strain values both increase (decrease) with more positive (negative) values of T-stress.

5.6.2 Effect of T-stress on crack-plane principal stresses

Figure 5.8 presents the values of normalized principal stresses (σ_1/σ_0, σ_2/σ_0, and σ_3/σ_0) with normalized radial distance ($r/(J/\sigma_0)$) on the crack plane ($\theta = 0°$). The imposed T-stress values again range over $\bar{T}$ =+0.25, 0, -0.25, and -0.5. Only $\bar{K} = 1$ loading is considered. The figure includes the plane-strain, principal stresses for a $\bar{T} = 0$ configuration.

The three principal stresses in Fig. 5.8 quantify the complete stress state for a steadily advancing crack front at the through-thickness locations, $Z/B = 0$ and $Z/B = 0.4$, and over distances ahead of the crack front where microfailure processes become active. Over the uncracked plane ($Y = 0$), only four non-zero stress components can exist under a mode I loading due to symmetry conditions – the normal stresses σ_{xx}, σ_{yy}, and σ_{zz} plus the shear stress σ_{xz}. Further, symmetry restrictions on the centerplane and zero out-of-plane tractions over the free surface ($Z/B = 0.5$) require $\sigma_{xz} \to 0$ at these locations and limit $|\sigma_{xz}| \leq 0.4\sigma_0$ over the entire crack plane. Consequently, the principal stresses in Fig. 5.8 largely represent normal stress states, with a modest contribution from σ_{xz} at $Z/B = 0.4$. Also, the second and third principal stress remain significantly below the first principal stress, *e.g.* both $\sigma_2 < 3\sigma_0$ and $\sigma_3 < 3\sigma_0$ for all $0 \leq X/(J/\sigma_0) < 20$. For a stress-based failure mechanism requiring a threshold level to trigger fracture, *e.g.* $3\sigma_0$ for a cleavage fracture event, Fig. 5.8 implies that the first principal stress contributes predominantly to the local driving force for brittle fracture during steady crack growth.

As discussed in Section 5.6.1, crack front location (Z/B) has the largest impact on the stress state, followed by a modest influence from the imposed T-stress. Near mid-thickness, the first and second principal stresses approach plane-strain, $T = 0$ levels over $0 \leq X/(J/\sigma_0) \leq 20$, but the third principal stress remains lower than the plane-strain values. Here, the third principal stress indicates the out-of-plane stress, σ_{zz}, and signifies some triaxiality loss at the centerplane in the thin plate, even for $\bar{K} = 1$ loading. For all T-stress levels, the principal stress values in Fig. 5.8 decrease for $\bar{T} < 0$ compared to the $\bar{T} = 0$ case and remain essentially unchanged for $\bar{T} = +0.25$.

5.7 Void Growth During Sustained Ductile Tearing

Sustained ductile tearing develops in structural metals most often through void nucleation, growth under continued deformation, and eventual coalescence to link with the advancing crack front. This section exam-

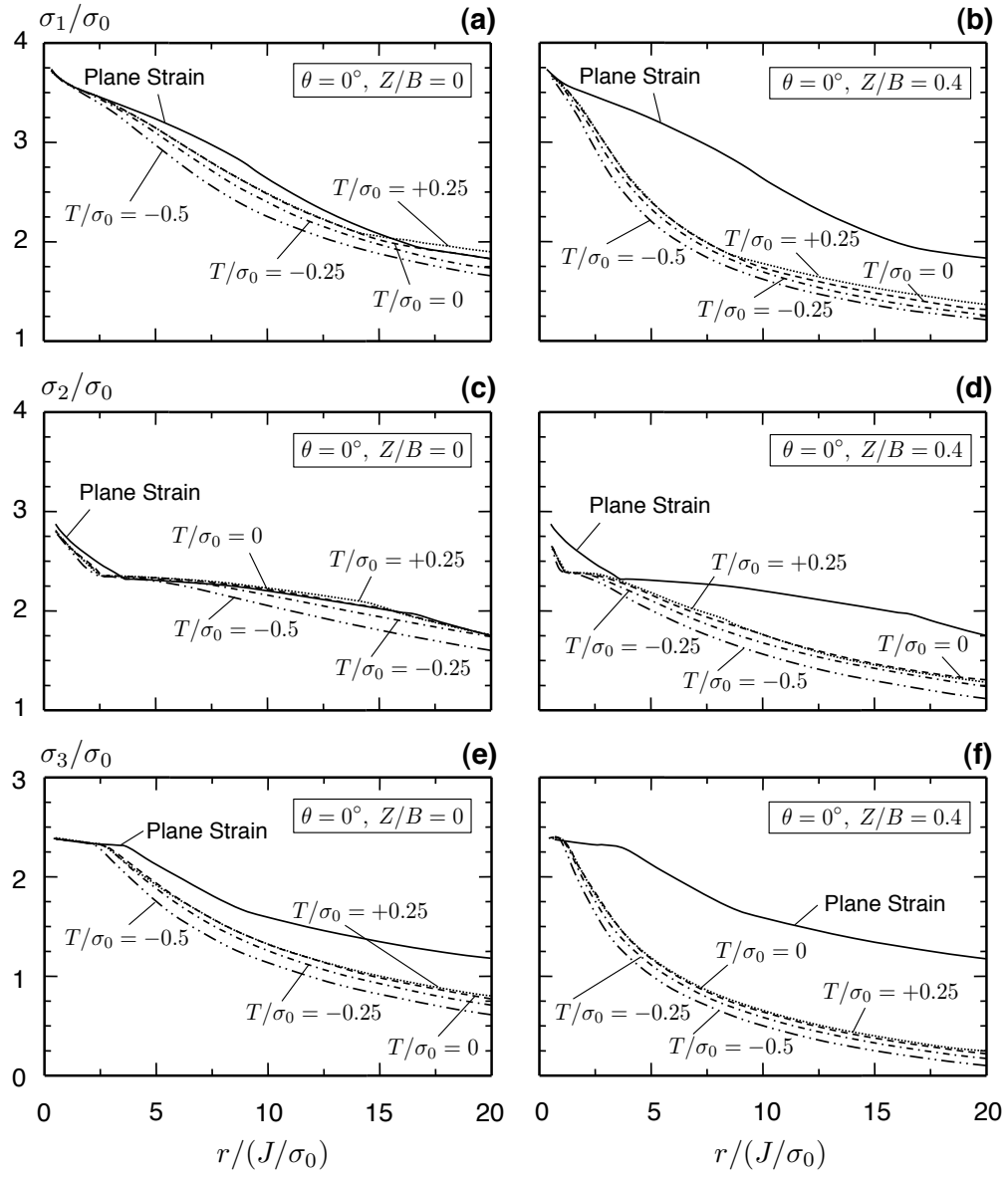

Figure 5.8: Normalized values of principal stress components – σ_1/σ_0, σ_2/σ_0, and σ_3/σ_0 – with scaled radial distance on the crack plane ($\theta = 0^\circ$). Results shown for $\bar{K} = 1$ loading and four levels of imposed $\bar{T}$ =+0.25, 0, -0.25, and -0.5. The steady-growth, plane-strain solution for $\bar{T} = 0$ is also presented for reference.

$K_I/\sigma_0\sqrt{B} = 1$

T/σ_0	$Z/B = 0$	$Z/B = 0.3$	$Z/B = 0.4$	$Z/B = 0.45$	$Z/B = 0.49$	$Z/B = 0.5$
+0.25	0.890	0.714	0.483	0.357	0.207	0.002
0	0.921	0.723	0.470	0.340	0.180	0
-0.25	0.870	0.661	0.416	0.304	0.148	0
-0.50	0.730	0.520	0.330	0.251	0.115	0

$K_I/\sigma_0\sqrt{B} = 3$

T/σ_0	$Z/B = 0$	$Z/B = 0.3$	$Z/B = 0.4$	$Z/B = 0.45$	$Z/B = 0.49$	$Z/B = 0.5$
+0.25	0.709	0.560	0.433	0.307	0.164	0.155
0	0.735	0.561	0.420	0.286	0.144	0.136
-0.25	0.721	0.542	0.396	0.260	0.122	0.115
-0.50	0.645	0.490	0.355	0.223	0.094	0.089

Table 5.3: Normalized values of void growth, ζ/ζ_{ref}, at the location $X/\left(J/\sigma_0\right) = 2.9$ for two loading levels: $\bar{K} = 1$ and $\bar{K} = 3$ for a range of T-stress values. Here, the normalizing void growth, $\zeta_{ref} = 0.0358$ at $X/\left(J/\sigma_0\right) = 2.9$, refers to a steadily advancing crack front in plane strain with zero T-stress.

ines the influence of imposed T-stress on 3D void growth rates ahead of the crack front. Section 5.7.1 casts a well-established void growth relationship into a form that facilitates integration along streamlines for the steady-state computational framework. Results described in Section 5.7.2 reveal loading effects – $\bar{K}$ and $\bar{T}$ – on void growth over the full crack plane in the 3D SSY model.

5.7.1 Void growth parameter computation at steady state

Rice and Tracey [92] examine the growth of an isolated, spherical void deforming within a rigid-plastic (Mises) material. At higher triaxiality levels experienced ahead of a crack front, spherical expansion exceeds elliptical deformation in a perfectly-plastic material under a remotely imposed tensile strain rate. Within a general strain field applied at the remote boundary of a void-containing volume, the void growth rate, $\dot{\rho}$, for a void with current radius, ρ, increases exponentially with the triaxiality level according to the well-known expression:

$$\frac{\dot{\rho}}{\rho} = \beta\dot{\bar{\varepsilon}}^p \exp\left(\frac{3\sigma_m}{2\sigma_e}\right). \tag{5.8}$$

Here, $\dot{\bar{\varepsilon}}^p$ denotes the equivalent plastic strain rate; σ_m defines the mean stress; and σ_e signifies the Mises stress. The non-dimensional constant, β, represents features of the remote strain field and lies between 0.275 (uniaxial compression) and 0.283 (uniaxial tension). The simplified expression of Eqn. (5.8) neglects some aspects of the ductile tearing process – material hardening, crack front interactions with voids, void coalescence mechanisms, nonuniform void spacing and shape, etc. [67, 44, 82]. Nevertheless, Eqn. (5.8) retains essential elements necessary for a first-order, local estimate of void growth suitable to understand T-stress effects on the ductile tearing process.

The present void growth calculations focus on the *relative* expansion of voids located on the crack plane, each with initial radius ρ_0 before the onset of plastic yielding at distance $X = X_{FF}$ ahead of the crack front. During steady crack growth, a time-distance relationship applies along streamlines, as shown in Eqn. (5.6), that produces a non-dimensional expression for ρ relative to ρ_0 at distance $X < X_{FF}$ from the crack front, *i.e.*,

$$\zeta\left(X\right) = \ln\left(\frac{\rho\left(X\right)}{\rho_0}\right) = \int_{X_{FF}}^{X} \beta \frac{\partial \bar{\varepsilon}^p}{\partial \lambda} \exp\left(\frac{3\sigma_m}{2\sigma_e}\left(\lambda\right)\right) d\lambda, \tag{5.9}$$

where the loading level, $\bar{K} = K_I/\sigma_0\sqrt{B}$, and imposed T-stress, $\bar{T} = T/\sigma_0$, strongly impact values of ζ. The definition of a reference field of void growth, ζ_{ref}, supports *relative* comparisons across ($\bar{K}$, $\bar{T}$) loadings. $\zeta_{ref}(X)$ refers to the values from Eqn. (5.9) for plane-strain conditions and $T/\sigma_0 = 0$ loading. $\zeta_{ref}(X)$ increases monotonically approaching the crack front ($X \to 0$), and appears (from values computed here) to define an upper bound for void growth due to the high triaxiality. This result supports observations of Varias and Shih [117] that $T = 0$ loading is the most severe constraint level in plane-strain, steady growth. Consequently, the pointwise values for ζ/ζ_{ref} remain less than unity near the crack tip, where ζ defines the void growth value from a 3D SSY analysis.

Farther from the crack front, plane-strain conditions restrict plastic yielding and reduce, then preclude, void growth along the crack plane. The values for ζ/ζ_{ref} exceed one and increase rapidly as $X/\left(J/\sigma_0\right)$ approaches the plane-strain, plastic boundary at $X/\left(J/\sigma_0\right) \simeq 9$. Ahead of this point on the crack plane, void growth develops in 3D SSY but not in plane strain, and the quantity ζ/ζ_{ref} becomes undefined. In general, lower triaxiality in the 3D SSY model promotes plastic deformation farther ahead of the steadily advancing crack, but leads to lower void growth levels near the crack front.

5.7.2 Effect of $\bar{K}$ and $\bar{T}$ on void growth

Table 5.3 summarizes the relative values of void growth at a fixed location $X/\left(J/\sigma_0\right) = 2.9$ along the steadily advancing crack front under the two loadings $\bar{K} = 1$ and 3 for various levels of T/σ_0. Over the mid-thickness region ($Z/B \leq 0.3$), maximum void growth develops for the $T = 0$ loading at both $\bar{K}$ levels. Near the outer surface, $Z/B > 0.3$, void growth levels decrease significantly and monotonically with more negative T-stress, but increase with a positive T-stress. The larger loading at $\bar{K} = 3$ generates somewhat lower void growth in the mid-thickness region but promotes increased void growth near the free surface.

Figure 5.9 displays the mid-thickness ($Z/B = 0$) values of ζ/ζ_{ref} ahead of the steadily advancing crack front ($\theta = 0°$) for (a) $\bar{K} = 1$ and (b) $\bar{K} = 3$. The imposed $\bar{T}$ varies from $+0.25$ to -0.50. The loading level, $\bar{K}$, strongly influences void growth during sustained ductile tearing.

Under low loading, $\bar{K} = 1$, in Fig. 5.9(a), high triaxiality ahead of the advancing crack promotes void

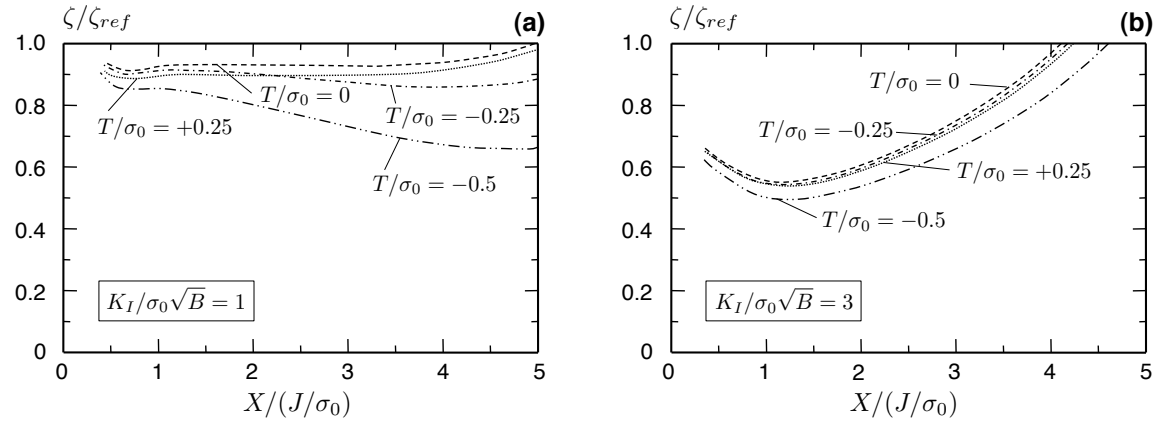

Figure 5.9: Normalized values of the void growth parameter, ζ, ahead of the advancing crack front at mid-thickness ($Z/B = 0$). The ζ_{ref} values derive from the plane-strain, steady growth solutions for $T = 0$ at each $\bar{K}$ value.

growth and leads to ζ values approaching plane-strain levels for $|\bar{T}| \leq 0.25$ over the scaled distances $X/\left(J/\sigma_0\right) \leq 5$. Non-zero T-stress values reduce void growth at the centerplane during 3D steady crack growth; Chapter 2 shows this trend for plane-strain conditions as well using the same form of Eqn. (5.9) to define void growth. Negative T-stress reduces void growth more strongly than positive T-stress, especially far from the crack front, due to both lower plastic strain and triaxiality levels.

Sustained ductile tearing under $\bar{K} = 3$ loading, shown in Fig. 5.9(b), acquires a more plane-stress character that reduces triaxiality but increases plastic deformation. Here, ζ decreases (relative to plane-strain levels) approaching the crack front over $1 \leq X/\left(J/\sigma_0\right) \leq 5$ due to triaxiality loss. Moderate T-stress values ($|\bar{T}| \leq 0.25$) have minimal impact at this higher loading. For both $\bar{K} = 1$ and 3 loadings, the effects of T-stress diminish over $X/(J/\sigma_0) < 1$.

Figure 5.10 presents normalized void growth values at four crack front locations – Z/B =0, 0.3, 0.4, and 0.49. The non-dimensional loading parameter remains constant ($\bar{K} = 1$), for each imposed $\bar{T}$ =+0.25, 0, -0.25, and -0.50. Void growth rates decrease strongly from the mid-thickness ($Z/B = 0$) to the edge-plane ($Z/B \rightarrow 0.5$). Near the free surface ($Z/B \rightarrow 0.5$), plane-stress conditions restrict possible stress states and reduce T-stress effects. The high constraint configuration ($\bar{T} = +0.25$) examined here lowers void growth values at the plate interior and raises values near the free surface. Within a plane-strain framework, positive T-stress values decrease the mean stress more strongly than the Mises stress during steady crack extension, and thus, void growth values decrease, as described in Chapter 2. Negative T-stress loading uniformly reduces triaxiality along the crack plane, leading to lower void growth values.

In summary, Table 5.3 and Figs. 5.9, 5.10, show 3D void growth values all fall below those for the

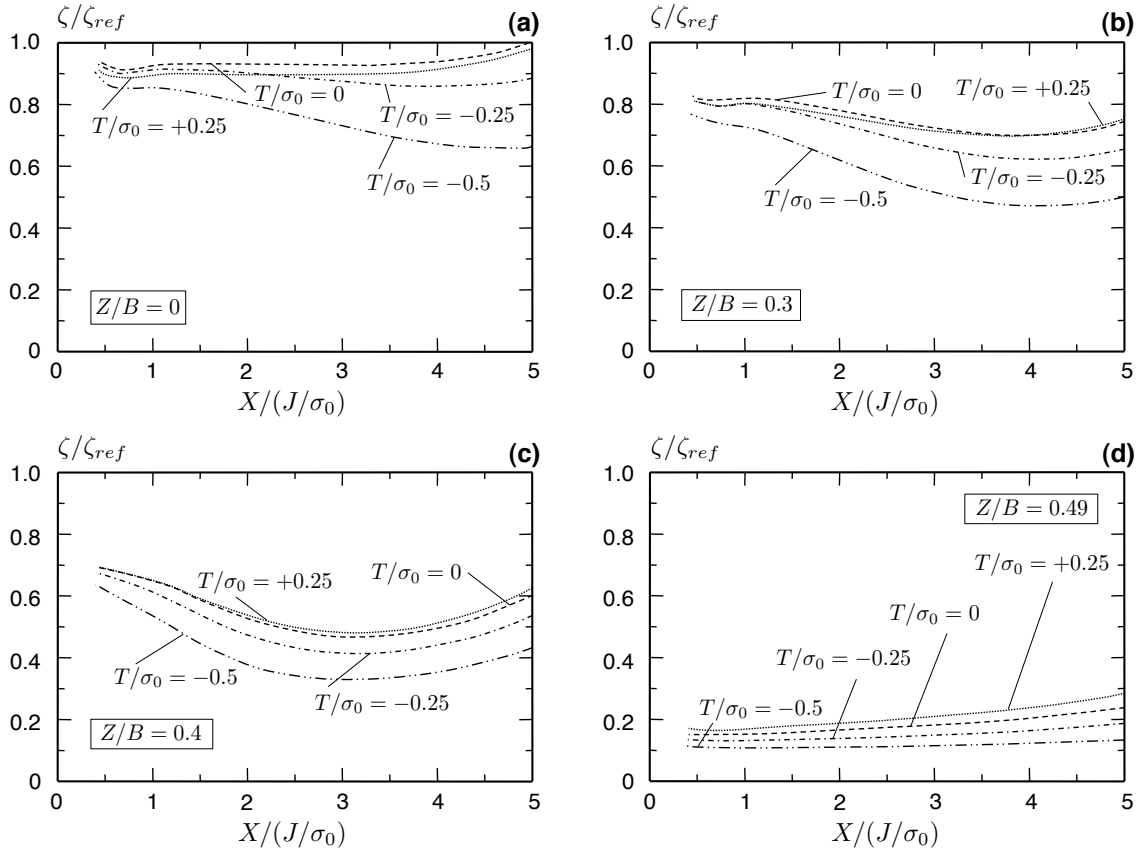

Figure 5.10: Normalized values of the void growth parameter, ζ, a head of the 3D advancing crack front over the thickness for $\bar{K} = 1$ loading. The ζ_{ref} values derive from the plane-strain, steady-growth solution for $T = 0$.

plane-strain, $T = 0$ loading of steady-state growth. These comparisons imply crack front tunneling over the mid-thickness region and the development of shear lips near the outside surface. Further, the simplified void growth model predicts minimum steady-state toughness values for ductile metals tested in $T \geq 0$ geometries (provided the plastic zone size remains a small fraction of the thickness, *i.e.* $\bar{K} < 1$ loading).

5.8 Summary and Conclusions

This work explores T-stress effects on the three-dimensional (3D), mode I crack-front fields for steady-state tearing in an elastic-plastic material. The computational framework employs a 3D boundary-layer model for small-scale yielding (SSY) having uniform thickness, B. The loading is imposed on the remote boundary by displacement fields from specified values of the plane-stress K_I and T-stress. A flat, straight, through-thickness crack advances at a quasi-static rate, and the model enforces a steady-state response through a 3D

implementation of the Dean and Hutchinson [21] streamline integration methodology. This model requires no crack-growth criterion. The material properties reflect those of a moderate hardening, structural aluminum alloy with $E/\sigma_0 = 250$, $\nu = 0.33$, and hardening exponent $n = 10$.

The 3D SSY conditions can be experienced in large but thin structural components or experimental specimens, *e.g.*, aerospace applications, M(T) and C(T) fracture specimens. The combined steady-state driving force – equivalent to the material steady-state toughness – and material flow properties generate in-plane plastic zone sizes on the order of the plate thickness (usually a few mm's). Once an advancing crack front tears through the initial plastic zone formed prior to growth and re-sharpens, the continued tearing resistance decreases and approaches a constant value as $dJ/da \to 0$, and the near-front fields approach the steady-state regime explored in this study.

Previously, Chapter 4 examines the influence of applied loading levels (K_I, $T = 0$), yield stress (σ_0), and thickness (B) on the crack-front fields during steady crack growth in the 3D SSY regime. That work demonstrates the existence of self-similar, crack-front fields expressed in normalized coordinates, *e.g.*, $r/(J^{far}/\sigma_0)$, θ, and Z/B, and a non-dimensional loading parameter $\bar{K} = K_I/\sigma_0\sqrt{B}$, where $J^{far} = K_I^2/E$. Here, we extend the analyses to include non-zero T-stress configurations that expand the range of applications and reach the following key conclusions:

1. The computational results demonstrate the similarity-scaling of crack-front fields (displacements, strains, stresses) controlled by two non-dimensional loading parameters: $\bar{K} = K_I/\sigma_0\sqrt{B}$ and $\bar{T} = T/\sigma_0$. The fields display a self-similarity scaling at locations around the crack front in normalized coordinates $\left(r/\left(J^{far}/\sigma_0\right), \theta, Z/B\right)$. Specific numerical results presented here show this scaling exists at low ($\bar{K} = 1$) and high ($\bar{K} = 3$) loading levels, and for $T/\sigma_0 = +0.25$ and -0.50. For ($\bar{K} = 1$, $\bar{T} = 0$) loading, the plastic zone does not extend beyond $0.3B$ from the crack front at mid-thickness and increases to $2.3B$ for ($\bar{K} = 3$, $\bar{T} = 0$) loading.

2. The similarity-scaling relationship, for example, implies the following practical result. Consider two, 3D SSY analyses both with $\bar{K} = 1$ and $\bar{T} = -0.50$ loading. Define a different thickness B in each model, but adjust the imposed value of K_I to maintain $\bar{K} = 1$. The computed, steady-growth fields in the two analyses remain identical when compared in normalized coordinates $\left(r/\left(J^{far}/\sigma_0\right), \theta, Z/B\right)$. Alternatively, the yield stress, σ_0, can be varied at constant thickness to realize the same scaling, or K_I, B and σ_0 may all vary provided $\bar{K} = 1$ (E/σ_0, ν and n must not change).

3. As suggested by Varias and Shih [117], the height of the actively yielding region normal to the crack plane, h_{pw}, plays a key role in energy dissipation during crack advance as it sets the size of the plastic

wake that trails the advancing front. A larger plastic wake may indicate reduced deformation levels at the crack front (*i.e.*, crack-front shielding). In 3D, h_{pw} varies over the thickness and with different combinations of ($\bar{K}$, $\bar{T}$). Negative T-stress loading significantly increases h_{pw} beyond the $T = 0$ levels; positive T-stress shows the same but less dramatic effect near mid-thickness. For $\bar{K} = 1$ and 3 loading, h_{pw} at mid-thickness remains the smallest for $T = 0$ loading, with values $= 0.3B$ and $1.4B$, respectively.

4. Examination of maximum principal stress (σ_1/σ_0) values along radial lines normal to the crack front at mid-thickness for $\bar{K} = 1$ loading reveals a negligible effect of T-stress at distances less than about $3(J/\sigma_0)$. Within a wedge of material ahead of the advancing crack front ($|\theta| < 54^\circ$), the maximum principal stress values match the plane-strain solution for $T = 0$ loading. These distances of $\leq 3(J/\sigma_0)$ ahead of the crack front compare with a realistic process zone size for a stress-controlled cleavage fracture mechanism. The present results thus suggest a minimal impact of T-stress on a possible transition to cleavage fracture during steady growth. This contrasts sharply to the very large impact of negative T-stress on cleavage fracture initiation in stationary cracks. Away from the mid-thickness at $Z/B = 0.4$, maximum principal stress values lie well-below both plane-strain and centerplane levels, and the principal stresses exhibit small differences for $|\bar{T}| \leq 0.25$.

5. Values of the plastic strain ($\bar{\varepsilon}^p$) often appear in models describing the local process of ductile fracture. For $\bar{K} = 1$ loading, the 3D steady-growth values of $\bar{\varepsilon}^p$ at mid-thickness generally lie above the values for plane-strain, $T = 0$ steady-growth, especially on the crack-plane for $r/(J/\sigma_0) < 10$. T-stress has some effect, with decreasing (increasing) $\bar{\varepsilon}^p$ for more negative (positive) T-stress. Values of $\bar{\varepsilon}^p$ increase significantly above mid-thickness levels at $Z/B = 0.4$. Both trends reflect the reduced stress triaxiality in the 3D SSY regime over the thickness (including the centerplane) compared to plane-strain conditions.

6. Applications of the Rice and Tracey [92] void growth model in a form suitable for streamline integration illustrate the relative importance of combined stress triaxiality and plastic strain effects on the ductile fracture process. For $\bar{K} = 1$ loading, void growth values on the crack plane at all T-stress levels across the thickness fall below plane-strain, $T = 0$ void growth values for $r < 5(J/\sigma_0) = B/50$. These comparisons thus apply at relevant length-scales for the local ductile fracture process. At mid-thickness, values of $|\bar{T}| \leq 0.25$ have a quite small impact on void growth values which attain 90% of those in plane-strain. Void growth values fall quickly away from mid-thickness, reaching only 10-20% of plane-strain values near the outside surface. These comparisons imply crack-front tunneling over the mid-thickness region, the development of shear lips near the outside surface, and minimum steady-

state toughness for materials tested in under $T \approx 0$ configurations that to maintain $\bar{K} \approx 1$ loading (for alignment with these specific numerical results).

The 3D SSY framework for steady-state crack growth employed here opens additional opportunities to advance the understanding of ductile fracture processes in thin structural configurations constructed of relatively high-strength materials. For example, the effects of curved crack fronts and side-grooves on relative void growth values over the thickness may be readily assessed with this framework (including the interaction with T-stress). Coupling crack-front fields from this framework in a Weibull-stress methodology for cleavage fracture appears quite feasible to better model the potential transition from ductile-to-brittle fracture. Finally, the especially challenging topic of steady-state, ductile slant fracture (over the thickness) under globally mode I conditions now appears computationally feasible with this 3D SSY approach.

Chapter 6

Summary and Conclusions

Limited amounts of stable crack growth provide an additional level of ductility for key civil, marine, and power generation structures subject to severe applied loadings and operating conditions. For the low toughness and moderate yield stress materials often used in large engineering applications, inelastic deformation remains contained near the crack front and within the wider structural component that continues to respond elastically. In-plane constraint of plastic deformation, the surrounding environmental conditions, and panel thickness introduce complex interactions at the metallurgical-scale response.

Within this framework, this thesis investigates the influence of applied loading, geometry, and material flow response on the near-front, mode I behavior of a steadily extending crack front. The computational framework – either plane strain or fully 3D – embeds plastic yielding from the through-thickness crack front within a larger elastic region and enables results from these studies to be transferred to corresponding structural components or experimental specimens subject to SSY conditions. This small plastic region remains fixed to and moves with the crack front at quasi-static rates. Mode I displacements and non-zero T-stress values, imposed on the far-field boundary, provide the applied loading experienced by the crack front, and during steady-state crack growth, approach near-constant values. When the active yielding region remains small compared to the thickness and with essentially uniform size over the thickness, the additional geometric length scale provided by the thickness dimension may be neglected and plane-strain conditions assumed. Thinner specimens lose triaxiality along the crack front and accurate estimates for the highly 3D, elastic-plastic field variations must include the additional dimension.

Hydrogen severely reduces the material tearing resistance of engineering materials by locally altering the near-tip response during ductile tearing. Classical plasticity theory (J_2-yield surface) adequately describes the incremental material response for the low-hardening, structural metals in the absence of hydrogen-induced plasticity, but must be significantly modified to account for hydrogen effects on the material response. Hydrogen alters the observed flow response of structural metals through complex interactions between the stress-state and the dislocation velocity. When hydrogen atoms remain in equilibrium at lattice and trap sites, the hydrogen-enhanced, localized plasticity (HELP) mechanism, utilized in the present studies, reflects

hydrogen-induced softening on the constitutive response for the saturated metal.

The determination, characterization, and application of the near-front response for a steadily advancing crack front, particularly in the presence of hydrogen and for thin, ductile plates, represents the major contribution of this thesis to the scientific literature. Specifically, this thesis extends the steady-state algorithm outlined by Dean and Hutchinson [21] into a 3D framework for the first time and develops the first, key computational tools to investigate the near-front response. The steady-state algorithm enables investigations of ductile crack growth, without setting a crack growth mechanism. Integration of the material response through the non-proportional strain history along straight streamlines provides the mechanical fields without the need for explicit time-history analyses. Each integration along a streamline can occur simultaneously with every other streamline integration using the estimate for the displacement fields. The special-purpose, finite element software FIREFLY implements this procedure using the OpenMP parallel paradigm to achieve high levels of efficiency. As a consequence of the streamline integration procedure, these analyses do not suffer from any spurious numerical issues introduced by time-stepping methods or caused by finite sized crack growth increments in traditional finite element procedures.

The individual chapters focus on characterizing various aspects of steady crack growth. The studies of hydrogen effects within a plane-strain framework show the wide applicability of the steady-state algorithm to advanced engineering applications where outside environmental factors affect the material response. Chapter 2 provides a parametric study for a niobium-like material with different values for the initial concentration of hydrogen and the intensity of plastic straining, whereas Chapter 3 concentrates on matched, under-matched, and over-matched welds of A533B steel. Constraint effects from a remotely imposed T-stress significantly alter the near-front response in these plane-strain studies. These investigations provided an opportunity to develop expertise with the steady-state algorithm while also solving a new, practically important problem of current interest to the fracture mechanics community. Success with the streamline integration technique also provided a platform to develop the new 3D capability. The following chapters study crack advance within the 3D SSY model and characterize the resulting self-similar fields using nondimensional quantities that describe the applied loading. Further, Chapter 4 explores the crack tip opening angle – an increasingly used parameter to describe material toughness in thin specimens. Void growth estimates in Chapter 5 characterize the influence of non-zero T-stress loadings on 3D steady crack growth.

The following sections outline key conclusions from the studies presented in the previous chapters. The major trends from the initial, plane-strain investigations of hydrogen effects during steady crack advance are presented in Sec. 6.1. Section 6.2 discusses core results from the central framework in this thesis: self-similarity scaling for the near-front displacements, strains, and stresses in 3D SSY conditions. Imposed

T-stress levels strongly influence mechanical fields during steady crack growth but display trends that differ from results for a stationary crack due to energy balance requirements, as the conclusions in Sec. 6.3 indicate. Section 6.4 outlines key tendencies for the examined local toughness measures – crack-tip opening angle, void-growth rates, and cleavage initiation. This section closes with a partial list of future topics that now can be explored using the new 3D numerical framework developed in this thesis.

6.1 Hydrogen effects on plane-strain, sustained ductile tearing

These results link earlier studies that investigate the early stages of crack growth in hydrogen-charged materials (*e.g.* Ahn et al. [1]) to the large body of scientific literature on ductile tearing at steady-state in hydrogen-free materials. The near-tip fields exhibit self-similarity with radial dimensions normalized by J/σ_0, as suggested by earlier studies of hydrogen-free materials [59]. In plane strain, $\bar{K}$-scaling is not a relevant loading parameter, and the imposed T-stress normalized by the yield stress represents the key nondimensional term.

Hydrogen effects dominate the crack-tip response compared with the smaller T-stress effect and control the elastic-plastic fields to a very large extent. As Chapter 2 demonstrates, hydrogen effects – primarily, initial reduction of the yield stress, and secondarily, the initial concentration of hydrogen – alter triaxiality and plastic strain fields ahead of the advancing crack fronts. The triaxiality measure ($3\sigma_m/2\sigma_e$) increases most strongly in materials with small initial concentrations of hydrogen and large initial flow stress reductions. Inelastic deformation also increases significantly in a hydrogen-softening material and is quite sensitive to the initial hydrogen concentration. The active yielding regions surrounding the crack front slightly expand in the presence of hydrogen but do not change from the characteristic shape observed during steady crack advance in hydrogen-free materials.

The plane-strain results in Chapter 2 for a crack extending in a hydrogen-free, "niobium-like" material largely agree with Varias and Shih [117]: non-zero T-stress values reduce the magnitudes for the near-front fields – both the triaxiality measure ($3\sigma_m/2\sigma_e$) and the equivalent plastic strain ($\bar{\varepsilon}^p$) – along the uncracked plane during steady crack growth. In contrast, the opening-mode stress for stationary cracks increase (decrease) in plane-strain SSY under a positive (negative) T-stress. Stationary cracks lack the trailing plastic wakes that develop during steady crack advance and that store elastic strain energy from the imposed T-stress. In the presence of hydrogen, non-zero T-stress levels reduce triaxiality and plastic deformation. Positive T-stress loadings impact the crack-front fields less strongly than negative T-stress fields.

Chapter 3 considers steady crack extension through a steel weld, where weld and base metals differ due to the initial yield stress mismatch (without hydrogen). Mismatch more strongly influences crack-tip response than T-stress levels for mismatched ferritic steel welds. The hydrogen concentration, and with it the mean stress, increases with weld-base metal mismatch, *i.e.* hydrogen concentration reaches a maximum value in over-matched welds and a minimum value in under-matched welds. Furthermore, under-matched welds promote inelastic deformation within the weld metal, and restrict plasticity in the base metal. Over-matched welds limit the accumulation of plastic strains and allow some plastic deformation outside of and separated from the weld metal.

Void growth in the presence of hydrogen is discussed in Sec. 6.4.2.

6.2 Self-similarity scaling

Advancing crack fronts develop near-front stresses, strains, and displacements that significantly differ from the mechanical fields surrounding a stationary crack front, yet the nondimensional quantities, $\bar{K} = K_I/\sigma_0\sqrt{B}$ and $\bar{T} = T/\sigma_0$ control the crack front response in both cases under 3D SSY conditions. Consequently, these loading terms provide a key link between the often complex, 3D behavior throughout the crack initiation and growth process. That is, the loading parameters $\bar{K}$ and $\bar{T}$ quantify material toughness and driving force values for structural integrity analyses similar to the geometry-independent quantities K_I and J that have been used for flaws in thin (plane stress) and thick-walled (plane strain) conditions.

For example, consider two crack fronts A and B that advance in separate 3D SSY models. Each crack front extends under the same loading level $(\bar{K}, \bar{T})$, though the stress intensity factor, T-stress, thickness, and yield stress may vary between A and B. The other properties of the material (E/σ_0, ν, and n) may not change. Then, in normalized coordinates ($r/(J/\sigma_0)$, θ, Z/B), the stresses, strains, and displacements remain invariant between each 3D SSY model A and B during steady crack advance.

The near-front fields in Chapter 4 demonstrate the self-similarity scaling in normalized coordinates for both low ($\bar{K} = 1$) and high ($\bar{K} = 3$) applied loading levels under a zero imposed T-stress. Section 4.4 provides a simple physical interpretation for the loading parameter $\bar{K}$: the extent of plastic yielding on the uncracked ligament and at the centerplane, r_{p0}, relative to the plate thickness, B, proportionally varies with $\bar{K}^2$ when $\bar{T} = 0$. Thus, the $\bar{K}$-level suggests very general trends regarding the overall near-front fields: low $\bar{K}$-levels reflect increasingly plane-strain conditions where comparatively large thicknesses strongly constrain out-of-plane plastic deformation; high $\bar{K}$-levels approach plane-stress conditions throughout the active yielding region; and intermediate $\bar{K}$-levels indicate crack front response that varies strongly over the thickness.

As shown in Secs. 4.5 and 4.6, material surrounding the crack front experiences near plane-strain conditions over some small radial fraction of the thickness. For $\bar{K} = 1$ loading, the near-front fields approach the plane-strain response very close to the crack front, $X/B \leq 0.02$, and these high constraint conditions continue over $-0.4 \leq Z/B \leq 0.4$. Farther ahead of the crack front, a complex 3D stress state develops throughout the thickness that extends beyond the active yielding region to $X/B = 1.5$, and the linear elastic, plane-stress solution – Williams' fields for mode-I stationary cracks – describes the material response beyond this point. At the higher loading level $\bar{K} = 3$, near plane-stress conditions prevail over much of the plastic zone, but a small region near the crack front (again $X/B \lesssim 0.02$) over the center 40% of the thickness maintains sufficient plane-strain levels of triaxiality. The near-front constraint rapidly declines outside of this near plane-strain region. Linear-elastic fields in plane stress develop under $\bar{K} = 3$ loading at $X/B \approx 5$. Relative to the Williams' solution, peak opening-mode stresses develop at the boundary of the active yielding region with the enclosing elastic material, *i.e.* $X = r_{p0}$. These strong 3D effects, through the thickness (Z/B) and with $\bar{K}$-loading, continue in the presence of non-zero T-stress loadings.

6.3 T-stress effects on 3D near-front fields

For the thin sheets examined in Chapter 5, constraint effects, imposed on 3D SSY model by the T-stress, impact the elastic-plastic fields for $r/(J/\sigma_0) \geq 3$. Closer to the crack front (as $r \to 0$), high triaxiality restricts possible stress states and produces fields near the plane-strain result. The energy arguments invoked by Varias and Shih [117] assume uniform plastic zones across the entire thickness (plane strain) that depend entirely on $\bar{T}$. In 3D SSY, both h_{pw} and r_{p0} change over the thickness (Z/B) and vary with the combined $\bar{K}$ and $\bar{T}$ loading. Consequently in the 3D SSY regime, the elastic-plastic fields during steady crack advance display the previously observed triaxiality loss for the zero T-stress loading, as well as additional T-stress effects.

For 3D SSY conditions under the low loading level $\bar{K} = 1$, the results in Chapter 5 suggest a straightforward relationship between negative T-stress loadings and the resulting crack-front response during sustained ductile tearing. Within an angular wedge ($|\theta| \leq 54°$) of material fixed to the advancing crack front, reduced stresses and lower levels of plastic deformation occur far from the crack front over 80% of the thickness ($|Z/B| \leq 0.4$). These elastic-plastic fields under $\bar{T} \leq 0$ loadings converge to the $\bar{T} = 0$ solution nearer to the crack front ($r \leq 3\,J/\sigma_0$). Significantly, this finding agrees with earlier plane-strain analyses of steady crack advance [117]. Triaxiality losses over the thickness lead to changes of σ_1 more than do the T-stress effects. Outside of $r/(J/\sigma_0) = 3$, σ_1 decreases by roughly the yield stress from $Z/B = 0$ to 0.4. The corresponding

effect of $\bar{T} = -0.5$ on σ_1 remains much smaller – roughly a 10% yield stress reduction compared to the zero T-stress case. The other principal stress components (σ_2 and σ_3), required to fully describe the stress-state, follow the same general trend under negative T-stress outlined for the first principal stress. Near the crack plane over $|\theta| \leq 27°$, negative T-stress levels limit plastic deformation, measured by the equivalent plastic strain ($\bar{\varepsilon}^p$), but the resulting plastic deformation exceeds plane-strain values over the entire thickness. Triaxiality loss becomes most apparent closer to the outside surface, where higher plastic strains develop at larger radial distances than in plane strain or at mid-thickness.

For $\bar{K} = 1$ loading, positive T-stress ($\bar{T} = +0.25$) slightly increases the stresses of a point far from the crack front, but the principal stresses rapidly tend to the zero T-stress variation near the crack front. The equivalent plastic strain rises under positive T-stress for $|\theta| \leq 27°$ from $-0.4 \leq Z/B \leq 0.4$ and tends to the plane-strain result very close to the crack front within this angular wedge. For the $T > 0$ case, the plastic wake expands near the centerplane and contracts near the free surface relative to the zero T-stress result. Thus, the crack front response in a positive T-stress loading exhibits the plane-strain trend to a lesser degree than expected, though it may become more visible under higher T-stress levels.

The higher loading level, $\bar{K} = 3$, remains relatively insensitive to T-stress during steady crack advance. Kim et al. [48] also observe this effect in 3D SSY for stationary cracks. Here, the predominately plane-stress response restricts possible stress states throughout the plastic zone and prevents large T-stress effects.

Appendix E provides an alternate method to quantify constraint effects during steady crack growth. Following the idea explained by Varias and Shih [117], these preliminary studies adopt a characteristic length scale, L_g, to describe the crack-front response under imposed constraint levels in convenient non-dimensional form. These results suggest that multiple values of such characteristic length scales, one for each principal stress, are required to describe the near-front fields. In contrast, one characteristic length scale reflects T-stress effects for all crack-tip fields in plane strain.

6.4 Local toughness measures

6.4.1 Crack tip opening angle

The crack tip opening angle (CTOA) reflects material toughness along the advancing crack front, analogous to the crack tip opening displacement for a stationary crack front. Researchers increasingly apply this methodology to thin ductile sheets that experience large amounts of sustained ductile tearing. The steady-state results presented in Sec. 4.7 reveal key features of the crack front response applicable to experimental programs that adopt CTOA as a macroscopic fracture parameter.

During steady crack extension, the crack opening profile at the free surface exhibits a distinctly "wedge-like" shape for the examined $\bar{K}$-loading levels. Curvature of the crack-opening profile remains small and confined to a region very close to the crack front, *i.e.* $X/\left(J/\sigma_0\right) \leq -2$. This result implies a relatively low sensitivity to the distance behind the tip adopted to define the CTOA values and supports the numerous experimental programs and the recent materials testing standard [5] that incorporates CTOA as a material toughness measure.

In general, CTOA values reflect triaxiality over the thickness during steady crack growth and thus vary along the crack front (Z/B) and with the loading level ($\bar{K}$). The CTOA peaks for low $\bar{K}$-levels near the centerplane ($Z/B = 0$), and decreases approaching the free surface ($Z/B = 0.5$), similar to the J-integral results for stationary crack front in 3D SSY [72]. CTOA values for increasing $\bar{K}$ reveal a more uniform crack-front opening. For sufficiently high $\bar{K}$ loadings, the 3D crack opening profiles match the plane-stress profile over the entire thickness, whereas for low $\bar{K}$ loadings, the crack opening profile near the mid-thickness attains the near plane-strain value over significant fractions of the plate thickness, *e.g.* $r \lesssim 0.03B$ at $\bar{K} = 1$. Computed CTOA values from steady-state crack growth analyses in the 3D SSY framework under-predict experimental results by 60-70%. Pre-damage of material before the crack front arrives (*e.g.* void growth) does not appear in the present computational framework and would likely raise CTOA values. Future studies discussed in Sec. 6.5 may improve CTOA correlations with experimental data.

6.4.2 Void-growth rates

Void growth contributes strongly to the micromechanical, ductile tearing process commonly found in structural metals, *e.g.* steels, titaniums, and aluminums, and thus represents a key factor in controlling the material toughness. These studies incorporate the simple analytical expression from Rice and Tracey [92] to estimate relative void-growth rates under various combinations of T-stress, weld-base metal mismatch, hydrogen-induced softening, and 3D triaxiality. Higher void-growth rates suggest less resistance to ductile tearing and lower toughness values, and vice versa for lower void-growth rates.

For the homogeneous, "niobium-like" metals investigated in Sec. 2.4, hydrogen-induced plasticity can increase void-growth rates by more than 30% compared to hydrogen-free materials. Reduction of the initial flow stress, induced by the combined intensity of hydrogen-induced softening (ξ) and initial concentration of hydrogen (c_L^0), most strongly increases void growth ahead of the crack front. Two competing mechanisms act on the void growth rates in the presence of hydrogen. Hydrogen-induced softening accelerates void growth by elevating triaxiality levels and intensifying plastic deformation along the crack front. Softening effects increase as the initial reduction of the flow stress decreases. In contrast, dilatational effects, which rise with

larger initial concentrations of hydrogen, lower the mean stress ahead of a steadily advancing crack front and thus suppress void growth. In these studies, hydrogen-induced softening dominates and thus increases void growth rates. Without the initial reduction of the flow stress, the dilatational effect from hydrogen reduces triaxiality and thus void growth. Under the examined plane-strain conditions, non-zero T-stress values – positive or negative – reduce void-growth rates in the presence of hydrogen. Low constraint configurations ($\bar{T} = -0.4$) lead to void-growth rates that cluster together based on the initial reduction for the flow stress.

In a high-strength, ferritic steel weld with a hydrogen saturated environment, the degree of weld-base metal mismatch (here indicated by relative yield stress values) most strongly influences the resulting void-growth rates, as shown in Sec. 3.5. Hydrogen-induced plasticity modestly accelerates the void-growth levels. More critically, under-matched welds exhibit significantly higher void-growth rates due to higher levels of inelastic deformation than observed for matched welds, whereas over-matched welds reveal reduced void growth. Under-matched welds limit plastic deformation largely to the weld metal (near-constant h_{pw}), and contrary to other plane-strain studies, the resulting void-growth rate increases under negative T-stress levels.

Section 5.7 discusses void growth rates under varying T-stress levels within the 3D SSY regime. The combined ($\bar{K}$,$\bar{T}$) loading has a pronounced effect on the resulting void growth levels along the crack plane and over the thickness. At low loading levels ($\bar{K} = 1$) and on the mid-thickness, void-growth rates approach, but do not reach, the plane-strain levels within the normalized radial distance $r/\left(J/\sigma_0\right) \leq 5$ for $\left|\bar{T}\right| \leq 0.25$. Void growth under the higher loading level ($\bar{K} = 3$) experiences a distinctly 3D response near the crack front on the centerplane. The negative T-stress level $\bar{T} = -0.5$ strongly reduces void-growth rates over the uncracked plane for the $\bar{K} = 1$ and less markedly for the higher $\bar{K} = 3$ loading. These results suggest significantly higher tearing resistance curves ($J - \Delta a$) for geometries and loadings that induce negative T-stress values in structural applications and testing configurations. Approaching the free surface, triaxiality loss reduces void growth levels from the peak values attained on the mid-thickness. For $\bar{K} = 1$, void growth rates decline from nearly 90% of plane strain levels at $Z/B = 0$ to $\sim 10\%$ of plane-strain levels at $Z/B = 0.49$. The lower triaxiality over the entire thickness under $\bar{K} = 3$ loading accelerates void growth near the free surface but restricts void growth at the centerplane relative to the $\bar{K} = 1$ values. Consequently, crack-front tunneling over the mid-thickness, shear-lip development near the free surface, and minimum steady-state toughness values in $T \approx 0$ experimental specimens are expected from the 3D void growth results.

6.4.3 Cleavage predictions

Results from the three-dimensional, steady-state analyses allow an examination of the numerous and often competing influences on the cleavage initiation mechanism observed in structural ferritic steels within the

mid-to-upper, ductile-to-brittle temperature region. The Weibull stress model provides a local measure of the cleavage-fracture driving force, dependent on micromechanical flow properties and the resulting first principal stress. Section 5.6.1 discusses relevant details to compute the Weibull stress values in 3D for steadily advancing crack fronts. The remote T-stress, under 3D SSY conditions, has a small influence on the first principal stress under $\bar{K} = 1$ loading within relevant micromechanical dimensions for a reasonable fracture process zone (material over which $\sigma_1 \geq 3\sigma_0$). Approaching the crack tip, the variations of the 3D first principal stress for $T/\sigma_0 = +0.25$, 0, -0.25, and -0.5 tend to the plane-strain result under a zero T-stress loading over $|\theta| \leq 54°$. The high triaxiality response applies from the centerplane to $|Z/B| = 0.4$. Consequently, Weibull stress values computed from plane-strain, steady growth analyses under a zero T-stress differ little from the 3D results. In contrast, the ductile tearing mechanism exhibits some sensitivity to the imposed T-stress, as discussed in the previous section. From these calculations, the steady-state value for the crack-growth resistance curve increases strongly under a negative T-stress, but the probability of cleavage initiation during sustained ductile remains nearly constant.

Appendix C provides a theoretical framework to quantify the probability of cleavage fracture following some amount of ductile crack growth. Under steady-state conditions, the derived expressions assume that the probability of cleavage fracture increases as the crack front advances and samples additional material at high stress levels – *i.e.* loading and temperature are ignored – and likely represent an upper bound expression. The preliminary results in Sec.C.3 compare the new predictions of cleavage initiation probability with crack growth to experimental results and show a good agreement between predictions and observations.

6.5 Future work

The 3D computational framework discussed here and implemented in the FIREFLY code provides an entirely new analysis capability to explore the interconnected and complex relationships that influence steady crack extension in ductile metals. The studies in this thesis provide the first key investigations linking the applied loading, geometry, and material flow properties to the 3D near-front response. The following sections list potential directions for future research and are divided into four major areas: geometry, material response, loading, and applications.

6.5.1 Geometry

- *Crack front tunneling.* During crack advance, the crack front at the plate interior extends beyond the crack front at the plate exterior and assumes an elliptical shape much smaller than the in-plane or

out-of-plane structural dimensions. This additional behavior introduces a new geometric parameter related to the amount of tunneling with respect to the plate thickness. Crack front tunneling may relax deformation on the plate exterior and increase CTOA values. For curved, stationary crack fronts, Wang and Lambert [123] demonstrate strong effects on the local stress intensity factors over the thickness, and this response likely continues for steadily advancing crack fronts.

- *Side-grooves.* Test specimens for quasi-static and dynamic fracture events often have material removed along the crack plane at the outside surface and parallel to the direction for crack advance. Side-grooves promote uniformity of the crack front fields based on their depth, notch radius, and slope and can easily be studied in a 3D SSY model with simple remeshing of the existing models used in this work.

- *Slant fracture.* The crack plane during sustained ductile tearing may rotate approximately 45° relative to the Z-axis under mode-I, far-field loading, but experiences mode I and more III loading types locally, due to the slanted fracture. Slant fracture breaks the symmetry planes present for mode I flat fracture and requires a full 3D SSY model, but otherwise requires no additional modifications to the basic FIREFLY framework. Computational requirements will thus quadruple and exceed the current capabilities of the server architecture used in these studies.

- *Delamination.* In common aluminum-lithium alloys favored by the aerospace industry, the intense out-of-plane stresses ahead of the advancing crack front separate individual layers on planes perpendicular to the thickness direction. Delamination alters the near-front loading parameter, $\bar{K}$, by reducing the thickness in inelastically yielding material (layers) approaching the crack front. Symmetric and non-symmetric, simultaneous and staggered, delamination analyses are now possible at steady-state. Cohesive zone elements, placed between thickness layers, could be integrated within these models to determine the evolution of the delamination process based on the traction-separation law.

- *Weld metal geometry.* In a 3D SSY context, common weld placement patterns include square-grooves, v-grooves, and bevel grooves; the welded metal itself may appear flat, convex, or concave with respect to the thickness; and the crack front may propagate at the weld center or closer to the heat affected zone. All of these factors are expected to influence the elastic-plastic fields and are clearly 3D problems.

- *Non-SSY geometries.* Many cracks propagate in geometries that cannot be described by the simplified 3D SSY model, yet reach steady-state under near-constant, well-defined remote loads, *e.g.*: axial pipeline cracks and cracks advancing through welded T-joints in plate girders. These studies would provide the first computational investigations of steady crack growth beyond the SSY regime.

- *Large displacements.* FIREFLY neglects finite deformation effects near the crack front. The relatively low singularity strength during steady crack growth limits the development of regions with significant deformation, but nonlinear geometric effects may influence the near-front response, particularly in the plastic wake region behind the finite deformation region. A total Lagrangian framework, with streamlines that originally pass through element Gauss points, appears to be the most convenient implementation.

6.5.2 Material response

- *Kinematic yield surface.* This thesis restricts investigations to ductile metals that do not exhibit the Bauschingler effect, *i.e.* reduced uniaxial yield stress in compression after being loaded beyond yield in tension, or vice versa. The "back-stress" in kinematic yield surfaces would particularly influence material that reloads inelastically within the plastic wake. Constraint effects depend on the "locked-in" stresses within the plastic wake, and the resulting 3D stresses may exhibit a pronounced sensitivity to mixed kinematic and isotropic yield surfaces.

- *Non-Mises yield surface.* For mode III, steady crack growth, Dean and Hutchinson [21] originally explore the effect of non-Mises yield surfaces on the active yielding region, specifically classical J_2-flow theory vs. J_2-corner theory. Corresponding studies in 3D SSY would provide key links between crack growth and the continuum material response without the need for an explicit failure model.

- *Weld mismatch.* Chapter 3 shows that weld mismatch strongly influences void growth in plane strain. In three-dimensions, weld mismatch can vary with distance from the crack plane and through the thickness, and thus, 3D crack growth analyses can capture differential residual stresses, from differential cooling, due to multiple welding passes.

- *Functionally graded materials.* Advanced structural applications often require strong material property gradiations to the function under severe loading and thermal events. Crack growth in a direction orthogonal to the material gradiation of elastic and plastic flow properties may be analyzed using the steady-state algorithm.

- *Rate-dependent plasticity.* Quasi-static crack propagation at low velocities through certain polymers triggers rate-dependence in the inelastic material response. The steady crack growth model provides a simple way to quantify key material parameters under slow, sustained loading. Landis et al. [52] explore rate dependence for such materials in the context of quasi-static crack advance ($\dot{a}$ less than 10% of the shear wave speed) without inertial effects.

- *Corrosion/Embrittlement.* Material degradation often spreads from the material surface near the corrupting environmental agent (hydrogen, water, gasoline) to the plate interior, and consequently, material conditions differ significantly through the plate thickness. An advancing crack front attracts certain contagions and further reduces the material toughness. Preliminary plane-strain studies are shown in Chapters 2 and 3 for high-diffusivity metals in the presence of hydrogen, and can easily be extended to a 3D context, perhaps with initial gradients of hydrogen concentration over the thickness.

6.5.3 Loading

- *Far-field mixed loading.* This thesis focuses on crack front effects of far-field mode I loading and varying imposed T-stress values in a 3D SSY framework. Future studies of mixed mode I, II, and III far-field displacements on the boundary layer model would allow evaluation of the complex stress fields that develop surrounding the advancing crack front.

- *Out-of-plane tractions.* Consider a crack front that advances steadily in 3D SSY. Some out-of-plane pressure develops on one or both outside surfaces – in contrast to the current investigations where tractions remain negligible. That is, tractions in the Z-direction are non-zero. High pressure, for example in a pressure vessel or pipeline, may restrict the development of plane-stress conditions along the crack front.

- *Dynamic loading and crack growth.* Crack growth can only be classified as quasi-static at velocities less than 10% of the shear wave speed (roughly 320 m/s for steel alloys), and cracks propagating at rates beyond this limit experience strong inertial effects. When inertia becomes significant, the applied tractions (see Freund [30]) and the equilibrium relationships depend on the crack velocity, as revealed by Appendix A. Viscoplastic effects also become important in key structural metals during dynamic crack extension. The 3D setting may also resolve the incompatible thermodynamic shocks observed in plane strain by Drugan [26].

- *Thermal gradients.* During the lifetime of major structural components, strong thermal gradients may develop through the thickness, *e.g.* an aerospace actively cooled, integral structure. Thermal strains alter the deformation patterns and/or induce residual stresses prior to the arrival for a through thickness crack front. The resulting through-thickness variations for the in-plane constraint and potential bending loads will change the near-front response.

6.5.4 Applications

- *Cleavage.* Appendix C describes preliminary investigations of the stochastic framework for cleavage initiation applied to the steady crack-growth regime. Further studies will examine 3D effects, specifically the influence of applied loading – $\bar{K}$ and $\bar{T}$ – on the key quantity that represents the Weibull stress variation, S_w^{HSS}, and will improve rational methods used to quantify the risk of a cleavage fracture event.

- *Damage mechanisms.* Major advances in the crack growth predictions are due to the adoption of micromechanically based damage models implemented at the continuum scale, *i.e.* Gurson or traction-separation laws. In a steady crack growth analysis, these mechanisms provide the far-field steady-state toughness based on the model description, and provide crack front boundaries based on through-thickness triaxiality variations. Specifically, mixed 3D SSY analyses that determine steady-state toughness values based on CTOA, Gurson, and traction-separation type criteria would resolve contradicting trends for the toughness in positive constraint configurations.

Appendix A

Steady-State Numerical Procedure

Consider a crack propagating from left of the right along the positive X_1 axis under steady-state conditions at a constant velocity $\dot{a}$. The time derivative of any quantity $(\bullet)$ follows the relationship:

$$\frac{\partial}{\partial t}(\bullet) = -\dot{a}\frac{\partial}{\partial X_1}(\bullet). \tag{A.1}$$

Equation (A.1) modifies the inertial term in the equilibrium equation into the form

$$\sigma_{ij,j} + b_i = \rho\dot{a}^2\partial^2 u_i/\partial X_1^2, \tag{A.2}$$

where σ_{ij} denotes the components of the stress tensor; b_i defines the components of the body force; ρ is the material density; u_i equals the components of the displacements; and standard indicial notation rules apply to Eqn (A.2) and subsequent equations with indices of 1, 2, and 3. Under quasi-static conditions, the crack tip velocity approaches zero, and the inertial terms in Eqn. (A.2) become negligible.

The steady-growth assumption does not affect the kinematic or constitutive relations of the boundary value problem. By adopting infinitesimal strain theory, the total strain, $\varepsilon_{ij} = \frac{1}{2}(u_{i,j} + u_{j,i})$, may be decomposed additively into an elastic term, ε_{ij}^e, and inelastic term, ε_{ij}^η, such that

$$\varepsilon_{ij} = \varepsilon_{ij}^e + \varepsilon_{ij}^\eta. \tag{A.3}$$

For the linear elastic constitutive equation, where $\sigma_{ij} = \mathcal{C}_{ijkl}\varepsilon_{kl}^e$, Eqn. (A.3) implies

$$\sigma_{ij} = \mathcal{C}_{ijkl}\left(\varepsilon_{ij} - \varepsilon_{ij}^\eta\right). \tag{A.4}$$

A set of virtual quantities, denoted by $\delta(\bullet)$, may be specified. Using standard arguments, the principle of virtual work states that for the quasi-static, steady-growth problem in a domain Ω and under tractions

T_i along the boundary $\partial\Omega$:

$$\int_{\Omega} \delta\varepsilon_{ij}\mathcal{C}_{ijkl}\left(\varepsilon_{kl}-\varepsilon_{kl}^{\eta}\right)dV = \int_{\partial\Omega} \delta u_i T_i dS. \tag{A.5}$$

To determine the inelastic terms in Eqn. (A.5), the computational procedures integrate incrementally the rate equations using the following idea: There exists a series of points A, B, C, ..., Z ordered left to right along a streamline parallel to the X_1 axis. The material at point A has passed through points B, C, ..., Z and in passing through these points, A has experienced the mechanical fields which currently exist at B, C, ..., Z, where Z is arbitrarily taken as the rightmost remote boundary. If a mechanical state, *e.g.* ε_{ij}^{η}, at A is unknown, it can then be found by integrating through B, C, ..., Z, from Z to A, which according to Eqn. (A.1), is equivalent to integrating these equations through time.

The following steps outline the algorithm proposed by Dean and Hutchinson [21]:

1. Compute the linear elastic system stiffness matrix $\boldsymbol{K}^{sys}$ from the assembled set of element stiffness matrices $\boldsymbol{k}^{elm} = \int_{elm} \boldsymbol{B}^T\boldsymbol{E}\boldsymbol{B}dA$, where $\boldsymbol{B}$ denotes the strain displacement matrix and $\boldsymbol{E}$ equals the linear elastic constitutive relationship in matrix form.

2. For a specified stress intensity factor, K_I, and T-stress value, T, compute the full value of the displacements at the remote boundary points (r,θ) from the asymptotic expansion of the mode I solution:

$$u_1 = \frac{K_I}{2\mu}\sqrt{\frac{r}{2\pi}}\cos\left(\frac{\theta}{2}\right)\left(\kappa - 1 + 2\sin^2\left(\frac{\theta}{2}\right)\right) + \left(\frac{1-\nu^2}{E}\right)\left(Tr\cos\left(\theta\right)\right), \tag{A.6}$$

$$u_2 = \frac{K_I}{2\mu}\sqrt{\frac{r}{2\pi}}\sin\left(\frac{\theta}{2}\right)\left(\kappa + 1 - 2\cos^2\left(\frac{\theta}{2}\right)\right) + \left(\frac{\nu\left(1+\nu\right)}{E}\right)\left(Tr\sin\left(\theta\right)\right), \tag{A.7}$$

   where μ, E , and ν are the shear modulus, Young's modulus, and Poisson's ratio, respectively; and κ equals $3-4\nu$ for plane strain. Impose these specified displacements on the finite element model. In the present work, we implement this procedure by standard partitioning of the displacements and a corresponding partitioning of the stiffness matrix, which leads to an efficient computation procedure.

3. Solve the system of linear equations $\mathbf{K}^{sys}\mathbf{U}^{sys} = \mathbf{P}^{sys}$ for $\mathbf{U}^{sys}$.

4. Compute the total strains $\boldsymbol{\epsilon} = \mathbf{B}\mathbf{u}^{elm}$ for each Gauss point, where $\mathbf{u}^{elm}$ is extracted from $\mathbf{U}^{sys}$ using standard methods. Integrate the inelastic constitutive equations along streamlines through element Gauss points to calculate the inelastic strain $\boldsymbol{\epsilon}^{\eta}$. For the $i+1$ Gauss point, increment the strains by $\Delta\boldsymbol{\epsilon} = \boldsymbol{\epsilon}^{i+1} - \boldsymbol{\epsilon}^{i}$, where $\boldsymbol{\epsilon}^{i+1}$ is the total strain at the $i+1$ Gauss point; and $\boldsymbol{\epsilon}^{i}$ is the total strain at the i Gauss point, *i.e.* the Gauss point immediately to the right of the $i+1$ Gauss point. The initial conditions for the $i+1$ Gauss point are the values of the converged solution of the i Gauss point.

5. Solve the system of equations $\mathbf{K}^{sys}\mathbf{U}^{sys} = \mathbf{P}^{sys} - \int_{elm} \mathbf{B}^T \mathbf{E} \boldsymbol{\epsilon}^{\eta} dA$ for $\mathbf{U}^{sys}$.

6. Check for convergence. The criteria compares the current value of the residual force vector, $\mathbf{R}$, and the original value of the residual force vector, $\mathbf{R}_0$, such that the analysis converges when $\|\mathbf{R}\| \leq tol \ \|\mathbf{R}_0\|$ where $\|\bullet\|$ signifies the L_2 norm of the quantity $\bullet$. Most of the unbalanced residual forces occur along the model boundary far behind the advancing crack tip where the imposed linear-elastic, asymptotic displacements conflict with the inelastic response. For the analyses in Chapter 2, in a semi-circular region with a radius equal to half the distance from the remote boundary to the crack tip, the residual norm drops to the order of 10^{-4} of $\|\mathbf{R}_0\|$. Additional iterations to further reduce the residual do not affect the values for the displacements, stresses, or strains. If the convergence criterion is not met, return to step 4.

Appendix B

Effect of the HELP Mechanism on the Concentration of Hydrogen

The constitutive model used in the present study reflects the HELP mechanism to determine inelastic strains due to both plasticity and hydrogen. We compute the change in the plastic strains, $\Delta\boldsymbol{\epsilon}^{plas}$, according to Von Mises yielding with normality, and hardening determined by Eqn. (2.1). The incremental hydrogen strains follow the expression:

$$\Delta\boldsymbol{\epsilon}^{hyd} = \frac{1}{3}\Lambda\left(c\right)\,\Delta c\,\mathbf{I}, \tag{B.1}$$

where: c denotes the converged value of the total hydrogen concentration which is the sum of the NILS concentration c_L and trap site concentration c_T both measured in hydrogen atoms per solvent atom; Δc signifies the incremental change in the total hydrogen concentration; and $\mathbf{I}$ is the second order identity tensor. The function, $\Lambda\left(c\right)$, connects the total hydrogen concentration at a point to the change in the inelastic mean strain [84] through the expression:

$$\Lambda\left(c\right) = \frac{3V_H/V_M}{3 + (c - c_0)V_H/V_M}. \tag{B.2}$$

In Eqn. (B.2), c_0 is the initial total hydrogen concentration equal to $c_L^0 + c_T^0$, where: c_T^0 is the initial hydrogen concentration at trap sites in equilibrium with c_L^0; V_M signifies the molar volume of the metal; and V_H denotes the partial molar volume of hydrogen. Eqn. (A.4) implies that the change in the stresses, $\Delta\boldsymbol{\sigma}$, follows the relationship:

$$\Delta\boldsymbol{\sigma} = \boldsymbol{C}^e : \left(\Delta\boldsymbol{\epsilon} - \left(\Delta\boldsymbol{\epsilon}^{plas} + \Delta\boldsymbol{\epsilon}^{hyd}\right)\right), \tag{B.3}$$

where $\boldsymbol{C}^e$ equals the linear-elastic constitutive matrix.

The determination of the local stresses requires the computation of c which is found from the relationship:

$$c = c_L + c_T = \left(C_L + C_T\right)/N_L. \tag{B.4}$$

Here, C_L and C_T equal the concentration of hydrogen atoms per unit volume at the NILS and trap sites, respectively, and N_L defines the number of solvent atoms per unit lattice volume. If N_A denotes Avogadro's

number, then

$$N_L = N_A / V_A. \tag{B.5}$$

The values of the hydrogen occupancy at NILS, θ_L, and at trap sites, θ_T, determine the values of C_L and C_T, respectively. Thus, at a NILS,

$$C_L = \theta_L \beta N_L, \tag{B.6}$$

where β equals the number of NILS per solvent atom. Similarly, if the number of traps per site, α, and trap density, N_T, are known, then,

$$C_T = \theta_T \alpha N_T. \tag{B.7}$$

The trap density follows the relationship

$$N_T = \sqrt{2}\rho / \alpha. \tag{B.8}$$

The dislocation density, ρ, varies with the equivalent plastic strain such that

$$\rho = \begin{cases} \rho_0 + \gamma \bar{\varepsilon}^p, & \bar{\varepsilon}^p \leq 0.5, \\ \rho_0 + 0.5\gamma, & \bar{\varepsilon}^p > 0.5, \end{cases} \tag{B.9}$$

where ρ_0 equals the initial dislocation density; and γ is a known parameter. Table 2.1 lists the material properties used in the present study.

The numerical implementation of this constitutive model employs a backwards Euler integration scheme during the computation of the updated stresses and strains. At the beginning of each update, the algorithm calculates a trial stress based on an assumed linear-elastic response and checks this result against the current value of the yield stress. If material does not yield, only strains influenced by the hydrogen concentration are updated; otherwise, the algorithm solves for both the new values of the plastic and hydrogen strains simultaneously. A Newton's method determines the incremental values of $\Delta\varepsilon^{plas}$ and $\Delta\varepsilon^{hyd}$ in both cases. This WARP3D manual [38] provides additional details regarding the formulation and solution procedures for this constitutive method.

Appendix C

Upper Bound Estimates for a Cleavage Fracture Event During Ductile Tearing

C.1 Cleavage initiation in the ductile-to-brittle temperature transition region

Fracture persists as a challenge in the ferritic steels that comprise the primary load bearing members in essential civil, marine, petro-chemical, and power generation structures. Current developments in engineering – such as life extension measures applied to older structures, widespread use of high-strength steel alloys, and repurposing of existing infrastructure (*e.g.* transport and storage of hydrogen gas in a steel pipeline) – potentially enhance the risk of fracture. Further, operating conditions within the ductile-to-brittle transition (DBT) region for ferritic steels, *e.g.* an offshore drilling platform in icy seas, or thermal shock in a nuclear reactor pressure vessel, exacerbate these concerns and require improved mitigation strategies.

Significant amounts of stable, ductile tearing (more than a few mm's) may precede a cleavage fracture event in ferritic steels operating in the mid-to-upper end of the DBT region. During ductile crack extension prior to reaching steady-state conditions, the size of the plastic zone surrounding the advancing crack front expands, and the intensity of the near-front fields (strains-stresses) increases. Thus the likelihood of triggering a cleavage fracture event increases through the higher loading intensity and the additional volume of material subjected to severe loading. A weakest-link, Weibull characterization readily describes the strongly stochastic features of the cleavage toughness values Beremin [10], Wallin [120].

Laboratory testing of large sets of fracture specimens, *e.g.* 1T-C(T)s extracted from a single steel plate considered metallurgically homogeneous, reveals a distribution of toughness values (J-integral or equivalent K_J-values) corresponding to the amounts of stable, ductile tearing (multiple mm) prior to the cleavage fracture event that terminates the test. If steady-growth or near steady-growth conditions are attained prior to a cleavage intervention, the strain-stress fields surrounding the advancing crack no longer vary. Only the volume of the fracture process increases as the crack advances and contributes further to the greater likelihood of a cleavage fracture.

The idealized conditions of steady growth generate near-front fields representing the most severe crack front loading, and thus if used to quantify cleavage fracture processes from the onset of tearing should define an *upper-bound* estimate for the cumulative probability of cleavage fracture at each point along the specimen's tearing resistance curve ($J - \Delta a$).

The "Weibull stress," introduced by the Beremin group [10], provides a stochastic measure of the local driving force for cleavage fracture acting on the crack front:

$$\sigma_w = \left[\frac{1}{V_0} \int_V \sigma_1^m dV \right]^{1/m}. \tag{C.1}$$

The value of the Weibull stress in Eqn. (C.1) depends on the material flow properties, the metallurgical-scale inclusions/flaws/microcracks that act as cleavage triggering points, and the applied loading: m characterizes an inverse power-law, probability density function for microscale crack size; σ_1 denotes the maximum principal stress; V signifies the total volume of the material under a sufficiently high loading to produce microcracks, *i.e.* the fracture process zone, and is typically defined as the crack-front plastic zone well-contained by linear-elastic material under SSY conditions; and V_0 denotes a required dimensional scaling volume equal to unity here but in some approaches is treated as a calibratable material property.

The Weibull stress for a stationary crack increases from zero under loading that elevates stresses in material surrounding the crack front and that expands the size of the process zone. Unstable cleavage fracture initiates at a critical value of the Weibull stress when a single, microscale flaw of sufficient size in V, under local loading σ_1, triggers macroscopic fracture along the crack front, *i.e.* the classical weakest link model. The cumulative probability distribution of critical values for σ_w at cleavage fracture follows a three parameter Weibull distribution based on the work of Wallin [120] and extended by Petti and Dodds [85]:

$$P_f\left(\sigma_w\right) = 1 - \exp\left[- \left(\frac{\sigma_w^{m/4} - \sigma_{w-\min}^{m/4}}{\sigma_u^{m/4} - \sigma_{w-\min}^{m/4}} \right)^4 \right]. \tag{C.2}$$

Ferritic steels exhibit a well-demonstrated threshold toughness of approximately $K_{I-\min} = 20\,\mathrm{MPa}\sqrt{\mathrm{m}}$, below which cleavage fracture does not occur. The value of $\sigma_{w-\min}$ corresponds to the crack front loading at $K_I = 20\,\mathrm{MPa}\sqrt{\mathrm{m}}$ and represents the minimum Weibull stress for fracture; σ_u defines the value of microscale material toughness corresponding to $P_f\left(\sigma_w = \sigma_u\right) = 63\%$. All values for the Weibull stress on the right side of Eqn. (C.2) contain the value $1/V_0$ in both the numerator and denominator, and thus the dimensional scaling volume, V_0, does not influence the probability distribution. Recent research [85] regarding the Weibull stress indicates that over the DBT region: (1) the Weibull stress parameter m remains invariant

of temperature and loading rate, (2) the microscale toughness σ_u depends (rather strongly) on temperature and loading rate. Our analysis of ductile tearing presumes quasi-static crack growth and thus low loading rates; the temperature, reflected through the material response, remains constant in these analyses.

C.2 Weibull stress formulation during steady crack advance

In laboratory fracture testing, the amount of tearing prior to cleavage varies significantly from specimen-to-specimen and produces a distribution of the critical Weibull stress values, reflective of the strong stochastic features with the cleavage fracture process. Before steady-state crack growth, as shown in Fig. 1.1 where the applied load increases as the crack extends, four contributions elevate the Weibull stress of Eqn. (C.1) during ductile tearing: the local loading, σ_1, increases within V due to the higher values of the remote loading ($K_{I-\Delta a}$) coupled with a change in the crack front fields, *e.g.* from a blunt stationary crack to a sharper growing crack; the volume V expands with the shape/size of the plastic zone as $K_{I-\Delta a}$ increases; and the volume V increases as the crack advances from ductile tearing and subjects ("samples") additional material to the high levels of strains-stresses surrounding the crack front.

Once crack growth reaches steady-state conditions, the near-front fields – specifically the size of the active plastic zone and principal stress (σ_1) field – surrounding the advancing crack remain invariant with respect to an observer traveling with the crack front. Only the additional material sampled by the advancing crack then elevates the Weibull stress values in Eqn. (C.1), and thus, through Eqn. (C.2), further promotes cleavage fracture. Figure C.1 illustrates this increase in "sampled" volume of material for the propagating crack at steady-state. Crack growth at steady-state represents the peak value of the remotely applied loading, as shown in the crack-growth resistance curve, Fig. 1.1, and consequently, the assumption that steady-state conditions hold throughout the ductile tearing from initiation at the blunted crack tip (the crack-growth resistance curve remains constant at K_I^{SS}) generates upper-bound values for the Weibull stress. *The three-dimensional, elastic-plastic solutions for steady crack growth developed in this work provide, for the first time, an opportunity to quantify this upper-bound condition of tearing on cleavage fracture.*

As illustrated in Fig. C.1 (a), the size and shape of the plastic zone at steady-state remain invariant on each Z = constant plane but change along the crack front due to the three-dimensional effects (*e.g.*, at the outside surface, $Z = B/2$, plane-stress conditions must be approached). During steady crack growth, each point on the crack front advances by the uniform amount Δa, and the additional volume of sampled material can be readily computed. Figure C.1 (b) shows the condition after crack advance by amount Δa.

The increased *area* on each $Z =$ constant plane is then simply:

$$\Delta A_{SS} = h\,(Z)\,\Delta a, \tag{C.3}$$

where $h\,(Z)$ denotes the maximum height of the plastic zone in Y at the plane $Z =$ constant along the crack front and occurs at distance $X = l_h\,(Z)$ ahead of the front. Over the crack front, from $-B/2 \leq Z \leq B/2$, both $h\,(Z)$ and $l_h\,(Z)$ vary, as Fig. C.2 shows, and together define a curved surface, denoted H_{SS}. Consider two points, a and b, that lie along the uncracked ligament ($Y = 0$) on H_{SS}. As shown in Fig. C.2: the differential length, dZ, separates a and b in the Z direction; the vector $\underset{\sim}{l}^{ab}$ connects these points; and the vector $\underset{\sim}{h}^{ab}$ represents the maximum height of the forward plastic zone over dZ. The vector formed by $\underset{\sim}{h}^{ab} \times \underset{\sim}{l}^{ab}$

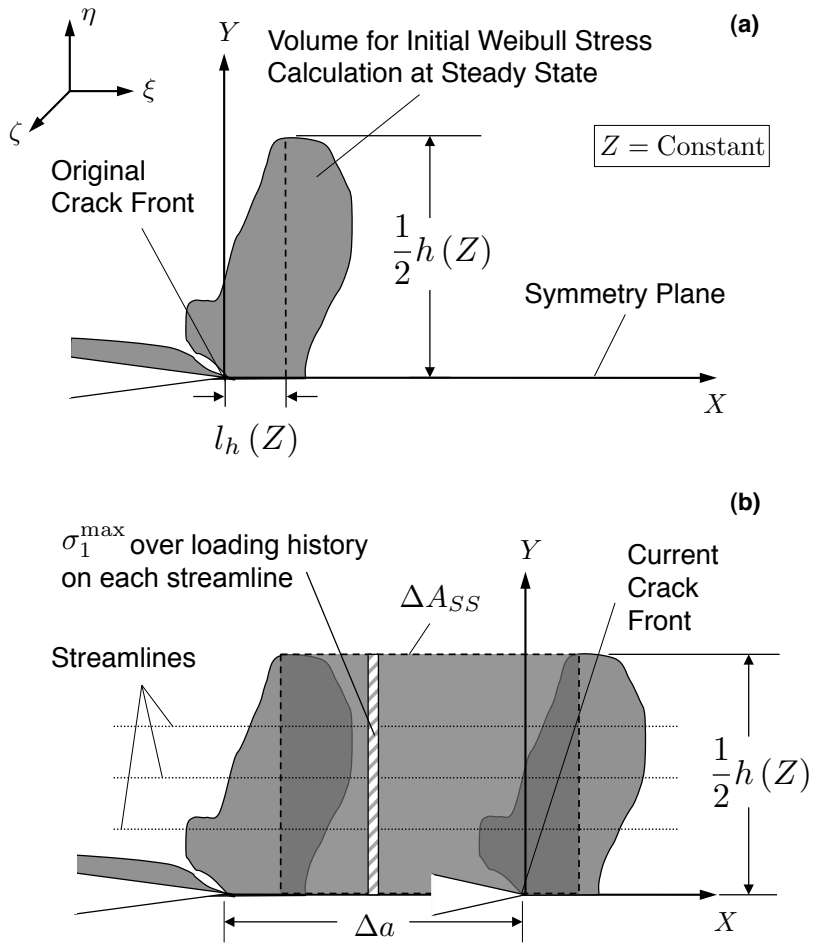

Figure C.1: Increase of the sampled volume for a steadily propagating Mode I crack after growth Δa. Crack growth adds additional area (hatched region) to ΔA_{SS}.

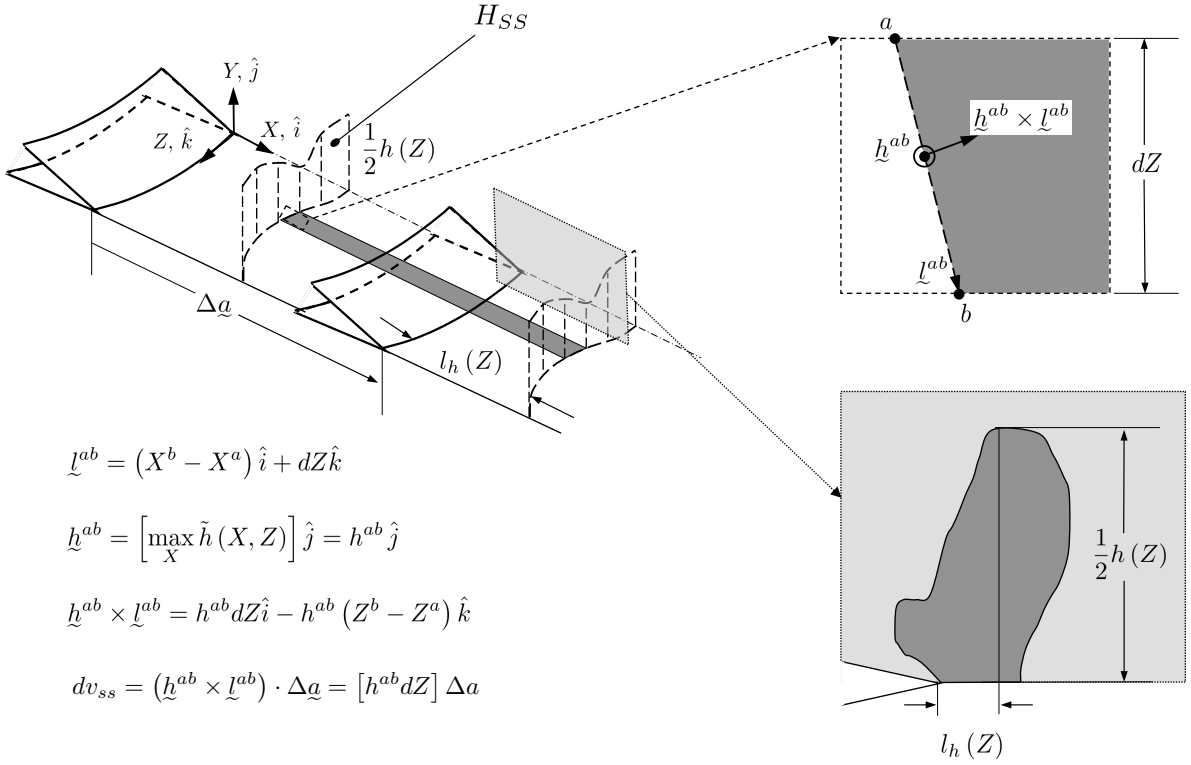

Figure C.2: The location for the maximum height of the plastic zone size along the crack front in a 3D framework produces a curved surface that advances with crack growth. A differential volume, dv_{ss}, increases by the amount of this surface perpendicular to the crack growth direction times the amount of crack growth.

describes the magnitude and direction of the surface area in H_{SS} between the points a and b. Thus, the additional differential volume generated by crack growth of amount Δa in the X-direction ($\Delta\underset{\sim}{a} = \Delta a\,\hat{i}$) between the points a and b equals:

$$dv_{ss} = \left(\underset{\sim}{h}^{ab} \times \underset{\sim}{l}^{ab}\right) \cdot \Delta\underset{\sim}{a} = \left(h^{ab}\Delta a\right) dZ = \Delta A_{SS}\left(Z^{ab}\right) dZ, \tag{C.4}$$

since $h^{ab} = h\left(Z^{ab}\right)$ over dZ. Then, the additional, sampled volume of material (ΔV_{SS}) during steady growth becomes:

$$\Delta V_{SS} = \int_{-B/2}^{+B/2} dv_{ss} = \int_{-B/2}^{+B/2} \Delta A_{SS}(X_3)\, dZ = \left(\int_{-B/2}^{+B/2} h(X_3)\, dZ\right) \Delta a = H_{SS}\Delta a. \tag{C.5}$$

During steady-state crack growth, H_{SS} (units of area) denotes the surface formed by connecting $h(Z)$ at each point Z along the crack front and, consequently, represents the maximum area perpendicular to the direction of the advancing crack front subject to plastic deformation. For example, a crack front in a plane-

strain framework (h invariant of Z) simplifies to $H_{SS} = hB$. In three dimensions, $H_{SS} = \bar{h}B$, where $\bar{h}$ is the mean value of $h(Z)$ over $-B/2 \leq Z \leq B/2$.

Evaluation of the Weibull stress in Eqn. (C.1) proceeds by integrating σ_1^m over the volume of all the plastically deformed material at the crack front and, for this calculation, σ_1 corresponds to the maximum principal stress experienced at each point *throughout the loading history*. This methodology ensures that the Weibull stress never decreases during ductile tearing – the material damage does not self-heal once stresses decrease. For steady-growth computations, we again consider the viewpoint of an observer situated at the moving crack front in $\xi - \eta - \zeta$ system shown in Fig. 4.2. At time t_0, the point $\alpha = A$ on the streamline at (Y, Z) experiences the maximum value of the principal stress, $\sigma_1^{\max}(X, Z)$. As the crack advances (Δa increases), all points on this streamline to the right of α pass through A and experience $\sigma_1^{\max}(Y, Z)$. Therefore, during the Weibull stress calculation, the value of σ_1 along the streamline (Y, Z) at and to the right of α is simply $\sigma_1^{\max}(Y, Z)$. Crack advance produces the same effect on every streamline. In summary, the surface H_{SS} sweeps forward with crack advance through new material, increases ΔV_{SS} proportionally to Δa, and leads to stresses within ΔV_{SS} equal to $\sigma_1^{\max}(Y, Z)$ along each streamline (Y, Z). Therefore, steady crack growth increases the cumulative Weibull stress raised to the m^{th} power by:

$$\left[\Delta\sigma_w^{SS}(\Delta a)\right]^m = \int_0^{\Delta a} \left[\frac{1}{V_0}\int_{H_{SS}} \left[\sigma_1^{max}(Y, Z)\right]^m dY\, dZ\right] dX = S_w^{H_{SS}}\Delta a, \tag{C.6}$$

where $S_w^{H_{SS}}$ denotes the invariant value of the bracketed integral in Eqn. (C.6). The calculation of $S_w^{H_{SS}}$ requires only minor adjustments during the solution for steady crack growth. At each point (Y, Z) on the surface H_{SS}, the maximum value of the principal stress along the streamline at (Y, Z) in the forward plastic zone is recorded, $\sigma_1^{\max}(Y, Z)$. While post-processing, the integration of $(\sigma_1^{\max})^m$ over H_{SS} produces $S_w^{H_{SS}}$ – a single, constant quantity that determines the Weibull stress as a function of steady crack growth. The value of $S_w^{H_{SS}}$ thus represents the rate of increase for the Weibull stress per unit of steady crack extension.

This approach generates an expression for the Weibull stress as a simple function of the steady crack extension, Δa:

$$\sigma_w^{SS}(\Delta a) = \left[\left(\bar{\sigma}_w^{SS}\right)^m + S_w^{H_{SS}}\Delta a\right]^{1/m}. \tag{C.7}$$

At $\Delta a = 0$ in Eqn. (C.7), $\sigma_w^{SS}(0) = \bar{\sigma}_w^{SS}$, *i.e.* the Weibull stress value at the onset of steady ductile tearing, and thus remains constant during subsequent crack growth. Differentiation of $\sigma_w^{SS}(\Delta a)$ in Eqn. (C.7) reveals that $d\sigma_w^{SS} \propto \left[\sigma_w^{SS}(\Delta a)\right]^{1-m} da$. Thus continued crack advance leads to diminishingly small increases in σ_w^{SS}, even in SSY.

The calculation of $\bar{\sigma}_w^{SS}$ requires the history dependent response for the propagating crack prior to steady-

state and cannot be determined from the steady-state analysis. However, if we assume steady-state conditions prevail right from the onset of ductile tearing, then the near-front fields from a finite element analysis of a stationary crack at the steady-state loading provides $\bar{\sigma}_w^{SS}$. This approach implies a flat crack-growth resistance curve at a constant value of the remote loading (equal to the steady-state value) and yields an upper-bound value for the Weibull stress. The expression for $P_f(\sigma_w)$ in Eqn. (C.2) leads to a cumulative probability of failure as a function of crack extension.

C.3 Experimental prediction comparisons

Wallin [121] developed an approximate analysis to characterize the stochastic behavior of cleavage fracture events in a ferritic steel with small amounts of ductile tearing. For a material with flow stress, σ_{flow}, the probability of failure increases with the applied loading and crack growth according to the expression:

$$P_f = 1 - \exp\left(-\left[\left(\frac{K - K_{\min}}{K_0 - K_{\min}}\right)\left(\frac{B}{B_0}\right)\left(1 + \frac{2\,\Delta a\,\sigma_{flow}^2}{K^2\beta}\right)\right]\right). \tag{C.8}$$

In Eqn. (C.8), K_0 and B_0 represent normalization factors for the fracture toughness and reference specimen thickness, respectively. The constant β denotes the size of the cleavage fracture process zone proportional to $(K/\sigma_{flow})^2$ and equals 0.0058 for the 2 1/4 Cr 1 Mo steel studied by Wallin.

Using this approximate analysis, Wallin examines several data sets of toughness for ferritic steels tested in the mid-to-upper DBT region using C(T) specimens. Wallin argues that the "effective" value of the applied load for cleavage fracture experienced by the crack front remains constant once high levels of plasticity are reached. This assumption reflects the observations of constraint loss even in C(T) specimens at gross plasticity when the opening mode stresses no longer increase. Thus Wallin's analysis adopts a constant value for the applied loading, *i.e.* $K = K_{eff}$, and the plastically deformed volume increases linearly with Δa. The approach described here with a Weibull stress framework reflects this same assumption. Wallin further assumes the probability of failure depends directly on the sampled volume, *i.e.* $P_f = 1 - \exp(-(V/V_0))$, whereas the probability of failure depends indirectly on the sampled volume through the Weibull stress in the Eqns. (C.2) and (C.7). Both the present and Wallin's approaches indicate the probability of failure increases nonlinearly with crack extension and generates vanishingly small changes in the cumulative failure probability for large levels of crack advance under high loads.

In one study, Wallin [122] investigates the probability of cleavage failure after ductile tearing in 105 tested C(T) specimens for a 2 1/4 Cr 1 Mo steel and compares the measured toughness distribution with the estimate from Eqn. (C.8). This steel yields at 300 MPa at room temperature and has an ultimate

m	$\sigma_{w-\min}$ (MPa)	$\bar{\sigma}_w$ (MPa)	σ_u (MPa)	$\left(S_w^{H_{SS}}\right)^{1/m}$ $\left(\text{MPa/mm}^{(1/m)}\right)$
14	187	365	389	362
16	228	410	434	413
18	268	451	474	459
20	304	488	510	499
22	339	521	543	536

Table C.1: Values for the estimate of the toughness distribution increasing with ductile tearing.

strength of 532 MPa. The thickness of the specimens with side-grooves equals 20 mm and is equivalent to the reference thickness, B_0. Maximum likelihood estimates using toughness values for the specimens without crack growth produce $K_{\min} = 20$ MPa$\sqrt{\text{m}}$ and $K_0 = 260$ MPa$\sqrt{\text{m}}$, and Wallin's estimate for $K_{eff} = 208$ MPa$\sqrt{\text{m}}$ where the applied K-values continue to increase but the crack front stresses remain unchanged. The prediction from Eqn. (C.8) for the increase in the probability of failure due to crack growth and the measured toughness distribution exhibit excellent agreement for $\Delta a \geq 0.5$ mm (Fig. 5 in [122]). Transient crack-growth conditions exist prior to $\Delta a \approx 0.6$ mm and preclude the application of steady-state assumptions.

Preliminary investigations described here explore the feasibility of the proposed Weibull stress framework for steady growth using the same 2 1/4 Cr 1 Mo toughness data set. The required crack-front stress fields at steady-state to compute $\sigma_w^{SS}(\Delta a)$ are developed using the *plane-strain*, steady growth finite element code. In these calculations, this steel hardens isotropically after yielding and follows approximately a power-law relationship with exponent $n = 10$. Test data sufficient for calibration of the Weibull exponent (m) are not available. Consequently, our analyses explore a range of m-values (14-22) calibrated previously for other, moderate-strength pressure vessel steels. The values of $\sigma_{w-\min}$, $\bar{\sigma}_w^{SS}$, and σ_u in Eqns. (C.2) and (C.7) correspond to the Weibull stress values for a SSY plane-strain analysis of a stationary crack and a remote load equal to Wallin's values for K_{min}, K_{eff}, and K_0, respectively. The steady-growth, finite element procedure produces the estimate for $S_w^{H_{SS}}$. Table C.1 displays the quantities $\sigma_{w-\min}$, $\bar{\sigma}_w^{SS}$, σ_u, and $S_w^{H_{SS}}$ as a function of m with V_0 equal to unity. The small-strain formulation adopted in the steady-state analyses produces singular stress values at the crack tip and thus requires a limit on the value of the maximum principal stress used in the Weibull stress computations. The limit here of 3.8 times the yield stress corresponds to the peak stress attained ahead of a stationary, blunting crack tip for the $n = 10$ flow properties. This restriction ensures that the crack-tip singularity does not artificially raise the Weibull stress.

Figure C.3 presents the results for Wallin's approximate analysis, the simple rank estimate probabilities for the raw experimental values and the present steady-state prediction, based on Eqns. (C.2) and (C.7). *These preliminary results are encouraging for the proposed steady-state, Weibull stress framework for the*

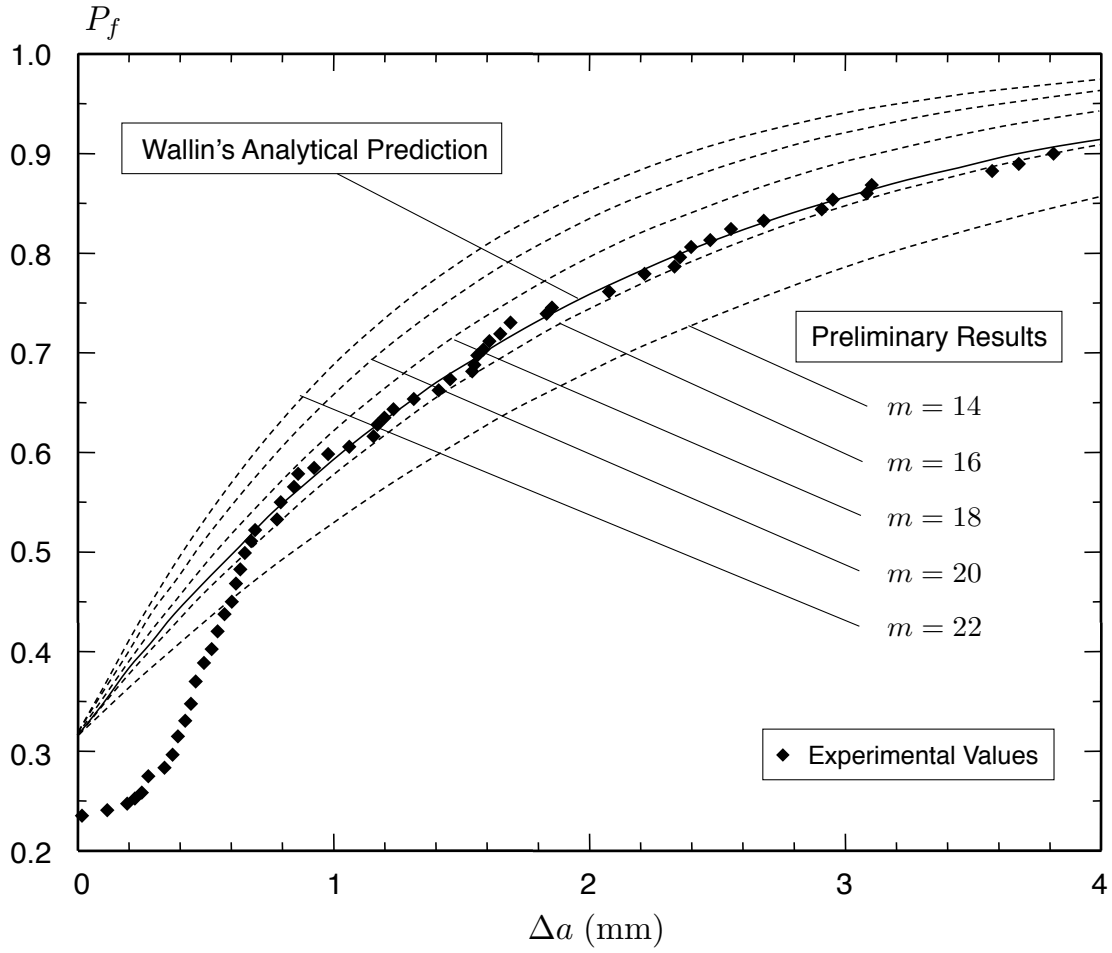

Figure C.3: Comparison of Wallin's probability of failure function [122] due to ductile tearing for a 2 1/4 Cr 1 Mo steel *vs.* the probability of failure prediction from the steady-state analysis for different values of the material parameter m. The experimental results show good agreement with both predictions following 0.6 mm of crack growth.

increasing probability that a cleavage event occurs with ductile tearing. As expected, the predicted toughness distribution depends strongly on the value of m as ductile tearing increases, and the probability of cleavage increases with m for the same amount of ductile tearing, Δa. When crack growth is negligible, the probability estimates collapse onto the prediction from Wallin's analysis regardless of m, and this result suggests the correctness of $\sigma_{w-\min}$, $\bar{\sigma}_w^{SS}$, and σ_u. The probability distributions based on the Weibull stress agree well with Wallin's approximate model and with the experimental values under steady-state conditions, especially for $m = 16$.

Our future analyses will employ the actual near-front fields for a steadily propagating crack from the 3D simulations. The proposed Weibull stress framework opens the opportunity to include, for example,

constraint loss and dynamic loading effects in a rational model and will introduce an advancement in failure assessment technology.

Appendix D

FIREFLY Software

The special-purpose finite element code, FIREFLY, developed in this work employs a mixed environment of Matlab code and compiled code (C++, F-90) to compute the near-front fields for a steadily propagating crack under 3D SSY conditions, using the streamline integration scheme presented in Sec. 4.2.3. The Matlab framework reduces code development effort and provides extensive native commands for data manipulation, memory management, read and write functions, the ability to save and restart analyses, graphics, etc... Yet as an interpretive language, user-generated Matlab code that contains control sequences (loops, etc...) operating on very large, finite element-type data structures leads to run-times that exceed many times those for the same routines developed using compiled languages, C++ or F-90. Such Matlab code also cannot directly bind itself to various pre-compiled libraries and cannot directly access parallel execution methods, such as threads via OpenMP. These characteristics of user-generated Matlab code lead to unrealistic execution times for the large-scale computations of 3D steady growth analysis of the type described in this study (multiple days per analysis).

FIREFLY couples conventional Matlab code with pre-compiled C++ and F-90 code through the Matlab-EXecutable (MEX) interface to exploit the much higher execution efficiency of compiled code and to access multiple processors/cores available on the hardware to achieve parallel processing. Matlab calls a "MEX" program during execution and transfers control to a MEX gateway function written in C++. These user-generated MEX functions focus on: assembly of the structural stiffness matrix; computation of strains and updating stresses at Gauss points; and factorization/solve of the equilibrium equations with the parallel, Intel direct sparse solver [65]. Individual routines indicate speed-ups on the order of 10^3 compared to computations using conventional Matlab code, as shown by Fig. D.1.

Using MEX-based interface routines provided with Matlab, the main gateway function maps large data arrays from Matlab internal forms into those accessible by the C++ and F-90 code. The gateway function passes the mapped data into these functions that organize computations over Gauss points in the required order along each streamline. Using OpenMP directives together with the streamline-based data structures, computations required to update all Gauss points located on a single streamline are assigned to one thread

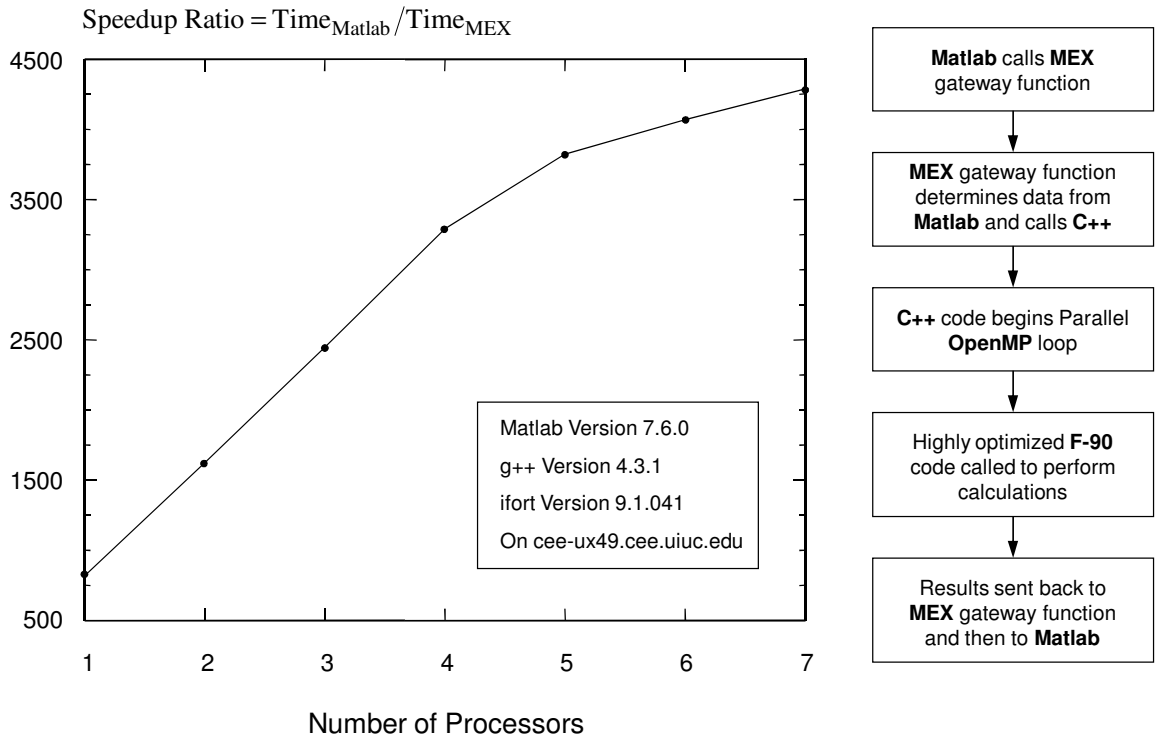

Figure D.1: Ratio of the average time required to compute the strains at ∼400,000 Gauss points by Matlab EXectuable (MEX) pre-compiled code to pure Matlab code. The MEX computational procedure, outlined to the right, executes in parallel with an increasing number of processors, whereas the pure Matlab code executes in serial.

for execution. Because updating each streamline requires no interaction with other streamlines, as many streamlines are processed concurrently in this code structure as available cores to execute the threads. Highly optimized F-90 routines perform the most computationally intensive calculations within each thread. By structuring the data and strain-stress updating code to execute in parallel over entire streamlines rather than over individual elements, the overhead to start/stop parallel execution becomes vanishingly small. To compute the residual forces at each iteration, the global vector is partitioned into groups of nodes, with the number of groups equal to the number of available threads. Each concurrently executing thread invokes element level routines to compute contributions to nodal forces from the updated stresses and to assemble (scatter) terms into the global group for the thread.

During the analysis, FIREFLY applies full displacements for the specified K_I to the remote boundary nodes, and then forms and factors the linear-elastic structural stiffness matrix (equilibrium equations) once, as in Dean and Hutchinson [21]. Global Newton iterations to reduce nodal residual forces require the bulk of the computational effect. Updating and integrating the material stress history along streamlines and

computation of element-level nodal forces requires the major effort, but executes concurrently on multiple processors/cores. For the steady growth analysis of the finite element model shown in Fig. 4.3, the structural stiffness matrix contains nearly 110 million non-zero entries. Using an eight core Linux compute server, FIREFLY completes the solution in 10 hours of wall clock time with less than 30 GB of RAM.

Appendix E

Self-similarity scaling in 3D SSY based on a single characteristic length

E.1 Introduction

Earlier studies of constraint effects on crack fronts in 3D SSY focus on stationary cracks or examine early transient stages of crack growth. Yuan and Brocks [133] employ a 3D boundary layer model for a stationary crack front under non-zero values for the T-stress. Their results show that the relationship between the T-stress and Q-stress depends strongly on the size of the plastic zone with respect to the thickness. Kim et al. [48] show that $J - A_2$ solutions for stationary crack fronts agree with finite element results on the centerplane but diverge from T-stress results near the free surface at high loading levels. Furthermore, local J-integral values along the crack front depend on the remotely imposed level of T-stress in 3D SSY, in contrast to plane-strain or plane-stress SSY conditions. Roychowdhury and Dodds [97] extend the 3D SSY framework to model fatigue crack growth and study T-stress effects on plasticity induced crack closure through the thickness. Non-zero values for the T-stress generate near uniform opening loads along the crack front.

Within a plane-strain SSY framework, Varias and Shih [117] provide the key study of T-stress effects on the steadily-advancing, crack-tip response and show that the near-tip fields – stresses, strains, and displacements – display a self-similarity scaling with a characteristic length influenced by the T-stress. Each field component collapses into a single curve described by normalized radial dimension within a forward angular sector translating with the crack tip. The characteristic length-scale provides a measure of the imposed constraint on the plastic deformation intensity along the uncracked plane. Furthermore, non-zero T-stress – positive and negative – influence the 2D mechanical fields similarly, *e.g.* opening-mode stresses along the uncracked plane reach a peak value under $T = 0$ loading. From these results, Varias and Shih [117] predict lower steady-state toughness in zero T-stress configurations.

Chapter 4 reports the first investigations of steady-state crack growth within a 3D SSY framework under mode I loading. These results demonstrate that a nondimensional loading parameter, $\bar{K}$, based on the remotely applied loading, material flow properties, and thickness, controls the straight crack-front response

in a normalized coordinate system. The quantity $\bar{K}^2$ proportionally measures the active yielding region size along the uncracked plane at the centerplane relative to the thickness. High triaxiality conditions (near plane strain) develop deep within the plastic zone over significant distances from the crack front only under low loading levels, and an increasingly plane-stress response occurs at high $\bar{K}$. These preliminary analyses only consider the relatively restricted constraint condition $T = 0$.

The present study extends the previous work in Chapter 4 to model in-plane constraint effects during steady crack growth within the 3D SSY regime. Analyses focus on the influence of the remotely imposed T-stress on the near-front response under low and high loading levels, $\bar{K}$ =1 and 3, and investigate the characteristic length scale approach of Varias and Shih [117]. These results demonstrate that the simple one parameter characterization fails to properly scale the crack-front response due to triaxiality loss through the thickness, but individual characteristic length scales exist for separate stress-strain components.

This appendix proceeds as follows. Section E.2 presents a theoretical approach to characterize the loading level and to achieve a self-similarity scaling based on the applied mode I loading and imposed T-stress. Section E.3 explores the characteristic length-scale method proposed by Varias and Shih [117] to provide a self-similarity scaling for the near-front fields within the 3D SSY regime.

E.2 Self-similar fields based on a characteristic length

Within a plane-strain SSY framework, the plastic zone size, r_p, provides the only physical length scale, and the near-tip fields exhibit a similarity scaling for radial distances normalized by some measure of r_p. Popular measures include $(K_I/\sigma_0)^2$ and J/σ_0 since both quantities scale proportionally with the plastic zone size along the uncracked plane, r_{p0}. Remotely imposed T-stress provides the only influence for the characteristic dimensions of the plastic zone. These considerations apply to both stationary and steadily advancing crack tip responses.

During steady-state crack growth, Varias and Shih [117] demonstrate the existence of a characteristic dimension, L_g, that is proportional to r_{p0}, and recognize that:

$$L_g = \gamma\left(T/\sigma_0\right)\left(\frac{K_I}{\sigma_0}\right)^2. \tag{E.1}$$

Here, the nondimensional parameter $\gamma\left(T/\sigma_0\right)$ reflects the influence of T/σ_0 on L_g. Varias and Shih [117] provide a convenient definition of L_g based on the equivalent plastic strain, $\bar{\varepsilon}^p$, along the uncracked plane

such that:

$$\bar{\varepsilon}^p\left(r=\frac{L_g}{\left(K_I/\sigma_0\right)^2},\theta=0^\circ;\frac{T}{\sigma_0}\right)=\bar{\varepsilon}^p\left(\frac{r_{p0}/2}{\left(K_I/\sigma_0\right)^2},0^\circ;\frac{T}{\sigma_0}=0\right). \tag{E.2}$$

According to Eqn. (E.2), $L_g = r_{p0}/2$ under a $T/\sigma_0 = 0$ loading, and thus L_g measures the influence of T-stress on the near-front fields deep within the active yielding region. Smaller L_g values, relative to $r_{p0}/2$, reflect less inelastic deformation from the T-stress.

Within the region $r/L_g \leq 1$ and $|\theta| \leq 90^\circ$, the scaled, strain, and displacement fields described by normalized radial dimensions, r/L_g, exhibit self-similarity under the T-stress levels: $-1 \leq T/\sigma_0 \leq +1$. Further, the self-similar region extends around the entire crack front from $r/L_g \leq 1.4$ under negative T-stress. Thus the following expression represents the plane-strain stress fields:

$$\sigma_{ij}=\sigma_0 h_{ij}\left(\frac{r}{L_g},\theta;\frac{E}{\sigma_0},n,\nu\right). \tag{E.3}$$

Varias and Shih [117] demonstrate that non-zero – positive or negative – T-stress values imposed at the far-field boundary shield the crack tip and decrease the stresses and strains ahead of the crack front. The variation of L_g with T/σ_0 reflects this trend; the value for L_g reaches a maximum value under $T/\sigma_0 = 0$ loading. Consequently, Varias and Shih [117] develop a strain-controlled relationship between T/σ_0 and the observed steady-state material toughness, and their calculations indicate that the steady-state toughness reaches a minimum value within a zero T-stress configuration.

Steady crack growth within a 3D context does not develop fully the high triaxial stresses characteristic of the plane-strain response, especially at high loading levels, *e.g.* $\bar{K} = 3$. Furthermore, r_{p0} and the plastic wake height vary with distance along the crack front, Z/B. These considerations suggest a reduced applicability for the characteristic length introduced by Varias and Shih [117] for crack growth within the 3D SSY framework.

Our results demonstrate the existence of a characteristic length scale, L_g, for each field component under constant $\bar{K}$ and that remains constant over the majority of the crack front. Each field component then displays a self-similar relationship for a constant $\bar{K}$ value, where L_g scales the radial dimension. For the principal stresses, σ_i $(i = 1, 2, 3)$, the relationship corresponding to Eqn. (5.5) becomes:

$$\sigma_i=\sigma_0 H_i\left(\frac{r}{L_g},\theta,\frac{Z}{B};\frac{K_I}{\sigma_0\sqrt{B}};\frac{E}{\sigma_0},n,\nu\right). \tag{E.4}$$

This result remains limited to regions where high triaxial stresses develop along the crack front. Furthermore, all near-front field quantities cannot be described as shown in Eqn. (E.4) and do not exhibit a self-similarity

	$\bar{T} = +0.25$		$\bar{T} = 0$		$\bar{T} = -0.25$		$\bar{T} = -0.50$		$\lvert\theta_{lim}\ (^\circ)\rvert$		
	$\frac{L_g}{J/\sigma_0}$	$\frac{L_g}{B}$	$\frac{L_g}{J/\sigma_0}$	$\frac{L_g}{B}$	$\frac{L_g}{J/\sigma_0}$	$\frac{L_g}{B}$	$\frac{L_g}{J/\sigma_0}$	$\frac{L_g}{B}$	$\frac{r_{lim}}{L_g} = 1,\ 2,\ 4$		
σ_1	5.015	0.0201	5	0.02	4.599	0.0184	3.941	0.0158	180	72	none
σ_2	5.124	0.0205	5	0.02	4.504	0.0180	3.769	0.0151	36	36	27
σ_3	4.947	0.0198	5	0.02	4.675	0.0187	4.019	0.0161	54	54	27
ε_1	4.898	0.0196	5	0.02	4.736	0.0189	4.124	0.0165	18	none	none

Table E.1: Characteristic lengths, L_g, of the principal stresses and strains for a steadily advancing crack front in a 3D SSY framework under $\bar{K} = 1$ loading and non-zero values of the imposed T-stress. The minimum region where the similarity scaling applies occurs within the angular sector $r \leq r_{lim}$ and $-\theta_{lim} \leq \theta \leq \theta_{lim}$ between $-0.4 \leq Z/B \leq 0.4$. Within this region, the maximum difference between stresses does not exceed 10% of the yield stress, or the maximum difference between strains does not exceed 10% of the yield strain. This table shows L_g for the principal stresses – σ_1, σ_2, and σ_3 – and the first principal strain, ε_1. The L_g scaling does not hold for ε_2 and ε_3.

scaling with the T-stress. Instead, these quantities require a full two-parameter description, as in Eqn. (5.5). Finally, non-zero values for the T-stress may increase near-front quantities relative to the $\bar{T} = 0$ configuration, *i.e.* L_g increases, and this result contrasts with the earlier response in plane strain. Section E.3 presents the characteristic length approach to self-similarity scaling during steady crack growth in 3D SSY.

E.3 Similarity scaling based on a characteristic length

Within a 3D SSY framework, the near-front fields exhibit a similarity scaling characterized by two nondimensional loading parameters, $\bar{K} = K_I/\sigma_0\sqrt{B}$ and $\bar{T} = T/\sigma_0$, during steady crack advance, as demonstrated by Chapter 5. Following the precedent of Varias and Shih [117], this section investigates a characteristic length, L_g, that varies with $\bar{T}$, to normalize radial dimensions, and to describe in-plane constraint effects over micro-structurally relevant length scales. Here we define L_g for each principal stress (strain) component as:

$$\sigma_i^* = \sigma_i \left(\frac{L_g}{J/\sigma_0}, \theta = 0^\circ, \frac{Z}{B} = 0; \frac{K_I}{\sigma_0\sqrt{B}}, \frac{T}{\sigma_0}; \frac{E}{\sigma_0}, n, \nu \right), \tag{E.5}$$

and in Eqn. (E.5), σ_i^* equals some arbitrary value for σ_i near the crack front. This discussion considers only the loading level $\bar{K} = 1$. At higher loading levels, *e.g.* $\bar{K} = 3$, the imposed T-stress has less influence on the near-front variation due to the increasingly plane-stress response and low triaxial stresses.

Table E.1 summarizes the characteristic length relationships (L_g with $\bar{T}$) computed for the principal stresses and strains – these relationships are further described in the following sections. Section E.3.1 presents the first principal stress variation along the uncracked plane and demonstrates the similarity scaling by L_g through the plate thickness (Z/B). In Sec. E.3.2, the results show that the characteristic length continues to

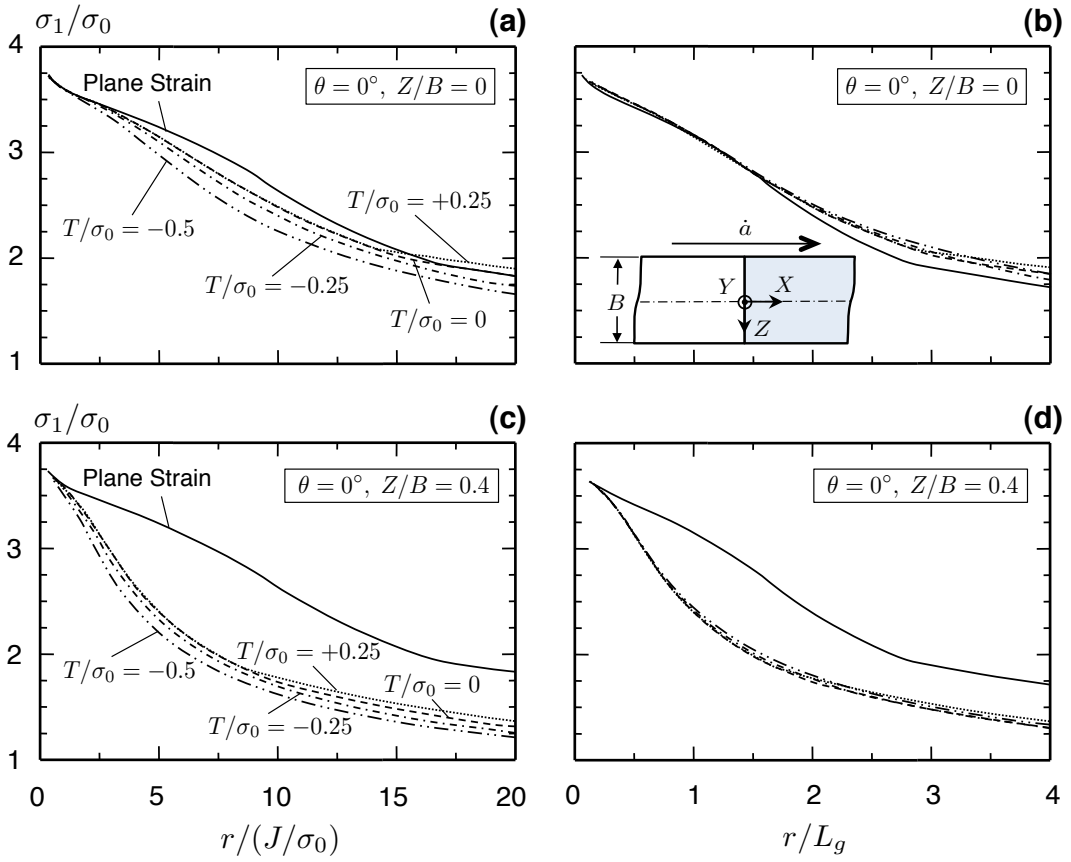

Figure E.1: Normalized first principal stress component, σ_1/σ_0, variation with scaled radial distance along the crack plane ($\theta = 0°$) under $\bar{K} = 1$ loading. Results are shown in (a,b) at mid-thickness ($Z/B = 0$) and in (c,d) closer to the outside surface ($Z/B = 0.4$). The steady-growth, plane-strain solution $T/\sigma_0 = 0$ is provided for reference. The distance J/σ_0 scales the radial dimensions in (a,c) whereas the characteristic length scale, L_g, scales the radial dimensions in (b,d). The near-front fields collapse into a single curve approaching the crack front in coordinates scaled by the characteristic dimension, L_g.

scale the first principal stress off the uncracked plane ($\theta \neq 0°$). Section E.3.3 demonstrates the characteristic length scaling for the first, second, and third principal stresses that fully describe the stress state ahead of the advancing crack front.

E.3.1 Similarity along the crack front

Figure E.1 demonstrates the similarity scaling for the first principal stress along the uncracked plane ($\theta = 0°$). The imposed T-stress values differ from $\bar{T}$ =0, +0.25, -0.25, and -0.5 imposed on the 3D SSY boundary, under the low loading level $\bar{K} = 1$. The crack front location (Z/B) varies between the two rows from $Z/B = 0$ in the upper row (a,b) to $Z/B = 0.4$ in the lower row (c,d). The length J/σ_0 normalizes the radial dimensions in the left column, whereas the characteristic length L_g (shown in Tab. E.1) normalizes

the radial dimension in the right column. Figure E.1 also presents the plane-strain principal stress in a $\bar{T} = 0$ configuration. The definition for L_g in Eqn. (E.5) is applied to the plane-strain results to determine a corresponding value for the characteristic length and yields the quantity $L_g/(J/\sigma_0) = 5.92$ with $\bar{T} = 0$. The radial dimensions shown in Fig. E.1 lie deep within the 3D active yielding region with $r/(J/\sigma_0) = 20$ corresponding to one-third of the distance from the crack front to the yielding boundary.

The characteristic length scale described in Eqn. (E.5) produces a similarity scaling along the crack front (Z/B) for the imposed constraint levels, as shown in Fig. E.1. The first principal stress along more than eighty percent of the crack front ($-0.4 \leq Z/B \leq 0.4$) collapses into a single curve along the uncracked plane. The quality of the similarity scaling degrades farther from the crack tip and indicates a transition from plane strain to more 3D characteristics. Closer to the free surface ($Z/B \rightarrow 0.5$), the similarity scaling with L_g breaks down due to the significantly reduced triaxiality.

The crack front location, Z/B, alters the near-front fields more strongly than $\bar{T}$. Near the mid-thickness, a low constraint configuration ($\bar{T} = -0.50$) reduces the principal stress from the zero T-stress configuration by a quarter of the yield stress, but σ_1 decreases by half the yield stress from Z/B =0 to 0.4 for $\bar{T} = 0$. The negative T-stress uniformly reduces the principal strain along the crack front. In contrast, a positive T-stress ($\bar{T} = +0.25$) has only a small influence on the first principal stress close to the crack front and compared to the $\bar{T} = 0$ results.

E.3.2 Similarity surrounding the crack front

Figure E.2 presents the similarity scaling variation for the first principal stress, σ_1/σ_0, with radial distance (r) on the centerplane ($Z/B = 0$) at different constant angular values (θ). The T-stress values vary from $\bar{T}$ =0, +0.25, -0.25, and -0.5 imposed on the 3D SSY boundary, under the low loading level $\bar{K} = 1$. The constant angle varies among the rows with (a,b) $\theta = 0°$, (c,d) $\theta = 27°$, and (e,f) $\theta = 54°$. The length J/σ_0 normalizes the radial dimensions in the left column, whereas the characteristic length L_g (shown in Tab. E.1) normalizes the radial dimension in the right column. Figure E.2 also presents the plane-strain principal stress value in a $\bar{T} = 0$ configuration.

Very close the crack front ($r/L_g \leq 1$), T-stress uniformly alters the first principal stress surrounding the crack front, *i.e.* over $-180° \leq \theta \leq 180°$ according to Table E.1. Here, negative T-stress reduces σ_1, and small positive T-stress ($\bar{T} = +0.25$) negligibly influences σ_1. Farther from the crack tip, triaxiality loss leads to the end of the characteristic scaling around the crack front. In applying these results to a stress-controlled micromechanical processes – cleavage initiation following sustained ductile tearing – leads to a strong dependence on the length scale, L_g, over a significant portion of the crack front. The characteristic

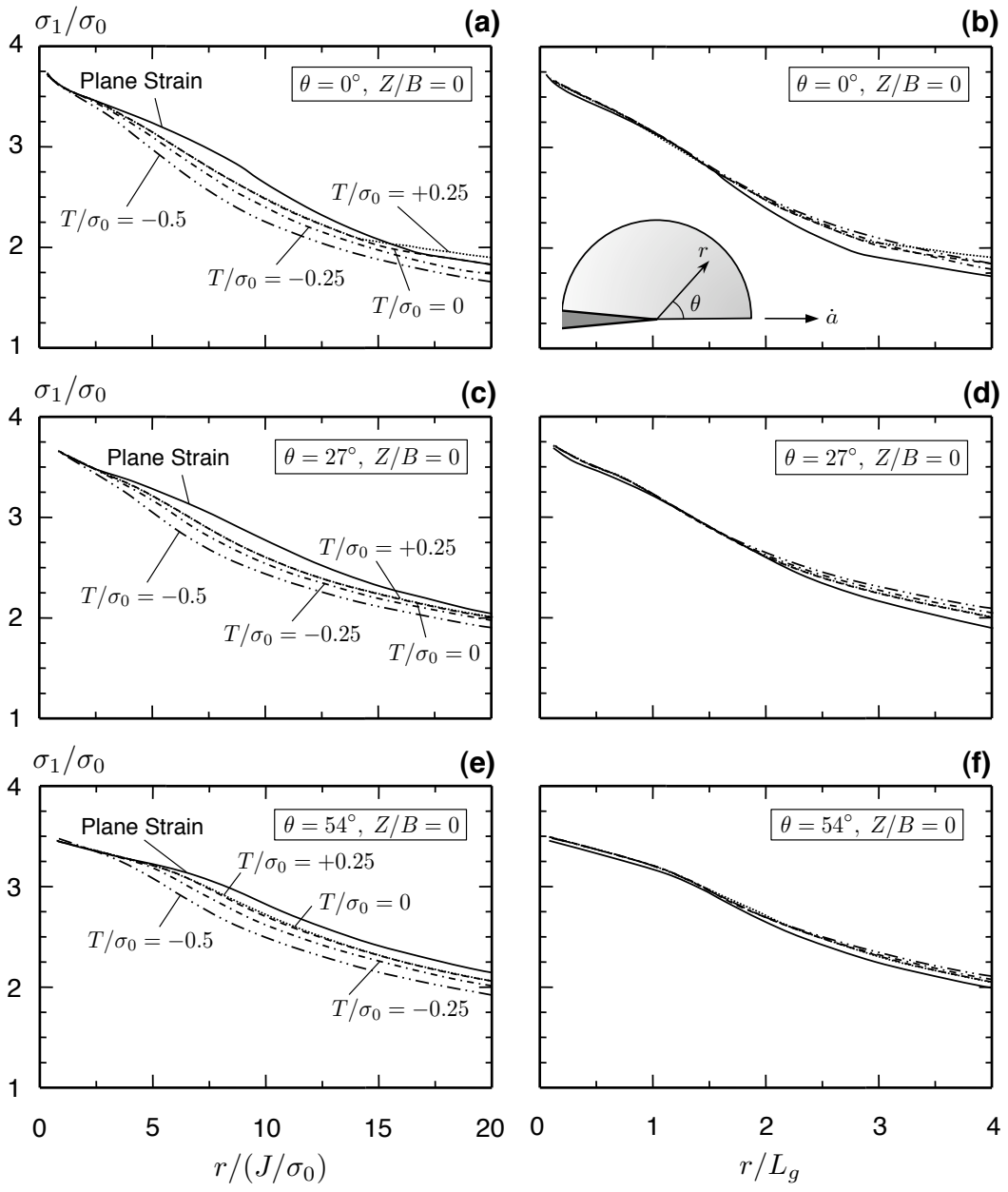

Figure E.2: Normalized first principal stress component, σ_1/σ_0, variation with scaled radial distance on the centerplane ($Z/B = 0$) under $\bar{K} = 1$ loading. Results are shown: in (a,b) at $\theta = 0°$; in (c,d) at $\theta = 27°$; and in (e,f) at $\theta = 54°$. The steady-growth, plane-strain solution at $T/\sigma_0 = 0$ is provided for reference. The distance J/σ_0 scales the radial dimensions in (a,c,e) whereas the characteristic length scale, L_g, scales the radial dimensions in (b,d,f). The near-front fields collapse into a single curve approaching the crack front in coordinates scaled by the characteristic dimension, L_g.

length scale, L_g, controls the volume of the fracture process zone in Weibull stress calculations where critical stresses develop during crack advance. The length scale, L_g, indicates that the process zone size for cleavage decreases in low constraint configurations. However, the incremental increase in the Weibull stress depends only on the principal stress level that, based on the L_g-scaling, approach plane-strain levels over $-0.5 \leq \bar{T} \leq +0.25$.

E.3.3 Similarity for entire stress/strain states

Figure E.3 depicts the similarity scaling for the three principal stresses with radial distance on the centerplane ($Z/B = 0$) and over the uncracked plane ($\theta = 0°$). The T-stress values differ equal $\bar{T}$ =0, +0.25, -0.25, and -0.5, under the low loading level $\bar{K} = 1$. The principal stress varies among the rows with (a,b) σ_1/σ_0, (c,d) σ_2/σ_0, and (e,f) σ_3/σ_0. The length J/σ_0 normalizes the radial dimensions in the left column, whereas the characteristic length, L_g, (shown in Tab. E.1) normalizes the radial dimension in the right column. Figure E.3 also presents the plane-strain principal stresses in a $\bar{T} = 0$ configuration.

Ahead of the advancing crack front, the normalized curves in Fig. E.3 describe the stress-state (σ_{ij}/σ_0) under the levels $\bar{T}$ =+0.25, 0, -0.25, and -0.5. Further, within a small angular sector, detailed in Table E.1, these results suggest only three equations similar to Eqn. (E.4) – one equation for each principal stress – and the corresponding L_g value (at $\left(\bar{K}, \bar{T}\right)$) represent the near-front stresses in 3D SSY. Alternatively, the similarity scaling described by Eqn. (5.5) requires a different set of relationships for each combination of $\bar{K}$ and $\bar{T}$.

Table E.1 demonstrates that the characteristic length, L_g, relationship with $\bar{T}$ changes with each principal component. For example, the first and second principal stress components increase under a positive T-stress (L_g increases), but the third principal stress slightly decreases. In plane strain, high constraint induces uniformly lower stresses during steady crack growth [117] due to the larger plastic wake height (h_{pw}) under positive T-stress. In 3D SSY, h_{pw} under $\bar{K} = 1$ and $\bar{T} = +0.25$ (shown in Table 5.2) shrinks near the free surface compared to the $\bar{T} = 0$ value for h_{pw}. Negative T-stress uniformly reduces the principal stresses and h_{pw}. These results support the earlier energy arguments invoked during plane-strain, steady crack growth, *i.e.* under constant remote loading, a larger plastic wake trailing the crack front and due to non-zero T-stress reduces the intensity for the near-front fields. During steady ductile tearing in 3D SSY, the h_{pw} variation with Z/B leads to the relatively more complicated expression, as shown in Eqn. (E.4).

Only the first principal strain, $\varepsilon_1/\varepsilon_0$, displays the similarity scaling with L_g, and second and third principal strains cannot be described by a relationship corresponding to Eqn. (E.4). Further, the characteristic scaling for $\varepsilon_1/\varepsilon_0$ develops in a more slender angular region compared to the principal stresses. Imposed T-

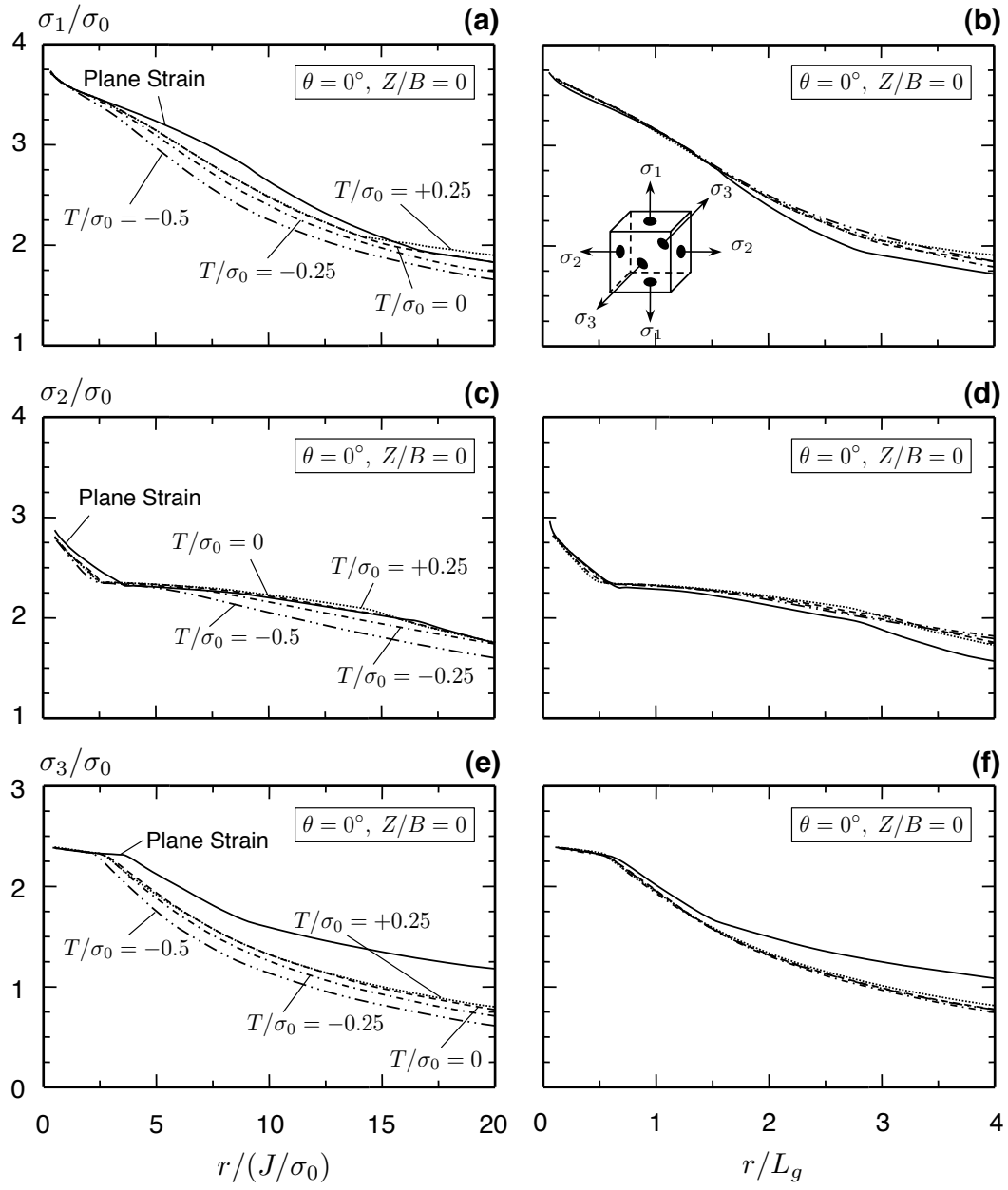

Figure E.3: Normalized principal stress components – σ_1/σ_0, σ_2/σ_0, and σ_3/σ_0 – variation with scaled radial distance on the centerplane ($Z/B = 0$) under $\bar{K} = 1$ loading. Results are shown along the uncracked plane, $\theta = 0^\circ$. The steady-growth, plane-strain solution at $T/\sigma_0 = 0$ is provided for reference. The distance J/σ_0 scales the radial dimensions in (a,c,e) whereas the characteristic length scale, L_g, scales the radial dimensions in (b,d,f). The near-front fields collapse into a single curve approaching the crack front in coordinates scaled by the characteristic dimension, L_g.

stress values in the 3D SSY framework alter the strain magnitude far from the advancing crack front. The second principal strain reaches a T-stress dependent, peak value ahead of the crack front, and, alternatively, the third principal strain strongly corresponds to ε_{zz} over most of the radial distance ahead of the crack front, and thus varies negligibly. Both strain components ε_2 and ε_3 require modifications to the strain-based version of Eqn. (E.4), *i.e.* T-stress dependent terms added to the right hand side of the equation. The relationship suggested by Eqn. (5.5) proves more robust and characterizes all strain components.

References

[1] Ahn, D. C., Sofronis, P., Dodds, R. H., 2007. Modeling of hydrogen-assisted ductile crack propagation in metals and alloys. Int. J. Frac. 145, 135–157.

[2] Ahn, D. C., Sofronis, P., Dodds, R. H., 2007. On hydrogen-induced plastic flow localization during void growth and coalescence. Int. J. Hyd. Energy 32, 3724–3742.

[3] Anderson, T. L., 1995. Fracture Mechanics, 2nd Edition. CRC Press.

[4] ASTM E 1820-09, 2009. Standard test method for measurement of fracture toughness.

[5] ASTM E 2472-06, 2006. Standard test method for determination of resistance to stable crack extension under low-constraint conditions.

[6] Baker, C., Birnbaum, H. K., 1972. On the hydrogen-dislocation interaction in niobium. Scr. Metall. 6, 851–853.

[7] Barenblatt, G. I., 1962. Mathematical theory of equilibrium cracks. Adv. Appl. Mech. 7, 56–129.

[8] Beachem, C. D., 1972. A new model for hydrogen-assisted cracking (hydrogen embrittlement). Met. Trans. 3, 437–451.

[9] Belytschko, T., Liu, W. K., Moran, B., 2000. Nonlinear Finite Elements for Continua and Structures. John Wiley and Sons.

[10] Beremin, F. M., 1983. Local criterion for cleavage fracture of a nuclear pressure vessel steel. Metall. Trans. A 14A, 2277–2287.

[11] Bernstein, I. M., Thompson, A. W., 1984. The role of microstructure in hydrogen embrittlement. In: Hydrogen Embrittlement and Stress Corrosion Cracking. pp. 135–152.

[12] Betegon, C., Hancock, J. W., 1991. Two-parameter characterization of elastic-plastic crack-tip fields. J. Appl. Mech. 58, 104–110.

[13] Birnbaum, H. K., Robertson, I. M., Sofronis, P., Teter, D., 1997. Mechanisms of hydrogen related fracture - a review. In: Magnin, T. (Ed.), Corrosion Deformation Interactions CDI'96 (Second International Conference, Nice, France, 1996). The Institute of Materials, pp. 172–195.

[14] Birnbaum, H. K., Sofronis, P., 1994. Hydrogen-enhanced localized plasticity - a mechanism for hydrogen-related fracture. Mat. Sci. and Eng. A176, 191–202.

[15] Burstow, M. C., Howard, I. C., Ainsworth, R. A., 1998. The influence of constraint on crack tip stress fields in strength mismatched welded joints. J. Mech. Phys. Solids 46 (5), 845–872.

[16] Cochran, K. B., 2009. Numerical modeling issues in finite element simulation of plasticity induced crack closure with an emphasis on material model effects. Ph.D. thesis, University of Illinois at Urbana-Champaign.

[17] Crisfield, M. A., 1991. Non-Linear Finite Element Analysis of Solids and Structures. Vol. 1: Essentials. John Wiley and Sons.

[18] Dadfarnia, M., Sofronis, P., Somerday, B. P., Liu, J. B., Johnson, D. D., Robertson, I. M., 2009. Modeling issues on hydrogen-induced intergranular cracking under sustained load. In: Somerday, B. P., Sofronis, P., Jones, R. H. (Eds.), Effects of Hydrogen on Materials (International Conference, Jackson Lake Lodge, WY). ASM, in press.

[19] Dawicke, D. S., Newman, J. C., Bigelow, C. A., 1995. Three-dimensional CTOA and constraint effects during stable tearing in a thin-sheet material. In: Walter, R. G., Underwood, J. H., Newman, J. C. (Eds.), Fracture Mechanics: 26th Conference. STP 1256. ASTM, pp. 223–242.

[20] Dean, R. H., 1983. Elastic-plastic steady crack growth in plane stress. In: Shih, C. F., Gudas, J. P. (Eds.), Elastic-Plastic Fracture: Second Symposium, Volume I - Inelastic Crack Analysis. STP 803. ASTM, pp. I–39–I–51.

[21] Dean, R. H., Hutchinson, J. W., 1980. Quasi-static steady crack growth in small-scale yielding. In: Paris, P. C. (Ed.), Fracture Mechanics: 12th Conference. STP 700. ASTM, pp. 383–405.

[22] Dhirendra, V. K., Narasimhan, R., 1998. Mixed-mode steady-state crack growth in elastic plastic solids. Eng. Frac. Mech. 59 (4), 543–559.

[23] Dodds, R. H., 1982. Effects of reduced integration on the 2-D quadratic isoparametric element in plane strain plasticity. Int. J. Frac. 19, R75–R82.

[24] Drugan, W. J., 1998. Limitations to leading-order asymptotic solutions for elastic-plastic crack growth. J. Mech. Phys. Solids 46, 2361–2386.

[25] Drugan, W. J., 1998. Thermodynamic equivalence of steady-state shocks and smooth waves in general media: applications to elastic-plastic shocks and dynamic-fracture. J. Mech. Phys. Solids 46, 313–336.

[26] Drugan, W. J., 1998. Thermodynamic equivalence of steady-state shocks and smooth waves in general media; applications to elastic-plastic shocks and dynamic fracture. J. Mech. Phys. Solids 46 (2), 313–316.

[27] Drugan, W. J., Rice, J. R., Sham, T.-L., 1982. Asymptotic analysis of growing plane strain tensile cracks in elastic-ideally plastic solids. J. Mech. Phys. Solids 30 (6), 447–473.

[28] Dugdale, D. S., 1960. Yielding of steel sheets containing slits. J. Mech. Phys. Solids 8, 100–104.

[29] Ferracin, T., Landis, C. M., Delannay, F., Pardoen, T., 2003. On the determination of the cohesive zone properties of an adhesive layer from the analysis of the wedge-peel test. Int. J. Solids and Struc. 40, 2889–2904.

[30] Freund, L. B., 1990. Dynamic Fracture Mechanics. Cambridge University Press.

[31] Freund, L. B., Douglas, A. S., 1982. The influence of inertia on elastic-plastic antiplane-shear crack growth. J. Mech. Phys. Solids 30 (1/2), 59–74.

[32] Freund, L. B., Hutchinson, J. W., 1985. High strain-rate crack growth in rate-dependent plastic solids. J. Mech. Phys. Solids 33, 169–191.

[33] Freund, L. B., Hutchinson, J. W., Lam, P. S., 1986. Analysis of high-strain-rate elastic-plastic crack growth. Eng. Frac. Mech. 23 (1), 119–129.

[34] Gao, X., Dodds, R. H., 2000. Constraint effects on the ductile-to-brittle transition temperature of ferritic steels: a Weibull stress model. Int. J. Frac. 102, 43–69.

[35] Gao, X., Shih, C., Tvergaard, V., Needleman, A., 1996. Constraint effects on the ductile-brittle transition in small scale yielding. J. Mech. Phys. Solids 44 (8), 1255–1282.

[36] Garber, R., Bernstein, I. M., Tompson, A. W., 1981. Hydrogen assisted ductile fracture of spheroidized carbon steels. Metall. Trans. A 12, 225–234.

[37] Garrison, W. M., Moody, N. R., 1987. Ductile fracture. J. Phys. Chem. Solids 48, 1035–1074.

[38] Gullerud, A., Koppenhoefer, K., Roy, A., RoyChowdhury, S., Walters, M., Bichon, B., Cochran, K., Carlyle, A., Dodds, R., 2007. WARP3D: 3-D dynamic nonlinear fracture analysis of solids using parallel computers and workstations. Tech. rep., University of Illinois.

[39] Gullerud, A. S., Dodds, R. H., Hampton, R. W., Dawicke, D. S., 1999. Three-dimensional modeling of ductile crack growth in thin sheet metals: computational aspects and validation. Eng. Frac. Mech. 63, 347–374.

[40] Gurson, A. L., 1977. Continuum theory of ductile rupture by void nucleation and growth: Part i - yield criteria and flow rules for porous ductile media. J. Engng. Mater. Technol. 99, 2–15.

[41] Hancock, J. W., Reuter, W. G., Parks, D. M., 1993. Constraint and toughness parameterized by T. In: Hackett, E. M., Schwalbe, K. H., Dodds, R. H. (Eds.), Constraint effects in fracture. STP 1171. ASTM, pp. 21–40.

[42] Hertzberg, R. W., 1996. Deformation and Fracture Mechanics of Engineering Materials. John Wiley and Sons.

[43] Hill, R., 1950. The Mathematical Theory of Plasticity. Oxford University.

[44] Hom, C. L., McMeeking, R. M., 1989. Three-dimensional void growth before a blunting crack tip. J. Mech. Phys. Solids 37, 395–415.

[45] Hom, C. L., McMeeking, R. M., 1990. Large crack tip opening in thin elastic-plastic sheets. Int. J. Frac. 45, 103–122.

[46] Joyce, J. A., Link, R. E., 1995. Effects of constraint on upper shelf fracture toughness. In: Reuter, W. G., Underwood, J. H., Newman, J. C. (Eds.), Fracture mechanics: 26th volume. STP 1256. ASTM, pp. 142–173.

[47] Joyce, J. A., Link, R. E., 1997. Application of two parameter elastic-plastic fracture mechanics to analysis of structures. Eng. Frac. Mech. 57, 431–446.

[48] Kim, Y., Zhu, X. K., Chao, Y. J., 2001. Quantification of constraint on elastic-plastic 3D crack front by the $J - A_2$ three-term solution. Eng. Frac. Mech. 68, 895–914.

[49] Krieg, R. D., Krieg, D. B., 1977. Accuracies of numerical solution methods for the elastic-perfectly plastic model. J. Pres. Ves. Tech., Trans. ASME 99, 510–515.

[50] Kumar, R. K., Narasimhan, R., Prabhakar, O., 1991. Temperature rise in a viscoplastic material during dynamic crack growth. Int. J. Frac. 48, 23–40.

[51] Lam, P. S., Freund, L. B., 1985. Analysis of dynamic growth of a tensile crack in an elastic-plastic material. J. Mech. Phys. Solids 33 (2), 153–167.

[52] Landis, C. M., Pardoen, T., Hutchinson, J. W., 2000. Crack velocity dependent toughness in rate dependent materials. Mech. Mater. 32, 663–678.

[53] Larsson, S. G., Carlsson, A. J., 1973. Influence of non-singular stress terms and specimen geometry on small-scale yielding at crack tips in elastic-plastic materials. J. Mech. Phys. Solids 21, 263–277.

[54] Lee, H. M., 1976. The solubility of hydrogen in transition metals. Metall. Trans. A 7, 431–433.

[55] Leevers, P. S., Radon, J. C., 1982. Inherent stress biaxiality in various fracture specimen geometries. Int. J. Frac. 19, 311–325.

[56] Levy, N., Marcal, P. V., Rice, J. R., 1971. Progress in three-dimensional elastic-plastic stress analysis for fracture mechanics. Nuc. Eng. Des. 17, 64–75.

[57] Li, J. C. M., Oriani, R. A., Darken, L. S., 1966. The thermodynamics of stressed solids. Z. Physik Chem. Neue. Folge 49, 271–291.

[58] Liang, Y., Ahn, D. C., Sofronis, P., Dodds, R. H., Bammann, D., 2008. Effect of hydrogen trapping on void growth and coalescence in metals and alloys. Mech. Mater. 40, 115–132.

[59] Liang, Y., Sofronis, P., Dodds, R. H., 2004. Interaction of hydrogen with crack-tip plasticity: effects of constraint on void growth. Mat. Sci. and Eng. A366, 397–411.

[60] Lin, G., Meng, X. G., Cornec, A., Schwalbe, K. H., 1999. The effect of strength mismatch on mechanical performance of weld joints. Int. J. Frac. 96, 37–54.

[61] Liu, N., Drugan, W. J., 1993. Finite deformation finite element analyses of tensile growing crack fields in elastic-plastic material. Int. J. Frac. 61, 189–210.

[62] Lubliner, J., 2008. Plasticity Theory. Dover Publications.

[63] Mahmoud, S., Lease, K., 2003. The effect of specimen thickness on the experimental characterization of critical crack-tip-opening angle in 2024-T351 aluminum alloy. Eng. Frac. Mech. 70, 443–456.

[64] Mahmoud, S., Lease, K., 2004. Two-dimensional and three-dimensional finite element analysis of critical crack-tip-opening angle in 2024-T351 aluminum alloy at four thicknesses. Eng. Frac. Mech. 71, 1379–1391.

[65] Manguoglu, M., Sameh, A., Schenk, O., Aug. 2009. PSPIKE parallel sparse linear system solver. In: Sips, H., Epema, D., Lin, H.-X. (Eds.), Proceedings of the 15th International Euro-Par Conference on Parallel Processing. EUROPAR 2009 Conference, pp. 797–808.

[66] McMeeking, R. M., 1977. Finite deformation analysis of crack-tip opening in elastic-plastic materials and implications for fracture. J. Mech. Phys. Solids 25, 357–381.

[67] McMeeking, R. M., 1977. Finite deformation analysis of crack-tip opening in elastic-plastic materials and implications for fracture. J. Mech. Phys. Solids 25, 357–381.

[68] Mendelson, A., 1968. Plasticity: Theory and Applications. Macmillian.

[69] Meyers, S. M., Baskes, M. I., Birnbaum, H. K., Corbett, J. W., Deleo, G. G., Estreicher, S. K., Haller, E. E., Jena, P., Johnson, N. M., Kirchheim, R., Pearton, S. J., Stavola, M. J., 1992. Hydrogen interactions with defects in crystalline solids. Rev. Mod. Phys. 64 (2), 559–617.

[70] Moran, B., Shih, C. F., 1987. Crack tip and associated domain integrals from momentum and energy balance. Eng. Frac. Mech. 37 (6), 615–642.

[71] Nakamura, T., Parks, D. M., 1988. Three-dimensional stress field near the crack front of a thin elastic plate. J. Appl. Mech. 55 (4), 805–813.

[72] Nakamura, T., Parks, D. M., 1990. Three-dimensional crack front fields in a thin ductile plate. J. Mech. Phys. Solids 38 (6), 787–812.

[73] Narasimhan, R., Rosakis, A. J., Hall, J. F., 1987. A finite element study of stable crack growth under plane stress conditions: Part I - elastic-perfectly plastic solids. J. App. Mech., Trans. ASME 54, 838–845.

[74] Narasimhan, R., Rosakis, A. J., Hall, J. F., 1987. A finite element study of stable crack growth under plane stress conditions: Part II - influence of hardening. J. App. Mech., Trans. ASME 54, 846–853.

[75] Needleman, A., 1987. A continuum model for void nucleation by inclusion debonding. J. Appl. Mech. 54, 525–531.

[76] Newman, J. C., Dawicke, D. S., Seshadri, B. R., 2003. Residual strength analyses of stiffened and un-stiffened panels - Part I: laboratory specimens. Eng. Frac. Mech. 70, 493–507.

[77] Newman, J. C., James, M. A., Zerbst, U., 2003. A review of the CTOA/CTOD fracture criterion. Eng. Frac. Mech. 70, 371–385.

[78] Niordson, C. F., 2001. Analysis of steady-state ductile crack growth along a laser weld. Int. J. Frac. 111, 53–69.

[79] O'Dowd, N. P., Shih, C. F., 1991. Family of crack-tip fields characterized by a triaxiality parameter-i. structure of fields. J. Mech. Phys. Solids 39, 989–1015.

[80] Oriani, R. A., 1970. The diffusion and trapping of hydrogen in steel. Acta Metall. 18, 147–157.

[81] Ostlund, S., 1990. On numerical modeling and fracture criteria of dynamic elastic-viscoplastic crack growth. Int. J. Frac. 44, 283–299.

[82] Pardoen, T., Hutchinson, J. W., 2003. Micromechanics-based model for trends in toughness of ductile metals. Acta Mater. 51, 133–148.

[83] Parks, D. M., Lam, P. S., McMeeking, M., 1981. Some effects of inelastic constitutive models on crack tip fields in steady quasistatic growth. In: Francois, D. (Ed.), Advances in Fracture Research. Vol. 5. 5th International Conference on Fracture, pp. 2607–2614.

[84] Peisl, H., 1978. Lattice strains due to hydrogen in metals. In: Alefeld, G., Volkl, J. (Eds.), Hydrogen in Metals I. Vol. 28. Springer, New York, pp. 53–74.

[85] Petti, J. P., Dodds, R. H., 2005. Calibration of the weibull stress scale parameter, σ_u, using the Master Curve. Eng. Frac. Mech. 72, 91–120.

[86] Petti, J. P., Dodds, R. H., 2005. Ductile tearing and discrete void effects on cleavage fracture under small-scale yielding conditions. Int. J. Solids and Struc. 42, 3655–3676.

[87] Pineau, A., 2008. Modeling ductile to brittle fracture transition in steels–micromechanical and physical challenges. Int. J. Frac. 150, 129–156.

[88] Reid, C. R., Drugan, W. J., 1993. Asymptotic finite deformation analysis of growing crack fields in elastic-perfectly plastic materials. J. Mech. Phys. Solids 41, 689–723.

[89] Rice, J. R., 1974. Limitations to the small scale yielding approximation for crack tip plasticity. J. Mech. Phys. Solids 22, 17–26.

[90] Rice, J. R., Drugan, W. J., Sham, T.-L., 1980. Elastic-plastic analysis of growing cracks. In: Paris, P. C. (Ed.), Fracture Mechanics: 12th Conference. STP 700. ASTM, pp. 189–219.

[91] Rice, J. R., Sorensen, E. P., 1978. Continuing crack-tip deformation and fracture for plane-strain crack growth in elastic-plastic solids. J. Mech. Phys. Solids 26, 163–186.

[92] Rice, J. R., Tracey, D. M., 1969. On the ductile enlargement of voids in triaxial stress fields. J. Mech. Phys. Solids 17, 201–217.

[93] Robertson, I. M., 2001. The effect of hydrogen on dislocation motion. Eng. Frac. Mech. 68, 671–692.

[94] Robinson, S. L., Stoltz, R. E., 1981. Toughness losses and fracture behavior of low strength carbon-manganese steels in hydrogen. In: Hydrogen effects in metals. The Metall. Soc. of AIME. The Metall., pp. 987–995.

[95] Roychowdhury, S., Dodds, R. H., 2003. A numerical investigation of 3-D small-scale yielding fatigue crack growth. Eng. Frac. Mech. 70, 2363–2383.

[96] Roychowdhury, S., Dodds, R. H., 2003. Three-dimensional effects of fatigue crack closure in the small-scale yielding regime - a finite element study. Fatigue Fract. Engng. Mater. Struct. 26, 663–673.

[97] Roychowdhury, S., Dodds, R. H., 2004. Effect of T-stress on fatigue crack closure in 3-D small-scale yielding. Int. J. Solids and Struc. 41, 2581–2606.

[98] Ruggieri, C., Dodds, R. H., 1996. A transferability model for brittle fracture including constraint and ductile tearing effects: a probabilistic approach. Int. J. Frac. 79, 309–340.

[99] Schwalbe, K.-H., Newman, J. C., Shannon, J. L., 2005. Fracture mechanics testing on specimens with low constraint-standardisation activities within ISO and ASTM. Eng. Frac. Mech. 72, 557–576.

[100] Seshadri, B. R., Newman, J. C., Dawicke, D. S., 2003. Residual strength analyses of stiffened and unstiffened panels - part II: wide panels. Eng. Frac. Mech. 70, 509–524.

[101] Shih, D., Robertson, I. M., Birnbaum, H. K., 1988. Hydrogen embrittlement of α titanium: In situ tem studies. Acta Metall. 36, 111–124.

[102] Simo, J. C., Hughes, T. J. R., 1998. Computational Inelasticity. Springer-Verlag.

[103] Sirois, E., Birnbaum, H. K., 1992. Effects of hydrogen and carbon on thermally activated deformation in nickel. Acta Metall. 40, 1377–1385.

[104] Sirois, E., Sofronis, P., Birnbaum, H. K., 1992. Effects of hydrogen and carbon on thermally activated deformation in nickel. In: Bruemmer, S. M., Meletis, E. I., Jones, J. H., Gerberich, W. W., Ford, F. P., Staehle, R. W. (Eds.), Parkins Symposium on Fundamental Aspects of Stress Corrosion Cracking. The Minerals, Metals, & Materials Society, pp. 173–190.

[105] Sofronis, P., 1995. The influence of mobility of dissolved hydrogen on the elastic response of a metal. J. Mech. Phys. Solids 43, 1385–1407.

[106] Sofronis, P., Birnbaum, H. K., 1995. Mechanics of the hydrogen-dislocation-impurity interactions - i. increasing shear modulus. J. Mech. Phys. Solids 43, 49–90.

[107] Sofronis, P., Liang, Y., Aravas, N., 2001. Hydrogen induced shear localization of the plastic flow in metals and alloys. Euro. J. Mech. A 20, 857–872.

[108] Tabata, T., Birnbaum, H. K., 1983. Direct observationsof the effect of hydrogen on the behavior of dislocations in iron. Scr. Metall. 17, 947–950.

[109] Taha, A., Sofronis, P., 2001. A micromechanical approach to the study of hydrogen transport and embrittlement. Eng. Frac. Mech. 68, 803–837.

[110] Tracey, D. M., 1976. Finite element solutions for crack-tip behavior in small-scale yielding. J. Engng. Mater. Technol. 98, 146–151.

[111] Tvergaard, V., 1990. Material failure by void growth to coalescence. Adv. Appl. Mech. 27, 83–151.

[112] Tvergaard, V., Hutchinson, J. W., 1992. The relationship between crack growth resistance and fracture process parameters in elastic-plastic solids. J. Mech. Phys. Solids 40 (6), 1377–1397.

[113] Tvergaard, V., Hutchinson, J. W., 1993. The influence of plasticity on mixed mode interface toughness. J. Mech. Phys. Solids 41, 1119–1135.

[114] Tvergaard, V., Hutchinson, J. W., 1994. Effect of T-stress on mode I crack growth in a ductile solid. Int. J. Solids and Struc. 31, 823–833.

[115] Tvergaard, V., Hutchinson, J. W., 1996. Effect of strain-dependent cohesive zone model on predictions of crack growth resistance. Int. J. Solids and Struc. 33 (20–22), 3297–3308.

[116] Tvergaard, V., Hutchinson, J. W., 1996. On the toughness of ductile adhesive joints. J. Mech. Phys. Solids 44, 789–800.

[117] Varias, A. G., Shih, C. F., 1993. Quasi-static crack advance under a range of constraints - steady-state fields based on a characteristic length. J. Mech. Phys. Solids 41 (5), 835–861.

[118] Varias, A. G., Shih, C. F., 1994. Dynamic steady crack growth in elastic-plastic solids - propagation of strong discontinuities. J. Mech. Phys. Solids 42 (11), 1817–1848.

[119] Volkl, J., Alefeld, G., 1978. Diffusion of hydrogen in metals. In: Alefeld, G., Volkl, J. (Eds.), Hydrogen in Metals I, Topics in Applied Physics. Vol. 28. Springer, pp. 321–348.

[120] Wallin, K., 1984. The scatter in K_{IC} results. Eng. Frac. Mech. 19, 1085–1093.

[121] Wallin, K., 1989. The effect of ductile tearing on cleavage fracture probability in fracture toughness testing. Eng. Frac. Mech. 32, 523–531.

[122] Wallin, K., 1989. The effect of ligament size on cleavage fracture toughness. Eng. Frac. Mech. 32, 449–457.

[123] Wang, X., Lambert, S. B., 1995. Stress intensity factors for low aspect ratio semi-elliptical surface cracks in finite-thickness plates subjected to nonuniform stresses. Eng. Frac. Mech. 51, 517–532.

[124] Wei, R. P., Simmons, K., Chou, G. W., 1984. Fracture mechanics and surface chemistry investigations of environment-assisted crack growth. In: Hydrogen Embrittlement and Stress Corrosion Cracking. Am. Soc. Metals. pp. 103–133.

[125] Wei, Y., Hutchinson, J. W., 1997. Nonlinear delamination mechanics for thin films. J. Mech. Phys. Solids 45, 1137–1159.

[126] Wei, Y., Hutchinson, J. W., 1997. Steady-state crack growth and work of fracture for solids characterized by strain gradient plasticity. J. Mech. Phys. Solids 45 (8), 1253–1273.

[127] Wei, Y., Hutchinson, J. W., 2008. Toughness of Ni/Al_2O_3 interfaces as dependent on micron-scale plasticity and atomistic-scale seperation. Philos. Mag. 88, 3841–3859.

[128] Williams, M. L., 1957. On the stress distribution at the base of a stationary crack. J. Appl. Mech. 24, 109–114.

[129] Xia, L., Shih, C. F., 1995. Ductile crack growth - II. void nucleation and geometry effects on macroscopic fracture behavior. J. Mech. Phys. Solids 43, 1953–1981.

[130] Xia, L., Shih, C. F., 1995. Ductile crck growth - I. a numerical study using computational cells with microstructurally-based length scales. J. Mech. Phys. Solids 43, 233–259.

[131] Xia, L., Shih, C. F., 1996. Ductile crack growth - III. transition to cleavage fracture incorporating statistics. J. Mech. Phys. Solids 44, 603–639.

[132] Xia, L., Shih, C. F., Hutchinson, J. W., 1995. A computational approach to ductile crack growth under large scale yielding conditions. J. Mech. Phys. Solids 43 (3), 389–413.

[133] Yuan, H., Brocks, W., 1998. Quantification of constraint effects in elastic-plastic crack front fields. J. Mech. Phys. Solids 46 (2), 219–241.